
Investigation and evaluation of atmospheric sulfur dioxide in the EMAC model

Ismail Makroum



München 2024

Investigation and evaluation of atmospheric sulfur dioxide in the EMAC model

Ismail Makroum

Dissertation
an der Fakultät für Physik
der Ludwig-Maximilians-Universität
München

vorgelegt von
Ismail Makroum
aus Fez, Marokko

München, den 05. September 2024

Erstgutachter: Prof. Dr. habil. Martin Dameris

Zweitgutachter: Prof. Dr. Bernhard Mayer

Tag der mündlichen Prüfung: 23. Oktober 2024

Zusammenfassung: Untersuchung und Bewertung des atmosphärischen Schwefeldioxids im EMAC-Modell

Schwefeldioxid (SO_2) ist ein Spurengas in der Erdatmosphäre mit vielfältigen Auswirkungen auf das Klima und die Umwelt. Der größte Beitrag zu atmosphärischem SO_2 sind anthropogene Emissionen, welche in erster Linie aus der Verbrennung von schwefelhaltigen Brennstoffen stammen. Zu den natürlichen SO_2 Quellen gehören vulkanische Ereignisse und die Oxidation von Schwefelspezies wie Dimethylsulfid (DMS) aus den Ozeanen. SO_2 kann direkt durch trockene und nasse Deposition aus der Atmosphäre entfernt oder in der Gas- und Flüssigphase zu Schwefelsäure (H_2SO_4) oxidiert werden. Diese Säure kann zur Bildung von saurem Regen führen, der sich negativ auf Ökosysteme auswirkt. Außerdem kann SO_2 in der Atmosphäre Sulfatpartikel bilden, die die einfallende Sonnenstrahlung reflektieren, was zu einer Abkühlung an der Oberfläche führt.

Diese Arbeit stellt erstmalig eine umfassende Untersuchung des atmosphärischen Schwefeldioxids im Klima-Chemie Modell EMAC vor. Zu Beginn wird gezeigt, dass das troposphärische Schwefelbudget in EMAC geschlossen ist, was eine wichtige Grundlage für die weiteren Untersuchungen darstellt. Mit dem Ziel, das atmosphärische SO_2 über verschmutzten Regionen zu untersuchen, werden die Ergebnisse von EMAC mit Beobachtungsdaten verglichen. Die Ergebnisse für das Jahr 2019 zeigen, dass die simulierten bodennahen SO_2 Konzentrationen etwa $1,7 \pm 0,3$ mal höher sind als die beobachteten SO_2 Konzentrationen aus bodengestützten Netzwerken. Diese Diskrepanz ist konsistent mit den Unterschieden zwischen simulierten und aus Beobachtungen (satellitengestützte Messungen) abgeleiteten vertikalen SO_2 Säulendichten über denselben Regionen. Das deutet darauf hin, dass die vorgeschriebenen SO_2 Emissionen in EMAC überschätzt sind. Desweiteren wird eine Fallstudie durchgeführt, um die emittierte SO_2 Menge und den anschließenden Verlust von SO_2 nach den Vulkanausbrüchen von Raikoke (48.3°N , 153.2°O) und Ulawun (5.05°S , 151.33°O) im Jahr 2019 zu bewerten. Zu diesem Zweck werden Sensitivitätssimulationen unter Berücksichtigung beider Vulkane durchgeführt. Die Ergebnisse zeigen eine sehr gute Übereinstimmung zwischen der simulierten zeitlichen Entwicklung der atmosphärischen SO_2 -Menge nach den Ausbrüchen und den satellitengestützten Beobachtungsdaten. Über einen längeren Zeitraum (2000-2019) reproduziert die EMAC-Simulation die gemessenen rückläufigen Trends der SO_2 -Konzentrationen und der Schwefeldeposition in den USA und Europa, kann jedoch die beobachteten Trends in Ostasien nicht adäquat wiedergeben. Dies ist höchstwahrscheinlich auf die vorgeschriebenen SO_2 Emissionen in den verwendeten Emissionsinventaren zurückzuführen. Für eine weitere Fallstudie, die sich auf lokale Messungen des troposphärischen SO_2 Mischungsverhältnisses mit Hilfe von Flugzeugdaten konzentriert, wird aufgrund seiner feinen räumlichen und zeitlichen Auflösung das ME-CO(n) Modellsystem verwendet. Die Analyse zeigt Unterschiede zwischen simulierten und gemessenen SO_2 Mischungsverhältnissen, die auf Ungenauigkeiten des Modells bei der korrekten Darstellung der Grenzschichthöhe zurückzuführen sind.

Zusammenfassend zeigen die Ergebnisse, dass das EMAC-Modell die räumliche und zeitliche Verteilung von SO_2 , wie sie von weltraum- und bodengestützten Instrumenten beobachtet wird, trotz einiger Diskrepanzen gut wiedergibt. Diese Diskrepanzen sind auf verschiedene Faktoren zurückzuführen, wie zum Beispiel die über- oder unterschätzten Messdaten, die Darstellung der Schwefeldepositionsflüsse im Modell und die verwendeten Emissionsinventare. Allerdings gibt es Einschränkungen bei der Berechnung der gemessenen SO_2 Mischungsverhältnisse entlang der Flugrouten in der Nähe von lokal verstärkten Quellen.

Abstract: Investigation and evaluation of atmospheric sulfur dioxide in the EMAC model

Sulfur dioxide (SO_2) is a harmful atmospheric pollutant with multiple impacts on the climate and environment. The largest contribution to atmospheric SO_2 are anthropogenic emissions, primarily stemming from the combustion of sulfur-containing fuels. Natural sources include volcanic emissions and the oxidation of sulfur species such as Dimethyl Sulfide (DMS) from the oceans. SO_2 can be deposited at the Earth's surface directly through dry and wet deposition, or oxidized in the gas and liquid phases to form sulfuric acid (H_2SO_4). This acid can lead to the formation of acid rain, which negatively affects ecosystems. Additionally, SO_2 can form sulfate particles in the atmosphere, which reflect incoming solar radiation, leading to a cooling of the atmosphere near the surface.

This work presents, for the first time, a comprehensive examination of atmospheric sulfur dioxide within the EMAC Chemistry-Climate Model. The tropospheric sulfur budget within EMAC is verified to be closed, which is an important groundwork for further investigations. In this thesis the results from EMAC are compared to observational data with the objective of examining atmospheric SO_2 over polluted regions. There, the EMAC results for 2019 show that the SO_2 concentrations near the Earth's surface are about 1.7 ± 0.3 times larger than observed SO_2 concentrations from ground-based networks. This discrepancy aligns well with the difference between simulated and retrieved (satellite-based measurements) SO_2 vertical column densities over the same regions. This indicates that the prescribed SO_2 emissions in EMAC might be overestimated. Furthermore, a case study is performed to assess the emitted amount and the subsequent loss (deposition) of SO_2 following the Raikoke (48.3°N , 153.2°E) and Ulawun (5.05°S , 151.33°E) volcanic eruptions in 2019. For this, sensitivity simulations considering both volcanoes were performed. The results show a very good agreement of the simulated temporal evolution of the amount of atmospheric SO_2 after the eruptions with that retrieved from satellite-based observations. Over a longer time period (2000-2019), the EMAC simulation reproduces the measured declining trends of SO_2 concentrations and deposited sulfur fluxes in the USA and Europe, but fails to simulate the observed trends in East Asia. This is most likely attributable to the prescribed SO_2 emissions in the applied emission inventories. A further case study within this thesis focuses on local tropospheric SO_2 mixing ratio measurements from airborne data. To accompany these adequately, the MECO(n) model system was used, due to its fine spatial and temporal resolutions. However, the MECO(n) model shows difficulties to reproduce the measured SO_2 mixing ratios along flight tracks, which are related to model's inaccuracies in correctly representing the boundary layer height.

In summary, the results indicate that the EMAC model represents the spatial and temporal distribution of SO_2 as observed by space- and ground-based instruments, despite some differences. These discrepancies can be attributed to various factors, such as over- or underestimated values from observations, the representation of sulfur deposition fluxes in the model, and the accuracy of used emission inventories. Finally, limitations particularly occur in reproducing measured SO_2 mixing ratios along flight tracks near strong localized sources.

Contents

Zusammenfassung	v
Abstract	vii
1 Introduction	1
1.1 Motivation	1
1.2 Research questions and outline	3
2 Scientific background	5
2.1 The radiative forcing of sulfur dioxide	5
2.2 Budget of atmospheric sulfur dioxide	6
2.2.1 Sources of sulfur dioxide	7
2.2.2 Sinks of sulfur dioxide	8
3 Methods	13
3.1 Model description	13
3.1.1 MESSy framework	14
3.1.2 The EMAC model	15
3.1.3 The MECO(n) model system	16
3.1.4 The OFFEMIS submodel	17
3.1.5 The AIRSEA submodel	17
3.1.6 The TNUDGE submodel	17
3.1.7 The SCAV submodel	18
3.1.8 The MECCA submodel	20
3.1.9 The DDEP submodel	21
3.1.10 The SEDI submodel	22
3.1.11 The SORBIT submodel	23
3.1.12 Description of the boundary conditions of the used sulfur emissions	24
3.2 Description of the used observational data	31
3.2.1 Satellite observations	31
3.2.2 Ground-based measurements	36
3.2.3 Airborne measurements	40
3.3 Description of the model setup	42

3.3.1	Post-processing of model data for comparison with satellite observations	42
3.3.2	Post-processing of model data for comparison with ground-based measurements	49
3.3.3	Post-processing model data for comparison with airborne measurements	50
4	Investigation of the tropospheric sulfur budget in the EMAC model	55
4.1	Tropospheric sulfur budget within EMAC	55
4.2	How does the tropospheric sulfur budget in the EMAC model compare to that of other atmospheric chemistry models?	64
4.3	The effect of aerosols on SO ₂ in EMAC	66
4.4	Discussion and conclusion	68
4.4.1	Tropospheric sulfur budget within EMAC	68
4.4.2	Tropospheric sulfur budget in EMAC against atmospheric chemistry models	69
4.4.3	The effect of aerosols on SO ₂ in EMAC	69
5	Comparing SO₂ simulated by the EMAC Model with TROPOMI data	71
5.1	Geo-spatial distribution and discrepancies of SO ₂ VCDs between EMAC results and TROPOMI retrievals for the year 2019	72
5.2	Effects of volcanic eruptions on the simulated atmospheric SO ₂ in the EMAC Model	77
5.3	Evaluation of SO ₂ from anthropogenic and outgassing volcano emissions . .	88
5.4	Discussion and conclusion	97
5.4.1	Geo-spatial distribution and discrepancies of SO ₂ VCDs between EMAC results and TROPOMI retrievals for the year 2019	97
5.4.2	Effects of volcanic eruptions on the simulated atmospheric SO ₂ in the EMAC Model	97
5.4.3	Evaluation of SO ₂ from anthropogenic and outgassing volcano emissions	98
6	Evaluation of simulated SO₂ with ground-based measurements	101
6.1	Sulfur concentration and deposition in the USA	102
6.2	Sulfur concentration and deposition in Europe	107
6.3	Sulfur concentration and deposition in China and Japan	109
6.4	Discussion and conclusion	112
6.4.1	Evaluation of sulfur simulation in the USA and Europe	113
6.4.2	Evaluation of sulfur simulation in China and Japan	114
7	Analysis of SO₂ from MECO(n) compared to airborne measurements	117
7.1	SO ₂ mixing ratios at flight levels over power plants in Serbia	118
7.2	SO ₂ mixing ratios within the boundary layer in Serbia	122

7.3 Discussion and conclusion	126
8 Conclusions and Outlook	129
Acronyms	137
A Appendices	141
A.1 Mechanism of the liquid phase chemistry	141
A.2 Mechanism of the gas phase chemistry	145
References	155
Danksagung	174

Chapter 1

Introduction

1.1 Motivation

Air pollution is a pressing global issue that affects not only human health but also the climate of the Earth (Wood et al., 2024). At present, the Earth's atmosphere mainly consists of the gases nitrogen (N_2), molecular oxygen (O_2), argon (Ar) and water vapor (H_2O) (Haynes, 2017). Many of the additional gases, so called trace gases, of the Earth's atmosphere have an impact on the climate due to their effect on the Earth's radiation balance and chemistry, and accordingly on human health, vegetation and water salinity (Seinfeld and Pandis, 2006). Historically, global climate change has been usually linked to the increase of carbon dioxide (CO_2) concentrations (Hansen et al., 1984). Later on, other less abundant trace gases, such as methane (CH_4), ozone (O_3), chlorofluorocarbons (CFCs), and sulfur dioxide (SO_2), came into focus (Dickinson and Cicerone, 1986).

SO_2 has a significant impact on life on Earth, the environment, and climate (Seinfeld and Pandis, 2006). Therefore, the aim of this thesis is to understand the distribution and behavior of SO_2 in the atmosphere, particularly in the troposphere. Tropospheric SO_2 has a relatively short lifetime of approximately one to three days (Koch et al., 1999). When SO_2 undergoes oxidation in aerosol particles or cloud droplets, its lifetime is reduced to even hours (von Glasow et al., 2009). Following the oxidation, the resulting sulfur-containing species are removed from the atmosphere through processes such as dry and wet deposition, as well as through aerosol sedimentation. SO_2 is a colorless trace gas and is the most abundant sulfur compound in the atmosphere. It affects the environment regionally and has also a global impact on climate, as it acts as a key precursor for the production of sulfate aerosols (Richter et al., 2006). SO_2 is a significant air pollution contributor, particularly in industrial and urban areas (Ramanathan, 2020). Anthropogenic sources of SO_2 are burning of sulfur-containing fuels, oil refining processes and metal ore smelting operations. Natural sources of SO_2 are eruptive and outgassing volcanoes (Dahiya et al., 2020), the production through the oxidation of Dimethyl Sulfide (DMS) from the oceans and biogenic emissions from terrestrial ecosystems (Andreae and Crutzen, 1997).

Sulfate aerosol particles reflect and scatter incoming solar radiation back into space, re-

ducing the amount of sunlight that reaches the Earth's surface and thus contribute to cooling air temperatures near the surface (Ye et al., 2023). Aerosol particles injected into the stratosphere at higher altitudes, such as those following volcanic eruptions, lead to stronger cooling of the atmosphere compared to aerosols at lower altitudes. This is primarily due to the longer residence time of aerosols in the stratosphere (Krishna-Pillai Sukumara-Pillai et al., 2019). Additionally, sulfate aerosols can serve as cloud condensation nuclei (CCN), that are particles around which cloud droplets can nucleate. An increased concentration of CCN can lead to the formation of clouds that reflect incoming solar radiation. The enhanced Earth's albedo contributes to a cooling of the near surface atmospheric layers (Albrecht, 1989).

However, the indirect cooling effect of SO_2 is short lived compared to the long-lasting effects of greenhouse gases such as CH_4 and CO_2 (hundreds to hundred thousands of years, Archer and Brovkin (2008); Archer et al. (2009)). Therefore, increasing SO_2 emissions could temporarily decrease the global warming of the troposphere, but it also raises concerns about regional environmental and health issues. High concentrations of SO_2 can cause skin inflammation and irritation of the respiratory system, especially for people with lung diseases, children, older adults and active people (U.S. National Park Service, 2023). The SO_2 oxidation with hydroxyl radical (OH) and other chemicals in the atmosphere leads to the formation of sulfuric acid, which then gets washed out from the atmosphere by precipitation (Seinfeld and Pandis, 2006). The rain is considered as "acid rain", when the pH-value, a measure of the acidity or alkalinity of an aqueous solution, of the rain is between 4.2 and 4.4 (United Nations Office for Disaster Risk Reduction, 2021). This has a variety of harmful effects on human and animal lives, as well as on plants and soils (Likens et al., 1979). Furthermore, SO_2 emitted into the stratosphere (mostly from highly eruptive volcanoes) oxidizes into sulfuric acids, which contribute to the formation of Polar Stratospheric Clouds (PSCs) at very low temperatures (as low as 188 Kelvin) during polar winter (Lowe and MacKenzie, 2008). These PSCs provide a surface where heterogeneous chemical reactions can take place, resulting in the production of active chlorine (Cl), which in turn enhances ozone (O_3) depletion (Solomon, 1999).

The majority of anthropogenic SO_2 is emitted in the Northern Hemisphere, primarily due to the high density of power plants and industrial facilities in this part of the world. According to Dahiya et al. (2020), India has been the globally largest emitter of anthropogenic SO_2 , releasing approximately 4.58 kilotonnes per year (kt/year) from 2005 to 2019, which amounts to more than 15% of the world's total anthropogenic SO_2 emissions. Russia follows in second place with 3.68 kt/year, while China, which was the leading emitter in 2010, dropped to third place by 2019 with 2.57 kt/year (Dahiya et al., 2020). This decline in China's emissions can be attributed to various SO_2 reduction measures implemented also earlier across the the United States of America (USA) and most parts of Europe, particularly within coal industries. Methods such as cleaner fuel, sulfur recovery units, flue gas desulfurization (FGD), and coal washing are among the methods actively employed to reduce SO_2 emissions worldwide (for a detailed list of SO_2 reduction measures, see Hanif et al. (2020)).

In conclusion, SO_2 exhibits unique characteristics as a trace gas. It plays a dual role by

firstly contributing to the cooling of the Earth's climate through the formation of sulfate aerosols, and secondly, by contributing to ozone depletion in the stratosphere and acid rains in the troposphere, with harmful effects on the environment and human health. Therefore, understanding the chemistry-climate interactions of sulfur species is important, for instance to assess mitigation methods. This thesis utilizes Chemistry-Climate Models (CCMs) to investigate the global and regional distribution, as well as the behavior of sulfur-containing species in the atmosphere, and particularly in the troposphere. This is done by evaluating the model results with satellite instruments, ground-based networks, and airborne systems during campaigns across regions with different emission intensities. The study aims to verify the model's capability in reproducing the spatial and temporal distributions of SO₂ and sulfur deposition. Furthermore, this thesis investigates for the first time the tropospheric sulfur chemistry cycle within the employed EMAC model. This is done by examining the SO₂ emissions and the associated chemical processes (including wet, dry deposition and sedimentation) to verify the model's ability to conserve sulfur mass. This conservation is a prerequisite for the comparative analysis and validation with other models and observational data, thereby ensuring the accurate representation of chemical processes simulated within the model.

1.2 Research questions and outline

The present thesis aims to answer the general research question:

- What is our current understanding of the global distribution and behavior of sulfur dioxide in the atmosphere, particularly within the troposphere?

Accordingly, this work aims to understand the SO₂ mixing ratios in the atmosphere, and the deposition flux of sulfur-containing species over areas with large emissions as well as over background regions. The evaluation focuses on tropospheric SO₂ by examining the sulfur budget and comparing the results derived from Chemistry-Climate Model (CCM) simulations with measurements, including space-, air-, and ground-based data. Additionally, the behavior of SO₂ in both, the troposphere and stratosphere, following significant volcanic eruptions that reach the stratosphere is investigated. The objective of this thesis is to determine whether the prescribed SO₂ emissions and the associated chemical mechanisms can accurately reproduce the observed SO₂ signals on both, global and regional scales.

To thoroughly address the general research question, it is broken down into the following specific research questions:

1. How well do we understand the tropospheric sulfur budget, and how do contemporary emission inventories represent SO₂ emissions?
2. What is the global distribution of atmospheric SO₂, and can anthropogenic and natural emission hotspots be identified with observations from satellite instruments? Do state-of-the-art CCM simulations represent these hotspots correctly?

3. How does the emitted and deposited mass of SO_2 evolve over time following an eruptive volcanic event?
4. What are the spatial patterns and long-term temporal trends of SO_2 concentrations and deposition fluxes of sulfur-containing species at the Earth's surface in highly polluted regions of the world (USA, Europe, and East Asia)?
5. How does the uncertainty in the representation of the boundary layer height in the CCM limit the interpretation of localized tropospheric SO_2 mixing ratio measurements for evaluating point source emission strengths?

The layout of the thesis includes the following sections: Chapter 2 provides the scientific background on the contribution of SO_2 to the Earth's radiative forcing and on the tropospheric sulfur budget, particularly focusing on the sources and sinks of SO_2 . Furthermore, the used models and measurement data are detailed in Chapter 3. To answer the first four specific research questions, the CCM ECHAM/MESSy Atmospheric Chemistry (EMAC) is used. The used EMAC model setup is illustrated in Section 3.3. The last and fifth research question is assessed by utilizing the MESSy-fied ECHAM and COSMO models nested n-times (MECO(n)) model system. The MECO(n) model system integrates the global CCM EMAC with the coupled regional CCM COSMO/MESSy model. To better investigate the simulated SO_2 mixing ratios with localized tropospheric measurements, the 4th instance of the MECO(n) model system (MECO(3)) is applied. MECO(3) offers the optimal temporal and spatial resolution, among the other instances, suitable for a localised comparison and analysis. A detailed study of the tropospheric sulfur budget in the EMAC model is presented in Chapter 4. Chapter 5 shows the evaluation of the global distribution of SO_2 , as well as the behavior of SO_2 following eruptive volcanic events, using data retrieved from the TROPOspheric Monitoring Instrument (TROPOMI) on board Sentinel-5P satellite. Chapter 6 assesses the comparison of simulated SO_2 concentrations and sulfur deposition fluxes at the Earth's surface with ground-based measurements. Chapter 7 describes the effect of the model's boundary layer on the simulated SO_2 mixing ratios over specific point sources in comparison with airborne measurements. The presented research questions are then answered in the conclusions in Chapter 8, followed by an outlook.

Chapter 2

Scientific background

2.1 The radiative forcing of sulfur dioxide

The emission of SO₂ into the atmosphere, whether from anthropogenic sources or released naturally from oceans or volcanic eruptions, plays an important role in atmospheric chemistry and climate. Once in the troposphere, SO₂ undergoes oxidation in the presence of oxidants, such as OH, O₃, and hydrogen peroxide (H₂O₂), leading to the formation of sulfate aerosols. These aerosols influence the Earth's radiative budget by reflecting incoming sunlight and outgoing terrestrial radiation (Harris et al., 2013). Additionally, sulfate aerosols act as a condensation nuclei, accelerating cloud formation. Therefore, sulfate aerosols are considered as negative contributors to Earth's radiative forcing (RF), resulting in cooling of the atmosphere near the surface. Figure 2.1 illustrates the primary contributors to both negative and positive RF in 2019 relative to the year 1750 (pre-industrial time). Here, the change in the total anthropogenic RF in 2019 was approximately +2.72 Watt per square meter (W m⁻²) compared to RF in 1750 (Forster et al., 2021). This increase is primarily driven by well-mixed greenhouse gases (GHGs), as depicted in Figure 2.1, namely nitrous oxide (N₂O), CH₄ and CO₂, which have contributed approximately by +0.21, +0.54, and +2.16 W m⁻² to the RF, respectively. In contrast, aerosols and their precursors, particularly sulfate aerosols, make a significant negative contribution to global anthropogenic RF by about -0.22 W m⁻² in 2019 relative to 1750 due to their ability to scatter solar radiation (Forster et al., 2021). Consequently, sulfate facilitates the formation of clouds, as they serve as a cloud condensation nuclei (CCN), which favor the uptake of water vapor (Boucher et al., 2013). These clouds also reduce the Earth's global warming, by approximately -0.84 W m⁻² between 1750 and 2019.

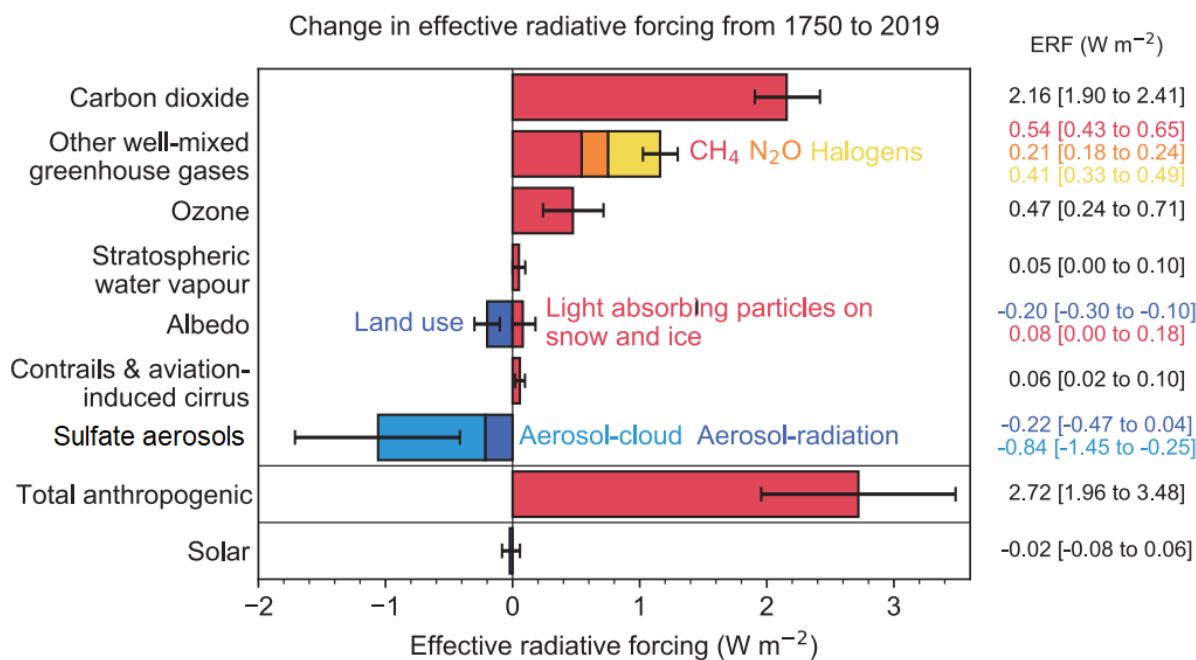


Figure 2.1: Change in effective radiative forcing estimates in 2019 relative to 1750 and aggregated uncertainties for the main drivers of climate change. Figure adopted from the Intergovernmental Panel on Climate Change (IPCC) AR6 (Forster et al., 2021).

2.2 Budget of atmospheric sulfur dioxide

Sulfur is emitted into the troposphere through natural sources, human activities and by oceanic phytoplankton as DMS. Upon release, DMS is oxidized in the gas phase into SO_2 , H_2SO_4 , and Methyl Sulfonic Acid (MSA) (Lappalainen et al., 2016). During volcanic eruptions, sulfur (S) can reach the stratosphere. Once in the atmosphere, SO_2 can be removed through various processes such as dry and wet deposition, and it can be oxidized to form sulfates in the atmosphere in both gas and liquid phases (see Figure 2.2).

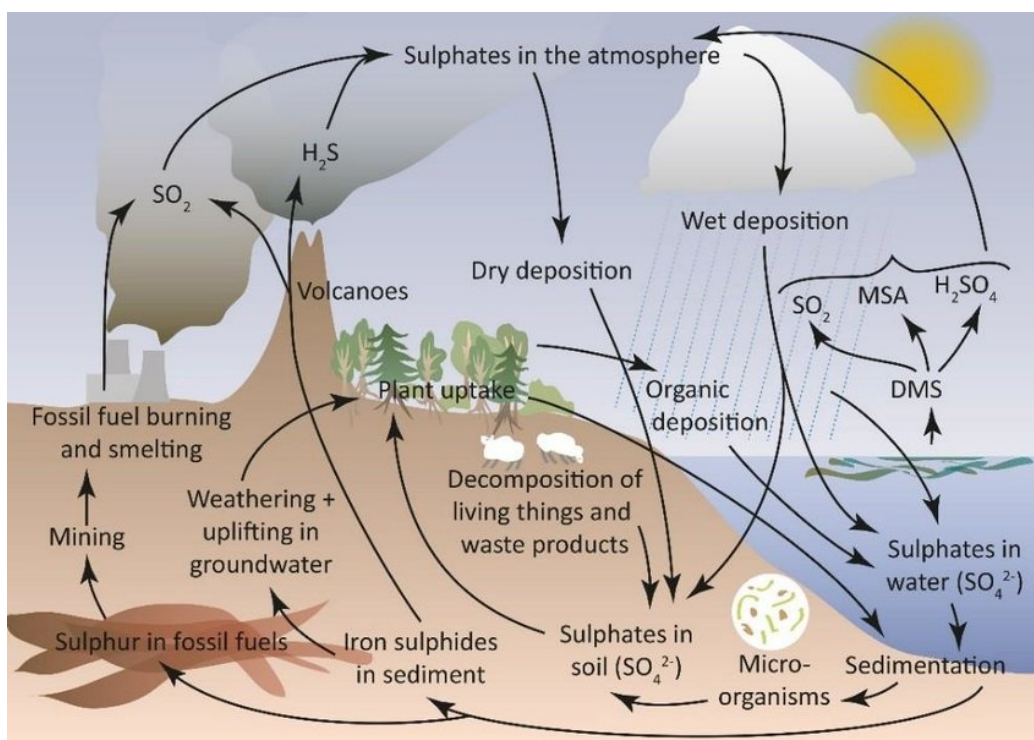


Figure 2.2: Schematic figure of the most important processes in the atmospheric sulfur cycle. Figure adopted from Lappalainen et al. (2016). The original figure is reproduced according to the Creative Commons Attribution 3.0 License.

These sulfuric acid molecules are subsequently removed from the atmosphere through wet deposition (such as acid rain), and dry deposition (Lappalainen et al., 2016). The deposited sulfur is then removed into the soil, with the oceans serving as the primary final sink (Lappalainen et al., 2016).

In Sections 2.2.1 and 2.2.2, the sources and sinks of sulfur dioxide are described in detail, respectively.

2.2.1 Sources of sulfur dioxide

On the one hand, SO_2 can indirectly be produced through the oxidation of other sulfur compounds such as carbon disulfide (CS_2), Dimethyl Sulfide (DMS), and hydrogen sulfide (H_2S) (SPARC, 2006). These sulfur compounds are naturally emitted from various sources including wetlands, biomass burning, volcanic eruptions, marine phytoplankton, soils, and rice fields (Kanda et al., 1992).

On the other hand, SO_2 is directly emitted into the atmosphere through both, natural and anthropogenic sources. The major natural sources, which directly emit SO_2 into the atmosphere are volcanic eruptions, which can inject significant amounts of SO_2 reaching the stratosphere. For instance, the Mt. Pinatubo eruption in 1991 and El Chichón in

1982 released approximately 20 and 7 Teragrams (Tgs) of SO_2 into the atmosphere, respectively (Bluth et al., 1992). Generally, the majority of SO_2 emissions are generated by human activities. These emissions are primarily produced during the combustion of sulfur-containing materials, such as the burning of fossil fuels, oil and gas combustion used in transportation sectors like cars, ships, and aircraft, as well as metal smelters (Smith et al., 2001).

Table 2.1 presents the anthropogenic SO_2 emissions in the atmosphere for the year 2019, based on the emission inventory of the Coupled Model Intercomparison Project Phase 6 (CMIP6), which includes contributions from fossil fuels, aircraft, ships, and car sectors. In 2019, the burning of fossil fuels released approximately 74.06 Tg/year of SO_2 into the atmosphere. The contributions from aircraft, ships, and cars were 0.3 Teragram (Tg), 5.18 Tg, and 2.7 Tg in 2019, respectively. This indicates that the burning of fossil fuels accounted for about 90% of the anthropogenic SO_2 emissions in 2019.

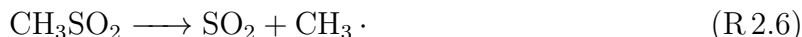
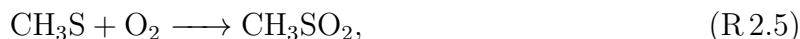
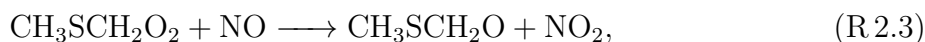
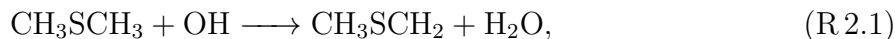
Emitting sectors	SO_2 emissions in Tg/year
Fossil fuels	74.06
Aircraft	0.3
Ships	5.18
Cars	2.7

Table 2.1: Global total anthropogenic SO_2 emissions in Tg/year for the year 2019 based on the CMIP6 emission inventory.

2.2.2 Sinks of sulfur dioxide

The emitted SO_2 into the atmosphere can be deposited directly through dry and wet deposition or chemically react with other molecules (Seinfeld and Pandis, 2006). The chemical oxidation of SO_2 is important for its removal from the atmosphere. Sulfur-containing gases such as Carbonyl Sulfide (OCS), CS_2 , DMS, and H_2S are classified as reduced sulfur compounds, with sulfur having oxidation states of -2 or -1 (Seinfeld and Pandis, 2006). The oxidation state of an element in a compound indicates the degree of oxidation (loss of electrons) or reduction (gain of electrons) of that element (Seinfeld and Pandis, 2006). For instance, to balance H_2S into a neutral molecule, the global oxidation state must be zero. Hydrogen typically has an oxidation state of +1 when bonded to non-metals. Therefore, in H_2S , each hydrogen atom has an oxidation state of +1, totaling +2 for hydrogen in H_2S . To achieve a neutral molecule, sulfur must therefore have an oxidation state of -2 to balance out the +2 from hydrogen. This makes the oxidation state of sulfur in H_2S to be -2, ensuring the molecule is electrically neutral. These reduced sulfur compounds undergo

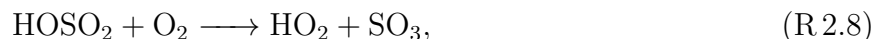
rapid oxidation in the gas phase by hydroxyl radicals (OH) and other species, leading to the formation of SO₂. Note, that all the reactions presented in this section were taken from Seinfeld and Pandis (2006). For example, DMS is oxidized to SO₂ through reactions with OH radicals (Seinfeld and Pandis, 2006), as follows:



In the gas phase, most of SO₂ is oxidized in the troposphere and, with a slower rate, in the stratosphere by reacting with OH via the Stockwell-Calvert-mechanism (Stockwell and Calvert, 1983),



where HOSO₂ leads to the production of sulfur trioxide (SO₃),



which further reacts with water molecules to produce H₂SO₄,



The presence of OH is crucial for the oxidation of SO₂, as OH is one of the primary products responsible for removing SO₂ from the atmosphere in the gas phase. OH radicals are predominantly generated through photochemical reactions involving O₃ and H₂O,



and further reaction of singlet oxygen atoms with a water molecule,



Reaction R 2.10 illustrates the importance of sunlight ($h\nu$) in the dissociation of ozone. During daytime, significant quantities of OH radicals are generated as a result of this photolysis process. However, at night, when sunlight is absent, OH radicals are not present

in sufficient amounts. Therefore, during nighttime, nitrate radicals (NO_3) serve as the primary oxidants for SO_2 :



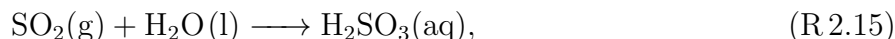
which then react with SO_2 to produce SO_3 ,



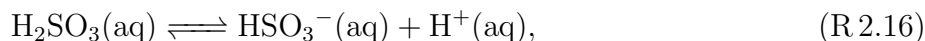
which forms H_2SO_4 in the presence of water vapor,



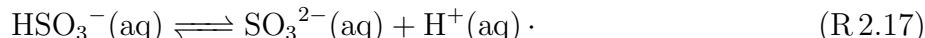
Sulfur compounds like SO_2 , which have a sulfur oxidation state of +4, can undergo further oxidation through reactions with H_2O_2 or O_3 in the liquid phase (Caffrey et al., 2001). Initially, SO_2 is dissolved in water, where it forms sulfurous acid (H_2SO_3),



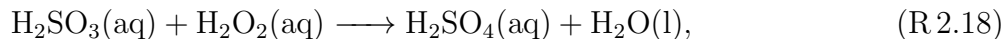
with "g" stands for the gaseous state, "l" for the liquid state and "aq" for aqueous, which indicates that the substance is dissolved in water. Afterwards, H_2SO_3 can further dissociate into bisulfite ions (HSO_3^-),



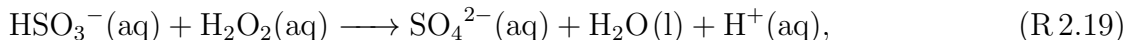
and sulfite ions (SO_3^{2-}),



Once in the aqueous phase, SO_2 can undergo a series of chemical reactions to form sulfuric acid (H_2SO_4) and sulfate ion (SO_4^{2-}) by H_2O_2 via



and



or by O_3 ,



The resulting sulfate molecules from both, gas and liquid phase, have a large water solubility due to the high sulfur oxidation state (+6 or +VI),





leading to nucleation with water vapor molecules or condensation onto existing aerosol particles, which results in sulfate aerosols formation. These aerosols subsequently influence Earth's radiative forcing, by reflecting incoming solar radiation. Furthermore, the sulfate aerosols are then removed from the atmosphere through wet and dry deposition, as well as sedimentation (Seinfeld and Pandis, 2006). Figure 2.3 provides a summary of the SO_2 chemistry mechanism in the atmosphere, discussed in this section.

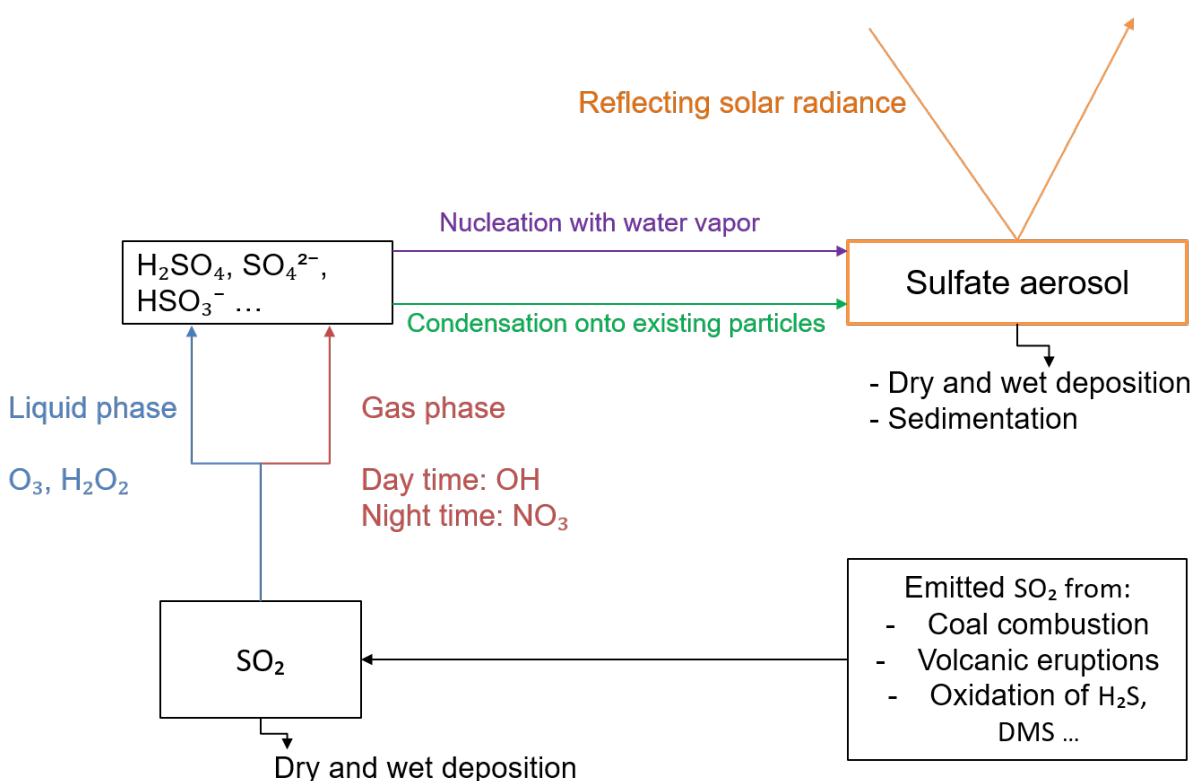


Figure 2.3: Sulfate aerosol formation from emitted SO_2 in the atmosphere.

Chapter 3

Methods

In this chapter, a comprehensive characterization of the global and regional Chemistry-Climate Models (CCMs) used in this study, including their parameterizations and the most important emission inventories applied, is given in Section 3.1. Additionally, in Section 3.2, a detailed explanation of the acquisition and representation of the used measurement data is provided. Finally, a description of the model simulations used in the present work, is described in Section 3.3.

3.1 Model description

In the present work, a detailed investigation and validation of sulfur dioxide (SO_2) within the global ECHAM/MESSy Atmospheric Chemistry model (EMAC; Jöckel et al. (2016)) integrated within the Modular Earth Submodel System (MESSy) framework (Jöckel et al., 2010) and the global/regional MESSy-fied ECHAM and COSMO models nested n-time (MECO(n)) (Mertens et al., 2016), are undertaken. EMAC is a numerical Chemistry-Climate Model (CCM) for exploring trace gases interactions and chemistry on a global scale and it computes chemical processes including sulfur interactions. Note that, CCMs treat individual dynamical, chemical and radiative processes in the Earth's atmosphere numerically. In contrast to Chemistry-Transport Models (CTMs), which use fixed, pre-defined meteorological fields, CCMs consider the interactions between the different atmospheric processes, allowing for instance the feedback of climate change on chemical processes in the atmosphere and vice versa.

For detailed analysis of specific regions, particularly focusing on localized areas such as power plants, a regional CCM with higher resolution is necessary. Thus, an online-coupled global-regional model system is used for this investigation. This system, known as MECO(n), includes both, the global EMAC model, and the regional COSMO/MESSy model, combining regional refinements depending on the specified study areas. This setup enables, among other things, the modeling of localized sulfur plume evolution.

This chapter is organised as follow: Section 3.1.1 outlines the general MESSy framework. Within this framework, a detailed description of EMAC and MECO(n) are provided

in Sections 3.1.2 and 3.1.3, respectively. The important MESSy submodels used for this study related to sulfur chemistry have been then selected and described. First, the OFFEMIS submodel is explained in Section 3.1.4. Moreover, the AIRSEA and TNUDGE submodels are described in Sections 3.1.5 and 3.1.6, respectively. Furthermore, chemical reactions of multiple trace gases in the troposphere and stratosphere are processed in both, aqueous and gas phase, through the SCAV and MECCA submodels, as discussed in Section 3.1.7 and Section 3.1.8, respectively. Additionally, the important role of processes responsible for the removal of atmospheric trace gases and particles through wet and dry depositions, as well as sedimentation is treated by the SCAV, DDEP and SEDI submodels. These are respectively described in Sections 3.1.7, 3.1.9 and 3.1.10. Finally, for comparing model data with satellite retrievals, the SORBIT submodel plays a significant role, as outlined in Section 3.1.11.

3.1.1 MESSy framework

The Modular Earth Submodel System (MESSy) provides a flexible and modular approach for enhancing geo-scientific models, such as Earth System Model (ESM), General Circulation Model (GCM) and CCM (Jöckel et al., 2010, 2005). MESSy contains multiple submodels, each responsible for managing a specific process. These submodels are coupled to each other and to a basemodel through the MESSy framework, which comprises four distinct software layers (see Figure 3.1). The basemodel layer (BML), the basemodel interface layer (BMIL), the submodel core layer (SMCL) and the submodel interface layer (SMIL) (Jöckel et al., 2010). BML comprises at the final developing stage, a central clock and run-time control. At the current developing state, a general circulation model (GCM) or a box model is used as a basemodel and it is directly connected to the BMIL (Jöckel et al., 2010). The BMIL contains the basemodel's specific implementation of the MESSy framework, which acts as a multiple socket outlet facilitating data transfer between the basemodel and the submodels. The BMIL is then connected to the specific submodels via the SMIL. Ultimately, the SMCL consists of the basemodel-independent implementation of a particular process within the Earth System or of a diagnostic tool of the model system (Jöckel et al., 2010).

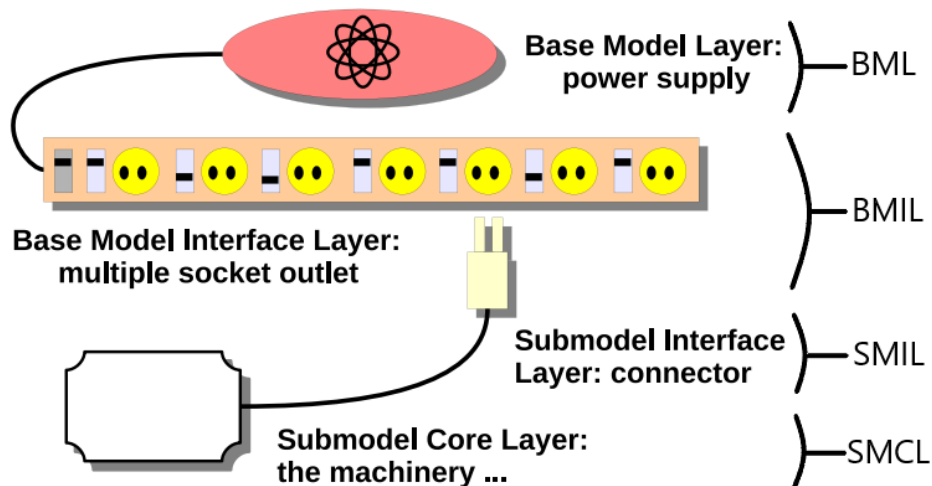


Figure 3.1: Presentation of the MESSy framework, adopted from Kerkweg and Jöckel (2012). The original figure is reproduced according to the Creative Commons Attribution 3.0 License.

The MESSy framework offers a flexible capability to enable or disable required submodels as needed. For example, the simulations conducted in this study utilize a CCM setup, necessitating the activation of chemistry-related MESSy submodels. These allow a detailed chemistry study, such as for sulfur within this thesis. However, when the focus is not on chemical interactions or composition changes, MESSy provides the possibility to deactivate chemistry-related submodels and use a General Circulation Model (GCM) setup, which reduces computational time and resource usage.

The available submodels can be found, for example, in several publications such as Jöckel et al. (2006, 2010, 2016), as well as on the MESSy website (<https://messy-interface.org/messy/submodels>, last access on the 26.06.2024).

3.1.2 The EMAC model

The EMAC (ECHAM/MESSy Atmospheric Chemistry) model is a state-of-the-art global atmospheric CCM describing tropospheric and middle atmosphere processes and their interactions with land, oceans and human impact (Jöckel et al., 2010, 2016). The second version of the Modular Earth Submodel System (MESSy2) and the 5th generation European Center Hamburg general circulation model (ECHAM5) as BML make up the EMAC model (Röckner et al., 2006) used in this study. The physics-related submodels within the MESSy framework have been adapted from the physics routines of ECHAM5 (Jöckel et al., 2016). However, only the spectral core, the flux form semi-Lagrangian (FFSL) large scale advection scheme (Lin and Rood, 1996), the time integration loop, and the Newtonian relaxation methods retain their original structure from the ECHAM5 base model. Note that the

Newtonian relaxation methods are used throughout all this work for "nudging" in specified dynamics (SD) setups (see Section 3.3), to constrain the model's state towards observations or reanalysis data, in order to maintain realistic atmospheric dynamics while allowing detailed studies of chemical processes.

EMAC allows for model setups for climate, air quality, and atmospheric chemistry research, which enable the study of important chemical and physical phenomena, including the formation and depletion of ozone, aerosols, and greenhouse gases. Depending on the scientific purpose, EMAC can be used in a variety of vertical and horizontal resolutions. Table 3.1 shows some examples of the spectral truncations and the associated number of longitudes and latitudes in the corresponding grid-point space.

Spectral truncation	Number of Longitudes	Number of Latitudes
T21	64	32
T42	128	64
T63	192	96
T85	256	128
T159	480	240

Table 3.1: Number of longitudes and latitudes at each spectral truncation, adopted from (Röckner et al., 2003).

In this study, for the first time, an extensive analysis of sulfur using the EMAC model with a spectral truncation of T42, is undertaken on a global scale. For more information about the EMAC model used in this study, refer to Section 3.3.

3.1.3 The MECO(n) model system

In this study the model system employed for regional studies is referred to as MECO(n), where MECO(n) represents "MESSy-fied ECHAM and COSMO models nested n-times" (Mertens et al., 2016). The MECO(n) system integrates the global CCM EMAC with the coupled regional COSMO/MESSy model system (Mertens et al., 2016; Kerkweg and Jöckel, 2012). The Consortium for Small-scale Modeling (COSMO) is a non-hydrostatic limited-area numerical weather prediction model (Rockel et al., 2008) that has been designed for both, operational numerical weather prediction (NWP) and various scientific applications, such as dynamical down-scaling, and regional air pollution studies (Kerkweg and Jöckel, 2012; Steppeler et al., 2003). Furthermore, COSMO enables the investigation of smaller-scale effects that cannot be adequately investigated at a global resolution. This includes studying the effects of emissions on climate and air quality from specific sources such as power plants. In this study COSMO/MESSy is nested online into the global EMAC model using the Multi-Model-Driver (MMD) submodel, which allows for frequent updates of meteorological and chemical boundary conditions (Kumar et al., 2021). MMD is made

of a library processing the two-way data transfer between the running models, as well as the MMD2WAY MESSy submodel, which ensures and manages the data exchange and interactions conducted by the MMD library (Kerkweg et al., 2018). This allows a connection between the EMAC and the COSMO/MESSy models, where the data exchange occurs at specific intervals within the model time of the respective coarser model domain. A detailed description of the used MECO(n) model setup is given in Section 3.3.3.

3.1.4 The OFFEMIS submodel

The OFFline EMISSions (OFFEMIS) submodel plays an important role in the process of converting initial raw input data of trace gas and aerosol emission fluxes into tracer tendencies (Kerkweg et al. (2006b), therein described as OFFLEM). To achieve this, prescribed emission fluxes of trace gases and aerosols from surface emissions or from volume emissions stored as NetCDF files, are read via the IMPORT_GRID submodel, regridded onto the EMAC grid and applied to the tracers by OFFEMIS (Kerkweg and Jöckel, 2015). In the present study OFFEMIS treats SO₂ emissions originating from various sectors across different regions. However, OFFEMIS is only able to handle prescribed emissions (i.e. not dependent on the current state of the atmosphere, biosphere or on the hydrological cycle) (Kerkweg et al., 2006b), such as agricultural waste burning, industrial activities, shipping. Emissions, which depend on the actual meteorology (e.g. wind speed, humidity, etc.), such as for instance sulfur emissions from the oceans, are calculated by other submodels within the EMAC model (see the next two submodels explained in Subsections 3.1.5 and 3.1.6).

3.1.5 The AIRSEA submodel

The AIRSEA submodel serves calculating the air-sea exchange of chemical species (Pozzer et al., 2006). In this work, AIRSEA calculates online Dimethyl Sulfide (DMS) emissions from the oceans (DMS_{airsea}) within the model simulations. This implies that DMS_{airsea} is obtained from the model's output data rather than being directly included as an input. In this submodel a DMS concentration in the water surface is given, from which an exchange with the air is online calculated in each model time step based on the sea-to-air transfer velocity (Pozzer et al., 2006). The resulting emission flux is then given in the model output and added to the DMS tracer. This process depends on multiple meteorological parameters such as sea activity, temperature and surface wind speed.

3.1.6 The TNUDGE submodel

The TNUDGE submodel, along with the other submodels, such as OFFEMIS (see Section 3.1.4), simplifies the inclusion of various emission types into the EMAC model (Kerkweg et al., 2006b). TNUDGE is designed to handle pseudo-sources and sinks using a technique known as "tracer nudging". This technique is particularly useful for species with highly uncertain emission fluxes, that cannot be directly calculated, such as Carbonyl Sulfide (OCS) (Kerkweg et al., 2006b). For sulfur originating from OCS, an artificial tracer flux

in the form of observed OCS mixing ratios at a given boundary is prescribed and nudged to the global model via the TNUDGE submodel (Kerkweg et al., 2006b). This helps in incorporating real-world observational data into the model, where direct emission data is uncertain or unavailable.

3.1.7 The SCAV submodel

The scavenging submodel for regional and global atmospheric chemistry modeling (SCAV) is designed to simulate and parameterize the scavenging processes in the atmosphere, including the interactions between trace gases, aerosols, and precipitation (Tost et al., 2006). These interactions are important to understand the chemical changes within the atmosphere, significant for both, weather prediction and air quality assessments. Coupled with the global-scale EMAC model system, the SCAV submodel addresses the atmospheric processes of scavenging, which includes the removal of aerosols and gases in the aqueous phase. This removal is essential for accurately modeling chemical transport and transformation in the atmosphere. Within the model, the scavenging processes are calculated on the basis of input parameters such as cloud water content, rain and snow flux, temperature, snow and precipitation formation, aerosol radius, as well as tracer mixing ratios and the chemical scavenging processes for gases and aerosols, as shown in Figure 3.2. The model intricately handles aerosol scavenging through mechanisms such as nucleation and impaction scavenging, as in detail explained by Tost et al. (2006). The efficiency of these processes is influenced by the physical properties of the aerosols and droplets, particularly their radius, which determine how effectively aerosols are incorporated into precipitation particles. In addition to aerosol scavenging, the SCAV submodel also simulates gas scavenging, which involves the dissolution of gases into rain droplets. This process is governed by Henry’s law, providing a framework for understanding transition between the gas and aqueous phases under different environmental conditions. Within the aqueous phase, the submodel simulates a variety of chemical processes. These include reduction-oxidation (redox) reactions, which alter the chemical composition within droplets, photolysis reactions, which involve the breakdown of chemicals through exposure to light, as well as the dissociation of species in the aqueous phase (depicted by the blue boxes in Figure 3.2). These processes are mathematically represented by a system of ordinary differential equations (ODEs), enabling detailed simulations of chemical interactions within clouds and precipitation (Tost et al., 2006). The computational framework of the SCAV submodel utilizes the Kinetic PreProcessor (KPP), which facilitates the implementation of feedback mechanisms between multi-phase chemistry and transport processes (Damian et al., 2002; Sandu and Sander, 2006). This integration ensures a comprehensive simulation environment that enhances the model’s predictive capabilities regarding atmospheric phenomena.

Following the scavenging and multi-phase chemistry processes, SCAV provides the tendencies for tracer mixing ratios, pH values in clouds and precipitation as well as wet deposition fluxes for the considered species as output. In EMAC, the wet deposition is calculated via large-scale (ls) and convective (cv) precipitation. This differentiation is important due to their separate treatment in various models and their reliance on different input para-

meters, as highlighted by Tost et al. (2006).

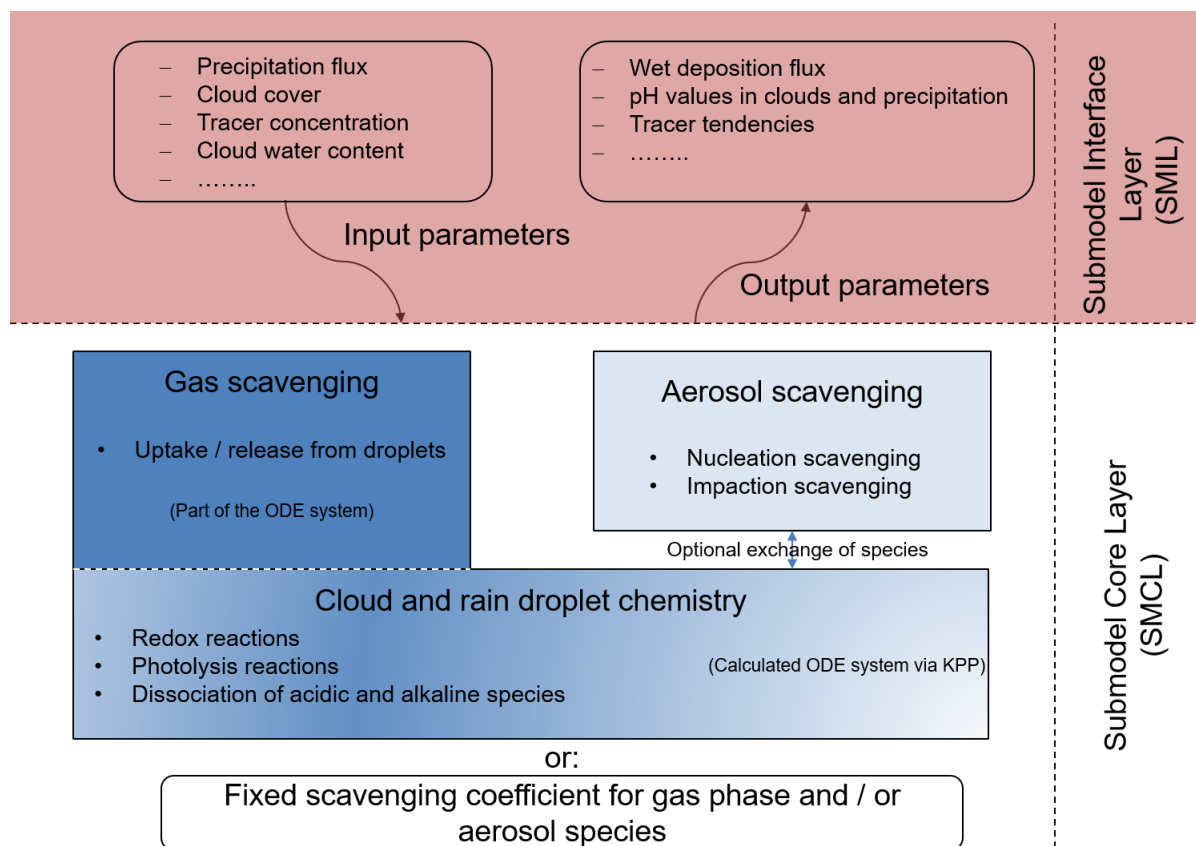
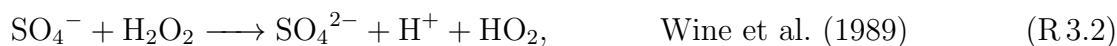
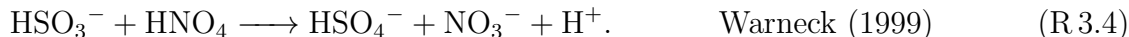


Figure 3.2: Visualisation of the scavenging mechanism and the multi-phase chemistry scheme of the SCAV submodel. Figure adopted from Tost et al. (2006). The original figure is reproduced according to the Creative Commons Attribution-NonCommercial-ShareAlike 2.5 License.

Below are some important sulfur chemical reactions conducted by the SCAV submodel in the aqueous phase for dissolved sulfate, which account for more than 90% of the deposited sulfur species through wet scavenging:





Note, that the mechanism of SCAV in the EMAC model covers the aqueous phase reactions of sulfur compounds, as partially described in Section 2.2.2. The complete mechanism of SCAV used in this study is part of the Appendix (see Appendix A.1).

3.1.8 The MECCA submodel

The Module Efficiently Calculating the Chemistry of the Atmosphere (MECCA) Sander et al. (2019) is the MESSy submodel, which calculates the chemical gas phase reaction mechanism used in EMAC. As for the previous SCAV submodel (Section 3.1.7), MECCA also uses the KPP software for the numerical integration of the set of ordinary differential equations describing the chemical reactions in the gas phase. MECCA plays an important role by incorporating a sophisticated chemical mechanism designed to simulate the behavior of various chemical species in the troposphere and stratosphere of both, the gas and the aqueous phases (Sander et al., 2005). In this study MECCA is applied for the gas phase chemistry, while SCAV addresses liquid/ice phase chemistry and associated removal processes consistently with the MECCA chemical mechanism (for chemistry reaction examples in the aqueous phase, see reactions R 3.1 to R 3.4 in Section 3.1.7). The chemistry submodel MECCA describes atmospheric chemical reactions of multiple tracers, such as methane (CH_4), non-methane volatile organic compounds (NMVOCs), mercury (Hg), and sulfur dioxide (SO_2). For a detailed investigation of sulfur dioxide, the chemical mechanism from Phase 2 of the Chemistry-Climate Model Initiative (CCMI-2, (CCMI, 2023)) comprising approximately 160 chemical species, is employed in the simulations of this study. The most important sulfur chemical mechanism in the gas phase is the oxidation of SO_2 with OH as follows:



Note, that the mechanism of MECCA in the EMAC model covers the gas phase reactions of sulfur compounds, as partially described in Section 2.2.2. The complete mechanism of MECCA used in this study is part of the Appendix (see Appendix A.2).

3.1.9 The DDEP submodel

The dry deposition submodel, referred to as "DDEP," was employed in this study to monitor and quantify the deposition of sulfur gases and aerosols undergoing dry deposition processes in the lowermost model layer. In DDEP, trace gases and aerosols in the model are accounted for, allowing the calculation of their dry deposition velocities and resulting fluxes (Kerkweg et al. (2006a), therein described as DRYDEP). This section provides a brief overview of the methodology employed to derive dry deposition of trace gases and aerosols within the EMAC model, with more details available in Kerkweg et al. (2006a).

The dry deposition process is based on the algorithm used for online calculation of dry deposition velocities, employing the big leaf approach as implemented in ECHAM3 (Klimarechenzentrum, 1993) and ECHAM4 (Röckner et al., 1996). The calculation of dry deposition relies on the determination of the dry deposition velocity specific to each species and aerosol. Consequently, two distinct calculation methods are employed within the EMAC model: one for the dry deposition of trace gases and another for aerosols.

For trace gases, each species has unique solubility and reactivity characteristics, thus influencing the dry deposition velocity differently. The dry deposition flux of a species X ($F_{\text{dep}}(X)$ in $\text{kg m}^{-2} \text{s}^{-1}$) is determined by:

$$F_{\text{dep}}(X) = \mu_g(X) \cdot \frac{M(X)}{M_{\text{air}}} \cdot \frac{\Delta p}{g \Delta z} \cdot v_d(X), \quad (3.1)$$

where the gas phase mixing ratio of species X ($\mu_g(X)$) is given in mol/mol. $M(X)$ represents the molar mass of species X and M_{air} denotes the molar mass of dry air (both in kg/mol). The gravitational force is denoted by g (m/s^2), where Δp and Δz stand for the layer thicknesses in Pa and m, respectively. The dry deposition velocity $v_d(X)$ (m/s) of a trace gas X is influenced by various factors, as expressed by the equation:

$$v_d(X) = \frac{1}{R_a + R_{qbr}(X) + R_s(X)}. \quad (3.2)$$

These factors include the aerodynamic resistance (R_a), the quasi-laminar boundary layer resistance (R_{qbr}), and the surface resistance (R_s), with all resistances expressed in units of s/m. Here, R_a is influenced by the atmospheric physical state, while $R_{qbr}(X)$ is primarily governed by molecular diffusion. Furthermore, the surface resistance $R_s(X)$ depends on the chemical, physical, and biological properties of the surface. In the DDEP submodel, four distinct surface types are considered: water, soil/snow, ice/snow, and vegetation surfaces. The dry deposition velocity is determined through the combined effects of R_a , $R_{qbr}(X)$ and $R_s(X)$. Detailed formulations for resistance calculations are provided by Kerkweg et al. (2006a).

For aerosols, the dry deposition calculation follows a similar approach as outlined in Equation 3.1 for trace gases. However, it is noteworthy that only three surface types

(soil/snow (indexed as slsn), water (indexed as wat), and vegetation (indexed as veg) surfaces) are considered for aerosols, thus affecting the dry deposition velocity. The later is determined as:

$$\begin{aligned}
 v_{d,p}(X) = & (f_{\text{snow}} + f_{\text{bs}}) \cdot v_{d,p,\text{slsn}}(X) \\
 & + (1 - f_{\text{snow}}) (1 - f_{\text{ws}}) f_{\text{veg}} \times v_{d,p,\text{veg}}(X) \\
 & + (1 - f_{\text{snow}}) f_{\text{ws}} \times v_{d,p,\text{veg}}(X) \\
 & + f_{\text{ice}} \times v_{d,p,\text{slsn}}(X) \\
 & + f_{\text{wat}} \times v_{d,p,\text{wat}}(X),
 \end{aligned} \tag{3.3}$$

where f_{snow} , f_{bs} , f_{wat} , f_{veg} , f_{ws} and f_{ice} represent the surface fractions of snow, bare soil, water, vegetation, wet skin and ice, respectively. The dry deposition velocities of each surface type are given in m/s and calculated as follows:

$$\begin{aligned}
 v_{d,p,\text{veg}}(X) &= \left(\frac{R_{a,\text{veg}}}{100} + \frac{1}{v_{kd,p,\text{veg}}(X)} \right)^{-1}, \\
 v_{d,p,\text{slsn}}(X) &= \left(\frac{R_{a,\text{slsn}}}{100} + \frac{1}{v_{kd,p,\text{slsn}}(X)} \right)^{-1}, \\
 v_{d,p,\text{wat}}(X) &= \left(\frac{R_{a,\text{wat}}}{100} + \frac{1}{v_{kd,p,\text{wat}}(X)} \right)^{-1}.
 \end{aligned} \tag{3.4}$$

Here, the dry deposition velocities depend on the aerodynamic resistances ($R_{a,\text{veg}}$, $R_{a,\text{slsn}}$ and $R_{a,\text{wat}}$) and the specific dry deposition velocities $v_{kd,p,\text{veg}}$, $v_{kd,p,\text{slsn}}$ and $v_{kd,p,\text{wat}}$. The detailed calculations of the specific dry deposition velocities are illustrated by Kerkweg et al. (2006a).

3.1.10 The SEDI submodel

The SEDI submodel for aerosol sedimentation, alongside wet scavenging and dry deposition processes, constitutes the third removal process of sulfur-containing aerosol species from the atmosphere used within the EMAC model. Implemented independently within the MESSy model, SEDI differs from DDEP submodel in its coverage of the entire vertical atmospheric column, as opposed to just the lowermost layer. In the model setup used here, SEDI calculates sedimentation fluxes for residual aerosols formed by SCAV through the evaporation of clouds and precipitation, ultimately leading to particle formation (Jöckel et al., 2016). Sedimentation is the process by which both, cloud droplets and ice crystals fall from higher to lower atmospheric layers due to gravitational force and depends on various factors. These include gravitational acceleration, mixing ratio, density, and particle radius. For aerosol sedimentation, SEDI provides a simple upwind zeroth-order scheme and a Trapezoid scheme of first order, as detailed by Kerkweg et al. (2006a). The zeroth

order sedimentation scheme is a basic upwind scheme used to model how particles settle out of the atmosphere within a grid system. The key assumption of this scheme is that particles within a grid box are uniformly distributed across the box's height (Kerkweg et al., 2006a). In this work the Trapezoid scheme has been used, as it provides an improvement of the zeroth order sedimentation scheme, by implementing first order polynomials for the vertical profile of the mixing ratio, as explained by Kerkweg et al. (2006a). This implementation ensures the model a more dynamic and realistic movement of particles, by using a straight line approximation for the mixing ratio profile within each grid box, from one grid box to the one below it, compared to what is observed with the zeroth order scheme. This adjustment leads to more precise modeling of particle dynamics and sedimentation processes, particularly in complex atmospheric conditions.

3.1.11 The SORBIT submodel

The sampling along sun-synchronous satellite orbits (SORBIT) submodel, as described by Jöckel et al. (2010), holds a significant relevance in the context of this work. It enables a direct comparison between simulated Vertical Column Densities (VCDs) of trace gases, particularly sulfur, which is of significance in this study, with data obtained from satellite measurements. It is developed in order to sample the model data along sun-synchronous satellite orbits. Their orbital inclination and altitude are selected in a manner that induces a precision of the orbital plane at a rate of completing one full circle annually due to the gravitational force gradient arising from the Earth's oblate shape (Jöckel et al., 2010). Consequently, the satellite crosses any specific point on the Earth's surface at an identical local mean solar time, each time it passes over. This local time (index L) $T_{L,O}$ of the orbiter's flyover (index O) at a given latitude Θ is defined as:

$$T_{L,O}(\Theta) = \left(T_{L,O}(0) \pm \arcsin \left(\frac{\tan \theta}{\tan \delta} \right) \frac{12}{\pi} + 48 \right), \quad (3.5)$$

where, $T_{L,O}(0)$ represents the local time at which a satellite crosses the equator, and δ signifies the inclination of the orbital plane. For the satellites ascending path, the sign is positive and for the descending path the sign is negative. This straightforward relationship describing the orbit geometry of sun-synchronous satellites facilitates the direct comparison between the model and satellite-based observations. A secondary variable, denoted as X_O for a given scalar variable X (e.g. the 3-dimensional distribution of the trace gas mixing ratio of SO₂) in Eulerian (or grid-point) representation is determined as follows:

$$X_O(i, j, k, l) = \begin{cases} X(i, j, k, l) & \text{if } |T_L(i, j, l) - T_{L,O}(0(j))| \leq \Delta T \\ X_U & \text{otherwise,} \end{cases} \quad (3.6)$$

where l is the time step of the model and i , j and k are the grid-box indices in longitudinal, latitudinal and vertical direction, respectively. At the time step l , T_L represents the local solar time (measured in hours of the day) in the corresponding grid-box with indices i and j , and is represented as:

$$T_L(i, j, l) = T_{UTC}(l) + \frac{\lambda(i, j)}{360}24, \quad (3.7)$$

where the geographical longitude is represented in degree as λ and $T_{UTC}(l)$ is the model time in Coordinated Universal Time (UTC) at time step l . The UTC is the primary time standard and it is used as the basis for civil time in most countries across the globe. Moreover, in Equation 3.6, X_U denotes an undefined value, particularly when the requirement for a grid-box is not given due to the discrete grid structure. In such instances, the recommended time interval ΔT is determined as half the length of the model's time step ($\Delta T = \Delta T/2$).

The output of SO_2 (and other quantities) from the SORBIT submodel are further processed (in Section 3.3.1) to facilitate a direct comparison with satellite measurements.

3.1.12 Description of the boundary conditions of the used sulfur emissions

Within the scope of this thesis, SO_2 originating from both, anthropogenic and natural sources, is examined. The following offline provided emission inventories include the emission fluxes as applied for the simulations:

- The inventory from the Coupled Model Intercomparison Project Phase 6 (CMIP6) is mainly used in this work to prescribe SO_2 anthropogenic surface emissions from fossil fuels, agricultural waste burning (awb), aircraft, ships, road traffic and biomass burning (Eyring et al., 2016). CMIP6 has a horizontal resolution of $0.5^\circ \times 0.5^\circ$ and it primarily uses bottom-up inventories to provide emission data for climate models. Bottom-up inventories involve estimating emissions based on detailed data about specific sources and activities, such as energy consumption and industrial processes. CMIP6 contains historical emissions from 1850 to 2014, provided by the Atmospheric Chemistry and Atmospheric Chemistry and Climate-Model Intercomparison Project (ACCMIP) developed by Lamarque et al. (2010). The historical data are then combined with the shared socio-economic pathways (SSPs) for projected future emissions from the IPCC Sixth Assessment Report (AR6) (Calvin et al., 2023). The SSPs used within the CMIP6 inventory provide a range of future scenarios based on varying levels of greenhouse gas emissions and societal changes, such as SSP1-1.9, SSP1-2.6, SSP2-4.5, SSP3-7, SSP4-6, and SSP5-8.5 (Riahi et al., 2017). These SSPs present different emission scenarios, in order to explore different future climate outcomes based on varying levels of greenhouse gas emissions and societal changes. In

the present work's simulation the SSP2-4.5 scenario is used to prescribe trace gases emissions, especially SO₂ emissions after 2014. The SSP2-4.5 is a middle-of-the-road scenario with moderate emissions, leading to a radiative forcing of 4.5 W m⁻² by 2100 (Riahi et al., 2017).

- The Coupled Model Intercomparison Project Phase 5 (CMIP5) involves 20 climate modeling groups from around the world and it aims to provide a state-of-the-art multi-model dataset to advance knowledge of climate variability and change (Taylor et al., 2012). Similar to CMIP6, CMIP5 also uses bottom-up inventories and provides anthropogenic surface emissions, such as fossil fuels, agricultural waste burning, aircraft, ships, road traffic and biomass burning. However, CMIP5 has been developed from the first phase of CCMI, in contrast to CMIP6, which was recommended by CCMI phase 2. The difference between CCMI and CCMI-2 lies, among other factors, in the available historical data and the future emission pathways. CMIP5 incorporates historical data spanning from 1850 to 2005, subsequently merged with Representative Concentration Pathways (RCPs) 2.6, 4.5, 6.0, and 8.5, from the IPCC Fifth Assessment Report (AR5) (Calvin et al., 2023). These pathways outline scenarios approximating the spectrum of potential future emission trajectories until 2100. In this work the RCP6.0 of the CMIP5 inventory is used for the MECO(n) global/regional model system. RCP6.0 is an intermediate scenario formulated for CMIP5 and considers a range of projections encompassing future population growth, technological advancements, and societal responses (Taylor et al., 2012). It is important to note, that the evaluated simulation in this work, which runs with the CMIP5 inventory, has been conducted by Mariano Mertens. This simulation is used for a case study to examine the effects of aerosols on SO₂ within the EMAC model (see Section 4.3). Generally, the CMIP5 focuses on RCPs as future emission scenarios, where the CMIP6 introduces SSPs combined with updated RCPs to reflect a broader range of socio-economic factors and mitigation/adaptation strategies (Arias et al., 2021; Stocker et al., 2013). Additionally, the CMIP5 Models have a lower spatial resolution and include fewer processes and interactions compared to the CMIP6, which features more sophisticated representations of physical processes, biogeochemical cycles, and human activities (Arias et al., 2021). Finally, the CMIP6 offers more detailed and comprehensive projections that address emerging scientific questions and policy needs highlighted in the IPCC AR6 (Calvin et al., 2023).

Therefore, throughout all this work the CMIP6 inventory is selected as the standard inventory for global EMAC simulations (especially the RD1SD-base-01 simulation, see Section 3.3), since it was recommended by the experimental protocol for participation in the CCMI-2 model intercomparison initiative. This initiative aims to improve models, compare model results to observations, and provide data for CCMI data users.

- For a regional case study the European Pollutant Release and Transfer Register (E-PRTR) is used as a database for the MECO(n) simulation in this work (see Sections

3.3.3 and 7). The E-PRTR is a comprehensive database that tracks the release and transfer of pollutants from industrial facilities across Europe, enabling a detailed and geographically precise identification of emission sources (Sörme et al., 2016). The E-PRTR is a bottom-up inventory (Nordborg et al., 2017) and contains annual data on the release of 91 key pollutants including heavy metals, pesticides, chlorinated organic substances, and greenhouse gases (Sörme et al., 2016). In the present work SO₂ emissions originating from power plants from the year 2017 are used.

- The terrestrial Dimethyl Sulfide (DMS_{terrestrial}) emissions are based on the global inventory developed by Spiro et al. (1992). This inventory was mainly developed to examine gaseous sulfur emissions, and is one of the first comprehensive attempts to quantify global DMS emissions. Over the years, this inventory has been validated with other studies, such as Chin et al. (2000); Vallina and Simó (2007), and Lana et al. (2011), maintaining its reliability within the scientific community. Nevertheless, future EMAC simulations should consider integrating updated emission inventories to reflect ongoing advancements and changes in global DMS emissions. DMS_{terrestrial} emissions originate from both, vegetation and soils, and are available as a monthly resolved annual climatology at a resolution of 1°x 1° (Bates et al., 1987).
- Volcanic sulfur emissions from both, continuously degassing and explosive volcanoes are represented by the Aerosol Inter Comparison (AeroCom) project initiative as a zonal mean climatology (Dentener et al., 2006). Note that, volcanic sulfur is emitted as 97.5% SO₂ and 2.5% SO₄. The data are based on the bottom-up Global Emissions Inventory Activity (GEIA) for the years 1750 (pre-industrial conditions) and 2000 (present-day conditions) with a common spatial resolution of 1°x 1° and a daily resolution for dust and sea-salt, monthly resolution for wild-land fires, as well an annual resolution for all other emissions including volcanic emissions (Andres and Kasgnoc, 1998). On the one hand, continuously degassing sulfur in AeroCom is equally distributed over the grid points with GEIA volcano locations and amounts to a multi-annual total emission of 12.6 Teragrams of Sulfur per annum or year ($Tg(S)/a$) over all the years (Dentener et al., 2006). The height of these emissions is modeled in the upper third of the volcano altitudes, simulating the degassing processes that occur predominantly at the volcano flanks. On the other hand, explosive volcanic emissions are quantified at approximately 2 $Tg(S)/a$ over all the years. This estimation is based on the Aerosol Index (AI) provided by the Total Ozone Mapping Spectrometer (TOMS) satellite sensors (Dentener et al., 2006). The emissions data are distributed evenly across grid boxes that include volcanoes active in the last century (Halmer et al., 2002). It is important to note that these emissions are modeled as being continuously released rather than episodic, due the fact that only about one-third of such emissions occur during violent explosive events (Dentener et al., 2006). Furthermore, these emissions are typically modeled to occur between 500 and 1500 meters above the peaks of the volcanoes to accurately represent their dispersal in the atmosphere. The injection height, time resolution and the sulfur flux of the different volcano types

are given in Table 3.2.

	Time resolution	Injection altitude	AeroCom Flux [Tg(S)/a]
Explosive volcanoes	yearly	From ($V_T + 500$ m) until ($V_T + 1500$ m)	2.0
Continuous volcanoes	yearly	From ($0.67 \cdot V_T$) until ($1.0 \cdot V_T$)	12.6

Table 3.2: Parameters of the AeroCom explosive and continuous volcanic emissions. V_T (Volcano top) corresponds to the altitude of the top of the volcano.

In addition to the offline emissions, sulfur from oceanic Dimethyl Sulfide (DMS_airsea) and from Carbonyl Sulfide OCS are calculated using AIRSEA (see Section 3.1.5) and TNUDGE (see Section 3.1.6) submodels, respectively.

The choice of the input emission inventories is important, since the simulation results depend on it. The emission inventories are subject to large uncertainties and therefore model results are subject to this uncertainty as well. Uncertainty is a statistical term that is used to represent the degree of accuracy and precision of data, as defined by McInnes (2001). The accuracy of the data is attributed to the insufficient understanding of the sources and extent of inaccuracies within an emission inventory, where uncertainty about the reliability of emission inventories arises from a lack of understanding regarding the extent to which they meet user-defined quality criteria (van Aardenne and Pulles, 2002). It is therefore important to examine how accurately emission inventories reproduce SO_2 emissions, considering their temporal characteristics, such as the evolution and variability over a defined time period, as well as their magnitude compared to other emission inventories.

Comparison of the used emission inventories

The temporal evolution of the SO_2 anthropogenic surface emissions from the CMIP6 emission inventory, utilized within the global EMAC model in this work, is depicted in Figure 3.3. This figure also includes comparisons of the CMIP6 inventory with other emission inventories, which were selected based on their representations of SO_2 anthropogenic emissions from sectors identical to those covered by CMIP6. Those emission inventories are the MACCity emission dataset, which is part of two projects funded by the European Commission, MACC and CityZen (MACC/CityZEN EU) projects (Granier et al., 2011) and the Emissions Database For Global Atmospheric Research (EDGAR) emission inventory (Crippa et al., 2022). MACCiTY provides SO_2 emission data from fossil fuels, agricultural waste burning, ships, roads and biomass burning. Comparable to the CMIP6 emission inventory, MACCity contains a historical dataset (1850 to 2000) from the ACCMIP historical emissions dataset on a decadal basis (1980, 1990, 2000, etc). However the emission data for future scenarios are based on the IPCC AR5, where RCP emission data have

been adapted and extended on a yearly basis for the period 1990-2010 (van Vuuren et al., 2011). After 2000 the RCP 8.5 emission scenario was used for the years 2005 and 2010. For biomass burning emissions, the dataset was extended on a monthly basis. On the other hand, EDGAR provides state-of-the-art estimates for greenhouse gas emissions and air pollutants, providing detailed assessments for emissions across countries and specific sectors (Crippa et al., 2022). Same as for the CMIP6 inventory, EDGAR is also considered a bottom-up inventory, with a finer horizontal resolution on grid-maps at $0.1^\circ \times 0.1^\circ$. The data is available as yearly and monthly mean and is emitted into 7 vertical tropospheric levels (0, 20, 92, 184, 324, 522 and 781 meter), as described by Bieser et al. (2011). In this comparative case study of inventories, the version 5.0 of EDGAR (EDGAR5) is used and contains solely anthropogenic emissions from different sectors such as fossil fuels, agricultural waste burning, ships and roads. Other emissions from large scale biomass burning, forest fires and sources from land-use forestry are excluded (Crippa et al., 2022). The purpose of this comparison is to provide insights into the magnitude and variability of SO_2 emissions over time from the CMIP6 emission inventory.

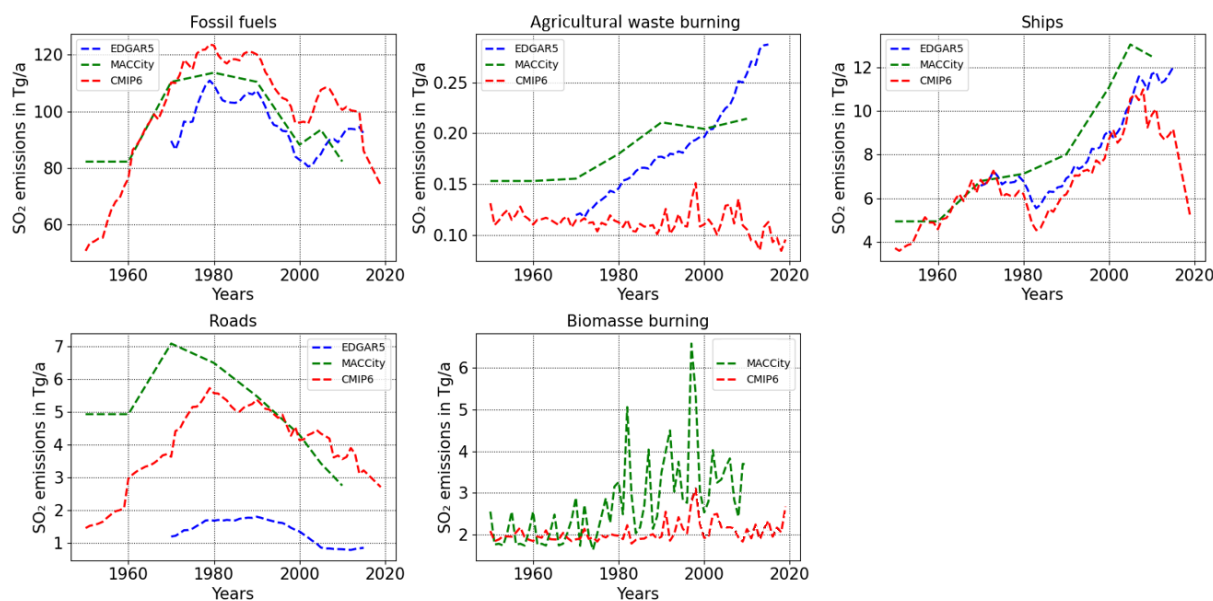


Figure 3.3: Global mean SO_2 emissions in Tg/a from multiple sectors based on different inventories (CMIP6 in red, EDGAR5 in blue, and MACCity in in green).

In Figure 3.3, SO_2 emissions from CMIP6, EDGAR5, and MACCity are compared across five different emission sectors. The data availability varies among the datasets, with CMIP6 offering the most extensive coverage spanning from 1950 to 2019, followed by MACCity from 1950 to 2010, and EDGAR5 from 1970 to 2015. This analysis is focused on the years where data is available from all inventories, specifically ranging from 1970 to 2010 for all sectors except biomass burning, where comparisons are conducted over the period from 1950 to 2010 between CMIP6 and MACCity.

It is noteworthy that the magnitude of SO₂ emissions presented in Tg/a varies across different sectors (values of about 120 Tg(SO₂)/a are estimated for fossil fuels, 12 Tg(SO₂)/a from shipping sector, 0.25 Tg(SO₂)/a emitted from agricultural waste burning, etc). Specifically, the fossil fuel and shipping sectors collectively account for approximately 90% of the total emitted anthropogenic SO₂ mass, while around 9% originates from road traffic and biomass burning activities, with less than 1% attributed to agricultural waste burning. In the fossil fuel and shipping sectors, which exhibit the largest emission rates, the temporal progression of SO₂ emissions appears similar across all three emissions inventories, with slight variations. Within the fossil fuel sector, CMIP6 reports approximately 13 Tg/a (10%) more SO₂ than EDGAR5 and 7 Tg/a (5%) more than MACCity between 1970 and 2010. However, in the shipping sector during the same period, CMIP6 claims approximately 3% less SO₂ than EDGAR5 and 10% less than MACCity. Conversely, the remaining sectors have a relatively minor contribution to the total SO₂ emissions, with differences between inventories being more pronounced. Nevertheless, these disparities are comparatively negligible, given their combined contribution of approximately 10% to the global emitted SO₂ from the sectors illustrated in Figure 3.3.

In summary, Table 3.3 illustrates the offline emission inventories presented in this section and their corresponding sulfur emission sectors. It is important to note that the EDGAR5 and MACCity emission inventories are not used within the model simulations in this study. Instead, they are included here just for comparison purposes against the CMIP6 inventory, which is employed within the global EMAC model throughout this work.

Emission inventory	Model	Sulfur emission sectors
CMIP6	EMAC	fossil fuels - agricultural waste burning - aircraft ships - roads biomass burning
AeroCom	EMAC	continuously degassing and explosive volcanoes
Spiro et al	EMAC	DMS_terrestrial
CMIP5	MECO(n)	fossil fuels - agricultural waste burning - aircraft ships - roads biomass burning
E-PRTR	MECO(n)	fossil fuels
MACCity	-----	fossil fuels - agricultural waste burning - ships roads - biomass burning
EDGAR5	-----	fossil fuels - agricultural waste burning - ships roads

Table 3.3: Emission inventories with the corresponding sulfur emission sectors used for the indicated models. Note that the EDGAR5 and MACCity emission inventories are not used within the model simulations in this study. The MECO(n) based on CMIP5 and MECO(n) based on E-PRTR are completely different simulations, used for different purposes in the present work, as described previously in the present section.

3.2 Description of the used observational data

3.2.1 Satellite observations

In this study the Copernicus Sentinel-5 Precursor mission (Sentinel-5P) is employed to investigate the SO₂ Vertical Column Density (VCD). Sentinel-5P is the first Copernicus mission specifically designed for atmospheric monitoring, as mentioned by ESA (2017). On board of the Sentinel-5P satellite, the TROPospheric Monitoring Instrument (TROPOMI) is responsible for atmospheric measurements, particularly for the quantification of various gases and aerosols. These include ozone, formaldehyde, nitrogen dioxide, carbon monoxide, methane, aerosols, and sulfur dioxide (Romahn et al., 2023), which is of specific importance in this work. TROPOMI represents a significant instrumental advancement following the Ozone Monitoring Instrument (OMI), Scanning Imaging Absorption Spectrometer for Atmospheric Chartography (SCIAMACHY), and the Global Ozone Monitoring Experiment-2 (GOME-2). It offers parameters related to the altitude and distribution with the highest spatial resolution among the mentioned satellite instruments, with a horizontal resolution of 3.5 km by 7 km (Theys et al., 2017). Comparatively, OMI provides a spatial resolution of 24 km by 13 km, SCIAMACHY offers a resolution of 60 km by 30 km, and GOME-2 has a resolution of 80 km by 40 km. The high resolution of TROPOMI enables more precise and comprehensive observations of atmospheric phenomena, including air quality assessment, ozone and UV radiation monitoring, contributing to a deeper understanding of Earth's atmospheric dynamics. The TROPOMI instrument, jointly funded by the European Space Agency (ESA) and the Netherlands Space Office, was launched on 13 October 2017 from Russia (ESA, 2017). Its selection stemmed from its capacity to provide enhanced observations, made possible by state-of-the-art technology and the integration of data from other instruments such as SCIAMACHY and OMI satellites. In this study two dimensional level-2 products from the TROPOMI are used. These products represent the original SO₂ data retrieved from the spectra observed by TROPOMI, including the geographical coordinates and resolution parameters such as scanline and ground pixel. The scanline refers to the swath width (approximately 2600 km) over which each satellite observation captures multiple ground pixels. In simpler terms, it represents the direction of the satellite's flight. On the other hand, the ground pixel dimension is perpendicular to the scanline and indicates the resolution of the data (Romahn et al., 2023). These dimensions constitute the so-called "satellite orbit". TROPOMI moves each day across the entire globe within 14 to 15 orbits with an orbital repeat cycle of 16 days, which results in 227 orbits in one orbit cycle. This allows a daily coverage of the Earth's surface, as presented in Figure 3.4. It shows the 14 orbital paths covered by the satellite in one day (here the 02.03.2019 is shown as an example).

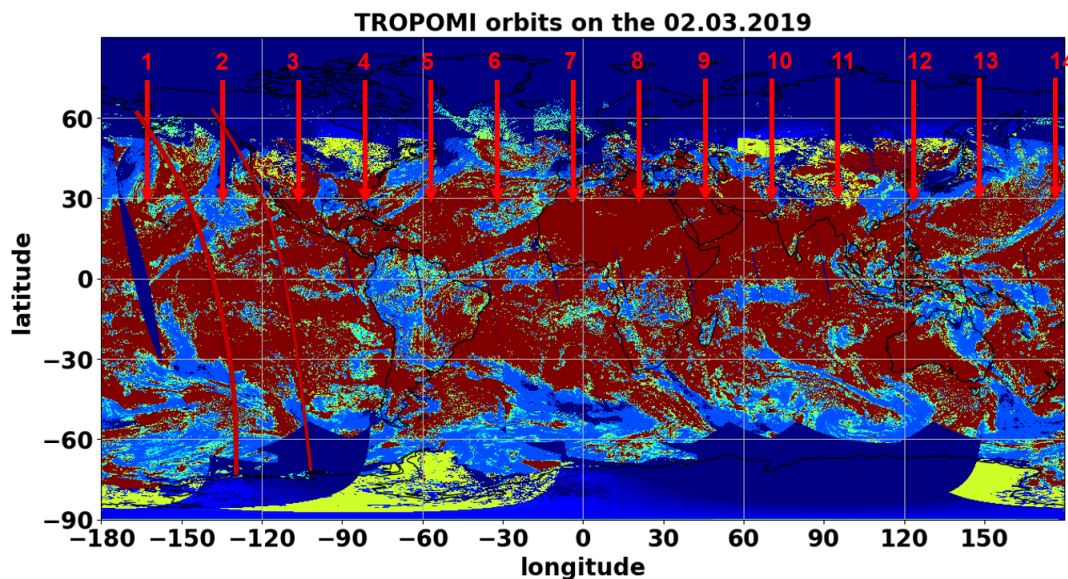


Figure 3.4: An example of the 14 measurement orbits on the 02.03.2019 covered by the TROPOMI/Sentinel-5P satellite.

The retrieval data in TROPOMI is organized vertically into pressure layers from an a-priori profile of a Chemistry-Transport Model (CTM), namely the Tracer Model 5 (TM5) (Huijnen et al., 2010). In the case of SO_2 , the data is divided into 34 distinct layers, varying approximately from the Earth's surface to 0.1 hPa (i.e. around 60 km).

In this work two distinct products are used for SO_2 retrievals from TROPOMI:

1. The operational product, which relies on a technique called Differential Optical Absorption Spectroscopy (DOAS), as proposed by Platt and Stutz (2008). Unlike directly measuring the light reflected from the Earth's surface, the satellite observes sunlight scattered by the atmosphere and reflected from the Earth's surface, with its intensity varying with the wavelength of light (as depicted by the red lines in Figure 3.5). As the measured sunlight traverses through the atmosphere, it interacts with various trace gases and particles, including NO_2 , O_3 , aerosols, and SO_2 (Thomas et al., 1996). These components absorb or scatter parts of the sunlight reaching the satellite (red lines). The cumulative concentration of SO_2 , for example, along the entire path is quantified as the Slant Column Density (SCD) associated with the footprint F, which denotes the point on the Earth's surface observed by the satellite.

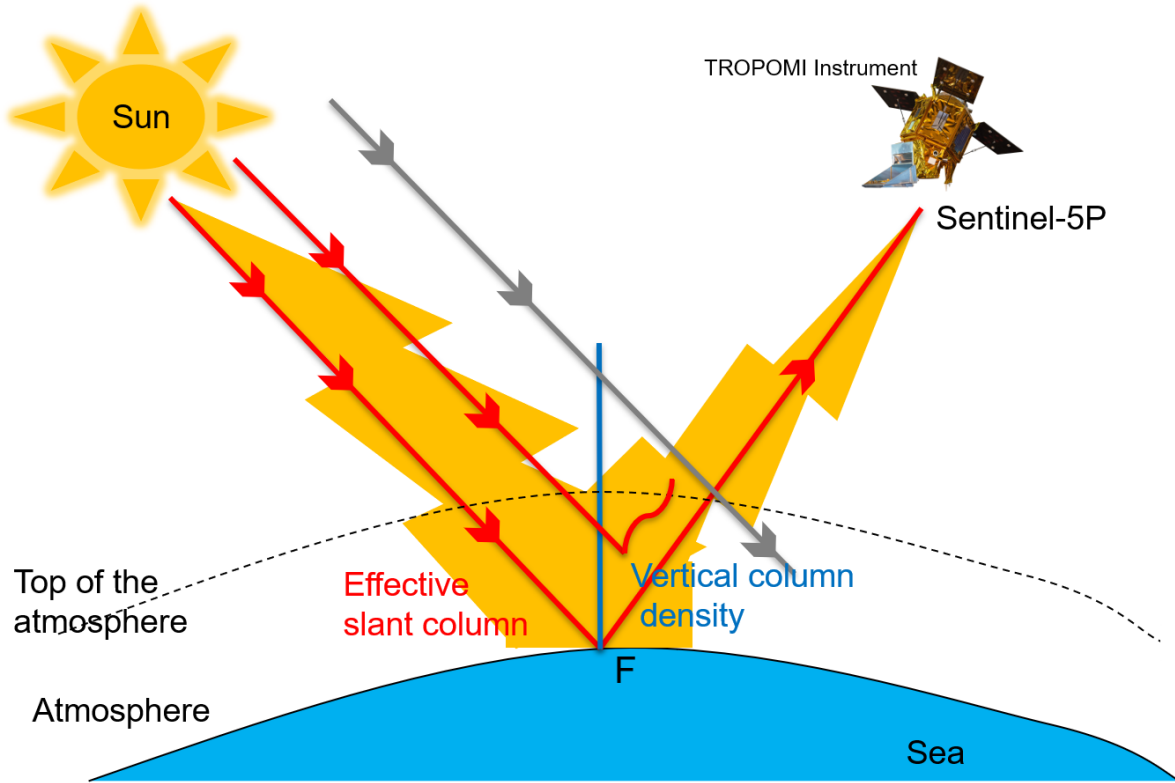


Figure 3.5: Schematic representation of the slant path (red lines) and the vertical column (blue line) of a clear sky case. One red line is reaching the satellite after getting reflected from the surface at the point F. The other red line is reflected higher up in the atmosphere. The grey path crosses the atmosphere without being reflected or absorbed by the satellite.

Multiple factors can influence the measured slant column densities (SCDs) by the TROPOMI instrument, as conditions in the atmosphere and at the Earth's surface affect the scattering and reflection of radiation back to the satellite. Clouds and aerosols are among the factors that contribute to the complexity of the measured SCD signal, leading to significant uncertainties. Therefore, Theys et al. (2017) introduced a slant column background correction scheme to reduce possible bias in the measured data. In this study the VCD is the one used for further investigations, as it provides the most pertinent and readily understandable insights into the dispersion and concentration of trace gases (Theys et al., 2021). In Figure 3.5, VCD is represented by the blue path. However, it's essential to note that VCD cannot be directly measured from the satellite. Thus, the conversion of the SCD into VCD becomes essential. This conversion process relies heavily on the air-mass factor "M":

$$VCD = \frac{SCD}{M}, \quad (3.8)$$

where the air-mass factor is calculated based on the formulation by Palmer et al. (2001), as follows:

$$M = \int m(p) \cdot s(p) dp. \quad (3.9)$$

Here, $m(p)$ is a weighting function reflecting the sensitivity of the satellite instrument to different altitudes. This function can be determined through pre-calculation or computational methods using a radiative transfer model. For the actual TROPOMI products, $m(p)$ is given by the Linearized Discrete Ordinate Radiative Transfer (LIDORT) model, as introduced by Spurr et al. (2001). The term $s(p)$ represents the vertical shape factor, which describes the normalized vertical profile of the SO_2 mixing ratio as a function of atmospheric pressure (Palmer et al., 2001). This profile can be obtained a-priori from any CCM or CTM. For instance, the CTM Tracer Model 5 (TM5) model is used as an a-priori profile for the TROPOMI/Sentinel-5P retrieval. Therefore, Equation 3.9 could also be written as:

$$M_{\text{TM5}} = \int m(p) \cdot s_{\text{TM5}}(p) dp. \quad (3.10)$$

One of the significant advantages of this approach is that it separates the contributions of the radiative transfer model from those of the atmospheric chemistry model. This separation ensures that $m(p)$ is independent of the selected a-priori profile, thereby allowing greater flexibility and accuracy in the air-mass factor calculation. In practical applications, $m(p)$ is pre-calculated using the LIDORT model for a wide range of conditions. The weighting function describes how the sensitivity of a remote sensing instrument varies with different atmospheric conditions, such as altitude, observation geometry, scene albedo, cloud top pressure; effective cloud fraction; and the position of the sun. These parameters are then systematically combined into a comprehensive look-up table (see Table 3.4), facilitating efficient and accurate retrieval of VCDs.

Parameter	Number of grid points	Grid values	Symbol
Atmospheric pressure (hPa)	64	1056.77, 1044.17, 1031.72, 1019.41, 1007.26, 995.25, 983.38, 971.66, 960.07, 948.62, 937.31, 926.14, 915.09, 904.18, 887.87, 866.35, 845.39, 824.87, 804.88, 785.15, 765.68, 746.70, 728.18, 710.12, 692.31, 674.73, 657.60, 640.90, 624.63, 608.58, 592.75, 577.34, 562.32, 547.70, 522.83, 488.67, 456.36, 425.80, 396.93, 369.66, 343.94, 319.68, 296.84, 275.34, 245.99, 210.49, 179.89, 153.74, 131.40, 104.80, 76.59, 55.98, 40.98, 30.08, 18.73, 8.86, 4.31, 2.18, 1.14, 0.51, 0.14, 0.03, 0.01, 0.001	p_l
Altitude corresponding to the atmospheric pressure, using a US standard atmosphere (km)	64	-0.35, -0.25, -0.15, -0.05, 0.05, 0.15, 0.25, 0.35, 0.45, 0.55, 0.65, 0.75, 0.85, 0.95, 1.10, 1.30, 1.50, 1.70, 1.90, 2.10, 2.30, 2.50, 2.70, 2.90, 3.10, 3.30, 3.50, 3.70, 3.90, 4.10, 4.30, 4.50, 4.70, 4.90, 5.25, 5.75, 6.25, 6.75, 7.25, 7.75, 8.25, 8.75, 9.25, 9.75, 10.50, 11.50, 12.50, 13.50, 14.50, 16.00, 18.00, 20.00, 22.00, 24.00, 27.50, 32.50, 37.50, 42.50, 47.50, 55.00, 65.00, 75.00, 85.00, 95.00	z_l
Solar zenith angle ($^\circ$)	17	0, 10, 20, 30, 40, 45, 50, 55, 60, 65, 70, 72, 74, 76, 78, 80, 85	θ_0
Line-of-sight angle ($^\circ$)	10	0, 10, 20, 30, 40, 50, 60, 65, 70, 75	θ
Relative azimuth angle ($^\circ$)	5	0, 45, 90, 135, 180	φ
Total ozone column (DU)	4	205, 295, 385, 505	TO3
Surface albedo	14	0, 0.01, 0.025, 0.05, 0.075, 0.1, 0.15, 0.2, 0.25, 0.3, 0.4, 0.6, 0.8, 1.0	A_s
Surface/cloud top pressure (hPa)	17	1063.10, 1037.90, 1013.30, 989.28, 965.83, 920.58, 876.98, 834.99, 795.01, 701.21, 616.60, 540.48, 411.05, 308.00, 226.99, 165.79, 121.11	p_s
Air-mass factor wavelength	3	313, 326, 375	

Table 3.4: Look-up table representing physical parameters for defining the $m(p)$ weighting function in Equation 3.9. Table adopted from Theys et al. (2017). The original table is reproduced according to the Creative Commons Attribution 3.0 License.

In this study the total amount of SO_2 present in a vertical column of air above the

surface of the Earth is expressed in Dobson Units (DU). Therefore, the SO₂ VCDs provided in molecules/m² by TROPOMI are divided by 2.6867e20 to get VCDs in DU, since 1 DU = 2.6867e20 molecules/m².

2. The Covariance-Based Retrieval Algorithm (COBRA) product represents the latest advancement in SO₂ retrieval techniques from TROPOMI onboard the Sentinel-5 Precursor satellite. As demonstrated by Theys et al. (2021), this method notably reduces both, noise and biases, present in the TROPOMI operational DOAS SO₂ retrievals by almost 50%. Another advantage of the COBRA product is its enhanced sensitivity to low SO₂ columns, leading to the detection and identification of numerous new SO₂ emission hotspots worldwide, such as low emitting volcanoes and power plants (Theys et al., 2021).

Finally, it is important to note that the TROPOMI level-2 products are provided with the corresponding averaging kernels (AKs) for each case (Theys et al., 2017). These qualify the vertical sensitivity of satellite instruments and are important for ensuring a fair comparison with other types of data, especially atmospheric chemistry model simulation results (Veefkind et al., 2012). In this study a detailed explanation of the AKs is provided in Section 3.3.1, where the model data is prepared for comparison with satellite measurements.

3.2.2 Ground-based measurements

Ground-based measurements offer insights in classifying emission sources, their strengths, and their environment. For an inter-comparison with model data near the Earth’s surface, ground-based measurements are used in this work from three key sulfur-emitting regions: the United States of America (USA), Europe, and East Asia. These regions are selected because of their available and extensive datasets spanning a period of two decades, from 2000 to 2019. Next, a detailed explanation of the data is presented, with each region described separately.

USA

In the USA, data of various trace gases, including SO₂, are obtained from the Clean Air Status and Trends Network (CASTnet). This network (accessible at <https://www.epa.gov/castnet>, last accessed: 24 February 2024, Finkelstein et al. (2000)), provides surface-level observations including monthly and yearly mean SO₂ concentrations and sulfur deposition fluxes over the USA. In this work the data ranging between 2000 and 2019 are evaluated. Given the large size of the USA’s land surface, a categorization of analyzed SO₂ has been undertaken, distinguishing between Eastern and Western sites. A total of 89 sites have been chosen for this study, as they represent data for both, SO₂ concentrations and sulfur deposition fluxes, over the two-decade period. Among these, 29 observation sites positioned West of 100°W longitude represent the Western USA, while the remaining

60 sites East of 100°W are representative for the Eastern regions. The spatial distribution of these site locations is presented in Figure 3.6.

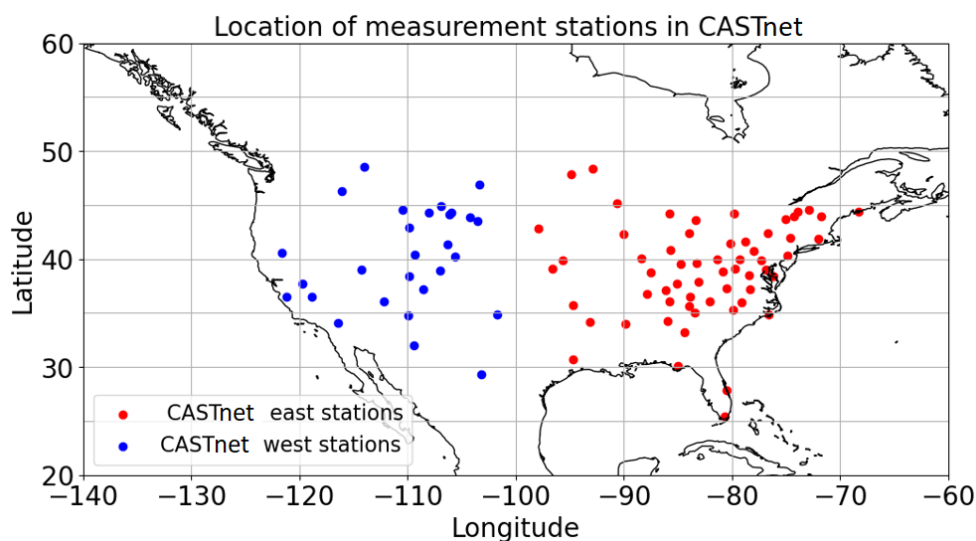


Figure 3.6: Map of the USA showing positions of Eastern (red points) and Western (blue points) CASTnet measurement sites used in this study.

In CASTnet, SO_2 and sulfate (SO_4^{2-}) concentrations are directly measured on a weekly basis at each of the stations. The concentration of sulfur compounds is multiplied by the volume of precipitation to calculate the deposition fluxes. This calculation provides the amount of sulfur deposited per unit area over a specific time period (in this work this is expressed in $kg(S)/hectares$ per year). However, measuring sulfur dry deposition fluxes faces some challenges, because it necessitates substantial instrumentation and technical resources (Hardacre et al., 2021). Therefore, deposition velocities from CASTnet are hourly estimated with the Multi-Layer Model (MLM, Meyers et al. (1998); Saylor et al. (2014)) and are integrated with measured SO_2 concentrations, land usage, and meteorological data to obtain the SO_2 dry deposition flux. The deposition velocity in the Multi-Layer Model (MLM) is based on the aerodynamic resistance, the quasi-laminar resistance to transport, and the surface uptake resistance (Baumgardner et al., 2002).

Europe

The observational data from Europe offers extensive long-term atmospheric SO_2 measurements, obtained from the European Monitoring and Evaluation Program (EMEP) since 1972. This data repository, accessible via the EMEP database (<http://ebas.nilu.no/>, last accessed: 27 February 2024; Tørseth et al. (2012)), contains observations up to the present day. From EMEP, a total of 48 observational sites, distributed across Europe, are considered for this analysis. These sites not only monitor SO_2 concentrations but also measure

sulfate (SO_4^{2-}) amount in precipitation samples (Aas et al., 2019) ranging from 2000 till 2019. The concentration of sulfur compounds in the precipitation is multiplied by the volume of precipitation to calculate the deposition fluxes. This calculation provides the amount of sulfur deposited per unit area over a specific time period (in this work this is expressed in $kg(S)/hectares$ per year). Figure 3.7 visually illustrates the distribution of these observational sites across Europe.

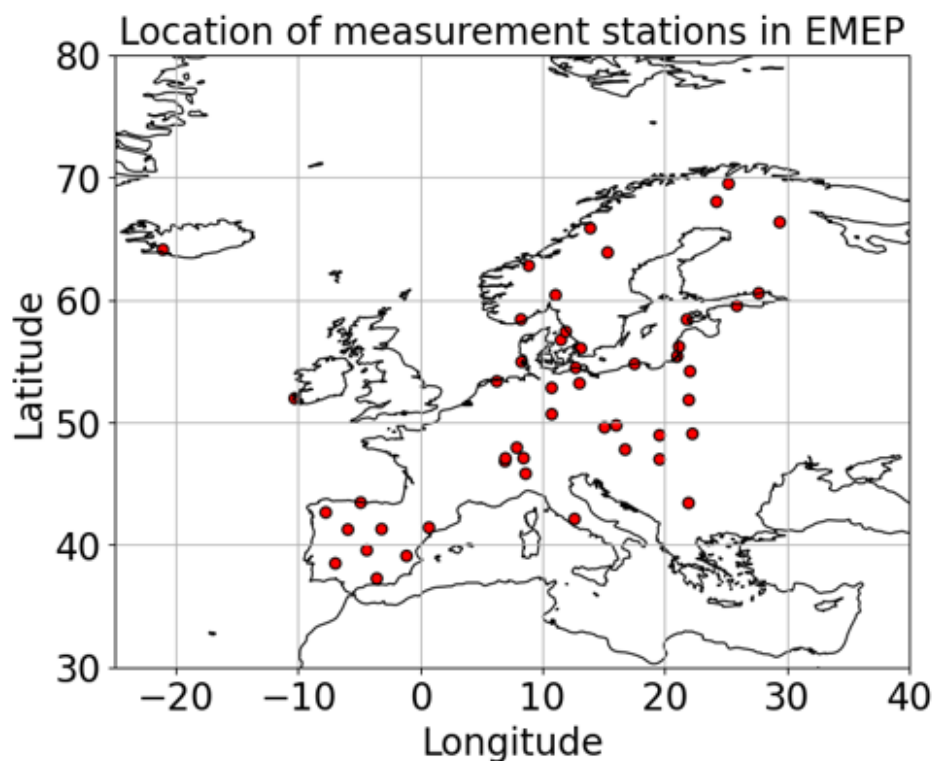


Figure 3.7: Map of SO_2 measuring sites from 2000 to 2019 in Europe from the EMEP network.

Note, that the availability of SO_2 dry deposition data is, unlike to the CASTnet network, not given from the EMEP network. Consequently, the comparative analysis of sulfur deposition in Europe between observed data and the model results must rely solely on sulfate wet deposition from precipitation.

East Asia

The data acquisition for the East Asia region posed significant challenges compared to Europe and the USA, primarily due to the historical lack of comprehensive and easily accessible environmental monitoring networks. Additionally, the less developed international cooperation and data agreements among East Asian countries further complicated

matters. Consequently, the main difficulty lay in locating representative monitoring stations equipped with continuous, long-term datasets (in this study from 2000 to 2019) of measured SO_2 concentrations and sulfur deposition fluxes. As a result, fewer observational stations were available in East Asia compared to Europe and the USA. 14 stations were selected from the Acid Deposition Monitoring Network in East Asia (EANET), comprising 2 urban, 3 rural, and 9 remote locations in China (specifically Southeastern China) and Japan, as depicted in Figure 3.8. Notably, EANET stands out as the only network in East Asia equipped to monitor both, acid deposition and air pollution, with a particular emphasis on SO_2 (Ohizumi, 2023).

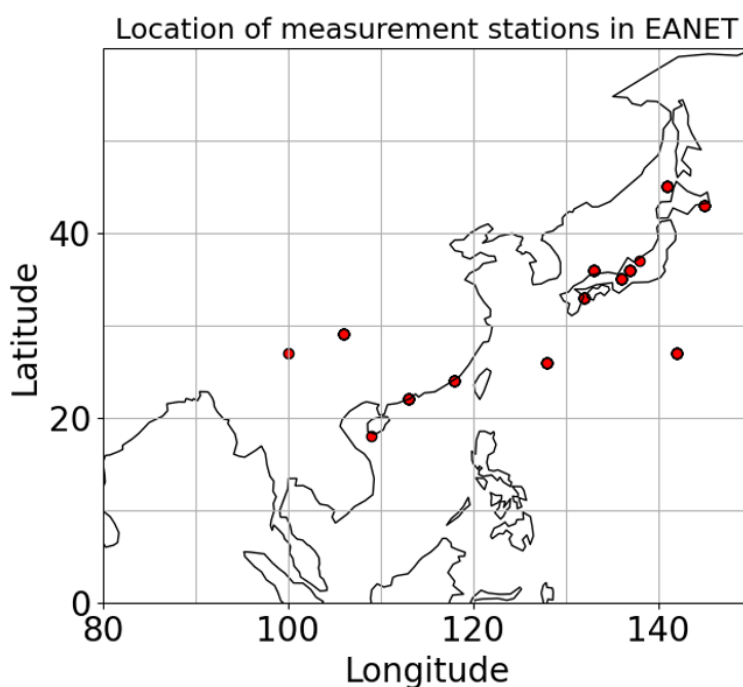


Figure 3.8: Map of SO_2 measuring sites situated in China and Japan from the EANET network.

Same as for European measurement stations, SO_2 dry deposition fluxes are neither measured nor simulated from Asian networks. Fortunately, EANET provided access to both, yearly mean SO_2 near-surface concentrations and SO_4^{2-} concentrations in precipitation. The concentration of SO_4^{2-} in the precipitation is multiplied by the volume of precipitation to calculate the deposition fluxes. This calculation provides the amount of SO_4^{2-} deposited per unit area over a specific time period (in this work this is expressed in mmol/m^2 per year).

3.2.3 Airborne measurements

In this study SO₂ mixing ratios from airborne in situ measurements, conducted by the German research aircraft "DLR Falcon (D-CMET)", are examined. These measurements were made during the METHANE-To-Go-Europe campaign, which took place in October and November 2020 over Italy and some of the Balkan countries (Croatia, Serbia and, Bosnia-Herzegovina). It aimed at measuring methane emissions from natural gas extraction platforms in the Adriatic Sea and SO₂ emission plumes from two coal-fired power plants in Serbia (Nikola Tesla) and Bosnia-Herzegovina (Tuzla) (Huntrieser et al., 2021). Here, the focus is only on the SO₂ mixing ratios, which were measured by the Chemical Ionization Mass Spectrometry (CIMS) (temporal resolution of about 3 seconds) and the Thermo Scientific 43i (temporal resolution of about 10 seconds) measurement instruments onboard of the DLR FALCON aircraft. The measurements were made in collaboration between the German Aerospace Center and local scientists in Bosnia-Herzegovina and Serbia, to investigate and study the Balkan region. This region was selected due to its classification as a hotspot for anthropogenic SO₂ emissions in Europe (Liu et al. (2018); Fioletov et al. (2020)), particularly notable for the presence of the Tuzla power plant in Bosnia-Herzegovina and the Nikola Tesla A and B (TESLA_A and TESLA_B) power plants in Serbia, which rank among the highest emitters of SO₂ in Europe (Jacimovski et al., 2016), as shown in Figure 3.9.

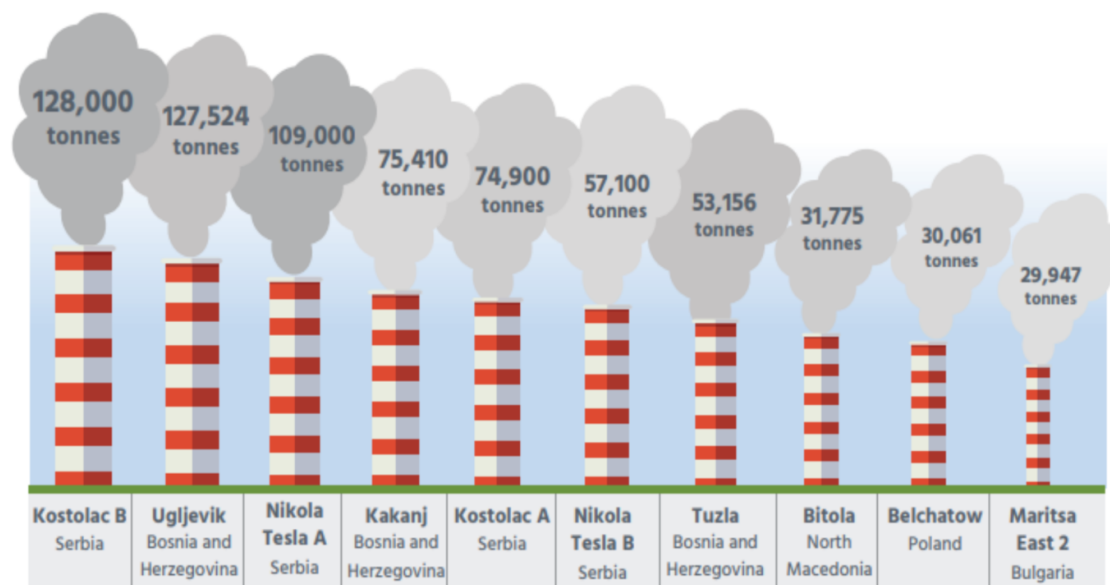


Figure 3.9: The top 10 SO₂-emitting power plants in Europe for the year 2016. The numbers show emitted SO₂ in tonnes per year. Figure adopted from Huntrieser et al. (2021).

The positions of the power plants in Bosnia-Herzegovina and Serbia are shown in Figure

3.10.

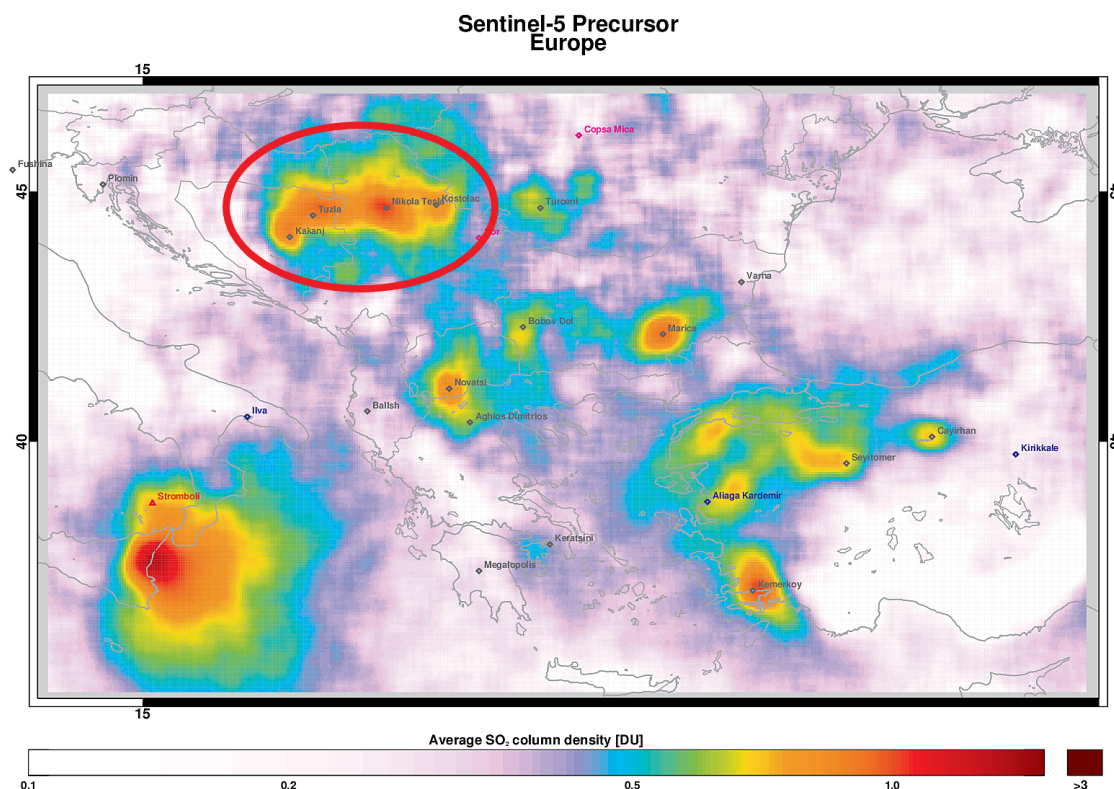


Figure 3.10: Visual map illustrating the mean SO₂ VCDs in DU across Southern Europe, as measured by the TROPOMI/Sentinel-5P satellite from May 2018 to December 2019 using the operational TROPOMI product. The red circle indicates the locations of three power plants (Tuzla in Bosnia-Herzegovina and Nikola Tesla in Serbia). The large SO₂ VCDs observed over Sicily and Southern Italy are attributed to natural SO₂ emissions from the Etna volcano.

It is important to note that Huntrieser et al. (2023) mentioned, that the CIMS and the Thermo Scientific 43i measurement instruments did not reproduce reliable measurement for very high mixing ratios, especially over the Tuzla power plant plume on the 2nd November 2020. Therefore, the measured SO₂ mixing ratios on that day could not be evaluated. For the flight on the 7th November 2020 over TESLA_A and TESLA_B power plants, one of the two airborne SO₂ instruments (the CIMS instrument) had problems to measure the unexpectedly large SO₂ mixing ratios (Huntrieser et al., 2023). For those time sequences, the measured SO₂ mixing ratios by the CIMS instrument are replaced by the second SO₂ instrument onboard (Thermo Scientific 43i) (Huntrieser et al., 2023) and are later corrected by the Thermo Scientific 43i based on laboratory experiments. Therefore, in this work only

corrected SO₂ mixing ratios from the flight on the 7th 2020 November over TESLA_A and TESLA_B power plants are examined.

3.3 Description of the model setup

In the following study a detailed analysis of the representation of the sulfur cycle focusing on atmospheric SO₂, including emissions and depositions, in the CCM EMAC was performed. The results presented in this work stem from the RD1SD-base-01 EMAC simulation that has been performed under the CCMI-2 protocol (CCMI, 2023). Here, the RD1SD-base-01 EMAC simulation runs with the CMIP6 emission inventory (see Section 3.1.12) between the years 1970 and 2019 and has a resolution of T42L90MA and a temporal resolution of 6 hours. That corresponds to a quadratic Gaussian horizontal grid of roughly $2.8^\circ \times 2.8^\circ$ in both, longitude and latitude coordinates, and 90 vertical layers (with a median lowest level height of 60 m) between the surface and the uppermost model layer centered around 0.01 hPa (Jöckel et al., 2010). Furthermore, for a triangular truncation of the spectral resolution at wave number 42, the number of longitudes and latitudes is 128 and 64, respectively (as previously shown in Table 3.1 in Section 3.1.2). For the RD1SD-base-01 simulation, the gas phase chemistry is calculated throughout the entire atmosphere using the Mainz Isoprene Mechanism (MIM1) based on Pöschl et al. (2000). This mechanism accounts for hydrocarbons up to 4 carbon atoms, along with Isopren (5 carbon atoms) and it is therefore chemically realistic. However, the simulation doesn't actively involve an interactive aerosol submodel. Therefore, aerosol effects were just prescribed in both, the troposphere and the stratosphere, to consider their impact on chemistry and interactions with radiation (Jöckel et al., 2016). Additionally, for a suitable comparison of the chemical tracers between the simulated and observational data, the RD1SD-base-01 simulation was operated in a mode called "specified dynamics" (SD), where the prognostic variables like temperature, divergence, vorticity and the logarithm of surface pressure are nudged towards the fifth generation of European Centre for Medium-Range Weather Forecasts (ECMWF) reanalysis for the global climate and weather (i.e. ERA5 (Hersbach et al., 2020)) by Newtonian relaxation. The model dynamics of the SD simulations (within a CCM) are then aligned with the observed dynamics, aiming a good reproduction of real meteorological situations.

3.3.1 Post-processing of model data for comparison with satellite observations

For a global investigation of atmospheric sulfur chemistry within the EMAC model, a comparison of model results from the SORBIT submodel (see Sect. 3.1.11) with SO₂ products from satellite measurements (TROPOMI in this work) is done. As previously mentioned in Section 3.2.1, TROPOMI SO₂ products are structured based on scanline and ground pixel, with the scanline represents the direction of the satellite's flight and the ground pixel indicates the resolution of the data, while the EMAC model operates on a

regular lat-lon grid. To facilitate a meaningful comparison, the TROPOMI data must be regridded to match the grid of the EMAC model, or both datasets need to be regridded onto the same grid. This process involves reducing the fine resolution of TROPOMI to align with the coarser resolution of the model. However, before conducting the comparison, the model data needs to be weighted with satellite averaging kernels (AKs) to ensure its compatibility with TROPOMI data (Theys et al., 2022). The Averaging Kernel defines the sensitivity of the retrieved column, obtained from satellite-based measurements, to variations in the true profile of the measured trace gases based on a CCM or CTM (Rodgers, 2000). As discussed in Section 3.2.1, TROPOMI products utilize a-priori profiles, corresponding to different cases, from the CTM TM5 model. These profiles can differ from those produced by other models, necessitating adjustments to account for these differences. The use of the AKs is important in reducing substantial systematic errors that could result from unrealistic a-priori assumptions (Eskes and Boersma, 2003). Additionally, the Averaging Kernel (AK) quantifies the impact of the stratosphere, troposphere and boundary layer on the observation, as well as describes the sensitivity of the satellite instrument for each layer (Eskes and Boersma, 2003). An ideal case with a complete clear sky, with no clouds, aerosols, and surface albedo effect, is unrealistic and therefore, averaging kernels are always below (for less sensitive cases) or above (for high sensitive cases) a value of 1. To properly weight the model data, it first needs to be brought onto the same resolution as the AKs. This involves horizontally interpolating the SO₂ mixing ratio from the SORBIT submodel (see Section 3.1.11) onto the instruments grid resolution using the nearest neighbor method. Subsequently, a vertical linear interpolation is executed to align the 90 pressure levels of the simulated SO₂ mixing ratio with the 34 layers of the a-priori profiles used for the retrievals. Afterwards, simulated SO₂ mixing ratio profiles are converted into a partial column for each of those grid-boxes (i.e. DU or molecules/cm²). The vertically interpolated model data is then ready to be multiplied at each level with the corresponding averaging kernel and vertically integrated to yield the VCD. This step is important as it translates the model SO₂ VCD into the signal that would be detected by the satellite. Finally, the VCDs of SO₂ from both, the model and the TROPOMI retrieval, are conservatively regridded from the instrument grid to the original EMAC latitude-longitude grid, and can be compared to each other.

Since the retrieved VCDs depend on simulated a-priori vertical profiles (represented as $s(p)$ in Equation 3.9), which in turn depend on prescribed, mainly anthropogenic and volcanic SO₂ emissions, the COBRA dataset (see Section 3.2.1) provides four different VCDs for specific cases:

- The standard case (or "polluted case") is obtained using profiles of daily forecasts from the global CTM TM5 (Tracer Model 5, version TM5-chem-v3.0; Huijnen et al. (2010)). TM5 operates with a spatial resolution of $1^\circ \times 1^\circ$ in latitude and longitude and with 34 pressure levels up to 0.1 hPa in the vertical column (van Geffen et al., 2016). TM5 uses 3 h meteorological fields from the ECMWF operational model, which include global distributions of wind, temperature, surface pressure, humidity, water content and precipitation (Theys et al., 2017). The SO₂ emissions originat-

ing from natural and anthropogenic sources are taken from the AeroCom project (Dentener et al., 2006).

- The 1 km case is obtained using 1 km thick box profile concentrating between the surface and 1 km (0 to 1 km), and representing a situation of passive degassing volcanoes and anthropogenic near-surface emissions.
- The 7 km case is obtained using 1 km thick box profile centered at 7 km (6.5 to 7.5 km), indicating a case of a moderate volcanic eruption.
- The 15 km case is obtained using 1 km thick box profile centered at 15 km (14.5 to 15.5 km), reflecting an explosive volcanic eruption case.

It is important to note that in order to compare the model VCDs with the four described VCDs cases from TROPOMI, similar assumptions need to be adopted to ensure a valid comparison. Specifically, assumptions on $m(p)$ and $s(p)$ profiles for TROPOMI products (see Equation 3.10) during the satellite data retrieval should be considered in model calculations. This means translating the model’s SO_2 simulated signal into the equivalent signal that the satellite would detect, as if the satellite were observing the model’s atmosphere instead of the actual Earth. This process involves the application of the averaging kernel, which adjusts the model’s profile to match the sensitivity and observational characteristics of the satellite measurements. By using the averaging kernel, one can ensure that the comparison between the satellite observations and the model output is meaningful, reflecting the same observational biases and sensitivities. In TROPOMI products, to conserve space, only the total column averaging kernel for the TM5 standard ”pollution” case is provided as described by Theys et al. (2017):

$$AK(p) = \frac{m(p)}{M_{\text{TM5}}}, \quad (3.11)$$

where M_{TM5} represents the total air-mass factor of the vertical profile of the TM5 model and is calculated following Equation 3.10. Importantly, $m(p)$ is consistent across all four cases, and the AK is calculated for the four distinct $s(p)$ profiles. Consequently, we can easily recalculate the AK for each situation by scaling the polluted (or standard) averaging kernel by air-mass factor ratios $M_{\text{TM5}}/M_{\text{box}}$, as described by Eskes and Boersma (2003):

$$AK_{\text{box}}(p) = AK(p) \cdot \frac{M_{\text{TM5}}}{M_{\text{box}}}. \quad (3.12)$$

Here, p represents the pressure level at which the averaging kernel is stored for the TROPOMI product. $M_{\text{TM5}}/M_{\text{box}}$ serves as the scaling factor reported in TROPOMI products as ”sulfurdioxide_averaging_kernel_scaling_box_{1,7,15}km”. For instance, the $AK_{15\text{km_box}}$ can be obtained using the following formula:

$$AK_{15\text{km}\cdot\text{box}}(p) = AK(p) \cdot \frac{M_{\text{TM5}}}{M_{15\text{km}\cdot\text{box}}}. \quad (3.13)$$

This approach ensures that the AK values are adjusted appropriately for each situation, facilitating an accurate comparison between the TROPOMI retrievals and the EMAC model results across different SO₂ emission cases. In this study the averaging kernels are referred to as AK_polluted, AK_1km, AK_7km and AK_15km, and the resulting VCDs are respectively expressed as, VCD_AK_polluted, VCD_AK_1km, VCD_AK_7km and VCD_AK_15km.

To provide a clearer understanding of the vertical profiles for the different averaging kernels and their influence on the shape of the SO₂ vertical profiles in the EMAC model, Figure 3.11 presents an illustrative example for one geolocation in China in February 2019. The right panel of the figure shows the vertical profiles of the AKs, while the left panel indicates their impact on the original, non-weighted SO₂ vertical profile (pink line). These profiles highlight the differences among the four AKs across various atmospheric pressure layers. It is noteworthy that, although the AKs exhibit the same shape in the vertical profile, differences in magnitude arise due to the scaling factors applied. As outlined in Equation 3.11, the essence of the AKs lies in the weighting function $m(p)$, which determines the overall shape. The function $s(p)$ can't influence the shape of the AKs and serves as a correction factor of the vertical profile of $m(p)$. Generally $s(p)$ describes the normalized vertical profile of the SO₂ mixing ratio. By vertically integrating and multiplying $m(p)$ with $s(p)$ at each layer (air mass factor calculation), the same assumptions applied to $m(p)$ and $s(p)$ in transforming retrieved SCD to VCD, described in Equation 3.8, are also applied to the AKs for model data adjustment. In this process, depending on the assumed vertical profile case (whether it be for the standard "polluted" case or the cases at 1 km, 7 km, or 15 km) the data from both TROPOMI and EMAC are processed using the same air mass factor, as mentioned in Equations 3.8 and 3.11, respectively. This means that the shape of the AK vertical profiles is determined by $m(p)$, where the air mass factor M is utilized as a correction or scaling factor. This factor is calculated for the four distinct $s(p)$ profiles (whether it be for the standard "polluted" case or the cases at 1 km, 7 km, or 15 km), ensuring consistency in the application of the AKs.

In general, the AK factors (i.e. the sensitivity of the instrument) are relatively low near the surface. This phenomenon occurs because the signal received by the satellite is affected by scattering and absorption by molecules and aerosols throughout the atmospheric column. Near the surface, these processes significantly weaken the signal, reducing the satellite's ability to accurately detect trace gases. Consequently, the satellite's sensitivity is lower near the surface and increases with altitude, where the atmosphere becomes more transparent. In Figure 3.11, the AK factors from all the prescribed situations are quite similar between the surface and approximately 900 hPa. However, beyond 800 hPa, the AK_polluted increases rapidly compared to the other AK profiles, reaching a factor of approximately 15 in the upper troposphere. In contrast, the AK_1km only reaches a factor of 5. In the moderate and eruptive volcano cases, the AKs exhibit smaller factors

throughout the entire atmospheric column, with a gradual increase in the vertical atmospheric pressure. Specifically, the AK factors reach a maximum of approximately 2.5 for the AK_7km and 2 for the AK_15km.

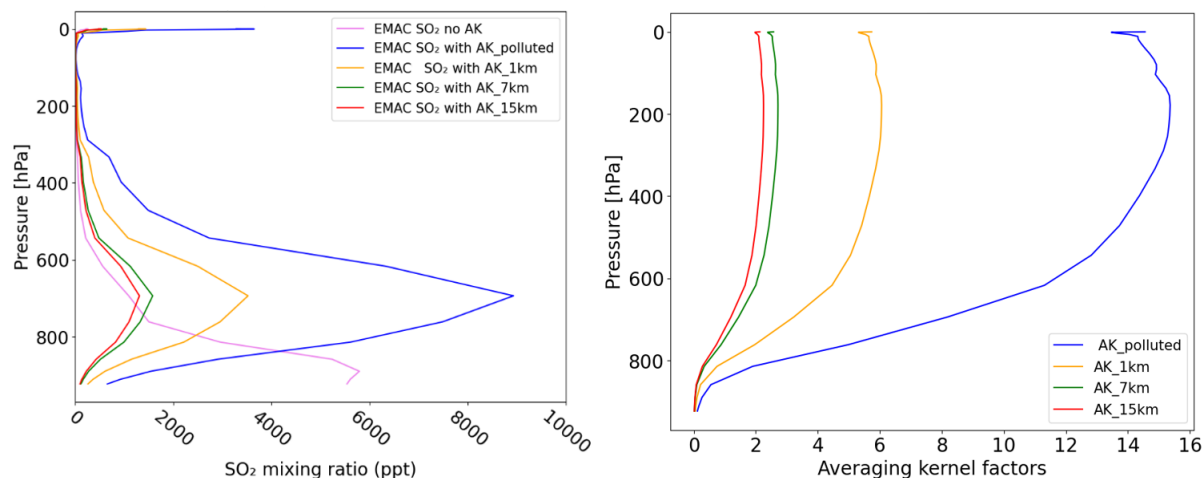


Figure 3.11: Vertical distribution of the original and weighted EMAC SO₂ mixing ratio profiles and averaging kernel factors at various pressure levels at one geolocation in China for February 2019. The right panel shows the change of the vertical profiles of the four distinct averaging kernels, where the left panel depicts the shape of SO₂ mixing ratio vertical profiles in part per trillion (ppt) from the original EMAC model without AK application (pink line) and the change in vertical profiles after applying the different AKs. Note that the increased SO₂ mixing ratios near 0 hPa are due to the artifacts originating from the interpolation of the EMAC vertical column.

The VCDs from the EMAC model are subsequently adjusted using these AKs, which significantly influence their actual values. In the left panel of Figure 3.11, the EMAC VCDs without AK application (pink line) indicate a larger SO₂ mixing ratio near the surface. However, when weighted with the AKs, the EMAC model simulates observations as they would be perceived by the Sentinel-5P satellite. Consequently, the EMAC SO₂ mixing ratios exhibit lower values near the surface due to the satellite's reduced sensitivity at lower altitudes. After applying the AKs, elevated values are observed at higher altitudes in all four profiles. Specifically, at approximately 670 hPa, the SO₂ profiles reach their maximum values, coinciding with the TROPOMI maximum sensitivity (large AK factors) and the original EMAC vertical profiles showing around 1000 part per trillion (ppt) at that level. Further up in the atmosphere, although the AKs indicate larger factors, the EMAC SO₂ mixing ratios decrease post-AK application due to the lower SO₂ mixing ratios in the original EMAC SO₂ profile.

Furthermore, applying AK_polluted in this example tends to yield larger VCD values compared to other AKs. For example, multiplying the SO₂ mixing ratios at around 200 hPa by AK_15km (factor of 2) and AK_polluted (factor of 15) can introduce a substantial

discrepancy, roughly by a factor of 7.5. Therefore, the selection of AKs requires careful consideration, reflecting the specific characteristics of the studied situation and the distribution of emissions within the regions under investigation. Incorrect AK selection can lead to either overestimation or underestimation, thereby leading to misinterpretation of model results. Notably, when comparing to TROPOMI VCDs, the differences among various AKs are consistent, as they differ only by a scaling factor, assuming the same quality flag is applied to select valid vertical profiles.

The global impact of applying AKs on the EMAC VCDs of SO_2 is illustrated in Figure 3.12. This figure presents a spatial comparison of the monthly mean SO_2 VCDs in EMAC, weighted by the four AKs for February 2019. Low SO_2 VCD values below 0.03 DU are not shown to avoid noise in the presented data. This figure aims to underscore the variations in SO_2 VCDs that emerge when different AKs are utilized, highlighting the importance of appropriate AK selection in obtaining accurate atmospheric composition data.

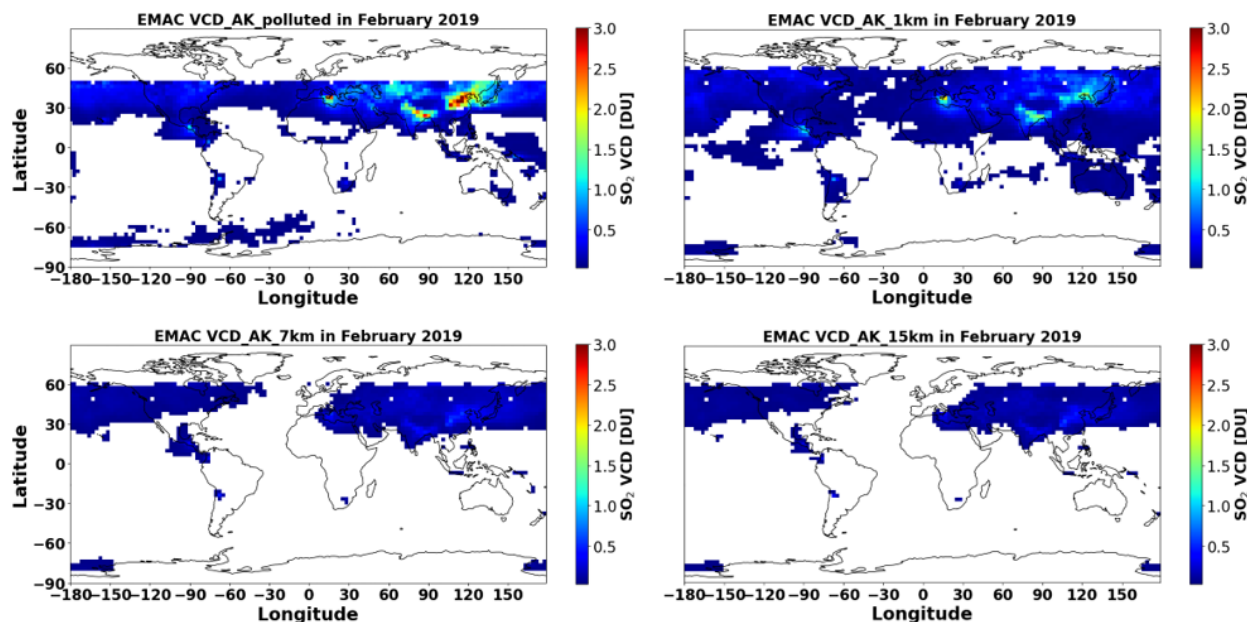


Figure 3.12: SO_2 VCDs in DU from EMAC in February 2019, weighted with the four different AKs.

In all the four panels in Figure 3.12, SO_2 signals are particularly visible in emission hotspot regions such as China, India and over the Etna volcano. However, the sensitivity of the SO_2 VCDs varies across the panels. The largest values (with VCDs around 3 DU) are evident in the top-left panel, in which EMAC VCDs are calculated with AK_polluted. In the panel representing EMAC VCDs calculated with AK_1Km (top-right panel), the SO_2 signals are also evident in the same hotspot regions, but with lower intensity, ranging between 1 and 1.5 DU. Conversely, for the AK_7km and AK_15km, the SO_2 VCDs in the hotspot regions are notably lower than 0.2 DU. Moreover, SO_2 VCDs in significant parts of

Europe, most of Africa, and South America are too low (falling below the applied threshold of 0.03 DU) and consequently are not represented in the lower panel of Figure 3.12. This signifies that in these hotspot regions, AK_polluted exhibits larger factors compared to AK_1km, AK_7km and AK_15km, as demonstrated in Figure 3.11 for China. However, in other regions such as Australia and central Northern Africa, stronger SO₂ signal is observed when applying the AK_1km. This suggests that in these areas, the AK_1km reports the highest sensitivity factors compared to the other averaging kernels, leading to a more pronounced detection of SO₂.

This comparison underscores the significance of employing appropriate AKs, particularly for the study of the absolute values of emitted SO₂ over both, anthropogenic and natural point sources. For example, the examination of anthropogenic SO₂ emissions in West Europe, utilizing AK_7km would not be feasible (bottom left panel in Figure 3.12), as the chosen AK is not suitable for studying the emitted SO₂ in that region. Another illustrative example concerns the SO₂ VCDs over China. Despite the fact that the SO₂ emission height and mass in the EMAC model for February are the same in all 4 panels, differences in SO₂ signal intensity are evident between the four panels. These differences can solely be attributed to the different magnitude of the applied AKs (as depicted in Figure 3.11). Specifically, the VCD over China is multiplied by a larger factor when AK_polluted is applied compared to other AKs. Hence, it is essential to consider the AK used when conducting a scientific evaluation of the absolute emissions over a specific point source. However, for relative comparisons between the model and TROPOMI, the choice of the AK becomes irrelevant. This is because the VCDs retrieved by TROPOMI and their corresponding AKs are derived under the same assumptions regarding the four different cases, as described in Equations 3.8 and 3.11, respectively. Here, the comparison between the model results and TROPOMI retrievals shows consistent VCDs, differing only by a constant factor from one case to another, as seen in the left panel in Figure 3.11.

Figure 3.12 also shows the available latitudinal coverage of each averaging kernel. While the panel for the standard "pollution" case (top left) indicates a range between 70°S and 50°N, the three remaining panels (for volcano cases) cover a region between 80°S and 60°N. This is due to the application of the recommended quality criteria, presented by Theys (2023). Following, a detailed description of the different SO₂ VCD products used by TROPOMI, is given:

- VCD_AK_polluted is used for the standard "pollution" case. Here the COBRA product (see Section 3.2.1) is used due to its enhanced sensitivity to detect low SO₂ column densities. Additionally, a quality flag mechanism is employed to filter out potentially erroneous inputs such as cloudy pixels or missing values, which could deteriorate the results. Therefore, only data points with a quality assurance value above 0.5 (qa_value > 0.5) are considered reliable for analysis, as recommended by Theys (2023). Multiple filtering criteria are accounted for this qa_value including, snow ice flag < 0.5, SO₂ total air mass factor polluted > 0.15, SO₂ total vertical column > -0.0015 mol/m², selected fitting window flag = 1, cloud fraction < 0.3, and solar zenith angle (SZA) < 70° (Theys, 2023). The quality assurance value

ranges from 0, indicating erroneous measurements, to 1, denoting high-quality data.

- VCD_AK_1km and VCD_AK_7km are also retrieved from the COBRA product. However, for volcanic activities, the prerequisite of the quality assurance value is no longer applicable. Instead, the only filtering criteria required is the SZA, where just data with $SZA < 70^\circ$ is considered (Theys, 2023). This can lead to higher signal-to-noise ratios in the satellite measurements, improving the quality of the data collected.
- The VCD_AK_15km product is applied specifically for eruptive volcano emissions. According to Theys et al. (2021), the COBRA product is not well-suited for large volcanic eruptions, particularly in handling extensive SO_2 columns. Hence it is recommended to use the operational TROPOMI product (see Section 3.2.1) for such significant eruptions (personal communication with N.Theys). Here, the filtering flag for volcanoes of $SZA < 70^\circ$ is similarly applied.

3.3.2 Post-processing of model data for comparison with ground-based measurements

For a comparison between ground-based data derived from the model simulation and measurements, it is necessary that both datasets are aligned on the same latitude-longitude grid. To achieve this, the measurement locations are interpolated to fit in the $2.8^\circ \times 2.8^\circ$ horizontal grid of the RD1SD-base-01 EMAC simulation (see Section 3.3). Therefore, the nearest neighbor method is applied to assign the station measurement positions to the model grid. Figure 3.13 presents an example showing the original positions of the ground-based measurement stations in Europe and after being interpolated onto the model grid.

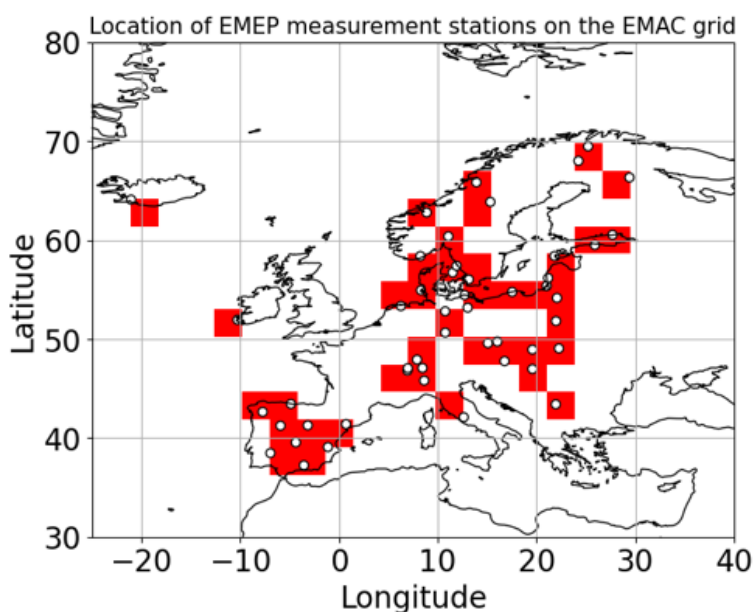


Figure 3.13: Visual representation of the original sulfur measurement sites in Europe (white circles) between 2000 and 2019 from EMEP network and after being mapped onto EMAC model's grid (red squares).

3.3.3 Post-processing model data for comparison with airborne measurements

In order to investigate SO_2 mixing ratios from airborne measurements conducted during the METHANE-To-Go-Europe campaign, the MECO(n) model system is used. As mentioned in Section 3.1.3, MECO(n) is applied because of its capability to simulate atmospheric processes on regional scale. The online coupling of EMAC and the COSMO/MESSy model allows a high resolution (about 0.01° in this study) for the simulation of regional chemical and meteorological processes. In this work the simulations used for MECO(n) comparison to the METHANE-To-Go-Europe campaign were conducted by Mariano Mertens. Figure 3.14 represents the used coupled EMAC/COSMO/MESSy model with an online nesting involving three nested COSMO/MESSy domains (MECO(3)) operated concurrently. To achieve regional refinement at a specific location, the size of the COSMO/MESSy domains decreases with each subsequent domain, thereby allowing for increased spatial and temporal resolution.

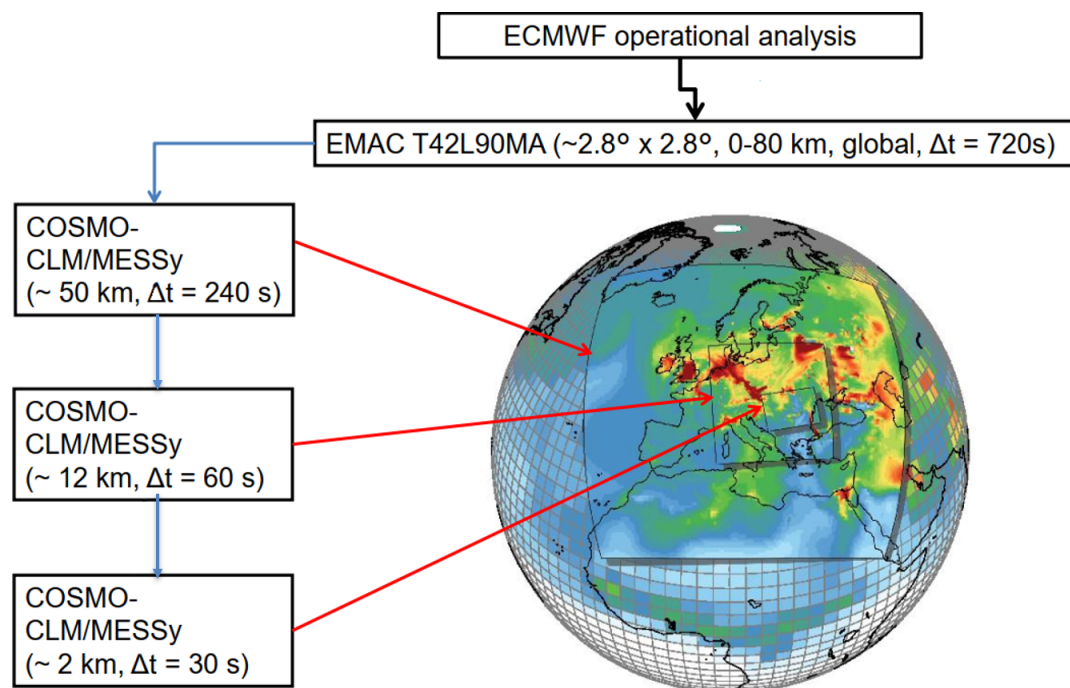


Figure 3.14: A schematic representation of the MECO(3) setup for simulating the METHANE-To-Go-Europe campaign is shown, with three COSMO/MESSy instances in Europe (CM50, CM12, CM2) and nested within the global EMAC model. Figure adapted from M. Mertens (DLR-IPA) (personal communication, 2020).

Each domain receives initial and boundary conditions from the corresponding coarser model domain (Mertens et al., 2020). In this work the initial and boundary conditions for the first MECO(1) domain, covering Europe with a resolution of 0.44° (~ 50 km) and a time step length of 240 s ("CM50"), are obtained from the global EMAC model with a T42L90MA resolution. Subsequently, MECO(2) with a resolution of 0.11° (~ 12 km, time step length 60 s, "CM12") covering central Europe, and MECO(3) with a resolution of 0.01° (~ 2.8 km, time step length 30 s, "CM2") covering Italy/Southeastern Europe, receive their initial and boundary conditions from MECO(1) and MECO(2), respectively. For Europe, CM50 and CM12 instances are set up with a vertical coordinate of 40 vertical model levels (with the lowest 1 km divided into 11 levels and the lowermost layer being 20 m thick) and CM2 operates with 50 vertical layers (with the lowest 1 km divided into 12 levels and the lowermost layer being 20 m thick) reaching from the Earth's surface to an altitude of around 22 km. Figure 3.15 provides a visual representation of the data exchange processes between the global EMAC model and the three COSMO/MESSy domains presented in Figure 3.14.

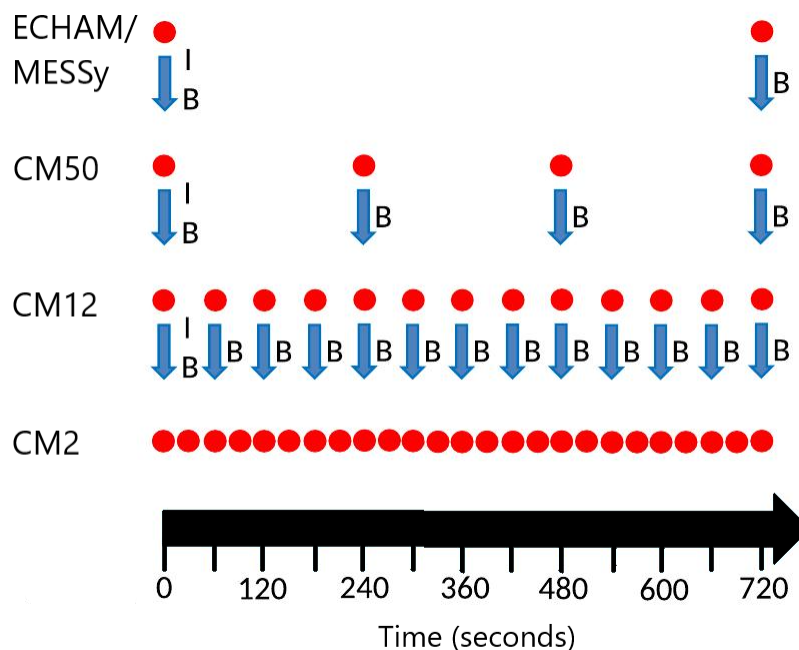


Figure 3.15: Visualisation of the data exchange between ECHAM/MESSy and the multiple COSMO/MESSy model domains of the MECO(3) used in this study. The data exchange (blue arrows) occur every model time step (red circles) of the respective coarser model domain. The initial and boundary data exchange are represented with (I) and (B) respectively. The figure is adopted from Nickl et al. (2020). The original figure is reproduced according to the Creative Commons Attribution 4.0 License.

The data exchange occurs at specific intervals within the model time of the respective coarser model domain. The number of grid boxes and the time step length vary between model domains, with finer domains having more grid boxes and shorter time steps.

In this study the actual MECO(n) simulation is covering the same period of the METHANE-To-Go-Europe campaign (i.e. from 15 October 2020 till 9 November 2020). Here the 4th instance of MECO(3) covers the Italy/Southeastern Europe area measured from the DLR Falcon (D-CMET) aircraft, aligning with the region of focus in this work. This instance gets the SO₂ emissions from the E-PRTR emission inventory (see Section 3.1.12). In the present work the global EMAC model runs with the emission inventory from the CMIP5 Project (see Section 3.1.12). The choice of the E-PRTR emission inventory in the 4th instance was driven by its significantly higher spatial resolution, which provides precise latitude/longitude coordinates for major emitters and offers emissions data for the year 2017. Specifically, in this work the focus is on analyzing the SO₂ mixing ratios from emission plumes originating from the TESLA_A and TESLA_B power plants on the 7th November 2020, as described in Section 3.2.3. Although the E-PRTR database indicates a uniform emission height of 100 m for most of the sources, it does not accurately represent the actual emission heights of these power plants. Therefore, the emission heights for these

specific power plants were adjusted based on data provided by Alina Fiehn, resulting in revised emission heights of 220 m for TESLA_A, and 280 m for TESLA_B.

Due to MESSy, the chemical processes, such as the offline prescribed and online calculated emissions of traces gases, MECCA chemistry, dry and wet deposition processes, between the three times nested COSMO/MESSy and EMAC models are consistent, ensuring the same diagnostics between the different instances and EMAC.

Chapter 4

Investigation of the tropospheric sulfur budget in the EMAC model

In this section, the global tropospheric sulfur budget is investigated using the CCM EMAC model. Ensuring the closure of the sulfur budget in a CCM model is important. In EMAC the production and removal of sulfur are analyzed for both, natural and anthropogenic sulfur emissions. A closed budget ensures a sulfur mass conservation within the system. In other words, it guarantees that the total amount of sulfur entering the system equals the total amount leaving the system. This provides confidence in the model's ability to simulate real-world conditions and helps validate its performance against observational data. However, if the budget is not closed, it suggests that there may be errors or biases in the model representation of certain processes. For example, if there is an unaccounted source or sink of sulfur, it could indicate a deficiency in the model, for instance stoichiometric deficiencies in the formulation of the chemical kinetics, or incompletely implemented source or sink processes. However, it could also point to an incomplete diagnostics of the budget. Last but not least, reliable estimates of sulfur budgets are essential for informing policy decision makers and designing effective mitigation strategies to reduce sulfur emissions and their environmental impacts. Accurate modeling of sulfur budgets helps policymakers understand the effectiveness of emission reduction measures and prioritize actions to improve air quality and protect human health and the environment. For this, a detailed investigation of the sulfur emissions and depositions within the EMAC model is described in Section 4.1. Additionally, the tropospheric sulfur budget of EMAC is compared to literature studies in Section 4.2. Furthermore, the role of aerosols on SO₂ chemistry is examined in Section 4.3. Finally, a discussion and conclusion of the results are given in Section 4.4.

4.1 Tropospheric sulfur budget within EMAC

This section provides a comprehensive evaluation of the global tropospheric sulfur budget within the EMAC model, thoroughly examining both, the prescribed sulfur emissions and the deposited sulfur-containing species, for the years between 2010 and 2019. The selection

of these particular years stem from their status as the most recent available years in the RD1SD-base-01 simulation. The aim of this evaluation lies in ensuring that the prescribed sulfur emissions, derived from various sources worldwide, are balanced in the form of sulfur deposition outputs. Essentially, the principle is straightforward: whatever is initially emitted in the model must ultimately be reflected in the corresponding outputs, thereby ensuring the integrity of the sulfur budget. In a year for example, it should look like this:

$$\begin{aligned} \mathbf{Burden}(\mathbf{end\ of\ the\ year}) - \mathbf{Burden}(\mathbf{beginning\ of\ the\ year}) = \\ \mathbf{Emission}(\mathbf{Year}) - \mathbf{Deposition}(\mathbf{Year}) \end{aligned} \quad (4.1)$$

In this context, burden signifies the overall mass of all sulfur present in the model atmosphere, including all species containing sulfur. "Burden(end of the year) - Burden(beginning of the year)" refers to the change of the burden throughout the year. Emission refers to the cumulative sum of all sulfur emissions, while deposition represents the total of all removed sulfur sinks from the atmosphere.

Sulfur prescribed emissions in EMAC originate from multiple offline emission inventories and online calculations, as explained in Section 3.1.12. These emissions arise from both, anthropogenic and natural sources. In the present study, fossil fuels, DMS from the ocean (denoted as DMS_{airsea}), DMS from terrestrial sources (denoted as DMS_{Terrestrial}), volcanic activity, and maritime shipping collectively contribute to nearly 95% of the sulfur emissions released into the EMAC model. Other sources, such as OCS, agricultural waste burning, and road emissions, constitute the remaining 5% of the emitted sulfur. Figure 4.1 illustrates an example of the year 2010 for the used sulfur emissions in the model.

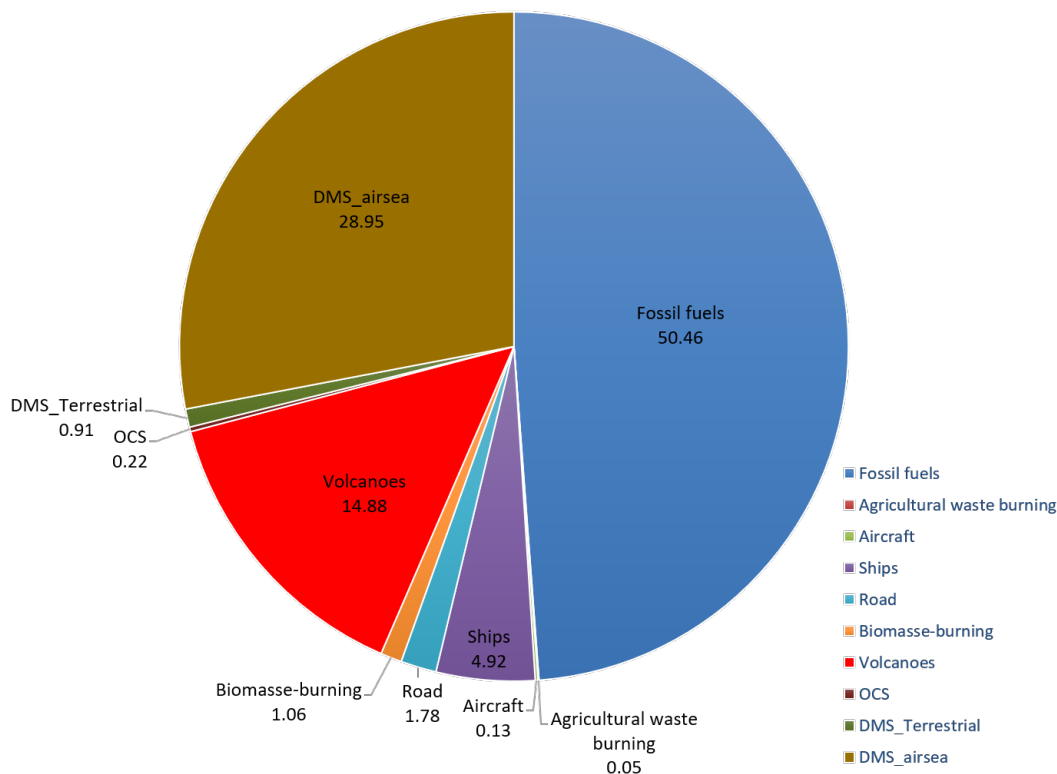


Figure 4.1: Emission fluxes of the natural and anthropogenic sulfur sources for the year 2010 in the global EMAC model in $Tg(S)/year$.

The released sulfur from these sectors becomes oxidized and get removed from the atmosphere through dry deposition, sedimentation and wet deposition/scavenging, which rinses sulfur through convective and large scale precipitation ($cv+ls$). The emitted, deposited and remaining sulfur species are examined for the year 2010 in Table 4.1. Note that the same underlying principles apply to all other years, with changes in in emission and deposition values being the only modifications from one year to the other.

Type of emissions		Tracers	Dry deposition	Scavenging (cv+ls)	Sedimentation	Change of burden
Emissions in Tg(S)/year		Depositions in Tg(S)/year				
Fossil fuels	50.46	SO_2	23.01			-0.08
Awb	0.05	CH_3SO_3H	7.7			0.01
Aircraft	0.13	H_2SO_4	3.67			0.004
Ships	4.92	$DMSO$	0,15			-4.47E - 05
Road	1.78	$SO_4_{res_cs}$	1.49	0.24	7.13	0.013
Biomass burning	1.06	SO_4^{2-}		49.26		0.08
Volcanoes	14.88	HSO_3^-		0.05		2.20E - 04
OCS	0.22	$CH_2OHSO_3^-$		0.58		0.01
DMS terrestrial	0.91	SO_5^-		0.02		1.66E - 04
DMS air-sea	28.95	HSO_5^-		1.11		0.002
		HSO_4^-		2.64		0.06
		Sum	36.05	54.07	7.13	0.11
Total sum	103.39	Total sum	97.38			
Emission total sum - (Deposition total sum + change of burden) = 6.01						

Table 4.1: Detailed examination of the emitted, deposited and remaining sulfur species for the year 2010 in the EMAC model. The green column represents the sulfur emission sectors and the red column shows the sulfur tracers deposited within the EMAC model. (cv+ls) refers to convective and large scale precipitation.

As a conclusion from Table 4.1, the closure of the tropospheric sulfur budget appears to be not established so far. The model indicates a difference between the emitted and deposited sulfur of about 6 Tg(S)/year. Table 4.2 presents the sulfur budget, calculated as the difference between sulfur emissions and the change of burden with total sulfur depositions (the sum of sulfur sedimentation, dry and wet deposition), for the years spanning from 2010 to 2019. Notably, the tropospheric budget analysis reveals an unresolved deficit ranging between 6 and 8.2 Tg(S)/year throughout this period.

Years	Sulfur emission	Sulfur dry deposition	Sulfur wet deposition	Sulfur sedimentation	Total sulfur deposition	Change of burden	Sulfur deficit
2010	103.39	36.05	54.07	7.13	97.27	0.11	6.01
2011	102.87	36.63	51.53	7.25	95.41	0.10	7.35
2012	102.66	35.64	51.64	7.17	94.46	0.11	8.08
2013	102.25	35.93	50.93	7.14	94.00	0.12	8.12
2014	101.41	34.98	51.17	7.10	93.26	0.08	8.06
2015	95.22	32.68	48.04	6.98	87.70	0.09	7.43
2016	92.96	31.64	47.37	6.54	85.56	0.10	7.29
2017	91.03	31.10	45.88	6.52	83.51	0.10	7.42
2018	88.95	29.98	45.07	6.55	81.61	0.12	7.21
2019	86.99	28.98	44.40	6.40	79.78	0.11	7.10

Table 4.2: Sulfur budget calculation from sulfur emissions, deposition and change of burden in $Tg(S)/year$ between 2010 and 2019 in the EMAC model.

This discrepancy is attributed to a missing budget term in the SCAV submodel. This has been analysed as follows: In the EMAC’s standard setup, the liquid-phase chemistry (submodel SCAV, see Section 3.1.7) is typically calculated separately from the gas-phase chemistry (submodel MECCA, see Section 3.1.8) so that equilibrium reactions between the gas- and liquid phase can be computed. For example, SO_2 is relatively soluble, and in areas with clouds or liquid aerosols, SO_2 dissolves to a certain amount into the liquid phase and then chemically reacts further in the liquid phase. This is done according to the liquid-phase mechanism of SCAV (see Section 3.1.7). Thus, at each model time step, the dissociation between gas- and aqueous phase is assumed to be in equilibrium, which is a good approximation for a typical time step length of about 10 minutes in a global model. In consequence, the dissolved species are not explicitly transported as individual tracers, but at the end of each time step released (evaporated) back into the gas-phase. This transition back into the gas phase, however, considers (for sulfur species) only SO_4^- . The SO_4^- is not transferred into the gas-phase, but it remains bound in an aerosol. Since in the RD1SD-base-01 model setup, no aerosol submodel is active, SCAV converts the SO_4^- into a so-called residual aerosol ($SO4_res_cs$, where "res" stands for residual, and "cs" for coarse mode). This residual aerosol is treated by other processes (large scale advection, convective and turbulent tracer transport, wet and dry deposition, sedimentation) as any other aerosol. Consequently, it is correctly accounted for in the budget analysis as shown in Table 4.1. In the EMAC standard setup, it is assumed that SO_4^- is the most important sulfur component in the aqueous phase, and the others species are simply neglected. To analyse the budget deficit further, a sensitivity simulation has been performed, in which all aqueous phase species are not re-evaporated each time step (and equilibrated in the next), but rather treated as individual aqueous phase tracers, which are subject to all other processes as listed above. Figure 4.2 provides a comprehensive illustration elucidating the

differences between the standard setup and the modified sensitivity simulation, in order to identify the deficits in the model.

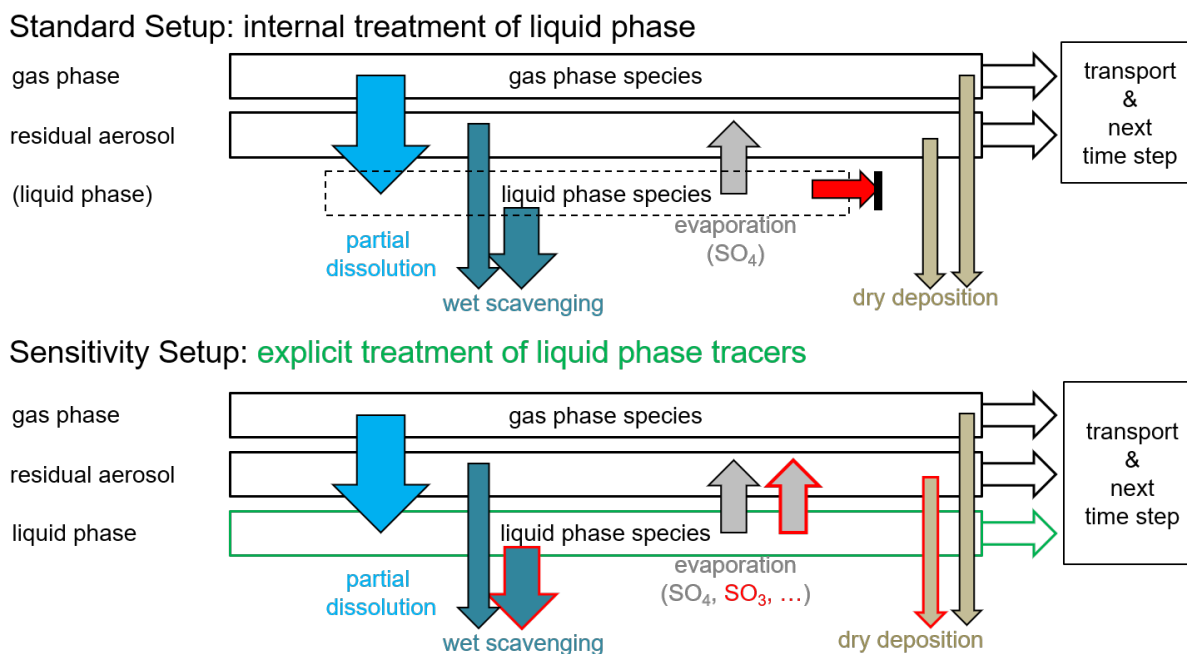


Figure 4.2: Treatment of liquid phase tracers within the EMAC model in the standard and sensitivity setup, respectively. (Personal communication with P. Jöckel).

In the standard setup (depicted at the top of Figure 4.2), the procedure at the beginning of each time step is:

1. Initially, the amount of tracer dissolving into the liquid phase is calculated (partial dissolution).
2. Subsequently, chemical kinetics in the liquid phase is computed. A fraction of the liquid phase tracer is removed through wet scavenging, induced by precipitation.
3. At the end of the time step, the remaining SO_4^- tracer in the liquid phase is transformed into a residual aerosol. The rest, indicated by the red arrow, is lost.
4. Gas phase and residual aerosol tracers are subject to dry deposition.

This entire process repeats in the subsequent time step, with no information from the liquid phase carried over to the next time step.

In the sensitivity simulation (indicated at the bottom part of Figure 4.2), the tracers in the liquid phase are consistently carried along throughout the entire process. This differs from the standard setup as follows:

1. Initially, the transition of tracers from the gas to the liquid phase is calculated, involving partial dissolution.
2. Following that, similar to the previous description, the chemical kinetics in the liquid phase is computed. A portion of the liquid phase tracers is removed through wet scavenging induced by precipitation.
3. In areas where liquid (such as clouds or precipitation) evaporates, the liquid phase tracers are completely transferred into the residual aerosol. It's crucial to emphasize that all species undergo this transition, while the remainder stays in the liquid phase until the next time step.
4. Similar to the standard setup, gas phase and residual aerosol tracers are also subject to dry deposition.

This sensitivity simulation is characterized by the continuous presence of tracers in the liquid phase. Furthermore, the sensitivity simulation utilizes the SCAV submodel's capability to explicitly define a corresponding aerosol tracer for each liquid-phase tracer. Consequently, `SO4_res_cs` is no longer employed, since all sulfur species are now explicitly addressed (no values for `SO4_res_cs` in Table 4.3). These sulfur species are listed in the top left portion of the dry deposition column in Table 4.3, denoted by the coarse mode, such as `SO3-_cs` and `CH2OHSO3-_cs` and `SO32-_cs`. This modification allows for a more detailed and explicit representation of each liquid-phase tracer and the corresponding aerosol tracers. Table 4.3 shows an example of the year 2010 for all the sulfur species used in EMAC.

Type of emissions		Tracers	Dry de- position	Scavenging (cv+ls)	Sedimen- tation	Change of burden
Emissions in <i>Tg(S)/year</i>		Depositions in <i>Tg(S)/year</i>				
Fossil fuels	50.46	SO_3^- _cs	7.23E - 13		2.88E - 12	1.63E - 13
Awb	0.05	HSO_4^- _cs	0.85		4.031	0.1319
Aircraft	0.13	$CH_2OHSO_3^-$ _cs	0.08		0.3	0.013
Ships	4.92	SO_5^- _cs	0.001		0.003	2.57E - 04
Road	1.78	HSO_5^- _cs	0.03		0.13	0.004
Biomass burning	1.06	SO_4^{2-} _cs	1.07		4.65	0.17
Volcanoes	14.88	SO_3^{2-} _cs	3.07E - 05		1.44E - 04	1.91E-06
OCS	0.22	SO_4^- _cs	2.61E - 12		1.19E-11	6.67E - 13
DMS ter- restrial	0.91	HSO_3^- _cs	0.002		0.009	3.90E - 04
DMS air- sea	28.95	SO_4 _res_cs				
		SO_2 _l		3.19E - 05		4.39E - 07
		H_2SO_4 _l		2.77E - 05		7.83E - 05
		SO_3^- _l				4.92E - 14
		HSO_4^- _l		14.15		0.06
		$CH_2OHSO_3^-$ _l		2.19		0.01
		SO_5^- _l		0.03		1.66E - 04
		HSO_5^- _l		2.09		0.002
		SO_4^{2-} _l		39.42		0.08
		SO_3^{2-} _l		0.002		1.22E - 06
		SO_4^- _l		6.38E - 12		3.72E - 13
		HSO_3^- _l		0.08		2.20E - 04
		OCS				0.06
		SO_3				-6.86E - 07
		SO_2	21.93			-0.08
		H_2SO_4	3.56			0.004
		CH_3SO_3H	7.86			0.01
		DMS				-0.007
		DMSO	0.15			-4.47E - 05
		CH_3SO_2				-1.68E - 07
		CH_3SO_3				3.09E - 04
		S				-4.11E - 16
		SH				3.63E - 10
		SO				-1.37E - 05
		Sum	35.54	57.98	9.14	0.48
Total emis- sions	103.39	Total depos- ition and bur- den	103.15			
Total emissions - (Total depositions + change of burden) = 0.24						

Table 4.3: Detailed examination of the emitted and deposited sulfur species for the year 2010 in the EMAC model. The green column represents the sulfur emission sectors and the red column shows the sulfur tracers deposited within the EMAC model.

In the sensitivity simulation, the sulfur species are also present in the liquid phase such as $\text{SO}_3^-_1$, $\text{CH}_2\text{OHSO}_3^-_1$, $\text{HSO}_5^-_1$, SO_2_1 , $\text{HSO}_3^-_1$, $\text{SO}_5^-_1$, where "1" stands for liquid phase. However these species are not lost at the end of the time step (as it is the case for the standard setup shown with the red arrow in Figure 4.2) but instead remain in residual aerosols, which get sedimented and deposited at the surface. This modification in the setup allows for a mass balance in the model for the year 2010 (103.39 Tg(S)/year is emitted and 103.15 Tg(S)/year including the change of burden is deposited) and shows that no mass is lost within the model. In conclusion, for the standard setup employed, the 6 Tg(S)/year deficit observed in Table 4.1 can now be attributed to the scavenging process. The tropospheric sulfur budget is nearly perfectly closed with a value near 0. In other words, this portion of sulfur is effectively removed from the atmosphere through wet scavenging. This clarification is important to emphasize that there is no error in the model, and the mass balance remains intact, with the sources and sinks aligning appropriately.

Years	Sulfur emissions in Tg(S)/year	Total sulfur deposition in Tg(S)/year	Change of burden in Tg(S)/year	Sulfur deficit in Tg(S)/year
2010	103.39	102.67	0.48	0.24
2011	102.87	102	0.50	0.37
2012	102.66	101.5	0.60	0.56
2013	102.25	101.03	0.62	0.60
2014	101.41	100.22	0.61	0.58
2015	95.22	94.33	0.54	0.35
2016	92.96	92.11	0.53	0.32
2017	91.03	90.15	0.52	0.36
2018	88.95	88.13	0.51	0.31
2019	86.99	86.13	0.52	0.34

Table 4.4: Sulfur budget closure in Tg(S)/year between 2010 and 2019 in the EMAC model.

Therefore, the remaining discrepancies in the other years shown in Table 4.2 can also be attributed accordingly to the wet deposition. Subsequently, upon considering all sulfur species, the mass conservation within the EMAC model holds true for the other years as well, as depicted in Table 4.4. This consistent adjustment ensures that the tropospheric sulfur budget is effectively balanced, accounting for the contributions of various sulfur species and their interactions over the specified time period.

4.2 How does the tropospheric sulfur budget in the EMAC model compare to that of other atmospheric chemistry models?

The examination of the tropospheric sulfur cycle is a subject extensively explored in various atmospheric chemistry models and scientific reports. After proving the closure of the sulfur budget in the EMAC model in the previous section, a comparison with other atmospheric chemistry models is important as it allows to assess the performance and credibility of the model. Additionally, this comparison can also reveal discrepancies between the models, allowing a better identification of areas for improvement within EMAC. A comparison with literature data helps to better understand the robustness of the model, before predictions under different scenarios can be reliable.

In their studies, Stevenson et al. (2003) and Penner et al. (2001) address the tropospheric sulfur budget within their atmospheric chemistry models for the year 1990. Stevenson et al. (2003) used the STOCHEM-Ed model, which is a global three-dimensional Lagrangian CTM, while Penner et al. (2001) studied the IPCC Third Assessment Report (IPCC AR3), which incorporates the average results from 11 distinct models providing a comprehensive overview of the global tropospheric sulfur budget. It is noteworthy that the RD1SD-base-01 simulation used in the previous Section 4.1 is also employed for the present comparison with the STOCHEM-Ed model and the IPCC AR3 for the year 1990, as the RD1SD-base-01 simulation runs from the year 1970 to 2019 (as mentioned in Section 3.3). To illustrate the chemical and physical processes of sulfur in the troposphere, Stevenson et al. (2003) provides a visual representation (see Figure 4.3) showing sulfur emission and deposition processes in both, the STOCHEM-Ed model, and the IPCC AR3. Note that in Stevenson et al. (2003), sulfur anthropogenic emissions were presented as a single sector, unlike the detailed breakdown presented in the EMAC model, which categorizes the prescribed emissions into sectors such as fossil fuels, aircraft and shipping emissions, among others. Additionally, both studies apply an active aerosol mechanism, unlike the EMAC model. Therefore, some sulfur species present in Stevenson et al. (2003) have not been considered in the EMAC model, such as the Methane Sulphonic Acid (MSA) and vice versa (such as OCS).

4.2 How does the tropospheric sulfur budget in the EMAC model compare to that of other atmospheric chemistry models? 65

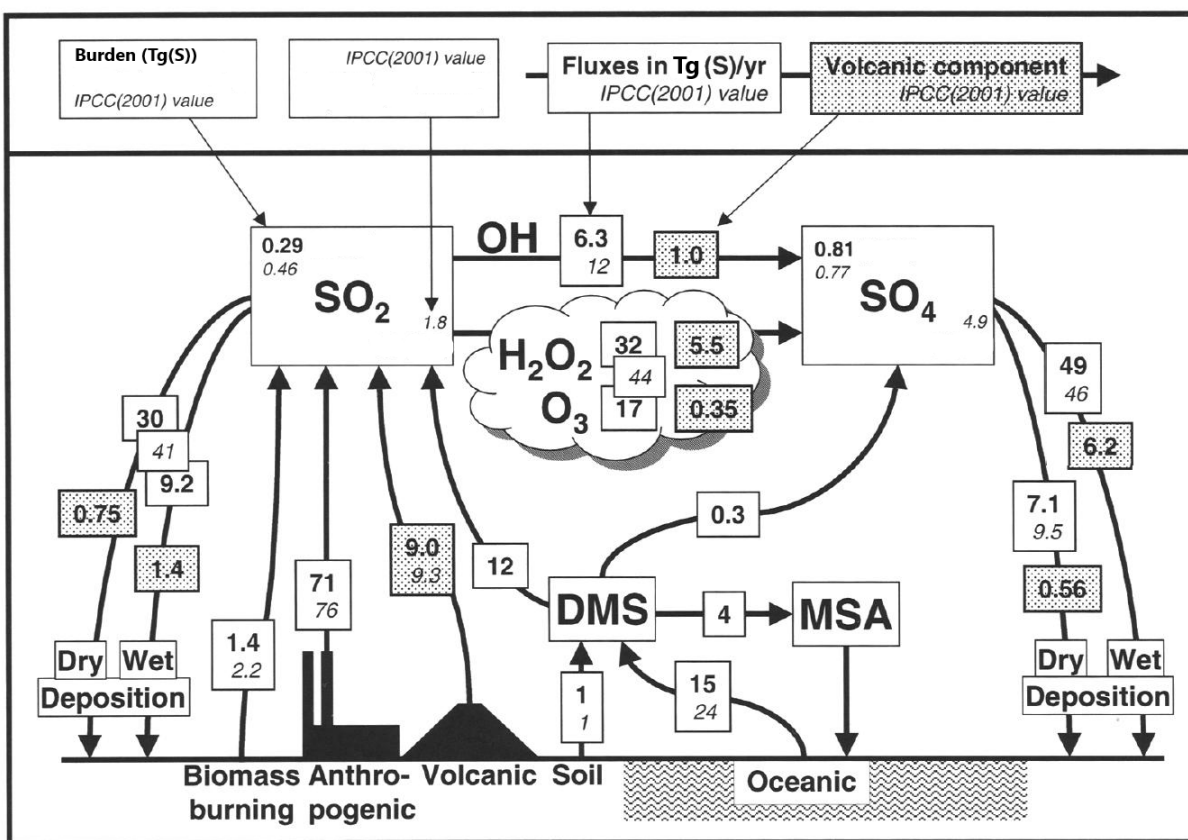


Figure 4.3: Representation of the global tropospheric sulfur budget in 1990 adapted from (Stevenson et al., 2003). The values in bold refer to the STOCHEM-Ed. Values in the shaded boxes refer to the volcanic component. Numbers in italics are from the IPCC AR3. Emission and deposition fluxes are given in $Tg(S)/year$, where burden values are expressed in $Tg(S)$.

For a clear comparison of the processes depicted in Figure 4.3 with those in EMAC, Table 4.5 provides the values for both, the prescribed emission and the deposition rates, for the year 1990. Despite minor discrepancies arising from the applied emission inventories between EMAC and literature, as well as differences in used chemical reactions and physical processes, this comparative analysis reveals a good agreement between the model outcomes and existing literature.

Sulfur emission/ deposition domains	EMAC model	STOCHEM-Ed model	IPCC AR3
Fossil fuels	60.29	71	76
Awb	0.063		
Aircraft	0.00015		
Ships	3.075		
Biomasse burning	0.969	1.4	2.2
Volcanoes	14.88	9	9.3
OCS	0.15		
DMS_terrestrial	0.901	1	1
DMS_airsea	28.1	15	24
Total emissions	111.13	97.40	112.50
Wet deposition	51.03	58.2	57
Dry deposition	42.76	37.1	39.5
Sedimentation	8.02		
Total depositions	101.81	95.3	96.5

Table 4.5: A comparison of emission/deposition fluxes in Tg(S)/year between EMAC, STOCHEM-Ed model and IPCC AR3 for the year 1990.

Consequently, the magnitudes of sulfur emissions across different sectors are consistent between EMAC and the compared models. The total emissions from EMAC align perfectly with those reported in the IPCC AR3, with a slight difference of about 1 Tg of sulfur per year in EMAC. Regarding the STOCHEM-Ed model, EMAC shows larger sulfur emissions by approximately 12%, related to the applied emission inventories. This strong agreement in magnitude is also apparent in the deposition rates. In EMAC, the deposited sulfur through wet and dry processes is 93.79 Tg(S)/year compared to 95.3 Tg(S)/year and 96.5 Tg(S)/year for the STOCHEM-Ed model and the IPCC AR3, respectively. The remaining deposited sulfur from sedimentation is present only in EMAC and not in the chosen literature.

This evaluation highlights the validity of the EMAC model in accurately capturing sulfur emission and deposition rates, despite minor differences in the chemical species and mechanisms used by the compared models. It underscores the model’s reliability in simulating sulfur chemistry, as demonstrated by its close agreement with values reported in literature studies.

4.3 The effect of aerosols on SO₂ in EMAC

Numerous studies across various scientific literature, as Jiménez and Ballester (2005), Rollins et al. (2017), and Charlson et al. (1978) highlight the important role of SO₂ emissions in driving aerosol chemistry. However, do aerosols reciprocally impact significantly the SO₂ chemistry and budget?

It is well-known that sulfate serves as an important sink for sulfur (as discussed in Section 4.1); therefore it cannot be a source of SO₂. This sink is primarily controlled by gas-phase species absorbed by cloud water, which then oxidize SO₂, regardless of the presence of aerosols. Indeed, aerosols do have feedback effects on clouds, cloud lifespan, and cloud formation, however these are considered secondary effects. This is because aerosols do not significantly alter the amount of cloud water in the atmosphere. Therefore, the influence of aerosols on SO₂ is relatively minor, and thus the chemistry occurring within aerosols, which is not explicitly considered in the model, can be effectively neglected.

To examine this argument, a simulation based on the MECO(n) model system (see Section 3.1.3) is utilized. For this analysis, the results from the global EMAC model are used. Note, that similar to the RD1SD-base-01 simulation, the computed simulation for the study of the effect of aerosols of SO₂ in EMAC (the fp-ae_02nm2 simulation), does not include any aerosol interactions. This decision was made to save computational time. Therefore, the objective is to assess the magnitude of the difference when considering another sensitivity simulation with include an interactive aerosol submodel (the fp-ae_02 simulation). Note that these simulations run with the CMIP5 (see Section 3.1.12) emission inventory and are generated by M. Mertens over a time period from May till July 2013. This evaluation aims to elucidate whether future model investigations can proceed without accounting for aerosols, when focusing on the SO₂ chemistry. Figure 4.4 illustrates a global comparison of the differences in SO₂ mixing ratios at the Earth's surface, between simulations conducted with and without interactive aerosol submodel. Specifically, the mean SO₂ mixing ratios over the three available months (May, June and July 2013) over the globe are calculated.

In Figure 4.4 both simulations show elevated SO₂ mixing ratios (between 1 and 2 part per billion (ppb)), in hotspot regions, such as China, Saudi Arabia, India, and specific volcanic areas, whether an interactive aerosol submodel is applied or not (as shown in panels a and b). In the lower panel (c), minimal disparities, approximately 0.05 ppb, are observed, over these hotspot regions, between simulations conducted with and without an interactive aerosol submodel. Consequently, in most background regions, such as over West Europe, central Africa, Australia and Southern America, differences of around 0.01 ppb are identified. Generally, over all the globe, the simulation with an interactive aerosols submodel shows lower SO₂ mixing ratios of about 1% to 2.5% compared to the simulation without aerosols. This analysis confirms the earlier hypothesis suggesting that the impact of aerosols on SO₂ is relatively insignificant. Consequently, the simulations utilized throughout this work are conducted without considering an interactive aerosol submodel.

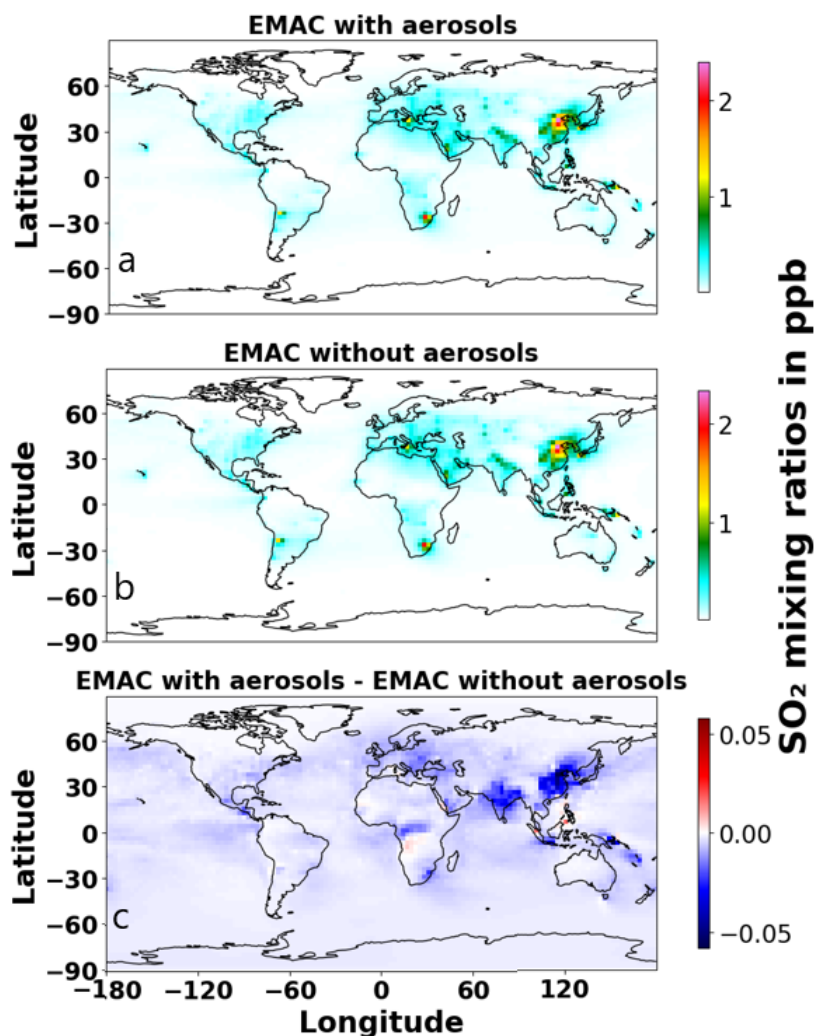


Figure 4.4: Shown are the mean SO_2 mixing ratios at the Earth's surface in parts per billion (ppb) in an EMAC simulation with aerosols (a) and without aerosols (b) over May, June and July 2013. The lower panel (c) illustrates the absolute differences between EMAC with and without an interactive aerosol submodel.

4.4 Discussion and conclusion

4.4.1 Tropospheric sulfur budget within EMAC

The prerequisite for a meaningful inter-comparison between various model simulations concerning the tropospheric sulfur budget is that the model maintains a balance, neither losing nor generating mass, as affirmed in Section 4.1. Within this study, the RD1SD-base-01 simulation, employing the CMIP6 emissions inventory, has been meticulously analysed

for this purpose. An examination of the tropospheric sulfur cycle with focus on SO_2 , spanning the years from 2010 to 2019 has been undertaken, including the emission sources and over 20 sulfur species accountable for sulfur deposition. Notably, the calculated deficit in the sulfur budget across all the analyzed years, as shown in Table 4.2, is attributable to the intricate scavenging processes at play within the atmospheric system.

4.4.2 Tropospheric sulfur budget in EMAC against atmospheric chemistry models

In this section, the model analysis for the studied years led to the conclusion that the EMAC model's tropospheric sulfur budget reproduces values consistent with those reported in the IPCC AR3 and as simulated by the STOCHEM-Ed model. However, for certain sulfur species, such as SO_2 from biomass burning or from fossil fuels, the model may occasionally shows higher or lower values than the results reported in the literature. This discrepancy is attributed to the sulfur emissions inventories utilized as input for the model, which play an important role in shaping both, sulfur mixing ratios and deposition processes. Further refinement and validation of these emissions inventories may help improve the models performance in representing the tropospheric sulfur cycle.

4.4.3 The effect of aerosols on SO_2 in EMAC

The role of aerosols concerning sulfur has been thoroughly examined, confirming the possibility of evaluating SO_2 without necessitating the consideration of aerosol interactions. These findings hold significant implications for facilitating comparisons with observational data and among various model simulations and scenarios. This is feasible because of the mass-conservation of sulfur in the EMAC model. With these understandings, sensitivity analyses can be systematically conducted using this model system, enabling focused examinations and assessments of specific processes. This forms the basis for further scientific inquiry and enables a detailed understanding of the complex interactions within the atmosphere.

In conclusion, it is essential to recognize that validating and verifying the EMAC model against the literature, as discussed in Section 4.2, does not inherently guarantee an accurate representation of reality. Such comparisons involves evaluating one model against others, each with its own uncertainties originating from the applied emission inventories and underlying processes. Therefore, there exists a pressing need for a comprehensive global data product to facilitate ongoing global monitoring, thereby enabling the detection of spatial and temporal changes in SO_2 and other sulfur components. This global monitoring framework is indispensable for assessing the quality of model simulations. For further analyses, the RD1SD-base-01 simulation from the Phase 2 of the Chemistry Climate Model Initiative (CCMI-2), without an interactive aerosol submodel, will be used.

Chapter 5

Comparing SO₂ simulated by the EMAC Model with TROPOMI data

The primary objective of this section is to conduct a comprehensive global-scale comparison between the EMAC simulations and TROPOMI retrievals. TROPOMI, notable for being the first satellite instrument to measure SO₂ columns with the highest spatial resolution among other satellites, serves as a pivotal dataset for this study. The analysis is focused on the year 2019, chosen for its status as the most recent complete annual cycle available in both datasets at the time of examination.

Performing a direct comparison between the EMAC model results and satellite datasets presents inherent challenges due to their different methodologies and resolutions. Therefore, Section 3.3.1 describes the methodologies adopted in this study to facilitate a fair and detailed analysis of SO₂ across both datasets. For a comparison with the TROPOMI retrieved VCDs for a standard case, EMAC's VCDs are calculated by applying the standard (so called "polluted") averaging kernel of the TROPOMI instrument (see Section 3.3.1), at each atmospheric layer, as shown in Equation 3.11. In this comparative framework, TROPOMI VCDs are derived using the SO₂ COBRA product, especially for anthropogenic cases and for outgassing volcanic eruptions (see Section 3.3.1), which is selected due to its enhanced sensitivity to low SO₂ columns. However, the operational product is applied in this work for the study of highly eruptive volcanic activities (see Section 3.3.1).

This section is divided in four subsections. A global comparison of the EMAC results, using the standard ("polluted") AK, against TROPOMI retrievals for the standard case is described in Section 5.1. The effects of eruptive volcanoes on the simulated SO₂ total column are discussed in Section 5.2. Furthermore, a relative evaluation of SO₂ from both, anthropogenic and outgassing volcanic emissions is detailed in Section 5.3. Last but not least, a discussion of all the results and a conclusion are presented in Section 5.4.

5.1 Geo-spatial distribution and discrepancies of SO₂ VCDs between EMAC results and TROPOMI retrievals for the year 2019

This section presents a comprehensive analysis of the global distribution and discrepancies of SO₂ VCDs as derived from the RD1SD-base-01 simulation based on the EMAC model and TROPOMI/Sentinel-5P satellite observations for the year 2019. Figures 5.1 and 5.2 illustrate the monthly geographical distribution of SO₂ VCDs. The left panels of these figures display the EMAC model simulation results, whereas the right panels depict the satellite-based retrievals obtained from the TROPOMI instrument.

The visual comparison of these datasets reveals significant insights into the spatial and temporal variations of SO₂ VCDs across the globe. Both datasets consistently show low SO₂ VCDs (below 0.5 DU) in regions such as Western Europe, Africa, and Australia. However, discrepancies become apparent in specific months and regions. Upon examination of these maps, two prominent patterns emerge. Firstly, significant discrepancies in the magnitude of SO₂ VCDs are evident between the EMAC model results and TROPOMI/Sentinel-5P satellite observations, especially over Southern Italy, Northeast China, India, central America, and Papua New Guinea, with larger SO₂ VCDs simulated by EMAC. In these regions, the discrepancies are particularly pronounced throughout all the months of the year 2019, excluding June and July. In the other 10 months, EMAC consistently depicts SO₂ VCDs exceeding 1 DU, whereas TROPOMI's measurements are typically below 0.5 DU, except in August, November, December, and January 2019. In August, elevated SO₂ signals recorded by TROPOMI over Papua New Guinea are attributed to the Ulawun volcano (Kloss et al., 2021). Secondly, the months June and July reveal different patterns. In these two months, TROPOMI detects larger and more widespread signals on the map in regions above 30° North. The strongest signal in June is measured Northeast of Russia and spreads across all of North America in July. The reason for this is the volcanic explosion of the Raikoke volcano in Russia (48.3°N, 153.2°E) in June 2019, with persistently enhanced SO₂ VCDs in the atmosphere until mid-July (De Leeuw et al., 2021). These signals are not present in the CMIP6 emission inventory used by EMAC in this study, because of the variability and unpredictability of eruptive volcanic eruptions.

5.1 Geo-spatial distribution and discrepancies of SO₂ VCDs between EMAC results and TROPOMI retrievals for the year 2019

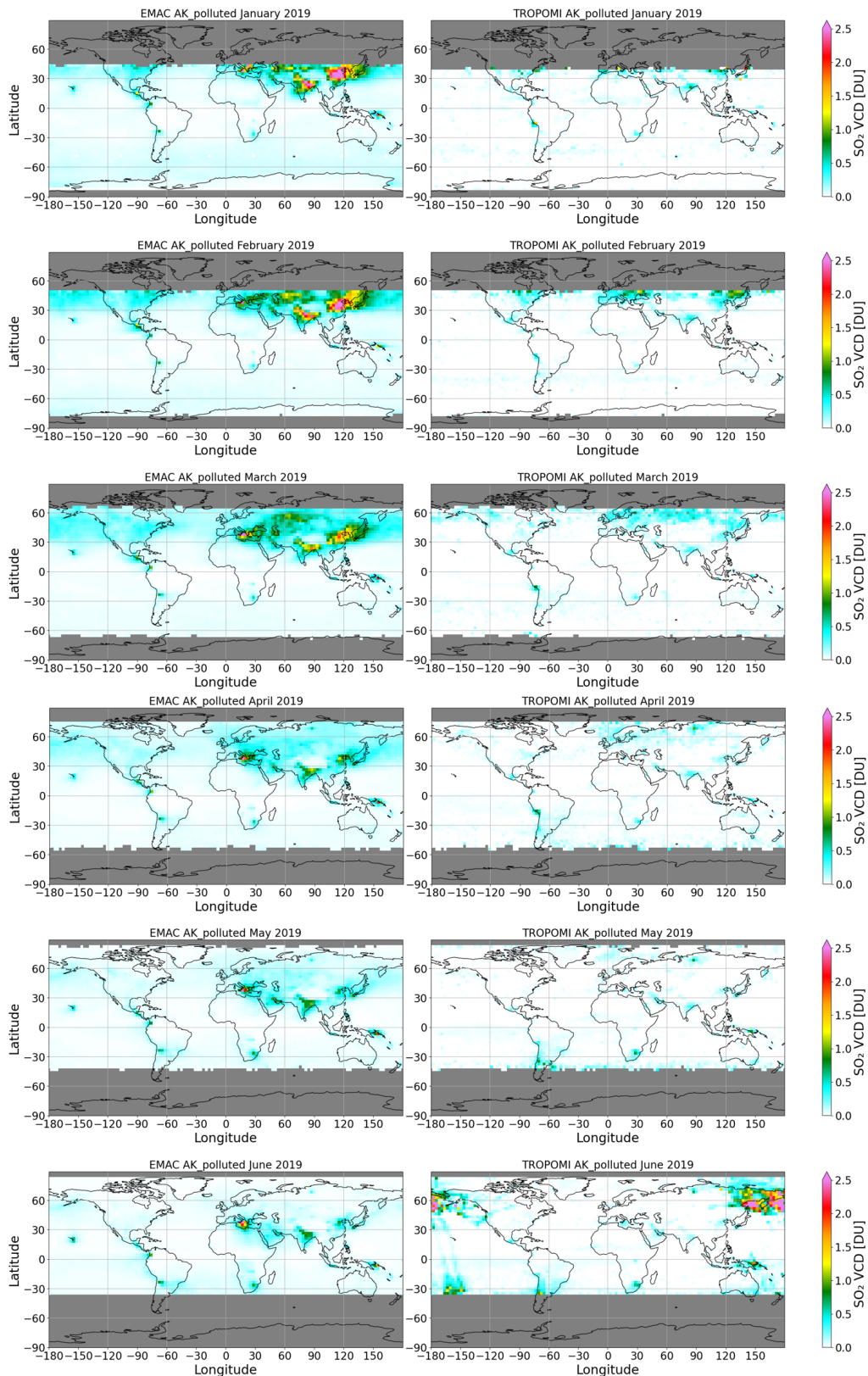


Figure 5.1: Geographical representation of SO₂ VCDs from EMAC, calculated with the standard AK (left panels), against TROPOMI retrievals (right panels) in DU for the first 6 months of 2019. The grey zones represent areas with no valid measurements.

74 5. Comparing SO₂ simulated by the EMAC Model with TROPOMI data

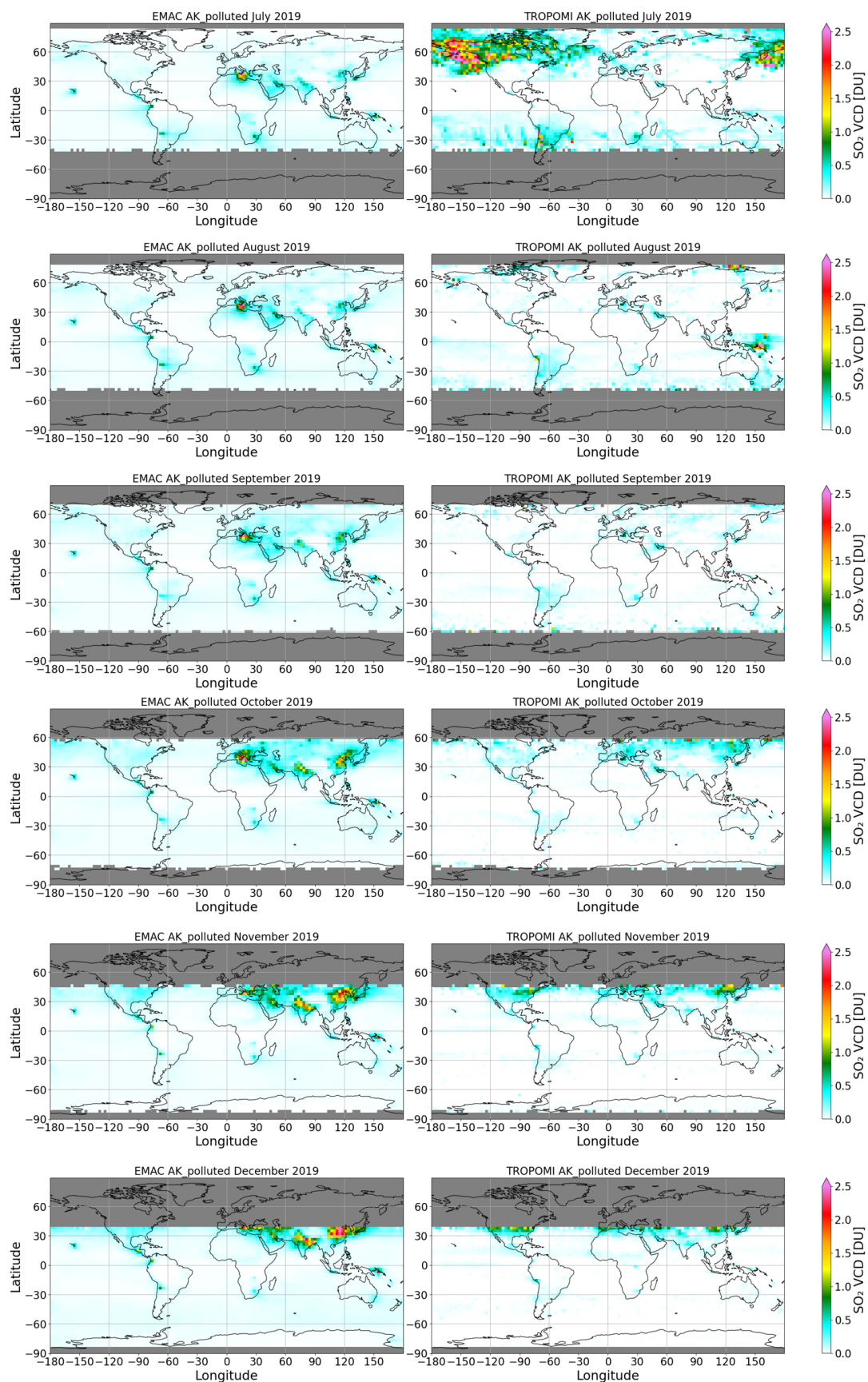


Figure 5.2: Continuation of Figure 5.1 for the last 6 months of 2019.

Because of the large influence of the eruption of the Raikoke volcano, the further analysis for quantitative comparison between EMAC results and TROPOMI observations, two cases are considered: Once an annual mean is calculated and once a 10 months average, i.e. without the months June and July. The results are shown in the right and left plots of Figure 5.3, respectively.

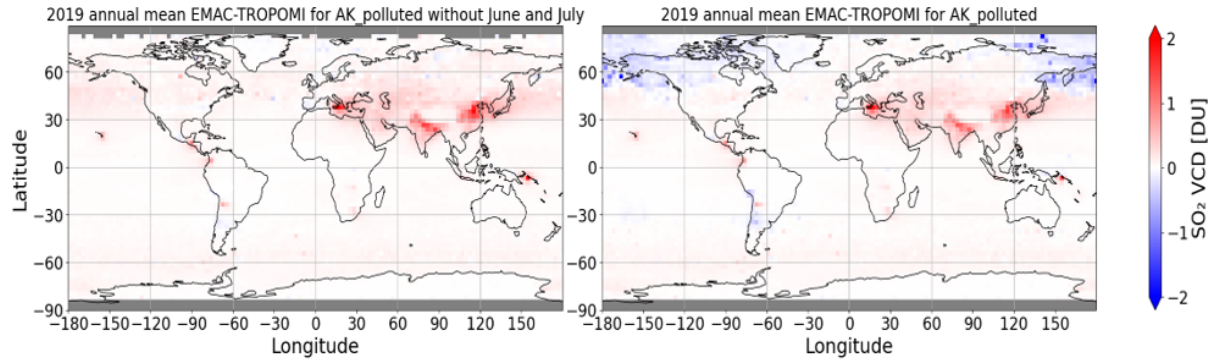


Figure 5.3: SO₂ VCD differences between the EMAC model results and TROPOMI retrievals in DU. The left panel shows the differences as a 10 months (no June and July) mean, whereas the right plot reveals discrepancies as a mean over all months in 2019, including June and July.

This comparison confirms what was shown in Figures 5.1 and 5.2, namely, that for all months, the largest differences are derived in Northeastern China, India, Southern Italy, and other localized sources in the Southern Hemisphere. In these regions, the model consistently reveals SO₂ VCDs approximately 1.5 to 2 DU larger than those measured by TROPOMI. Additionally, in the right panel, larger SO₂ VCDs are observed by TROPOMI over 30°N, showing SO₂ VCD values about 1 DU larger than EMAC. This discrepancy, in the absence of data on explosive volcanic eruptions in EMAC, is related to the Raikoke volcanic eruption in June 2019. Conversely, there is a good agreement, with minor discrepancies ranging between 0.1 and 0.5 DU, in Western Europe, the USA, Africa, Australia, and most parts of South America. These results were anticipated due to the relatively low SO₂ emissions in these regions compared to other SO₂ emission hotspots such as India, China, and volcanic areas. In these regions, the largest differences in both plots in Figure 5.3 are derived. Notably, areas with either active volcanoes or enhanced anthropogenic emissions from industrial activities exhibit the most significant differences between both datasets. Regions such as Southern Italy, with the Etna volcano (37.74°N, 14.99°E), Japan with the Mt. Fuji volcano (35.36°N, 138.72°E), Papua New Guinea with the Ulawun volcano (5.05°S, 151.33°E), Chile with the Nevado Ojos del Salado volcano (27.10°S, 68.54°W), and the Northwestern Tibetan Plateau with the Kunlun volcano (35.74°N, 81.64°E) show the largest values in EMAC results compared to TROPOMI retrievals. Furthermore, large SO₂ VCD differences are also noticeable over Beijing in Northeast China and in India, driven by anthropogenic SO₂ emissions.

Related to Figure 5.3, Figure 5.4 displays correlation plots aimed at examining the relationship between the VCDs from EMAC weighted with AK_polluted and from the corresponding TROPOMI VCDs for the standard ("polluted") case. Here, correlation plots of the yearly mean SO₂ VCDs from EMAC against those from TROPOMI for 10 (i.e. excluding the data of June and July) and 12 months in 2019 are presented. In the correlation plot between both datasets for 10 months (left panel), the Pearson's correlation coefficient is approximately 0.55, indicating a moderately strong positive linear relationship between the two datasets. The outliers from EMAC (values larger than 1 DU) correspond to the larger values presented in Figures 5.1 and 5.2, as well as with the SO₂ VCD differences from Figure 5.3, which are observed at volcano locations. As an example of the magnitude relationship between both datasets, the largest SO₂ VCD value from EMAC is around 3.5 DU, compared to about 0.5 DU from TROPOMI, representing a factor of approximately 7 between the datasets. The negative SO₂ VCD values from TROPOMI arise from observations of SO₂ VCDs at large SZAs, which lead to biases in most satellite datasets (Theys et al., 2017).

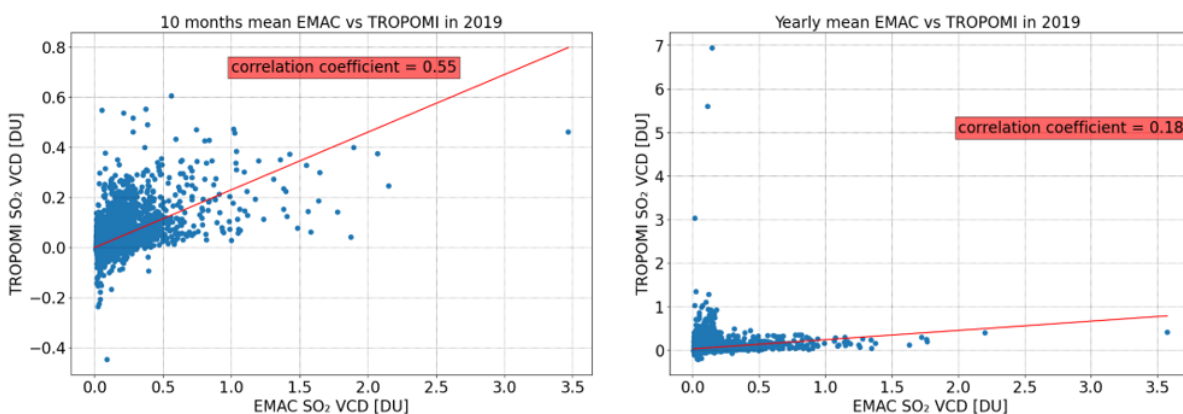


Figure 5.4: Correlation plots of global mean SO₂ VCDs calculated with AK_polluted between EMAC results and TROPOMI retrievals. The left plot shows the relationship between both datasets as 10 months (no June and July) mean, where the right plot reveals discrepancies over all months in 2019. Note that the vertical axes have different scales in both plots.

In the correlation plot spanning the entire year (right panel in Figure 5.4), the Pearson's correlation coefficient of approximately 0.18 indicates a weak positive linear relationship between the two datasets. This weak correlation is attributed to the absence of SO₂ emissions in EMAC originating from Raikoke and Ulawun eruptive volcanoes in June 2019. The signal from Raikoke is noticeable in TROPOMI, which reveals SO₂ VCDs values up to 7 DU, compared to maximum 0.6 DU in the 10 months mean correlation plot, excluding June and July (left plot in Figure 5.4). Therefore, the values larger than 1 DU in the TROPOMI dataset represent clear outliers and are attributed to the retrieved SO₂ from the eruptive volcanoes.

Consequently, the hypothesis suggests that the standard polluted case for VCDs may not universally be applicable to the study of absolute SO₂ emissions from different emitting sources. Therefore, different types sources of SO₂ emissions require processing with appropriate TROPOMI product types and corresponding AKs. This approach is implemented in Section 5.2, where the specific impact of explosive eruptions from Raikoke and Ulawun volcanoes on emitted and deposited SO₂ mass within the EMAC model is examined. For this analysis, the AK_15km is suitable (see Section 3.3.1), as it reproduces best the released tracers mixing ratios from an eruptive volcano, for a detailed analysis of EMAC results with the corresponding VCD_15km from the TROPOMI instrument.

Moreover, in Section 5.3, only the magnitude relationship between SO₂ VCDs from anthropogenic sources and outgassing volcanoes between EMAC results and TROPOMI retrievals is evaluated, without directly assessing the absolute emitted and deposited SO₂ mass from individual point sources (as made for the case of the Raikoke volcano). Therefore, the choice of the AK for this case is less critical, as the comparison between TROPOMI VCDs for all four cases and EMAC weighted with the corresponding AKs will show constant ratios across all cases, as explained in detail in Section 3.3.1.

5.2 Effects of volcanic eruptions on the simulated atmospheric SO₂ in the EMAC Model

As shown in Figures 5.1, 5.2 and 5.3, the significant SO₂ signals detected in June and July were exclusively captured by TROPOMI and not visible in the analysed RD1SD-base-01 EMAC simulation, due to the absence of volcanic eruptive events in the CMIP6 emission inventory used by the EMAC model. Several studies have documented eruptive volcanoes which occurred during the year 2019. In June, the Raikoke eruption (48.29°N, 153.25°E) took place in the Northern Hemisphere (Kloss et al., 2021; De Leeuw et al., 2021; Khaykin et al., 2022; Smirnov et al., 2021; Cai et al., 2022; Jing et al., 2023), while the Ulawun volcano (5°S and 151°E) erupted near the equator in Papua New Guinea (Kloss et al., 2021; McKee et al., 2021; Tidiga et al., 2022; Vaughan et al., 2021). The eruptions of Raikoke and Ulawun in 2019 resulted in the injection of volcanic emissions up to the stratosphere, consequently increasing the stratospheric Aerosol Optical Depth (sAOD) across the Northern and Southern Hemispheres as well as the tropics (Kloss et al., 2021). The eruption of Raikoke in 2019 is particularly noteworthy, as it is considered the largest injection of SO₂ into the Upper Troposphere and Lower Stratosphere (UTLS) since the 2011 Nabro eruption, and it represents the first significant volcanic event since the deployment of TROPOMI (Cai et al., 2022). Estimates suggest that the 2019 Raikoke eruption injected approximately 1.5 ± 0.2 Tg of SO₂ into the atmosphere (Muser et al., 2020; De Leeuw et al., 2021). Additionally, TROPOMI/Sentinel-5P data indicates an SO₂ load of approximately 0.14 Tg from the plume of Ulawun in June and 0.2 Tg on 3-4 August 2019 (Kloss et al., 2021). According to Crafford and Venzke (2019) a serie of eruptions occurred at Raikoke between 21 (18:00 UTC) and 22 (05:40 UTC) June 2019. Hedelt

et al. (2019) reported plume altitudes for Raikoke ranging from 6–8 km up to 20 km. For Ulawun, Kloss et al. (2021) indicates SO₂ emissions at altitudes between 13 and 17 km for the initial eruption on 26 June, and a larger eruption on 3 and 4 August injecting between 14 and 17 km.

These unpredictable volcanic emissions provide a valuable opportunity for the model. Through a sensitivity simulation, which considers the eruptive volcanic activities in the RD1SD-base-01 reference simulation, it is now possible to investigate and analyse atmospheric processes such as, sedimentation, and deposition. This approach allows for a more comprehensive understanding of how these dynamic volcanic events impact the atmosphere. For this purpose, the EMAC results have been integrated vertically with the averaging kernels for the 15 km profile for a comparison with the corresponding VCDs from TROPOMI. These AKs are suitable for large volcanic eruptions reaching the stratosphere, as explained in the methods Section 3.3.1.

The EMAC sensitivity simulations of the Raikoke and Ulawun eruptions involved injecting volcanic SO₂ into model grid boxes corresponding to the geographical locations of the volcanoes. The Raikoke volcano is situated on the Kuril Islands in the Western Pacific Ocean, while the Ulawun volcano is located near the equator in Papua New Guinea. The injections were active over a 6-hour duration. Table 5.1 provides an overview of the volcanic SO₂ emission mass and injection altitude range for both eruptions in the EMAC model setup. The eruption parameters for Raikoke were based on the emission profiles from De Leeuw et al. (2021), while the data for the Ulawun eruptions were sourced through personal communication with Anja Schmidt.

Volcano	Eruption date	Emitted SO ₂ mass	Injection altitude range
Raikoke	21-22 June 2019	1.5 Tg	9-16 km
Ulawun	26 June 2019	0.14 Tg	16-19 km
Ulawun	3-4 August 2019	0.2 Tg	11-15 km

Table 5.1: Emitted SO₂ mass, injection altitude range, and the eruption time of the Raikoke and Ulawun volcanoes as applied in the EMAC model.

Firstly, two SO₂ emission profiles (named StratProfile and VolRes1.5, respectively, adopted from De Leeuw et al. (2021)) are utilized for the Raikoke eruption simulations in this work. These two profiles, were chosen due to their close agreement with the SO₂ mass measured by TROPOMI, as well as their difference in emission heights. In EMAC, the StratProfile has been applied in the RD1SD-raik-02 (raik-02) sensitivity simulation, where the VolRes1.5 injection profile was used in the RD1SD-raik-03 (raik-03) simulation. Both simulations release approximately 1.5 Tg (1.57 for raik-02 and 1.5 for raik-03) of SO₂ into the atmosphere; however, the difference lies in the vertical distribution of SO₂ emission. In raik-02 (similar to the StratProfile profile from De Leeuw et al. (2021)), 69% of the volcanic SO₂ mass (1.09 Tg) is emitted into the stratosphere, with the primary peak occurring at 12-13 km altitude. In contrast, for raik-03 (equivalent to the VolRes1.5 profile in De Leeuw

et al. (2021)), only 43% of the SO₂ mass (0.64 Tg) is emitted into the stratosphere, with the primary peak located around 10 km altitude in the upper troposphere. Table 5.2 describes the set-ups applied in all sensitivity simulations.

Sensitivity simulation	Volcano	SO ₂ emission date in 2019	Stratospheric emission altitude [km]	Emitted SO ₂ mass into the stratosphere [Tg]	Total emitted SO ₂ mass into all layers [Tg]
raik-02	Raikoke	21-22 June	12-13	1.09	1.57
raik-03	Raikoke	21-22 June	12-13	0.64	1.5
raik-04	Raikoke	21-22 June	12-13	1.09	1.57
	Ulawun	26 June	16-19	0.14	0.14
	Ulawun	3-4 August	11-15	0.2	0.2

Table 5.2: Input parameters of the three sensitivity simulations used in this study. The table shows the prescribed volcanoes for each sensitivity simulation, with their eruption time and the injected SO₂ mass in the stratosphere and in all layers.

For a detailed study focusing solely on the SO₂ mass burden originating from volcanic eruptions, the results of the the RD1SD-base-01 reference simulation have been subtracted from the sensitivity simulations. This approach isolates the SO₂ mass specifically attributable to volcanic activity from other anthropogenic or outgassing volcanic emissions, thereby enabling a more precise analysis of its impact. Figure 5.5 illustrates the SO₂ mass emitted at different altitudes in both simulations.

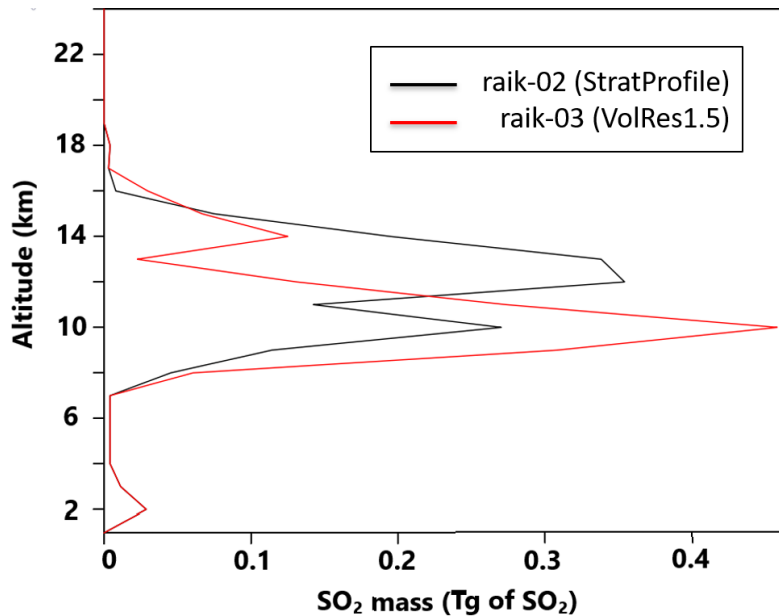


Figure 5.5: Shown is the estimated total emitted SO₂ mass for the Raikoke eruption in 21 and 22 June 2019 for two different EMAC set-ups. In the first one, represented by raik-02 (black line), most of the SO₂ mass (69%) is emitted into the stratosphere (De Leeuw et al., 2021). Conversely, in the second set-up (raik-03), most of the SO₂ mass (57%) is emitted into the troposphere (De Leeuw et al., 2021).

The altitude of the SO₂ emissions significantly influences their atmospheric distribution and dispersion patterns, impacting their climate effects, lifetime, and oxidation rates (Höpfner et al., 2015). Figure 5.6 illustrates the temporal distribution of the emitted SO₂ mass into the troposphere and stratosphere for raik-02 and raik-03 simulations, highlighting the differences of SO₂ mass distribution during and after the Raikoke eruption.

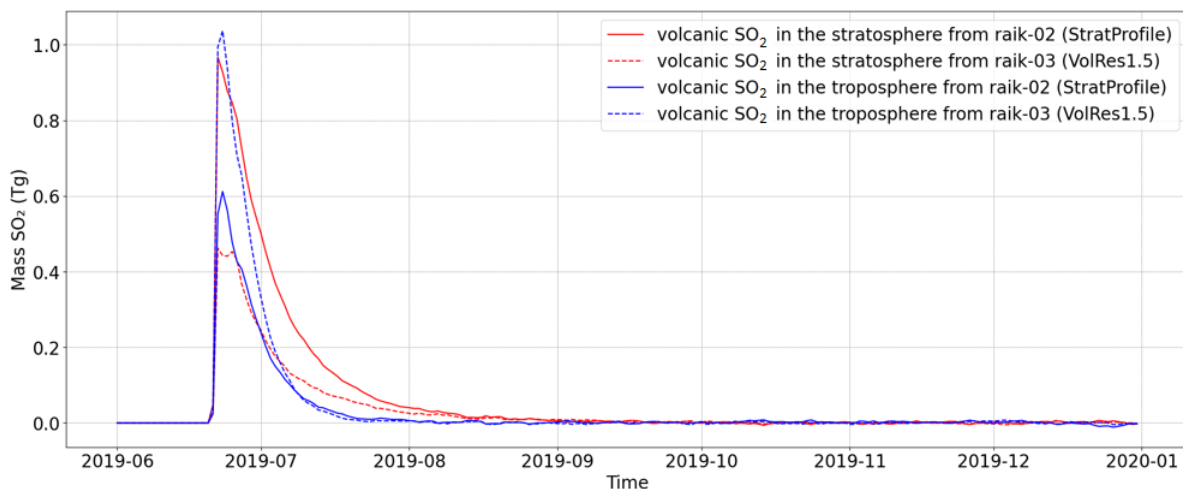


Figure 5.6: Total emitted SO₂ mass of the Raikoke eruption in 21-22 June 2019. The blue lines represent the emitted SO₂ mass in the troposphere, while red lines denote SO₂ mass emitted in the stratosphere in Tg. raik-02 simulation is presented in solid lines and raik-03 simulation in dashed lines.

In the raik-02 and raik-03 simulations, the largest SO₂ mass is emitted in the stratosphere and troposphere, respectively. In both simulations, the tropospheric SO₂ mass (blue lines) declines sharply to nearly zero around 15 July 2019. Meanwhile, stratospheric SO₂ is removed slower, persisting until mid-August 2019. The combined SO₂ mass in the troposphere and stratosphere represents the total SO₂ mass burden from the Raikoke eruption. This mass burden is then compared with the global SO₂ mass burden measured by the TROPOMI/Sentinel-5P satellite after the Raikoke eruption and till mid-July 2019 (see Figure 5.7). The raik-02 simulation (red line), which assumes a larger emission of SO₂ into the stratosphere, aligns more closely with TROPOMI’s measured SO₂ data than the raik-03 simulation (orange line), in which a larger proportion of SO₂ is released into the troposphere.

Both simulations accurately capture the SO₂ mass burden peak at approximately 1.8 Tg. The peak values of the EMAC SO₂ mass distribution are slightly larger than the total emissions presented in Table 5.1, due to the application of AK.15km to the EMAC results. Moreover, raik-02 (red curve) shows a better long-term agreement with TROPOMI estimates than raik-03 (orange curve), consistently remaining within the uncertainty range. For TROPOMI, uncertainties of SO₂ in the stratosphere are approximately $\pm 30\%$ of the retrieved VCDs (Theys et al., 2017). Conversely, the raik-03 simulation exhibits a more rapid decline of the SO₂ mass in the stratosphere, compared to the TROPOMI data after the Raikoke eruption, suggesting a faster removal of SO₂ from the atmosphere, with an exception for the first two days after the SO₂ mass burden peak, where raik-03 agrees better with the measurements than raik-02.

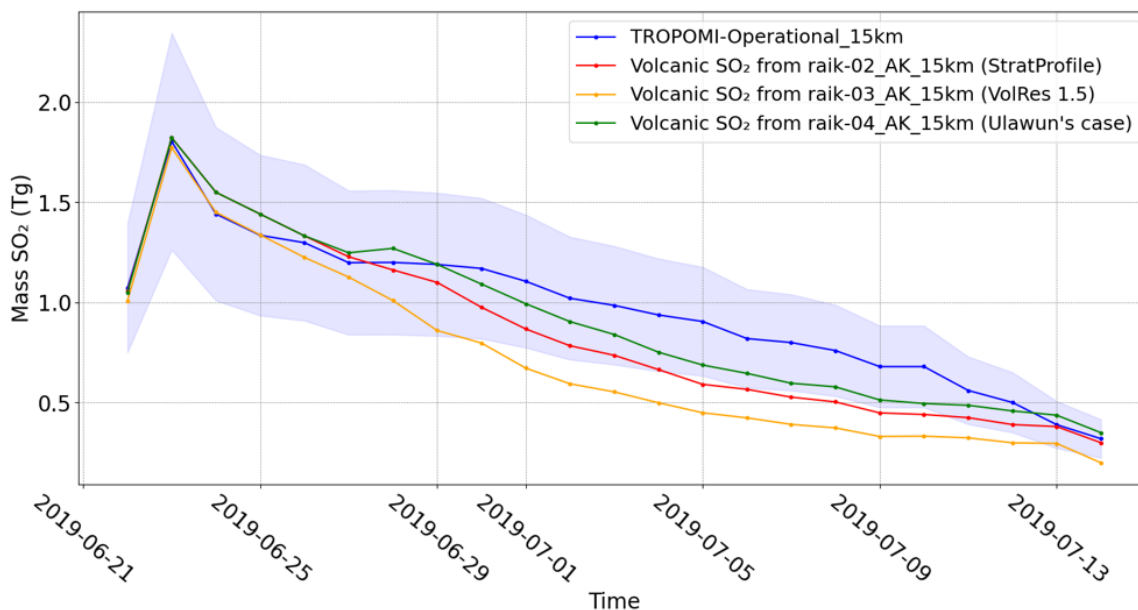


Figure 5.7: The daily evolution of the total SO₂ mass burden (Tg of SO₂) after the 2019 Raikoke and Ulawun volcanic eruptions in TROPOMI and different EMAC sensitivity simulations. raik-02 and raik-03 represent simulations with SO₂ mass from Raikoke emitted mostly in the stratosphere and troposphere, respectively. raik-04 is based on raik-02 with additional emitted SO₂ mass into the stratosphere originating from the Ulawun volcano.

The discrepancies between satellite SO₂ measurements and EMAC simulation results can be attributed to the different vertical injection profiles or rather to the rate of sulfur removal from the atmosphere. Cai et al. (2022) suggest that additional injections are required after the initial Raikoke plume to accurately replicate the observed SO₂ mass, underscoring the complexity of modeling volcanic SO₂ emissions and their interactions in the atmosphere. To address these differences, a sensitivity simulation labeled raik-04 (green curve in Figure 5.7) was conducted, using the same emission parameters of the raik-02 simulation. raik-02 was chosen because it best matches the temporal evolution of TROPOMI SO₂ mass measurements. In the raik-04 simulation, emissions from the Ulawun volcano in the Southern Hemisphere were additionally considered. The Ulawun eruptions on 26 June 2019, at 12:00 UTC and 3 August 2019 at 12:00 UTC were taken into account in EMAC results, with each eruption lasting six hours. During the first eruption, 0.14 Tg of SO₂ was injected at altitudes between 16 and 19 km in the model. For the second eruption, 0.2 Tg of SO₂ was emitted at altitudes between 11 and 15 km. As shown in Figure 5.7, these adjustments improved the temporal evolution of SO₂ mass, slowing the decline in the raik-04 simulation following the Ulawun emission injections on June 26 due to the increased SO₂ mass in the stratosphere.

During the Raikoke eruption and up to 29 June 2019, all simulations consistently show a continuous decrease in SO₂ mass. TROPOMI data indicates a decline rate of approximately 0.08 Tg(SO₂)/day, which is slower than the deposition rates simulated in the EMAC sim-

ulations. The raik-03 simulation demonstrates a decay rate of around 0.14 Tg(SO₂)/day, indicating a lower SO₂ mass compared to TROPOMI. Conversely, the raik-02 simulation exhibits a slower decay rate of 0.1 Tg(SO₂)/day. However, raik-04 aligns most closely with TROPOMI, with a decay rate of 0.09 Tg(SO₂)/day. This closer match can be attributed to the additional Ulawun emissions injected into the stratosphere on 26 June 2019, which increases the mass of SO₂ in the atmosphere. Note that for the first two days following the SO₂ mass burden peak, TROPOMI observations indicate a rapid decline rate of approximately 0.15 Tg(SO₂)/day. This rate aligns most closely with the raik-03 simulation, where a significant amount of SO₂ is emitted at lower altitudes, resulting in a decline rate of 0.14 Tg(SO₂)/day. In contrast, the raik-02 and raik-04 simulations, which involve the majority of SO₂ being emitted into the stratosphere, exhibit a slower decrease rate of about 0.12 Tg(SO₂)/day. Between 29 June and 15 July 2019, all EMAC simulations show a decay rate similar to TROPOMI, at approximately 0.05 Tg(SO₂)/day.

Over the period from 22 June to 15 July 2019, raik-04 aligns most closely with TROPOMI observations, by simulating about 3% lower SO₂ mass than TROPOMI over the entire period. raik-02 indicates a mean relative difference of 10%, while raik-03 reports lower values than TROPOMI with a mean relative difference of 25% due to differences in the decay rate and SO₂ vertical injection profile. The fact that all EMAC simulations fall within the 30% uncertainty range of the SO₂ total column in TROPOMI provides confidence that EMAC accurately captures the main processes required to represent SO₂ dispersion. The differences between retrieved and simulated SO₂ VCDs are not only caused by the emitted SO₂ mass or the injection altitude, but the difference in the temporal and spatial resolution of both datasets also plays a significant role. EMAC has 90 vertical layers between the surface and the uppermost model layer centered around 0.01 hPa (i.e. around 80 km) and operates at a spatial resolution of 2.8° × 2.8° (approximately 300 km × 300 km) (see Section 3.3). Whereas, TROPOMI has a finer resolution of 3.5 km by 7 km and the data is organized vertically into pressure layers from the TM5 model, which are divided into 34 distinct layers, varying approximately from the Earth's surface to 0.1 hPa (i.e. around 60 km) (see Section 3.2.1). This process of averaging high-resolution satellite data to match the model's grid can introduce artifacts and smooth out significant spatial variability.

Additionally, the overall lower SO₂ mass in the raik-03 simulation compared to TROPOMI data and the other sensitivity simulations could be due to larger emission injected into the troposphere. To verify this, cumulative deposited sulfur mass rates (in Tg) from the Raikoke and Ulawun eruptions were calculated. Subsequently, for a better comparison with the SO₂ mass burden in Figure 5.7, the deposited sulfur mass is converted to an SO₂ equivalent. This conversion accounts for the molecular weights of sulfur and SO₂. The atomic weight of sulfur is approximately 32.06 g/mol, while the molecular weight of SO₂ is approximately 64.07 g/mol. Therefore, the deposited sulfur mass is multiplied by a conversion factor of approximately 2 to obtain the deposition mass of an SO₂ equivalent, as shown in Figure 5.8. This mass was determined as the sum of sulfur originating from wet, dry deposition and sedimentation. In Figure 5.8, the raik-03 simulation shows a rapid increase in the deposited SO₂ mass between the Raikoke eruption period and the end of

July, at a rate of 0.035 Tg(SO₂)/day, compared to a weaker increase rate of about 0.028 Tg(SO₂)/day in both the raik-02 and raik-04 simulations. However, a different pattern in SO₂ deposition rates emerges after the beginning of August. At this point, larger SO₂ deposition rates are simulated in the raik-02 and raik-04 simulations, at 0.003 Tg(SO₂)/day and 0.005 Tg(SO₂)/day, respectively, while raik-03 shows a slower deposition rate of about 0.0018 Tg(SO₂)/day. These differences in the rates can be explained by the amount of SO₂ emissions and the injection height in the model. The faster increase in deposited SO₂ mass following the Raikoke eruption until the end of July in the raik-03 simulation is due to the large amount of injected SO₂ into the troposphere compared to raik-02 and raik-04.

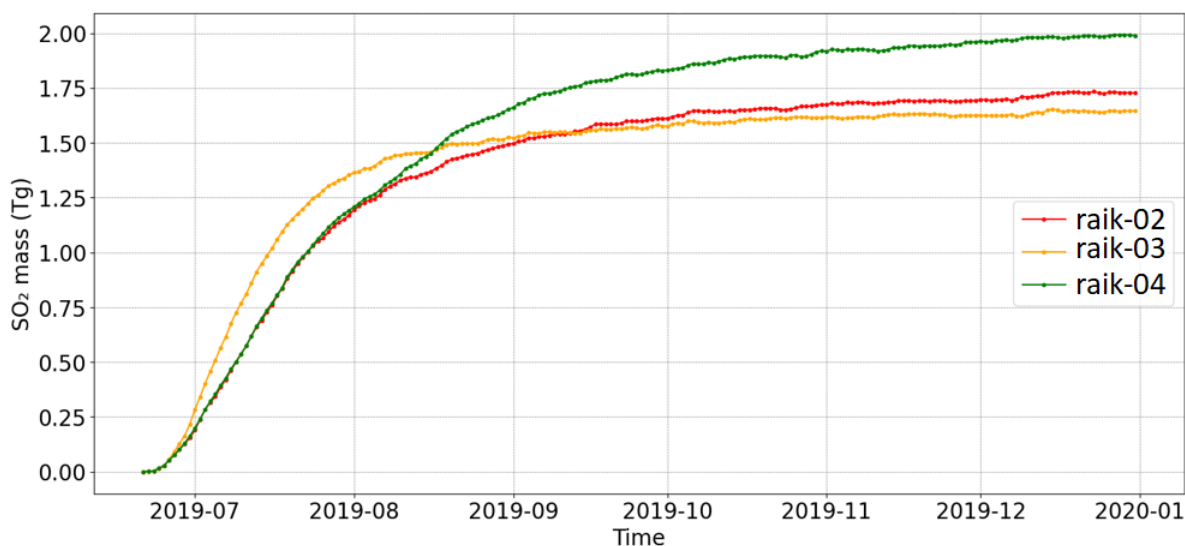


Figure 5.8: Cumulative total deposition (wet, dry deposition and sedimentation) of SO₂ mass on the Earth’s surface from the 2019 Raikoke and Ulawun volcanic eruptions.

This resulted in more effective scavenging and deposition due to proximity to the surface and larger humidity (Textor et al., 2006). In the troposphere, SO₂ is oxidized through various reactions, in both gas and liquid phase, involving OH, O₃, and H₂O₂ into sulfate particles (see Section 2.2.2), which are then deposited on the surface via wet, dry deposition and sedimentation. Tropospheric SO₂ has a relatively short atmospheric lifetime of 1 to 3 days, while tropospheric sulfate aerosols have lifetimes of around 3 to 5 days (Koch et al., 1999). This explains the faster removal rates of sulfur species within the raik-03 simulation in Figure 5.7.

In contrast, from early August onward, the deposition rates of raik-02 and raik-04 exceed those of raik-03 because of the larger SO₂ amount emitted into the stratosphere. Furthermore, sulfur species from raik-02 and raik-04 deposit more slowly compared to raik-03. This delay is attributed to the longer life time of stratospheric SO₂ compared to tropospheric SO₂. In the stratosphere, SO₂ undergoes oxidation to H₂SO₄ (see Reactions R 2.7 to R 2.9 in Section 2.2.2), a process that is slower than in the troposphere due to

lower water vapor availability. Zhu et al. (2020) and Myhre et al. (2004) reported that the lifetime of stratospheric SO₂ ranges from several weeks to months. As no interactive aerosol submodel is used in the actual set-up of the EMAC model (see Section 4.1), the formed H₂SO₄ (in gaseous form) in the stratosphere is transported downward into the troposphere via the Brewer-Dobson circulation. In the case of the Ulawun volcano, located in the tropics, the remaining sulfur compounds are transported by the Brewer-Dobson Circulation from tropical to higher latitudes, where they descend into the troposphere (Randel and Jensen, 2013). Upon reaching the troposphere, H₂SO₄ dissolves in cloud water and re-evaporates into residual pseudo-aerosols, which are then removed from the atmosphere through dry deposition, sedimentation and wet deposition/scavenging (see Section 4.1).

In addition, Figure 5.8 provides insight into the cumulative SO₂ deposited mass from the onset of the Raikoke eruption until the first of January 2020. Both raik-02 and raik-03 simulations exhibit a cumulative SO₂ mass of approximately 1.75 Tg and 1.65 Tg by the end of 2019, respectively. The slight variance between these values could be attributed to the extra 0.07 Tg SO₂ mass emitted in raik-02. Additionally, raik-04 illustrates a cumulative mass of about 2 Tg of SO₂ by the end of 2019. The elevated deposited mass simulated in the raik-04 simulation compared to raik-02 can be attributed to the incorporation of additional SO₂ emissions originating from the Ulawun volcanic eruptions in the Southern Hemisphere, amounting to approximately 0.34 Tg (SO₂). This augmentation significantly amplifies the total SO₂ mass available for oxidation and subsequent deposition.

To summarize, this analysis shows the capability of all sensitivity simulations, to reproduce the TROPOMI measured peak after the Raikoke and Ulawun eruptions. Furthermore, the consistent decay rates between TROPOMI data and sensitivity simulations, particularly raik-04 (which encompasses both the Raikoke and Ulawun eruptions in the stratosphere), as well as accounting the deposition of most of the initially emitted SO₂ mass within EMAC, further validate the model's chemistry scheme in capturing the intricate processes of SO₂ emission, oxidation, and deposition associated with volcanic eruptions. Nevertheless, over extended durations, various factors such as simulated wind patterns, radiative heating effects, and mixing dynamics can introduce deviations between model results and real-world observations. These complexities highlight the ongoing challenges in achieving complete concordance between model simulations and empirical data over prolonged temporal scales.

Following the validation of the model's ability to reproduce measured SO₂ mass after volcanic eruptions and simulate deposition processes, Figure 5.9 illustrates the spatial distribution of SO₂ VCDs from the raik-04 simulation in June and July using AK_15km and AK_polluted. This figure aims to highlight differences in analyzing explosive eruptive volcanoes with AK_15km compared to applying AK_polluted.

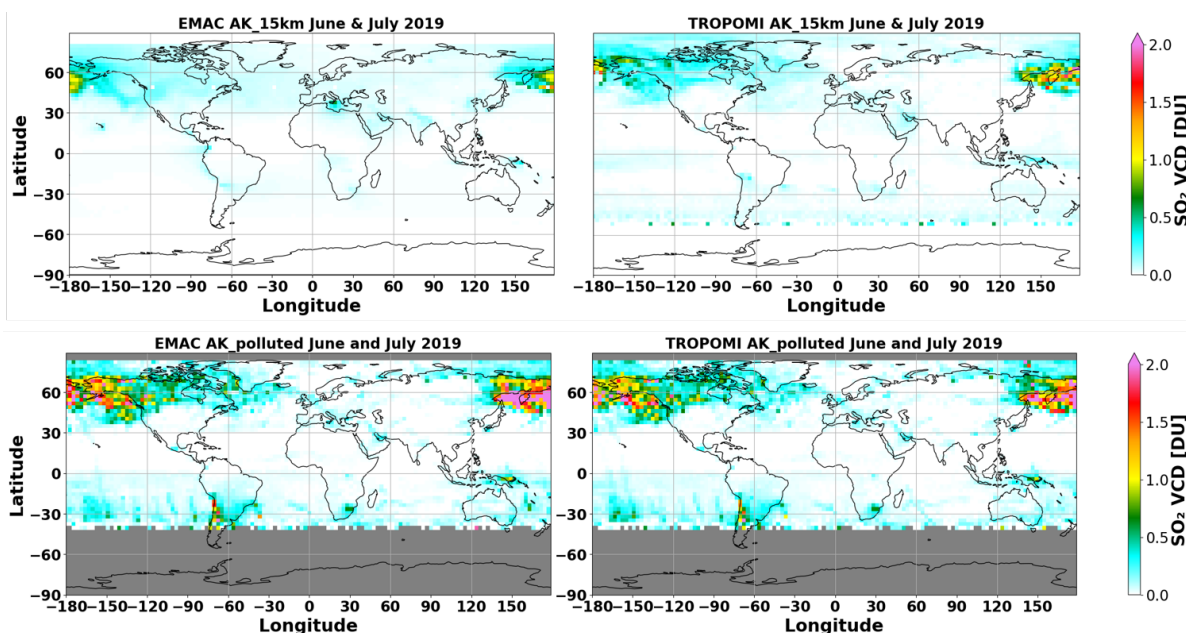


Figure 5.9: SO₂ VCD mean over June and July 2019 for both, EMAC raik-04 simulation (left panels) and TROPOMI (right panels). The VCDs are generated by AK_15km (upper panels) and AK_polluted (lower panels) for the case of volcanic activity present in these months.

For VCDs from TROPOMI and EMAC calculated with AK_polluted during June and July (lower panels in Figure 5.9), SO₂ VCDs show elevated values (exceeding 3 DU) with a large bias primarily in the Northern Hemisphere, and notable noise signals in the Southern Pacific and over Southern America. The enhanced signals are attributed to the utilization of the AK_polluted, which is not ideally suited for the analysis of volcanic activities (see Section 3.3.1). However, using the AK_15km (upper panels in Figure 5.9), prescribed for highly eruptive volcanoes, leads to a better SO₂ spatial distribution and volcanic intensity representation in both datasets. In the upper panels in Figure 5.9, TROPOMI- and EMAC-derived SO₂ VCDs peak around 1.7 DU, mainly concentrated North of 40°N, near the Raikoke eruption site. Notably, the signal of the Ulawun volcano is less pronounced compared to Raikoke, primarily due to Ulawun emitting 0.14 Tg of SO₂ in June, whereas Raikoke emits 1.57 Tg of SO₂ during the same period. This case study demonstrates that utilizing AK_15km and incorporating explosive volcanic emissions into the EMAC model enhances its ability to reproduce the retrieved SO₂ signal and geographic distribution post-eruption. This confirms what has been discussed in Section 3.3.1, that the importance of choosing the appropriate AK lies in reproducing the retrieved emitted mass over specific point sources (Raikoke and Ulawun in this work), as shown in the upper panels of Figure 5.9, where the prescribed AK_15km for high eruptive volcanoes is used. To better understand the impact of different AKs on the vertical profile and total SO₂ mass, Figure 5.10 presents the SO₂ mixing ratio vertical profile over Raikoke in June 2019.

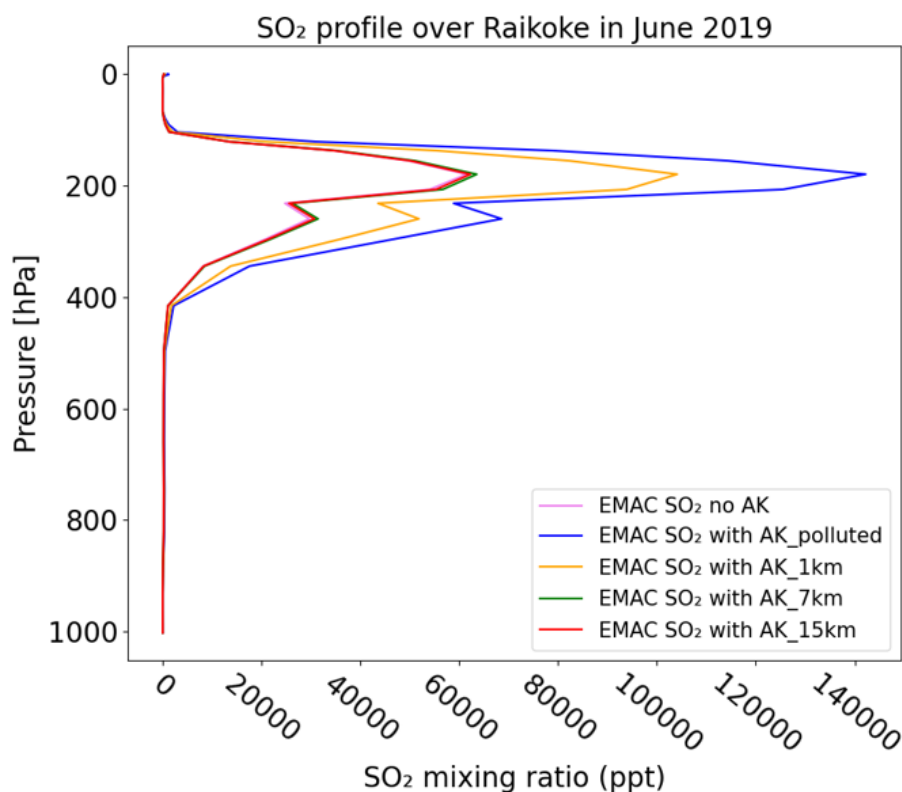


Figure 5.10: Vertical SO₂ mixing ratio profiles in ppt over Raikoke in June 2019. The figure shows the EMAC SO₂ original no weighted vertical profile (pink line), multiplied with AK_polluted (blue line), AK_1km (orange line), AK_7km (green line) and AK_15km (red line). Note that the pink line is so close to the green and red lines that a difference in the vertical profile is barely visible.

The original non-weighted SO₂ vertical profile (pink line) remains largely unaffected when multiplied by AK_7km or AK_15km (green and red lines, respectively). However multiplying with AK_polluted (as in the lower panels of Figure 5.9) results in significantly larger SO₂ mixing ratios (blue line), with values more than twice the original EMAC SO₂ mixing ratios (pink line). This highlights the importance of using appropriate averaging kernels for specific emission sources when analyzing SO₂ mass over point sources (see Section 3.3.1). If the focus is solely on comparing EMAC results to TROPOMI retrievals without assessing the absolute SO₂ mass, any averaging kernel could be employed, since they differ only by a constant factor (as depicted in Figure 5.10). Additionally, in Figure 5.9, VCDs for the 15 km case show lower values compared to the VCDs for the standard ("polluted") case in both datasets. This indicates that the ratio between the two datasets remains consistent. However, VCDs for the standard case exhibit larger values (SO₂ VCDs exceeding 3 DU) over Raikoke and Ulawun than those reported in the literature (SO₂ VCDs around 1.5), whereas VCDs for the AK_15km case accurately reproduce the actually released SO₂ mass following the Raikoke and Ulawun eruptions.

5.3 Evaluation of SO₂ from anthropogenic and outgassing volcano emissions

EMAC SO₂ emissions from both, anthropogenic and outgassing (non-eruptive) volcanic sources, are derived from prescribed emission inventories, specifically CMIP6 and the AeroCom Project, respectively. Each of these emission inventories is based on distinct assumptions that may not accurately reflect the actual emitted SO₂ masses and injection heights. Consequently, only a relative comparison of SO₂ hotspots (i.e. with large SO₂ emissions) and background regions between the EMAC model results and TROPOMI observations is feasible. A detailed analysis of the absolute values of SO₂ emissions from each source would be unrealistic due to the lack of precise information on emission masses and injection heights. This limitation contrasts with the case study of eruptive volcanoes discussed in Section 5.2, where sensitivity simulations were performed to reproduce retrieved SO₂ mass from satellite data after volcanic eruptions. This detailed study was possible, because of the available data and information on the amount of emitted SO₂ and the injection altitude. Therefore, a specific AK (AK_15km suitable for eruptive volcanoes) was applied to EMAC results to reproduce the emitted SO₂ mass by the studied volcanoes. However, for the comparison discussed in this section, only the ratios and the relationship between EMAC results and retrieved TROPOMI SO₂ VCDs are investigated. This study, can be performed using any vertical profile case, whether it be the standard ("polluted") case, 1 km, 7 km, or 15 km box profile cases. This is because both VCDs are calculated using the same air mass-factor (depending on the studied case), as detailed in Section 3.3.1, leading to the same ratios between both datasets across all four profile cases.

As shown in the left panel of Figure 5.3, the differences in SO₂ VCDs are most pronounced over regions such as China, India, and volcanic areas including the Tibetan Plateau, Etna, and Ulawun, with a lower difference intensity over Europe and the USA. In contrast, background regions like Africa and Australia exhibit minimal differences. Similar patterns of differences are also notable in the same SO₂ emission regions, as shown in Figure 5.11. This comparison aims to clarify how the application of AKs influences the original EMAC SO₂ VCDs and to identify where the largest differences occur.

5.3 Evaluation of SO₂ from anthropogenic and outgassing volcano emissions89

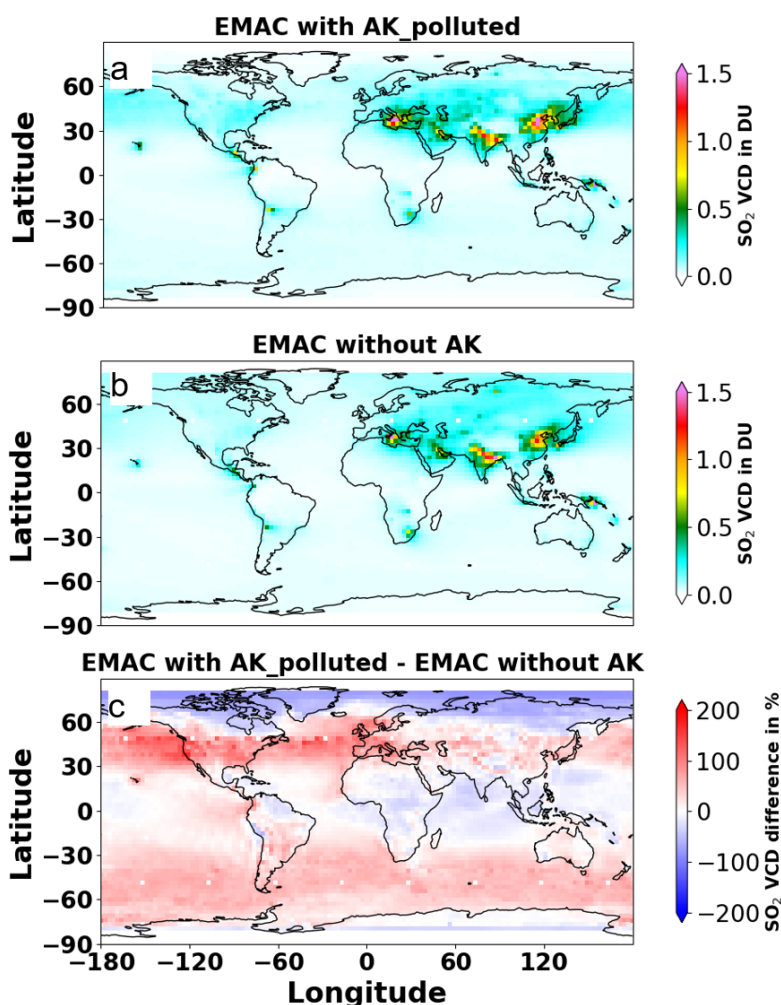


Figure 5.11: SO₂ VCDs in DU for weighted EMAC data with AK_polluted (panel "a") and original EMAC data without AK (panel "b") on a global scale. The lower panel "c" presents relative differences in % between EMAC VCDs with AK and EMAC without AK. All the panels represent annual mean data for the year 2019, excluding June and July.

The EMAC SO₂ VCDs with AK_polluted as seen by the satellite (panel "a" in Figure 5.11), exhibit increased SO₂ VCDs compared to EMAC SO₂ VCDs without AK (panel "b" in Figure 5.11), over regions such as Etna, China, the Tibetan Plateau, as well as over Europe and the USA, as seen in panel "c" from Figure 5.11. Conversely, the EMAC weighted with AK_polluted model shows decreased SO₂ VCDs over India, South Africa, and the Ulawun volcano (panel "c" in Figure 5.11). Notably, in the Northern polar regions, with latitudes polewards of 65°N, the EMAC model without AK shows larger SO₂ VCDs compared to EMAC with AK_polluted (panel "c" in Figure 5.11). This is attributed to missing values in the EMAC data with AK, due to the application of quality assurance flags (see Section 3.3.1). The derived positive and negative differences in SO₂ hotspots are

related not only to the vertical distribution of SO₂ mixing ratios in the EMAC model, but also to the vertical distribution of the AKs, which represent the satellite sensitivity at each atmospheric layer.

Figure 5.12 presents the vertical distribution of the four averaging kernels and their influence on the original vertical distribution of the EMAC SO₂ mixing ratios in selected regions, as a yearly mean in 2019, excluding June and July. These regions include China, Europe, India, Etna, and the Nevado Ojos del Salado volcano in Chile, where the differences between the EMAC model with and without AKs are most pronounced, as shown in panel "c" of Figure 5.11. By examining these regions, a better understanding of the positive and negative differences in SO₂ VCDs is aimed. The vertical profiles, in the left panel of Figure 5.12, illustrate how each averaging kernel affects the EMAC SO₂ mixing ratios, demonstrating the role of AKs in modifying the original vertical distribution. The different vertical profiles resulting from the application of averaging kernels to the original shape of the EMAC model show the same vertical distribution shape, with difference in magnitude related to the applied AKs. This step is essential for making the model results comparable to what the satellite observes. By applying these kernels, specific layers in the model are weighted more strongly while others are weighted less. This adjustment is necessary to facilitate a valid comparison with satellite data. These insights are crucial for interpreting the impact of AKs on the model results and for identifying the altitude, where the vertical distribution of SO₂ is significantly influenced by the application of averaging kernels.

5.3 Evaluation of SO₂ from anthropogenic and outgassing volcano emissions⁹¹

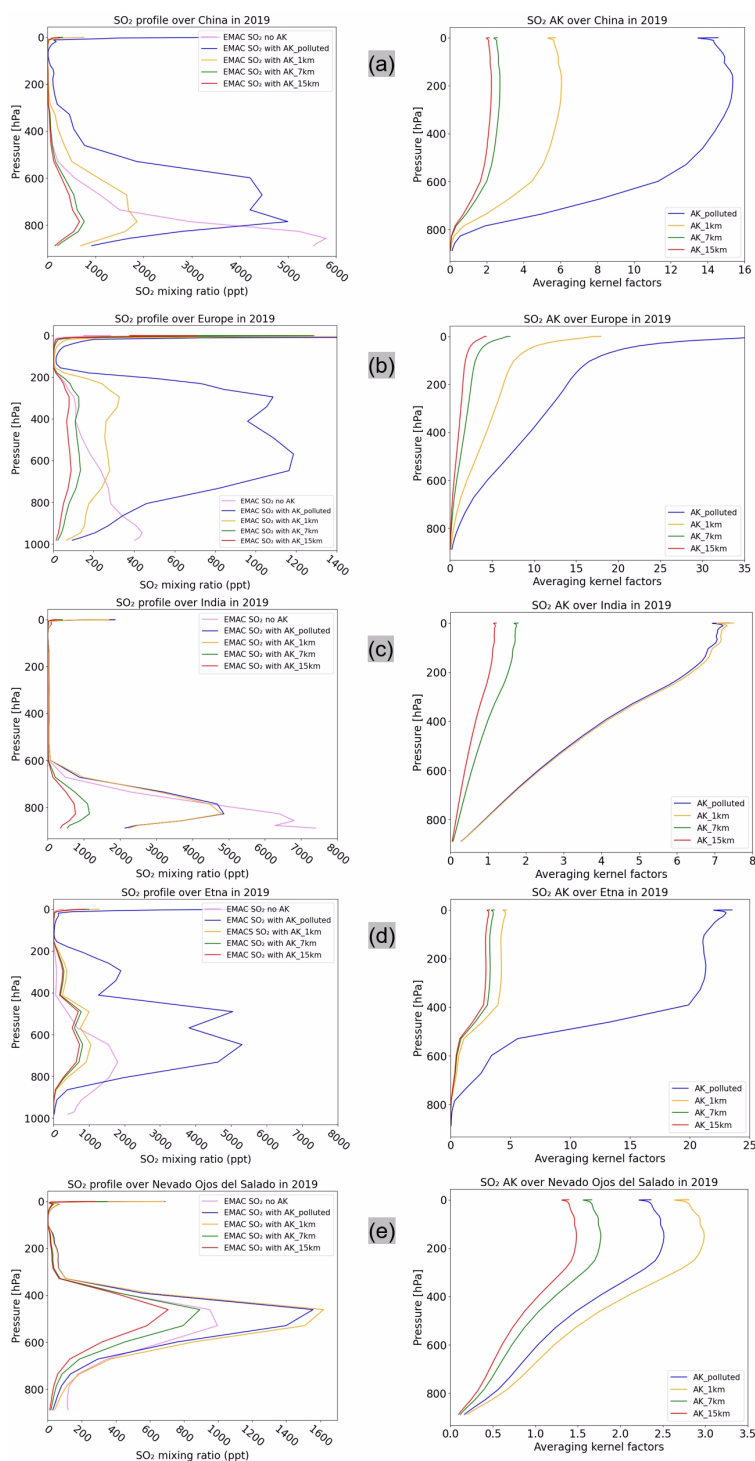


Figure 5.12: Vertical distribution of the different AKs (right panels) and their impact on the SO₂ mixing ratio vertical profiles in ppt (left panels) on 5 regions in 2019. (a) is over China, (b) Europe, (c) India, (d) Etna and (e) Nevado Ojos del Salado volcano in Chile. Note that the increased SO₂ mixing ratios near 0 hPa are due to the artifacts originating from the interpolation of the EMAC vertical columns to the TM5 vertical grid.

On the right panels of Figure 5.12, the AKs from each selected regions display similar sensitivity shapes, differing only by a scaling factor. These AKs influence the vertical profile of the original EMAC SO₂ mixing ratios (represented by the pink line on the right panels of Figure 5.12) depending on the vertical profile used. As the comparison in Figure 5.11 was conducted using AK_{polluted}, the resulting vertical profiles of EMAC multiplied by AK_{polluted} (blue lines in the left panels of Figure 5.12) is more investigated for the selected regions.

The satellite's low sensitivity near the Earth's surface results in low AK factors. Consequently, the EMAC model with AK_{polluted} generally shows lower SO₂ mixing ratios than EMAC without AK near the surface, as CCMs do not encounter any limitations near the surface as satellite retrievals. Conversely, higher in the atmosphere, the situation reverses. Here, the EMAC model with AK_{polluted} shows larger mixing ratios compared to the EMAC model without AK above 700 to 600 hPa, except for the case of India. This is because the model simulates low mixing ratio signals at higher altitudes, where the satellite exhibits large sensitivity. Therefore, the low EMAC mixing ratios are multiplied by the large AK factors, resulting in larger SO₂ mixing ratios and consequently larger VCD values. This pattern is evident over China, Europe, Etna and Nevado Ojos del Salado volcanoes, where the model still provides SO₂ mixing ratios at higher altitudes. Over India, the situation is different. Here, the model's SO₂ mixing ratios tend to zero above 600 hPa. That means, that even when multiplying the model's SO₂ mixing ratio by a large AK factor at that altitude, the values remain near zero, meaning the VCD is primarily controlled by the mixing ratios below 600 hPa. In this region, the model provides large SO₂ mixing ratios near the surface; however, due to the low satellite sensitivity in the boundary layer, multiplying by AK_{polluted} results in lower VCD values. These changes in the SO₂ mixing ratio vertical distribution in the original EMAC data after applying the AKs lead to the observed differences seen in Figure 5.11. Consequently, the EMAC model with AK_{polluted} shows lower VCDs over India compared to the EMAC model without AK and larger VCDs over Europe, China, Etna, and Nevado Ojos del Salado volcanoes.

Next, a comparison is conducted between the VCDs of the EMAC model and the Sentinel-5P/TROPOMI instrument. For this analysis, the AK_{polluted} is further used. Table 5.3 shows the differences between SO₂ VCDs in the EMAC model compared to those retrieved from TROPOMI over outgassing volcanoes, presented as a yearly mean for 2019. The table indicates that EMAC SO₂ VCDs are generally larger than TROPOMI values over volcanic regions. Note that, when comparing the satellite data to models multiplied with the AKs, COBRA data reveals an uncertainty of approximately 27% to 32% on the retrieved SO₂ column, mainly due to instrumental noise (Theys et al., 2022).

5.3 Evaluation of SO₂ from anthropogenic and outgassing volcano emissions93

Volcanoes	SO ₂ emissions at heights [hPa] in molec /m ³ /s						SO ₂ VCD in EMAC divided by SO ₂ VCD in TROPOMI
	577hPa	746hPa	845hPa	926hPa	966hPa	989hPa	
Etna in Southern Italy	1.46e14	9.62e14	—	—	—	—	7
Trajumulco in central America	6.84e13	1.29e14	—	—	—	—	6
Mt Fuji in Southern Japan	2.74e12	4.81e12	4.85e11	1.12e15	2.85e14	—	5
Nevado Ojos del Salado in Chile	2.44e14	—	—	—	—	—	2.5

Table 5.3: Shown is a comparison of SO₂ VCDs between EMAC results and TROPOMI retrievals over different volcano types in 2019. The emitted SO₂ in molec /m³/s in different altitudes, from 989 hPa till 577 hPa, for all the selected volcanoes, are presented. The ratios between EMAC SO₂ VCDs calculated with AK_polluted and TROPOMI SO₂ VCDs calculated for the standard case over all the selected volcanoes, show the relationship between both datasets.

For instance, the volcanoes located in Southern Italy, central America, Southern Japan,

and Chile stand out in this comparison. Particularly noteworthy are the ratios between both datasets, derived for Etna, Tajumulco, and Mt. Fuji, amounting to 7, 6, and 5, respectively. Similarly, a ratio of approximately 2.5 is evident between EMAC results and TROPOMI measurements in Nevado Ojos del Salado. These ratios can alternatively be expressed as percentage differences, revealing a 600%, 500%, 400%, and 150% deviation between EMAC results and TROPOMI retrievals at Etna, Tajumulco, Mt. Fuji, and Nevado Ojos del Salado, respectively. Notably, these differences are out of the error margin of the satellite measurements, which typically ranges between 27% and 32%.

These differences are attributed to the volcanic emission inventory used within the EMAC model. The larger ratios derived for the first three volcanoes could be attributed to both, the SO₂ emission masses and the emission heights. In the AeroCom inventory (Dentener et al., 2006), the Etna, Tajumulco, and Mt. Fuji volcanoes are considered not only as outgassing, but also explosive volcanoes. The top of Etna is approximately 3300 meters, Tajumulco about 4000 meters, and Mt. Fuji about 3700 meters, with emissions reaching up to around 4500 meters (577 hPa). This indicates explosive volcanic activity, with emissions ranging from the "top of the volcano + 500 meters" to "top of the volcano + 1500 meters", as detailed in Section 3.1.12. Conversely, the volcano in Chile is categorized solely as an outgassing volcano, thus showing the lower ratio between EMAC results and TROPOMI retrievals. Continuous volcanoes, within the used model setup, emit from "the height of the volcano * 0.67" until the height of the volcano. Volcanic SO₂ emission amounts and heights are challenging to accurately reproduce within a CCM. Therefore, the AeroCom emission inventory used by EMAC for volcanic activities likely does not reflect the actual volcanic activity accurately.

For anthropogenically influenced regions, the EMAC model also shows weaker SO₂ VCDs compared to those from TROPOMI, but with smaller ratios in most regions compared to volcanic areas. Table 5.4 shows a comparison of EMAC SO₂ VCDs with TROPOMI in SO₂ background and hotspot regions.

5.3 Evaluation of SO₂ from anthropogenic and outgassing volcano emissions⁹⁵

Study regions	Ratios between SO ₂ VCD in EMAC for standard case and SO ₂ VCD in TROPOMI for standard case
South Atlantic Ocean	1.1
Africa	1.2
Europe	1.6
USA	1.8
Northeastern China	3.2
Southeastern China	2
India	2.5

Table 5.4: Analysis of the relationship of SO₂ VCDs between EMAC results and TROPOMI retrievals in different background and hotspot regions in 2019. The ratios between EMAC SO₂ VCD for standard case and TROPOMI SO₂ VCD for standard case, in all the selected regions, are shown.

In background regions, a specific area in central Africa is selected for its low SO₂ VCDs, bounded by the coordinates (12°N, 15°E), (2°N, 15°E), (12°N, 27°E), and (2°N, 27°E). Additionally, a region in the South Atlantic Ocean, bounded by (20°S, 20°W), (30°S, 20°W), (20°S, 5°W), and (30°S, 5°W), is also considered. In these background regions, the discrepancies are small, ranging between 10 to 20%. In other anthropogenically influenced regions such as Europe (bounded by (60°N, 5°E), (45°N, 5°E), (60°N, 25°E), and (45°N, 25°E)) and the USA (bounded by (45°N, 70°W), (30°N, 70°W), (45°N, 120°W), and (30°N, 120°W)), factors of 1.6 (i.e. 60% difference) and 1.8 (i.e. 80% difference), respectively, are calculated, indicating larger SO₂ VCDs from EMAC compared to those from TROPOMI. In India (bounded by (26°N, 71°E), (12°N, 71°E), (26°N, 85°E), and (12°N, 85°E)), a factor of 2.5 (i.e. 150% difference) is derived. In China, a differentiation is made between a hotspot region in Northeastern China (around Beijing) and a moderate region in Southeastern China. The boundary coordinates for the Northeastern China region are (42°N, 105°E), (30°N, 127°E), (42°N, 127°E), and (30°N, 127°E). For Southeastern China, the boundaries are (28°N, 105°E), (20°N, 105°E), (28°N, 123°E), and (20°N, 123°E). The SO₂ VCD is a factor of 3.2 (i.e. 220% difference) in Northeastern China and 2 (i.e. 100% difference) in Southeastern China for the year 2019. For a better visualization of the regions under study, Figure 5.13 provides a geographical map depicting the different areas. It is important to

note that, apart from the selected background regions in the South Atlantic Ocean and Africa, the discrepancies in all other regions exceed the error margin inherent to satellite measurements, which falls within the range of 27% to 32%.

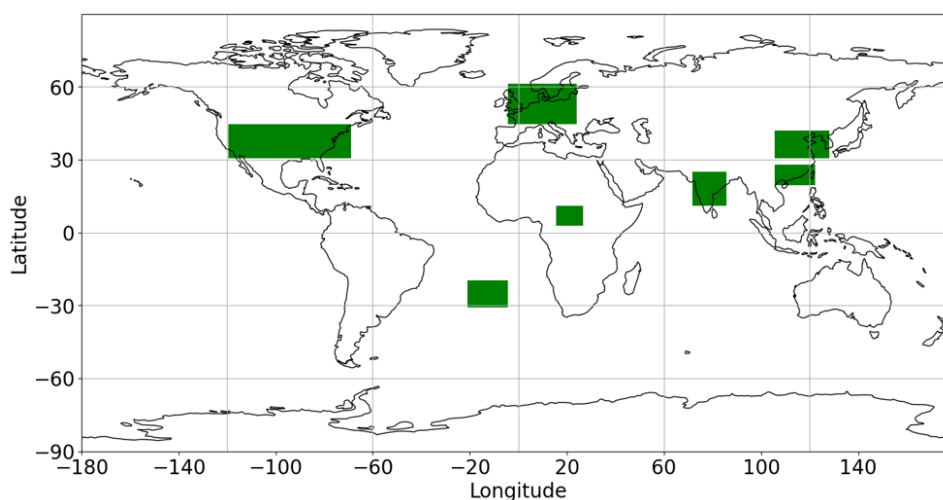


Figure 5.13: Geographical map highlighting the studied anthropogenically influenced regions selected for this study. Specific areas in central Africa, South Atlantic Ocean, Europe, the USA, India, as well as Southeastern and Northeastern China are shown.

From this analysis, it is evident that the ratios vary significantly depending on the regions analyzed. A cause of the discrepancies is the different spatial resolution of both, EMAC and TROPOMI. As explained for the case of eruptive volcanoes (see Section 5.2), EMAC with a coarse spatial resolution of approximately $300 \text{ km} \times 300 \text{ km}$, may not reproduce the same SO₂ mixing ratios retrieved by the TROPOMI/Sentinel-5P satellite. TROPOMI/Sentinel-5P has a high spatial resolution of $3.5 \text{ km} \times 7 \text{ km}$, allowing it to capture fine-scale variations in SO₂ mixing ratios that can arise from localized emission sources such as volcanoes, power plants, and urban areas. This disparity in the spatial resolution means that the model averages emissions over a larger area, which can smooth out local peaks and results in underestimated SO₂ mixing ratios over a specific area around a power plant, for example. Consequently, localized pollution areas detected by TROPOMI may appear less or more pronounced in the model output, leading to discrepancies when comparing the two datasets. In background regions, such as Africa, the differences between the SO₂ VCDs of EMAC results and TROPOMI retrievals are minimal, falling within the uncertainty range of TROPOMI retrievals. This indicates a strong agreement between the two datasets in these areas. However, in regions with larger SO₂ emissions, such as India and China in 2019, as shown in Figures 5.1, 5.2 and reported by Dahiya et al. (2020), the ratios between both datasets are considerably larger. In contrast, in regions like Europe, the USA, and Southeastern China, the agreement between EMAC results and TROPOMI retrievals is relatively good.

5.4 Discussion and conclusion

5.4.1 Geo-spatial distribution and discrepancies of SO₂ VCDs between EMAC results and TROPOMI retrievals for the year 2019

The global-scale comparison between the EMAC model results and TROPOMI retrievals undertaken in this study provides valuable insights into the distribution and discrepancies of SO₂ VCDs for the year 2019. The TROPOMI/Sentinel-5P satellite, distinguished for its high spatial resolution among satellite instruments, serves as a crucial dataset for this analysis, offering opportunities for assessing atmospheric composition simulated with the EMAC model. The chosen year, 2019, represents the most recent complete annual cycle available in both datasets.

The geographical distribution and temporal variations of SO₂ VCDs, as illustrated in Figures 5.1 and 5.2, highlight significant discrepancies between the EMAC model simulation results (based on the RD1SD-base-01) and TROPOMI satellite retrievals. The consistent larger SO₂ VCDs from the EMAC model results compared to TROPOMI retrievals in regions with active volcanoes or significant anthropogenic emissions underscores the need for improved process descriptions, mainly emission inventories, in the models and refined retrievals for TROPOMI measurements.

5.4.2 Effects of volcanic eruptions on the simulated atmospheric SO₂ in the EMAC Model

The analysis of SO₂ emissions from eruptive volcanoes such as Raikoke and Ulawun in 2019 reveals critical insights into the vertical distribution and subsequent atmospheric processes. The significant SO₂ signals detected by TROPOMI in June and July were not present in the CMIP6 emission inventory used by EMAC. Sensitivity simulations (raik-02, raik-03 and raik-04) with EMAC using different vertical emission profiles were important in understanding the dispersion and removal of SO₂. The examination indicated that the raik-04 profile, which emitted a larger fraction of SO₂ into the stratosphere, from both Raikoke and Ulawun, aligned more closely with TROPOMI observations.

Further analysis of the cumulative deposited SO₂ mass revealed that the larger deposition rates in the raik-03 simulation were due to significant emissions in the troposphere, leading to more effective scavenging and deposition. The raik-02 and raik-04 simulations, with larger stratospheric emissions, showed slower deposition rates and longer atmospheric residence times for SO₂.

5.4.3 Evaluation of SO₂ from anthropogenic and outgassing volcano emissions

The comparison of SO₂ VCDs from EMAC results and TROPOMI retrievals over outgassing volcanoes, such as in Southern Italy, America, Japan, and Chile, reveals generally larger SO₂ VCDs simulated by the EMAC model compared to TROPOMI retrievals. The differences, highlighted in Table 5.3, are attributed to the AeroCom volcanic emission inventory used within EMAC, which may not accurately reflect the actual volcanic activity.

The largest ratios are derived in Southern Italy, America, and Japan, with values of 7 (i.e. 600% difference), 6 (i.e. 500% difference), and 5 (i.e. 400% difference), respectively. These differences are likely due to the larger prescribed emitted SO₂ mass and higher emission altitude in the AeroCom inventory, where these volcanoes are considered both, outgassing and explosive. In contrast, the volcano in Chile, categorized solely as an outgassing volcano, shows a smaller ratio of 2.5 (i.e. 150% difference). The varying emission heights and amounts are challenging to reproduce accurately within a CCM, emphasizing the need for more precise emission inventories. Notably, the differences in SO₂ VCDs derived over the selected volcanoes consistently surpass the error margin (about 27-32%) inherent to TROPOMI/Sentinel-5P satellite measurements, underscoring the necessity to enhance the data quality of emission inventories for volcano cases.

On the other side, the comparison of SO₂ VCDs from EMAC results and TROPOMI retrievals in anthropogenically influenced regions indicates that the EMAC model generally simulates larger SO₂ VCDs compared to the TROPOMI retrievals, albeit with lower factors than in volcanic regions. Table 5.4 presents the differences across various regions, showing the larger discrepancies in highly polluted areas such as India and Northeastern China.

In background regions such as central Africa and the South Atlantic Ocean, the discrepancies are small, with differences ranging from 10-20%, indicating good agreement between the datasets. In more polluted regions like Europe, the USA, and Southeastern China, the EMAC model shows larger SO₂ VCDs by factors of 1.6 (i.e. 60% difference), 1.8 (i.e. 80% difference), and 2 (i.e. 100% difference), respectively.

The larger SO₂ VCDs from the EMAC model results compared to TROPOMI retrievals in India and Northeastern China, with factors of 2.5 (i.e. 150% difference) and 3.2 (i.e. 220% difference), respectively, could be attributed to the large SO₂ emissions in these regions, originating from the CMIP6 emission inventory. These findings align with previous studies indicating strong SO₂ emissions from industrial activities in these areas. The application of AK_polluted ensures a consistent comparison between the model results and satellite data retrievals, but it also highlights the impact of emission heights on the derived SO₂ VCDs. With the exception of the chosen background areas in the South Atlantic Ocean and Africa, it's noteworthy that the disparities derived across all other regions exceed the error margin associated with satellite measurements, typically falling between 27% and 32%.

Since TROPOMI only provides total VCD values, a detailed analysis of the entire vertical profile between both datasets is not possible. Therefore, it is difficult to ascertain whether the differences originate near the surface or higher up in the atmosphere. To

address this, a comparison of the simulated SO_2 concentrations at the Earth's surface and in the boundary layer are conducted in the next sections.

In conclusion, the comparison between the EMAC model results and TROPOMI retrieved data highlights the strengths and limitations of the EMAC model in representing atmospheric SO_2 VCDs on a global scale. It also enables the study of the deposited sulfur species in the EMAC model after large volcanic eruptions. The analysis underscores the importance of accurately representing emission heights and profiles, particularly for eruptive and outgassing volcanoes. The larger SO_2 VCDs simulated over outgassing volcanoes are related to the injections of SO_2 mass at higher altitudes. Therefore, the model tends to exhibit elevated SO_2 mixing ratio values at these altitudes, where the satellite retrieval is most sensitive. In other words, if the model has the biggest error in those high altitudes, where TROPOMI is the most sensitive, then the biggest discrepancy between the end results is produced. The findings also indicate that while the EMAC model generally shows larger SO_2 VCDs than TROPOMI retrievals in anthropogenically influenced and volcanic regions, the discrepancies vary depending on the emission sources and regions analyzed. These differences are retrieved between the total VCD of the model results and the total VCD of the TROPOMI retrievals, making it challenging to determine the specific altitudes at which these differences originate. Therefore, a model evaluation with ground-based measurements at the Earth's surface in regions, where reliable data are available, could provide a more accurate assessment of the model's SO_2 concentrations and sulfur deposition fluxes (see Section 6).

Finally, the good agreement in background regions and the ability to capture peak SO_2 mass burdens from large volcanic eruptions validate the model's capability in reproducing retrieved SO_2 VCDs within the uncertainty range of TROPOMI retrievals. However, the ongoing challenges in accurately simulating SO_2 emissions and their vertical distribution highlight the need for improved emission inventories and validated observational data.

Chapter 6

Evaluation of simulated SO₂ with ground-based measurements

Shifting from a global dataset to a more localized analysis, this chapter focuses on a comparative examination of sulfur species from the EMAC model results against ground-based measurements sourced from observation networks in major SO₂-emitting regions worldwide. Specifically, the analysis centers on SO₂ concentrations and sulfur deposition fluxes over the USA, Europe, and at selected observational stations in China and Japan. These regions are chosen due to the availability of extensive and reliable datasets covering a two-decade period, from 2000 to 2019.

Ground-based measurements provide invaluable insights into SO₂ concentrations, primarily stemming from point sources such as power stations and smelters. Upon release into the atmosphere, SO₂ has a relatively short lifetime of approximately two days, although this duration can vary between 15 to 65 hours during summer and winter, respectively (Lee et al., 2011). These variations are influenced by a complex interplay of factors including meteorological conditions, atmospheric chemistry, and regional emission patterns. The oxidation of SO₂ leads to the formation of sulfate ions (SO₄²⁻), representing the predominant mechanisms responsible for removing SO₂ from the atmosphere (see Section 4.1).

Examining sulfur deposition fluxes within the RD1SD-base-01 simulation from the EMAC model in comparison to observations from these specific regions provides a nuanced understanding of the temporal evolution of deposited sulfur. Within the RD1SD-base-01 simulation, SO₂ emissions, including those from anthropogenic sources, are originated from the CMIP6 inventory (as mentioned in Section 3.3). The processes governing the removal of SO₂ from the atmosphere, including wet and dry depositions, are elaborated upon in Sections 3.1.7 and 3.1.9, respectively. Moreover, the data products of ground-based measurements are prescribed in Section 3.2.2.

This approach allows for a more detailed and region-specific understanding of SO₂ emissions and the simulation outcomes in predicting sulfur chemistry. An evaluation of sulfur in EMAC with ground-based measurement is described for the USA, Europe and the China-Japan region in Sections 6.1, 6.2 and 6.3, respectively.

It is important to note, that for the time series analysis in this section, mean/average

values and standard deviation across stations are calculated for each year for both, the EMAC model results and the data from observational networks, across the stations in Eastern and Western USA, Europe, and over the China-Japan region. This is calculated through several steps. First, the monthly mean values from each of the available observational stations are aggregated to compute yearly mean values. This aggregation is performed for each station individually over the period from 2000 to 2019. Furthermore, the observational stations are geographically dispersed and do not directly align with the spatial grid used by the EMAC model. Therefore, a spatial regridding process (the nearest neighbor method is used in this work) is necessary to map the observational data onto the model's grid for a direct comparison (see Section 3.3.2). For EMAC grid boxes containing multiple observational stations, the mean value of all stations within that box is computed, in order to obtain a single representative value per grid box. Afterwards, the weighted mean over those grid boxes is determined by summing all the grid box values weighted by the area of the grid boxes, as follows:

$$\mu_w = \frac{\sum_{i=1}^N w_i x_i}{\sum_{i=1}^N w_i}, \quad (6.1)$$

where μ_w is the weighted mean, x_i represents the value in grid box i , w_i is the area (weight) of grid box i , and N is the total number of the grid boxes. Consequently, the weighted standard deviation σ_w is then expressed as:

$$\sigma_w = \sqrt{\frac{\sum_{i=1}^N w_i (x_i - \mu_w)^2}{\sum_{i=1}^N w_i}}. \quad (6.2)$$

For the spatial analysis, the calculated mean values and the corresponding standard deviations over the whole time series, i.e. for 20 years, are calculated.

Through all this thesis the results are shown for the measurement sites mapped onto the model grid. Therefore, these measurement sites are referred to as 'grid-mapped sites'.

6.1 Sulfur concentration and deposition in the USA

In the United States, sulfur species simulated at the Earth's surface are evaluated against observation data obtained from the CASTnet network. As detailed in Section 3.2.2, CASTnet provides surface-level observations, including monthly and yearly mean SO₂ concentrations in $\mu\text{g}/\text{m}^3$ and sulfur wet deposition fluxes in $\text{kg}(S)/\text{ha}$ per year. The SO₂ concentrations and sulfate amounts in precipitation samples are measured, whereas the dry deposition fluxes are simulated based on a Multi-Layer Model (see Section 3.2.2).

In the present work the years spanning from 2000 to 2019 are evaluated. This extensive dataset enables a comprehensive analysis of long-term trends and fluctuations in SO₂

concentrations. Over the USA, 98 stations were selected for examination, providing detailed data on both, SO_2 concentrations and sulfur deposition fluxes over the two-decade period. Specifically, 34 observation stations positioned West of 100°W longitude represent the Western USA, while the remaining 64 stations East of 100°W represent the Eastern USA region. The spatial distribution of the locations is depicted in Figure 3.6 in Section 3.2.2.

Figure 6.1 shows the SO_2 concentration measured at the CASTnet grid-mapped sites (right panel) and the EMAC simulated concentration (left panel). In both cases, 20 year averages are calculated. It is important to note that the EMAC results are only shown for grid boxes where observational stations are located, which explains the presence of "empty boxes" in the EMAC model results.

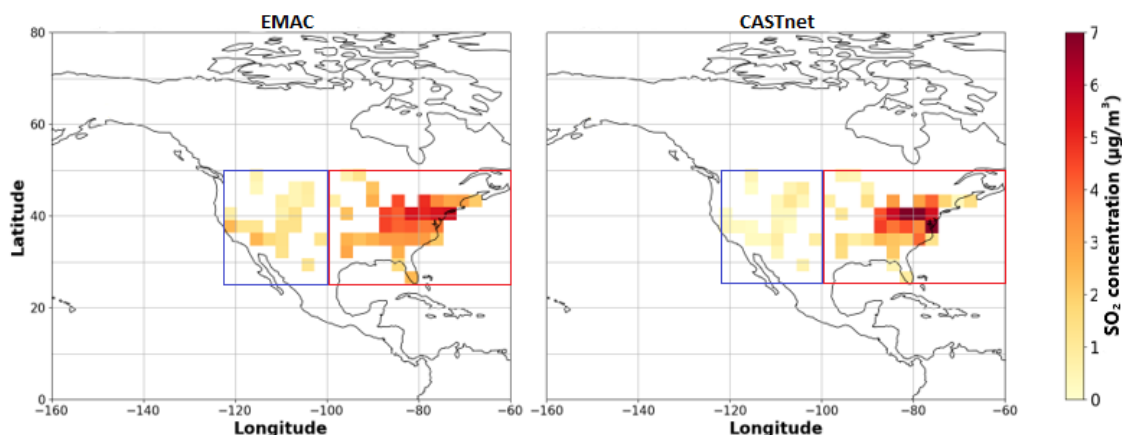


Figure 6.1: Geographical distribution of mean SO_2 concentrations for the years between 2000 and 2019 at the Earth's surface as simulated with EMAC and observed at the CASTnet grid-mapped sites in $\mu\text{g}/\text{m}^3$. The red and blue boxes indicate the regions, where the SO_2 emissions from the CMIP6 and EDGAR5 emission inventories are compared (details see text).

Figure 6.1 indicates that Eastern grid-mapped sites exhibit larger SO_2 concentrations compared to the grid-mapped sites in the Western region in both datasets. This disparity is attributed to the higher density of SO_2 emission sources concentrated in the Eastern USA compared to the Western part. This is also reported by Hardacre et al. (2021) and Qu et al. (2019), which affirm that SO_2 emissions and concentrations are more significant in the Eastern part of the USA compared to the Western part.

As shown in Figure 6.1, CASTnet (right panel) measures approximately $7 \mu\text{g}/\text{m}^3$ at some individual grid-mapped sites in the Eastern USA, with other Eastern grid-mapped sites showing very low SO_2 concentrations of about $0.5 \mu\text{g}/\text{m}^3$. On the left panel in Figure 6.1, the RD1SD-base-01 simulation driven by the CMIP6 inventory indicates that SO_2 concentrations at some individual Eastern grid-mapped sites are less intensive than those reported by CASTnet. However, on average, EMAC results show overall consistent

SO₂ concentrations between 1.5 $\mu\text{g}/\text{m}^3$ and a maxima of about 5.5 $\mu\text{g}/\text{m}^3$ at Eastern grid-mapped sites. In the Western region, both datasets show lower SO₂ concentrations, averaging around 1 $\mu\text{g}/\text{m}^3$ across all grid-mapped sites. However, the RD1SD-base-01 simulation results in larger SO₂ concentrations reaching up to 3 $\mu\text{g}/\text{m}^3$ at some Western grid-mapped sites. This comparative analysis highlights the range of the distribution across the different grid-mapped sites in both datasets. The larger distribution range of the SO₂ concentrations in the EMAC model across the grid-mapped sites in Western USA compared to the smaller distribution range of the SO₂ concentrations across the grid-mapped sites in the same region from CASTnet measurements, results in larger standard deviation values in the EMAC results compared to those from the CASTnet measurements (see panel (a) in Figure 6.2). For the Eastern USA, the picture is different. Here, the CASTnet network shows a larger range of the SO₂ concentrations across the grid-mapped sites compared to the EMAC model. Consequently, this results in larger standard deviations in the CASTnet measurements compared to those from the EMAC results (see panel (b) in Figure 6.2).

Figure 6.2 provides a comparison between both, the RD1SD-base-01 simulation (driven by the CMIP6 emission inventory) and CASTnet SO₂ concentration, and sulfur deposition flux across different regions in the USA. Specifically, SO₂ concentrations and sulfur deposition fluxes from Western grid-mapped sites (panels (a) and (c), respectively), and from Eastern grid-mapped sites (panels (b) and (d), respectively), are shown. The comparison involves calculating the annual mean of SO₂ concentration in $\mu\text{g}/\text{m}^3$ and sulfur deposition flux (wet and dry processes) in $\text{kg}(\text{S})/\text{ha}$ per year, averaged over Eastern, and Western USA grid-mapped sites, respectively.

For both, surface SO₂ concentration and sulfur deposition flux, the RD1SD-base-01 simulation driven by the CMIP6 emission inventory effectively captures the decline across both regions of the USA for the period 2000-2019. As shown in Figure 6.2, the model tends to simulate larger surface SO₂ concentrations than CASTnet by a factor of 2 (i.e. 100% difference) in the Western region over the 20-year period (panel (a)), while showing approximately 20% (i.e. factor of 1.2) larger SO₂ concentrations over the Eastern USA grid-mapped sites (panels (b)). At Western USA grid-mapped sites, EMAC shows decreasing surface SO₂ concentrations after 2000, which brings the simulated results into better agreement with the observations over time (see panel (a) in Figure 6.2). The large standard deviation derived from the datasets are attributed to the extensive dispersion of sulfur sources across a broad geographical area.

In the Eastern and Western USA, the largest part of sulfur removal occurs via wet deposition. This is effectively simulated by EMAC in agreement with CASTnet observations. Note that for the calculation of deposition flux within the RD1SD-base-01 simulation, the deposited sulfate and SO₂ were converted to a sulfur equivalent. For example, to convert SO₂ into a sulfur (S) equivalent, this conversion accounts for the molecular weights of sulfur and SO₂. The atomic weight of sulfur is approximately 32.06 g/mol, while the molecular weight of SO₂ is approximately 64.07 g/mol. Therefore, the deposited SO₂ flux is divided by a conversion factor of approximately 2 to obtain the deposition flux of sulfur equivalent. The same is also done with all the other deposited sulfur species. In panel

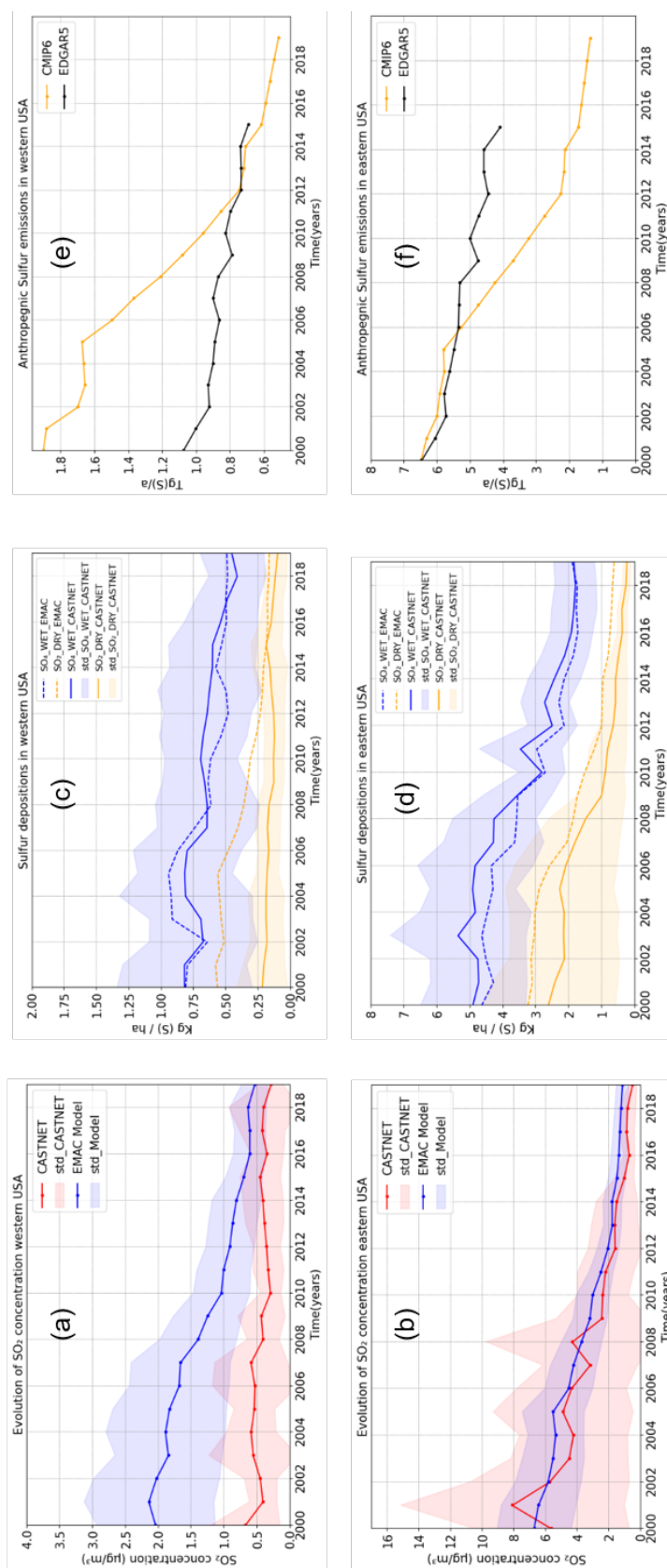


Figure 6.2: Time series of SO₂ concentrations from both, EMAC and CASTnet between 2000 and 2019 in the Western (panel (a)), and Eastern USA (panel (b)). The middle panels (c and d) represent the evolution of wet and dry sulfur deposition fluxes between 2000 and 2019. Note that for the calculation of deposition fluxes, the deposited sulfate and SO₂ were converted to sulfur equivalent. The right panels (e and f) show the comparison between the temporal evolution of CMIIP6 and EDGAR5 anthropogenic sulfur emissions in Western and Eastern USA, as a yearly area integral between 2000 and 2019 (2015 for EDGAR5) of all the model grid boxes situated in the region marked by the blue and red boxes, respectively, in Figure 6.1.

(d) in Figure 6.2, EMAC shows a lower sulfur deposition flux over the Eastern USA, for wet deposition (10% lower EMAC values compared to CASTnet) and larger values for dry deposition (30% larger EMAC values compared to CASTnet) over the 20-year period. In the Western USA, EMAC also simulates a 5% lower sulfur wet deposition flux compared to CASTnet over the entire 20-year period (panel (c) in Figure 6.2). Here, EMAC does not show lower values over all the time range, but indicates larger wet sulfur deposition between 2002 and 2008. For the sulfur dry deposition flux (orange lines), EMAC shows a factor of 2 larger values over the entire 20 year-period compared to CASTnet.

Since the concentration simulated by the model is directly affected by the prescribed emissions, it is important to understand the differences between the used CMIP6 emission inventory (see Section 3.1.12) and other emission inventories. In this work the EDGAR5 emission inventory (see Section 3.1.12) is used for this comparison. For this, the temporal evolution of sulfur emissions in Tg(S)/a from the CMIP6 emission inventory (orange lines in panels (e) and (f) in Figure 6.2) is compared with those from the EDGAR5 emission inventory (black lines in panels (e) and (f) in Figure 6.2). This comparison, as shown in Figure 6.2, highlights the discrepancies and potential biases between the different emission inventories, allowing to assess the robustness of the model's input data. Note that for the calculation of sulfur emissions, the emissions from SO₂ were converted to sulfur equivalent. The anthropogenic emissions (particularly from fossil fuels, ship, road, and aircraft sectors) from both emission inventories are calculated as a yearly area integral over a Western USA region (see panel (e) in Figure 6.2) bounded by the coordinates (50°N, 100°W), (28°N, 100°W), (50°N, 123°W), and (28°N, 123°W), and over an Eastern USA region (see panel (f) in Figure 6.2) located at the coordinates (50°N, 60°W), (28°N, 60°W), (50°N, 100°W), and (28°N, 100°W). Both regions are shown in Figure 6.1, where the red and blue boxes represent the selected Eastern and Western USA regions, respectively.

Over the western USA (panel(e) in Figure 6.2), CMIP6 shows 50% larger sulfur emissions than EDGAR5 between 2000 and 2015. The picture is different in the Eastern USA region (panel(f) in Figure 6.2), where CMIP6 indicates 10% lower emitted sulfur compared to EDGAR5 between 2000 and 2015. The difference between the two emission inventories, particularly the larger anthropogenic sulfur emissions in CMIP6 compared to those in EDGAR5 over the Western USA, could be a major factor contributing to the larger SO₂ concentrations simulated by EMAC compared to those observed at the CASTnet in Western USA (see panel (a) in Figure 6.2). Consequently, using the EDGAR5 emission inventory over the Western USA would likely result in smaller SO₂ concentrations in the EMAC model, thereby reducing the bias between the CASTnet measurements and the EMAC results in that region.

For the final year of the study, 2019, the used CMIP6 emission inventory within the RD1SD-base-01 simulation leads to a larger SO₂ concentration by a factor of approximately 1.6 compared to the CASTnet measurements.

6.2 Sulfur concentration and deposition in Europe

In Europe, 48 observational stations from the EMEP database are analyzed, as detailed in Section 3.2.2. Similar to the USA, these stations were selected due to the extensive data availability spanning from 2000 to 2019. Additionally, measured SO_2 concentrations in $\mu\text{g}/\text{m}^3$ and sulfur wet deposition fluxes in $\text{kg}(\text{S})/\text{ha}$ per year are provided (see Section 3.2.2). A representation of the positions of the observational stations used in Europe for this study is available in Figure 3.7 in Section 3.2.2. It is important to note that, unlike in the USA, the EMEP does not provide simulated sulfur dry deposition data.

First, the spatial distribution of SO_2 concentration over Europe from both datasets, is shown in Figure 6.3. It is important to note that the EMAC results are only shown for grid boxes where observational stations are located, which explains the presence of "empty boxes" in the EMAC model results. Here, EMAC (left panel) shows the largest SO_2 concentrations (between 4 and 8 $\mu\text{g}/\text{m}^3$) over central East Europe, with lower SO_2 concentrations (between 0.3 and 3 $\mu\text{g}/\text{m}^3$) over grid-mapped sites in the United Kingdom and Western Europe. On the other side, EMEP measures one very large SO_2 concentration (about 7.5 $\mu\text{g}/\text{m}^3$) over a grid box situated in Serbia, while showing lower SO_2 concentrations at the remaining grid-mapped sites (between 0.2 and 3.3 $\mu\text{g}/\text{m}^3$).

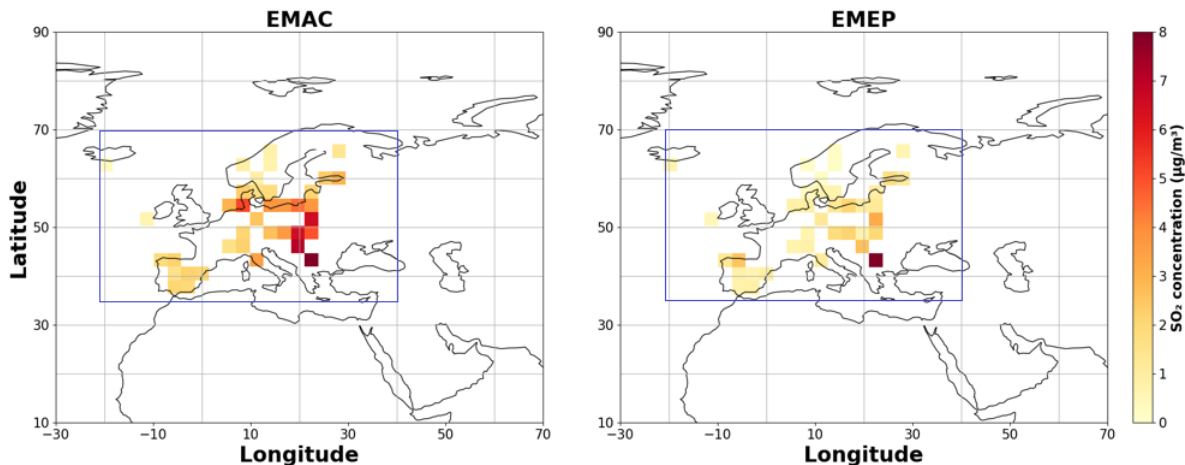


Figure 6.3: Geographical distribution of mean SO_2 concentrations for the years between 2000 and 2019 at Earth's surface as simulated with EMAC and observed at the EMEP grid-mapped sites in $\mu\text{g}/\text{m}^3$. The blue box indicates the region, where the SO_2 emissions from the CMIP6 and EDGAR5 emission inventories are compared (details see text).

Figure 6.4 illustrates the decline of SO_2 concentration across Europe, which is well captured by EMAC throughout the 20-year period (top left panel in Figure 6.4). Consequently, the temporal reduction in sulfur loss due to wet deposition is also accurately represented by EMAC (top right panel in Figure 6.4). However, the used CMIP6 emission inventory tends to produce larger SO_2 concentrations within the RD1SD-base-01 simulation compared to

observational data within the European domain (top left panel in Figure 6.4). Specifically, SO₂ surface concentrations from the model show a gradual decline between 2000 and 2012, with an annual decrease rate of $0.11 \mu\text{g}/\text{m}^3$, whereas ground-based observational data indicates a slower reduction rate of $0.04 \mu\text{g}/\text{m}^3$ per year during the same period. After 2012, both, model results and observational datasets, exhibit a more pronounced acceleration in the decline of SO₂ concentration, with rates of approximately 0.22 and $0.12 \mu\text{g}/\text{m}^3$ per year, respectively.

Over the entire 20-year period, EMAC driven by the CMIP6 emission inventory consistently shows larger annual mean surface SO₂ concentrations in Europe by a factor of approximately 1.8 compared to the EMEP dataset. Specifically, EMAC indicates larger SO₂ concentrations relative to observational data by a factor of 2 between 2000 and 2012, and with a lower factor of approximately 1.5 between 2012 and 2019. Regarding sulfur wet deposition flux, EMAC also simulates consistently larger values than EMEP by a factor of 1.3 over the entire 20-year period. Notably, a consistency is observed in the decline rates of both datasets, characterized by a yearly mean decrease of about $0.05 \mu\text{g}/\text{m}^3$ throughout the duration from 2000 to 2019. Despite the differences in SO₂ concentration and sulfur deposition flux, it is noteworthy that the model exhibits a good alignment with observational data, as shown in the temporal progression of both, SO₂ concentration and sulfur deposition flux.

Similar to the study of sulfur emissions over the USA (see Section 6.1), the prescribed CMIP6 emission inventory in Europe used by the RD1SD-base-01 simulation, shows differences in the temporal evolution of emitted sulfur compared to the EDGAR5 emission inventory (see the low panel of Figure 6.4). Note that for the calculation of sulfur emissions, the emissions from SO₂ were converted to sulfur equivalent. Here, the anthropogenic sulfur emissions (particularly from fossil fuels, ship, road, and aircraft sectors) from both emission inventories are calculated as a yearly area integral (taking into account the grid box area of the different grid boxes) between 2000 and 2019 (2015 for EDGAR5) of all model grid boxes over a region in Europe bounded by the coordinates (70°N, 40°E), (35°N, 40°E), (70°N, 22°W), and (35°N, 22°W). The chosen region is marked by a blue box, as shown in Figure 6.3. In the lower panel of Figure 6.4, an identifiable reduction of anthropogenic sulfur emissions across Europe is evident throughout the temporal evolution of both emission inventories. Specifically, the sulfur emissions in the CMIP6 inventory are 20% larger than those from the EDGAR5 inventory between 2000 and 2015 over Europe. This implies that using the EDGAR5 emission inventory would result in 20% less SO₂ being emitted in the model. Consequently, using the EDGAR5 emission inventory in Europe would likely result in lower SO₂ concentrations and therefore lower sulfur wet deposition fluxes in the EMAC model, thereby reducing the bias between the EMEP measurements and the EMAC results.

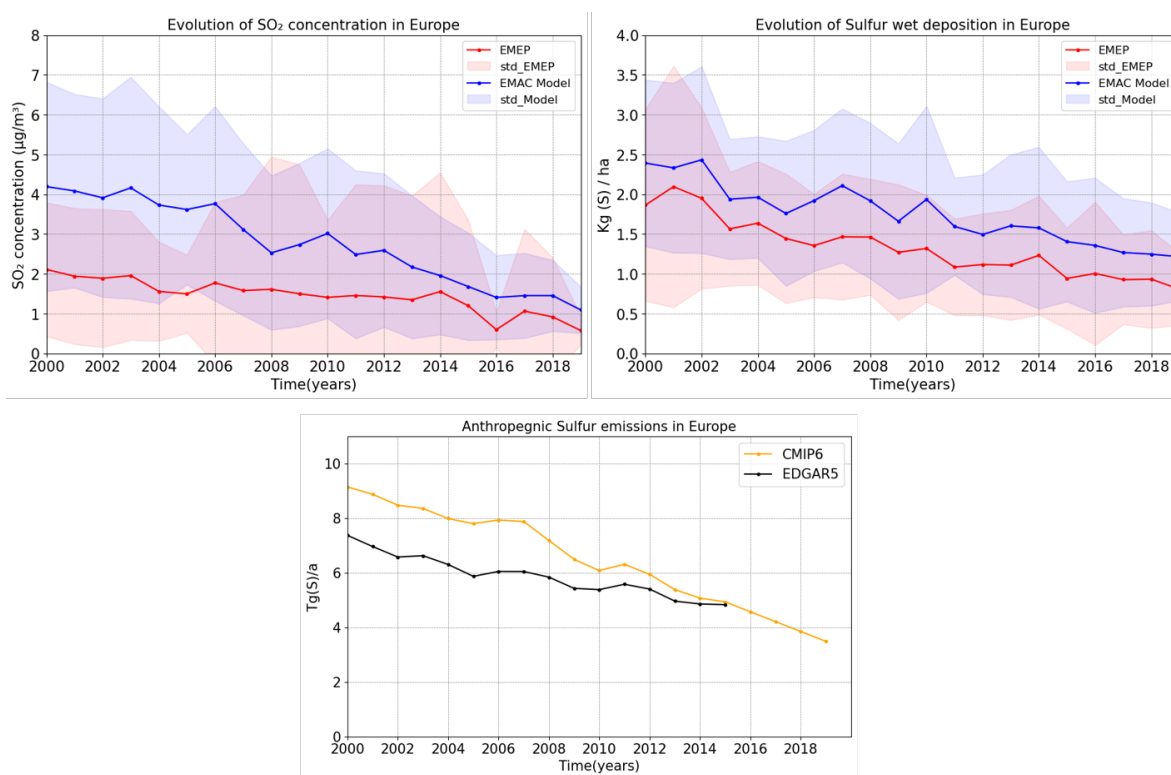


Figure 6.4: Temporal evolution of mean annual surface SO₂ concentration and sulfur wet deposition flux from EMAC (blue lines) and EMEP (red lines) between 2000 and 2019 at the grid-mapped sites in Europe (top panels). The lower panel shows the comparison between the temporal evolution of CMIP6 and EDGAR5 anthropogenic sulfur emissions as a yearly area integral between 2000 and 2019 (2015 for EDGAR5) of all the model grid boxes situated in the region marked by the blue box in Figure 6.3.

For the final year, 2019, the used CMIP6 emission inventory within the RD1SD-base-01 simulation leads to a larger EMAC SO₂ concentration by a factor of approximately 1.45 compared to EMEP measurements.

6.3 Sulfur concentration and deposition in China and Japan

In the context of East Asia, a comprehensive investigation of SO₂ and its associated processes, particularly within China, is imperative due to the substantial contribution of Chinese SO₂ emissions, which account for 64–71% of the total emissions across Asia (Kuribayashi et al., 2012). Furthermore, the pronounced enhanced SO₂ VCD values from both, EMAC model simulation and TROPOMI observational data across the East-Asia region, and especially in Northeastern China, as depicted in Figures 5.1 and 5.2 in Section 5.1, underscore the importance of this region. However, as described in Section 3.2.2, it

is complicated to find representative monitoring stations providing continuous, long-term datasets of measured SO₂ concentrations and sulfur deposition fluxes. Consequently, only 5 stations in Southeastern China and 9 over Japan from the EANET network have been selected for the present work (see Section 3.2.2). This selection was based, as for the previous networks in the USA and Europe, on long-term measurements (2000 to 2019 for this study) providing both, measured SO₂ concentration in $\mu\text{g}/\text{m}^3$ and sulfate deposited fluxes in mmol/m^2 per year in EANET (see Section 3.2.2). The geographical distribution of selected stations in China and Japan are shown in Figure 3.8 in Section 3.2.2.

In Figure 6.5, both, EMAC and EANET datasets indicate larger SO₂ concentrations at grid-mapped sites situated in China compared to those in Japan. On the right panel in Figure 6.5, EANET measures large SO₂ concentrations with a maxima of about $12 \mu\text{g}/\text{m}^3$ at three grid-mapped sites in China, while showing lower SO₂ concentrations ranging between 1 and $3 \mu\text{g}/\text{m}^3$ at the other grid-mapped sites in Japan. On the left panel of Figure 6.5, the EMAC results show overall more consistent SO₂ concentrations with one grid-mapped site in China showing around $12 \mu\text{g}/\text{m}^3$, while SO₂ concentrations at the other grid-mapped sites in China and Japan range between 2 and $8 \mu\text{g}/\text{m}^3$. This elucidates, the larger range of the SO₂ concentrations of the EANET network, compared to the smaller range of the SO₂ concentrations across the grid-mapped sites from the EMAC model. These distributions of both datasets result in corresponding larger standard deviations in the EANET measurements compared to those from the EMAC results (see the left upper panel in Figure 6.6).

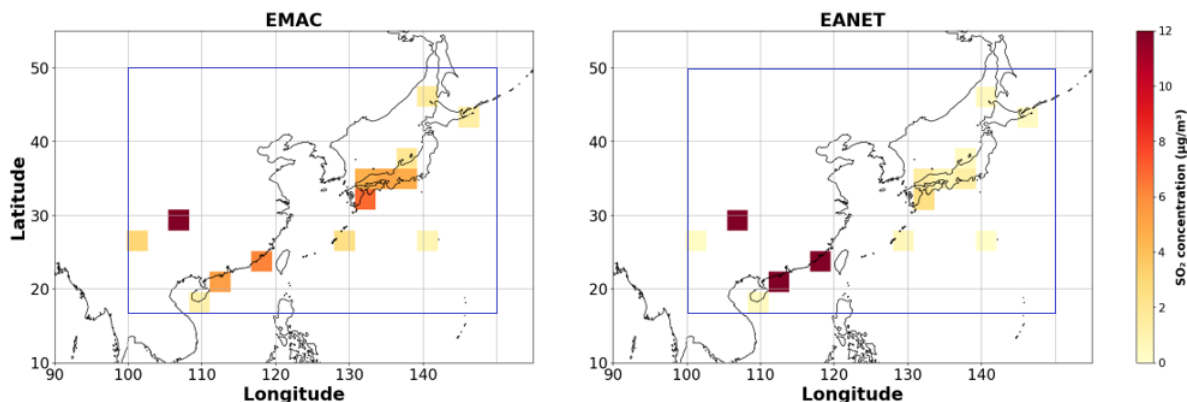


Figure 6.5: Geographical distribution of mean SO₂ concentrations for the years between 2000 and 2019 at Earth’s surface as simulated with EMAC and observed at the EMEP grid-mapped sites in $\mu\text{g}/\text{m}^3$. The blue box indicates the region, where the SO₂ emissions from the CMIP6 and EDGAR5 emission inventories are compared (details see text).

Lu et al. (2010) and Ohara et al. (2007) reported a significant increase of SO₂ emissions in China during the early 2000s, a trend confirmed by CMIP6 and EDGAR5 emission inventories, as depicted in the lower panel of Figure 6.6 (SO₂ emissions were converted to sulfur equivalent). This rise of sulfur emissions is also reflected in the SO₂ concentrations

and the deposited mass flux of SO_4^{2-} , as illustrated in the same figure (top left and top right panels, respectively). EMAC indicates an overall increase of SO_2 concentration and the deposited mass flux of SO_4^{2-} from 2000 till 2014. However, data from EANET reveals a different trend. According to the EANET network, SO_2 concentration increased until 2006 at a rate of $0.7 \mu\text{g}/\text{m}^3$ per year. On the other side, the deposited mass flux of SO_4^{2-} also increased until 2006 at a rate of $0.11 \text{ mmol}/\text{m}^2$ per year. Afterwards, a decline of SO_2 concentration by $0.5 \mu\text{g}/\text{m}^3$ per year and of the deposited SO_4^{2-} mass flux by $1.3 \text{ mmol}/\text{m}^2$ per year until 2014, was measured.

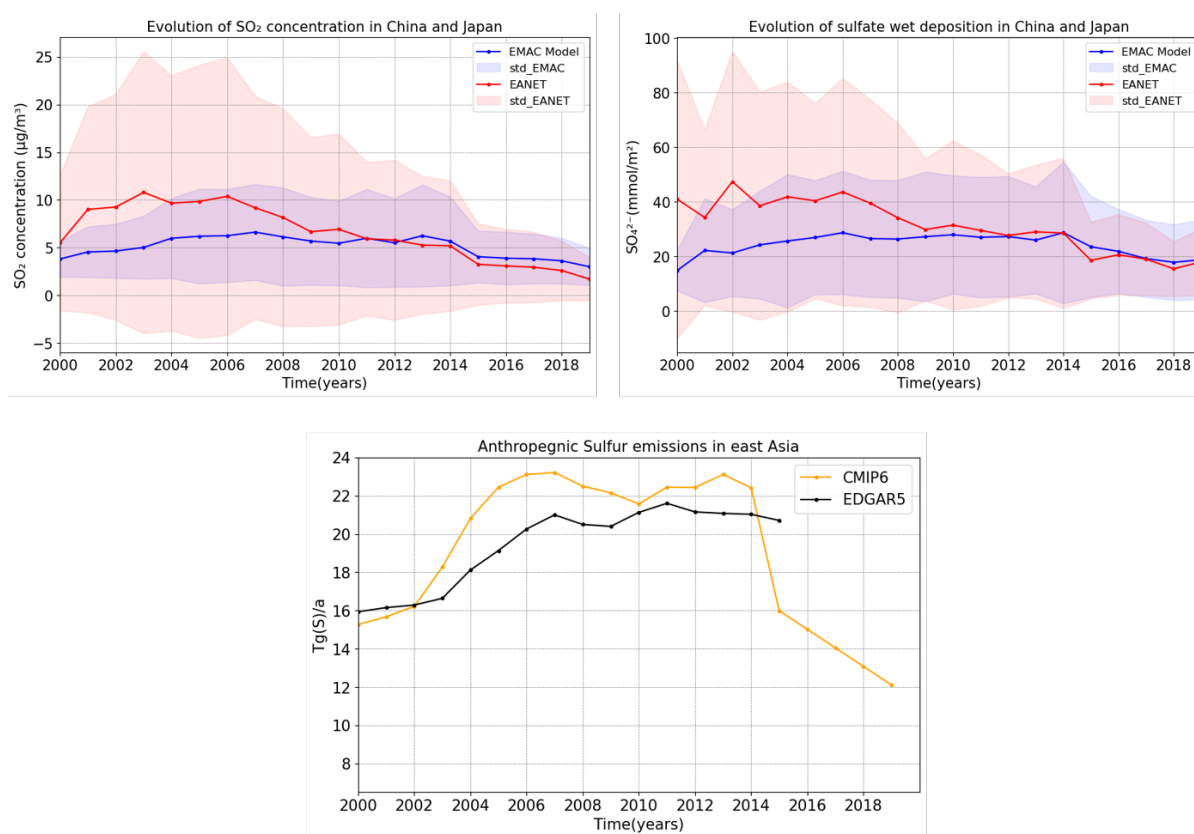


Figure 6.6: Temporal evolution of mean annual surface SO_2 concentration and sulfate wet deposition flux from EMAC (blue lines) and EMEP (red lines) between 2000 and 2019 at the grid-mapped sites in China and Japan (top panels). The lower panel shows the comparison between the temporal evolution of CMIP6 and EDGAR5 anthropogenic sulfur emissions as a yearly area integral between 2000 and 2019 (2015 for EDGAR5) of all the model grid boxes situated in the region marked by the blue box in Figure 6.5.

Following 2014, numerous reports from environmental agencies and satellite observations have consistently indicated a significant decrease of China's SO_2 emissions. Studies by Wei et al. (2023) and Ronald et al. (2016) have highlighted that SO_2 emissions in China experienced a sharp decline post-2014, nearly vanishing by 2020. This reduction in SO_2

emissions after 2014 is also noticeable in the time evolution of sulfur emissions from the CMIP6 inventory utilized in this study (low panel in Figure 6.6). From 2014 to 2019, a reduction exceeding 50% have been documented across the China-Japan region, with sulfur emissions decreasing from about 22 Tg(S)/a to 12 Tg(S)/a, within the CMIP6 emission inventory. This decline of sulfur emissions notably influences the SO₂ concentration and the deposited SO₄²⁻ mass flux over that region. Consequently, a remarkable reduction, from about 5.5 $\mu\text{g}/\text{m}^3$ of SO₂ concentrations in 2014 to approximately 3 $\mu\text{g}/\text{m}^3$ by 2019, is detected (see the upper left panel in Figure 6.6). Additionally, a good agreement is also evident between EMAC results and EANET measurements regarding the evolution of deposited SO₄²⁻ mass flux. Here, the deposited SO₄²⁻ mass flux from both datasets indicate a decrease from 28 mmol/m^2 in 2014 to 18 mmol/m^2 in 2019 (see the upper right panel in Figure 6.6).

In contrast to Europe and the USA, a comparative analysis of SO₂ concentration and the deposited mass flux of SO₄²⁻ from the RD1SD-base-01- simulation with measurements in China and Japan reveals noticeable differences in their temporal evolution. Notably, the RD1SD-base-01 simulation based on CMIP6 consistently exhibits lower SO₂ concentrations than EANET between 2000 and 2012, with a factor of approximately 1.5. Subsequently, larger SO₂ concentrations from EMAC of approximately 15% are detected in the years between 2012 and 2019. This pattern extends to sulfate deposition temporal evolution, where EMAC consistently simulates lower values than EANET from 2000 until 2014, with a factor of approximately 1.6. However, from 2014 onwards, EMAC exhibits a reversal in trend, indicating larger values than EANET measurements by approximately 10% until 2019.

In the low panel of Figure 6.6, the anthropogenic emissions from both, the used CMIP6 emission inventory and the EDGAR5 emission inventory are calculated as a yearly area integral over a region in China-Japan bounded by the coordinates (50°N, 150°E), (17°N, 150°E), (50°N, 100°W), and (17°N, 100°W). The chosen region is marked by the blue box shown in Figure 6.5. Note that for the calculation of sulfur emissions, the emissions from SO₂ were converted to sulfur equivalent.

In 2019, the used CMIP6 emission inventory within the RD1SD-base-01 simulation leads to a SO₂ concentration of 3.6 $\mu\text{g}/\text{m}^3$ compared to 2 $\mu\text{g}/\text{m}^3$ measured by the EANET network, giving a bias of 1.6 $\mu\text{g}/\text{m}^3$ and a ratio of 1.8.

6.4 Discussion and conclusion

Based on the previous detailed analysis over the USA, Europe and China-Japan, several key observations and insights emerge regarding the performance of the EMAC model in reproducing sulfur concentrations and deposition rates across those regions.

6.4.1 Evaluation of sulfur simulation in the USA and Europe

The analysis of SO₂ concentrations and sulfur deposition fluxes over the USA and Europe reveals insights into the performance of the EMAC model within these regions. Overall, EMAC demonstrates the capability of capturing the temporal trends and spatial distributions of sulfur species, across both, the USA and Europe. The comparison with ground-based measurements from the CASTnet network highlights the model's ability to replicate the observed declining trend and the historical changes in sulfur concentrations and deposition fluxes over the two-decade period from 2000 till 2019, as confirmed by Hardacre et al. (2021) and Aas et al. (2019). For the studied 20-year period, the EMAC model generally shows larger surface SO₂ concentrations over both, Europe and USA regions.

A model's tendency to overestimate atmospheric SO₂ concentrations can stem from two primary sources: insufficient removal processes, such as deposition or oxidation, and inaccurately large emissions. To address these issues, it's important to evaluate both, the chemical mechanisms and the emission inventory utilized in the model.

As mentioned earlier, the EMAC model is driven by the CMIP6 emission inventory. The choice of the emission inventory directly impacts the simulated SO₂ concentration, which in turn effects the deposition processes (see Section 3.1.9). Pope et al. (2021) reported larger SO₂ emissions in CMIP6 (115 Tg/a) by approximately 15 Tg/a, compared to EDGAR5 (Crippa et al., 2022) (102 Tg/a) and OMI-HTAP (Liu et al., 2018) (100 Tg/a). Additionally, Hardacre et al. (2021) mentioned that SO₂ emissions from CMIP6 are especially too large over the Western USA, where the largest bias in SO₂ concentration and consequently dry deposited sulfur between EMAC and CASTnet were derived.

Sulfur dry deposition in EMAC shows larger values of about 30% at Eastern USA grid-mapped sites, while indicating 100% more pronounced dry deposited sulfur over Western USA. The 30% difference over the Eastern USA is also reported by other studies, for instance by Baumgardner et al. (2002), who highlighted that the SO₂ dry deposition flux (simulated by the MLM model) from CASTnet could be up to 30% lower than direct observations. However, this means that over Western USA grid-mapped sites, EMAC still simulates more dry deposited sulfur than the CASTnet measurements. This could be explained by the earlier mentioned larger SO₂ emissions from CMIP6 over Western USA, which increase the bias between SO₂ concentration and dry deposited sulfur of EMAC and CASTnet, as described in Section 6.1.

The wet deposition in EMAC over both, Europe and the USA is in good agreement with EMEP and CASTnet networks, respectively. In Section 6.1, over the entire 20-year period, EMAC shows consistently lower sulfur wet deposition fluxes compared to the measurements networks, by about factors of about 1.1 and 1.05 over Eastern and Western USA regions, respectively. These differences in the wet deposition fluxes in the USA between the model results and the measurements could be partly attributed to the missing budget term in the SCAV submodel of the RD1SD-base-01 simulation (see Table 4.2 in Section 4.1). Over all the studied years between 2010 and 2019 (see Table 4.2 in Section 4.1), an average of 7.41 ± 0.59 Tg(S)/year deficit is calculated, where 89.80 ± 5.98 Tg(S)/year are simulated. This means that the simulated wet deposition flux needs to be scaled by a correction factor

of approximately 1.07, under the assumption that the species of the missing budget term are equally spatially and in time distributed as the explicitly resolved deposited species. By applying this correction factor, the sulfur wet deposition flux in the EMAC model would be a factor 1.07 larger, which reduces the regional bias of simulated compared to measured wet deposited sulfur fluxes over the USA. In contrast, over Europe, the EMAC model simulates sulfur wet deposition fluxes that are about 1.3 times larger than those measured by the EMEP network. These findings suggest that the larger simulated SO₂ concentrations compared to the measured data in both the USA and Europe are unlikely to be due to insufficient removal processes. Instead, the discrepancy is more likely attributable to the large CMIP6 SO₂ emissions used in the RD1SD-base-01 simulation.

Moreover, Mulcahy et al. (2020) and Hardacre et al. (2021) reported that injecting SO₂ emissions into the lowest model layer may increase the bias in surface SO₂ concentrations. Consequently, Buchard et al. (2014) demonstrated that injecting SO₂ emissions from various sectors across multiple vertical layers above the lowest model layer has enhanced the agreement between SO₂ concentrations simulated by the Goddard Earth Observing System version 5 (GEOS-5) global model, and the observational stations. In EMAC, a varying emission height is already implemented. For instance, SO₂ emissions originating from fossil fuels are injected in 45, 140, 240, 400, 600, and 800 meters, considering a more realistic emission height.

In this work comparing localized observations with the simulated values by the EMAC model on a coarse spatial resolution of approximately 300 km × 300 km, could also increase the bias between the datasets. The EMAC model's resolution may inadequately represent the transport dynamics of SO₂ in complex terrain, such as the Rocky Mountains in Western USA, amplifying biases in SO₂ concentration and dry deposited sulfur between EMAC results and CASTnet measurements. Therefore, conducting high-resolution model studies would not only enhance our understanding of local-scale SO₂ dispersion patterns but also provide insights into the accurate estimation of SO₂ losses, especially near point sources.

Finally, the RD1SD-base-01 simulation driven by the CMIP6 emission inventory shows larger SO₂ ground-concentrations than the observational networks in 2019 over both, the USA and Europe, with ratios of approximately 1.6 and 1.45, respectively. These factors align well with the differences derived between SO₂ VCDs in EMAC and those retrieved by TROPOMI (1.8 over the USA and 1.6 over Europe) (see Section 5.3). This means that the bias between the simulated and the measured SO₂ concentrations at the Earth's surface corresponds consistently to the bias between the simulated and the retrieved SO₂ VCDs. This strengthens the earlier hypothesis that the prescribed SO₂ emissions in the RD1SD-base-01 simulation might be overestimated over Europe and the USA.

6.4.2 Evaluation of sulfur simulation in China and Japan

Unlike the consistent temporal evolution of EMAC's SO₂ concentration and sulfur deposition flux over the USA and Europe, EMAC fails to capture the observed declining trend over China and Japan. From 2000 to 2014, both, SO₂ concentration and SO₄²⁻ wet deposition flux simulated by EMAC show an increase, albeit with values lower than those

measured by the EANET network. Starting from 2014, EMAC begins to show a decreasing trend similar to that observed by EANET for both, SO₂ concentrations and SO₄²⁻ wet deposition flux. Furthermore, EMAC shows larger fluxes for both, SO₂ concentrations and SO₄²⁻ wet deposition flux compared to EANET after 2014.

As discussed in Section 6.3, evaluating EMAC's performance over East Asian regions poses challenges due to limited data availability. Moreover, the comparison underscores the importance of ongoing refinement and validation efforts to enhance the predictive capabilities of atmospheric models in capturing complex regional variability and trends, especially in China.

Similar to the analysis over the USA and Europe, the RD1SD-base-01 simulation driven by the CMIP6 emission inventory shows larger SO₂ ground-concentrations in 2019 over China (specifically Southeastern China) and Japan, with a ratio of 1.8. The simulated SO₂ VCD in EMAC over Southeastern China is 2 times larger than those retrieved by TROPOMI (see Section 5.3). This indicates, like over the USA and Europe, that the bias between the simulated and the measured SO₂ concentrations at the Earth's surface corresponds consistently to the bias between the simulated and the retrieved SO₂ VCDs. This difference could be attributed to the prescribed SO₂ emissions in the RD1SD-base-01 simulation, which might be overestimated.

In conclusion, this section highlights several key findings based on the analysis of SO₂ concentrations and sulfur deposition fluxes across the USA, Europe, and parts of East Asia using the EMAC model. EMAC effectively captures temporal trends and spatial distributions of sulfur species in the USA and Europe, albeit with tendencies to overestimate surface SO₂ concentrations. The choice of the CMIP6 emission inventory significantly impacts the model performance. CMIP6's larger SO₂ emissions compared to those from the EDGAR5 emission inventory result in elevated SO₂ concentrations, particularly over the Western USA and Europe, where discrepancies with ground-based measurements are most pronounced. Challenges in modeling sulfur over East Asia underscore data limitations, yet EMAC generally reproduces trends of SO₂ concentrations and sulfur deposition fluxes, though improvements are needed. High-resolution modeling is recommended to better resolve local-scale transport dynamics and refine emission estimates. Furthermore, other factors, such as the sulfur chemistry in the model (i.e. oxidation and dry/wet deposition processes) must be considered to minimize the bias, when comparing model results to observational data. Overall, this analysis provides insights into EMAC's strengths and limitations, suggesting future model refinement and validation to enhance understanding of sulfur chemistry and support environmental policy decisions.

Chapter 7

Analysis of SO₂ from MECO(n) compared to airborne measurements

Previous comparisons of the CCM EMAC simulation results against global and regional measurements, such as measurements from space covering the entire globe (see Section 5), as well as the comparison with ground-based measurements over regional areas such as Europe, the USA, and China-Japan (see Section 6), have provided valuable insights into the spatial, temporal and vertical distribution of atmospheric SO₂ as simulated by the CCM. This approach has revealed important information about the major sources of SO₂ emissions, both, anthropogenic and natural, that contribute to atmospheric SO₂ and highlighted the SO₂ deposition processes (such as dry and wet depositions) within the EMAC model. Conducted over the entirety of 2019 for comparisons with TROPOMI/Sentinel-5P satellite data and spanning a 20-year period from 2000 to 2019 for ground-based measurements, these comparisons offer an understandable analysis of atmospheric SO₂ processes, particularly in the troposphere.

In contrast to the previous analysis, which utilized the global EMAC model, this section employs the 4th instance of the global/regional MECO(n) model system (MECO(3)), with a resolution of 0.01° (~2.8 km, time step length 30 s), as outlined in Section 3.3.3. MECO(n) is specifically suitable for regional comparisons over small areas with high temporal and spatial resolutions. Therefore, it is applied in the present investigation with airborne measurements derived from the DLR Falcon aircraft during the METHANE-To-Go-Europe campaign, as detailed in Section 3.2.3 and by Huntrieser et al. (2023). Here, the focus shifts towards a more localized comparison over a smaller time-frame, aiming to analyze SO₂ mixing ratios above specific SO₂-emitting point sources. This section deals with the analysis of the flight conducted during the METHANE-To-Go-Europe campaign, which took place in October and November 2020, specifically flying through the plumes of the Nikola Tesla A and B (TESLA_A and TESLA_B) power plants in Serbia on the 7th November 2020.

The evaluation in this section differs from the analyses conducted for the comparisons with satellite and ground-based measurements. Here, the interest shifts towards a highly localized examination of SO₂ emissions from specific point sources over a significantly

shorter time-frame of approximately 2 hours.

7.1 SO₂ mixing ratios at flight levels over power plants in Serbia

The airborne measurements conducted during the campaign are simulated by the MECO(n) model system, aligning with identical measurement periods and flight trajectories, as described in the methods section (see Section 3.3.3).

As mentioned by Huntrieser et al. (2023) and in Section 3.2.3, the quantification of SO₂ mixing ratios is conducted utilizing the CIMS and the Thermo Scientific 43i instruments installed onboard the DLR Falcon (D-CMET) aircraft. However, none of the measurements instruments operated properly during the probing of the Tuzla power plant on the 2th November 2020, and therefore, the results from this flight are not examined. In this work the evaluation of SO₂ mixing ratios is focused on the flight measurements conducted on the 7th November 2020, over the Nikola TESLA_A and TESLA_B power plants in Serbia. The emitted SO₂ mass and the emission heights are prescribed by the E-PRTR database (see Section 3.1.12). For the studied power plants, the emission heights in MECO(n) are situated at about 220 m for TESLA_A, and 280 m for TESLA_B above the surface, as mentioned in Section 3.3.3.

It is important to note that even during the flight over the Nikola Tesla power plants, the CIMS instrument encountered difficulties in measuring large SO₂ mixing ratios and the Thermo Scientific 43i instrument featured the problem of frequent data gaps. To address this issue, the SO₂ mixing ratios measured by the CIMS instrument were corrected using the Thermo Scientific 43i instrument, based on laboratory experiments (personal communication with Harlass, 2022; see Section 3.2.3). In these experiments, SO₂ mixing ratios between 1 and 250 parts per billion (ppb) were injected to both, the CIMS and Thermo Scientific 43i instruments. The Thermo Scientific 43i demonstrated good linearity with the injected SO₂ mixing ratios, whereas the CIMS instrument did not exhibit a linear relationship and became saturated at approximately 80 ppb. Consequently, the SO₂ mixing ratios measured by the CIMS instrument need to be multiplied with correction factors to align with those measured by the Thermo Scientific 43i instrument, as detailed in Table 7.1:

SO ₂ injection in ppb	Correction factor
≤ 80	1
80 – 130	1.5
130 – 180	2
> 180	2.5

Table 7.1: Shown are the correction factors for the CIMS instrument to the corresponding injected SO₂ mixing ratios in ppb (personal communication with Harlass 2022).

As previously mentioned in the methods section, the CIMS instrument has a temporal resolution of 3 s (see Section 3.2.3), while the 4th instance of the MECO(n) (MECO(3)) model operates with a temporal resolution of 30 s (see Section 3.3.3). Therefore, to ensure compatibility and reduce noise that could arise from high-frequency measurements (every 3 s), the CIMS measurements are averaged to match the MECO(n) time step length. Consequently, throughout this work only the averaged and corrected SO₂ mixing ratios measured by the CIMS instrument are evaluated. Figure 7.1 shows a comparison between the simulated SO₂ mixing ratios and the measured SO₂ mixing ratios (averaged and corrected SO₂ mixing ratios measured by the CIMS instrument) for the flight conducted on the 7th November 2020, over the Nikola TESLA_A and TESLA_B power plants in Serbia.

On the 7th November 2020, the airborne measurements (averaged and corrected CIMS measurements) captured notably larger SO₂ mixing ratios (blue lines), peaking around 500 ppb, compared to the simulated SO₂ mixing ratios (green lines) of approximately 60 ppb, indicating a factor of 8 difference. These signals were particularly detected around 14:30 UTC, corresponding to the period during which the aircraft tried to measure the SO₂ plume emitted from the power plants. At around 13:50 UTC the airborne measurements detected an SO₂ signal of about 450 ppb, which was not simulated by the MECO(n) model system.

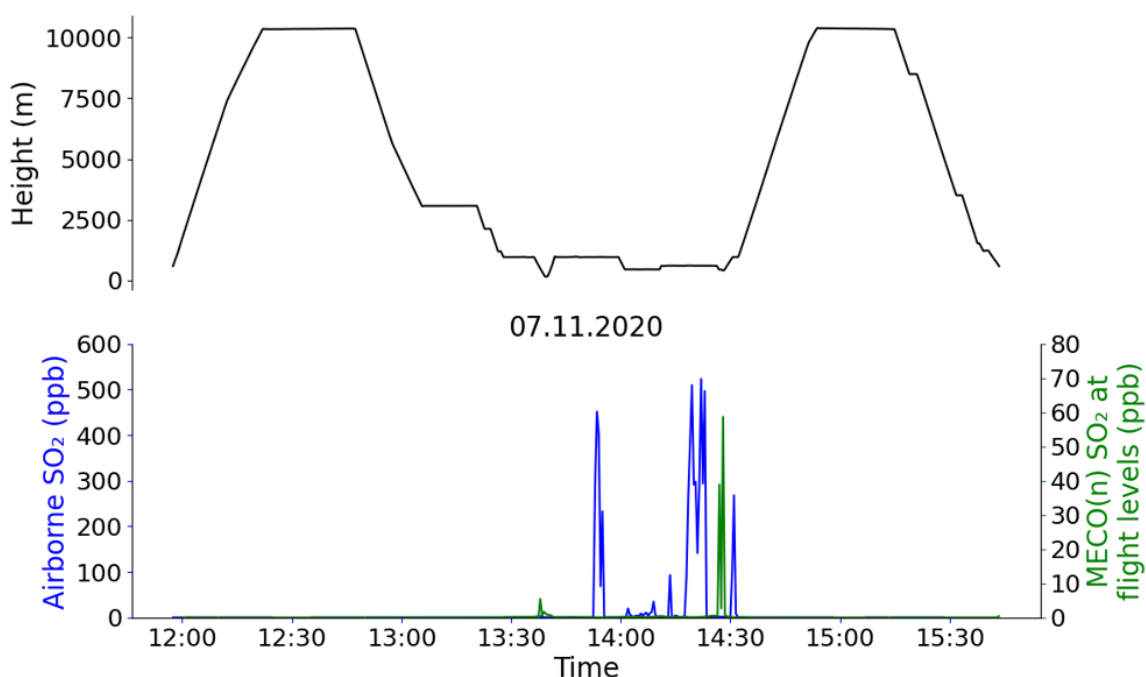


Figure 7.1: Shown are the simulated (green lines) and measured (blue lines) SO₂ mixing ratios in ppb (with a temporal resolution of 30s) corresponding to the time and altitude levels of the Falcon aircraft's flight. Flight altitude levels (in meters) are indicated by black lines in the upper panel. The lower panel shows the analysis of the flight undertaken on the 7th November 2020 over the Nikola Tesla power plants in Serbia. Note that the airborne SO₂ mixing ratios are measured by the CIMS instrument and corrected based on Table 7.1.

The examination of this flight underscores the challenges faced by the MECO(n) model system in accurately reproducing elevated SO₂ mixing ratios at flight altitudes above highly emitting power plants. For a better understanding of the SO₂ plume distribution in MECO(n) originating from the examined power plants, Figure 7.2 provides a geographical map for the study case on the 7th of November 2020.

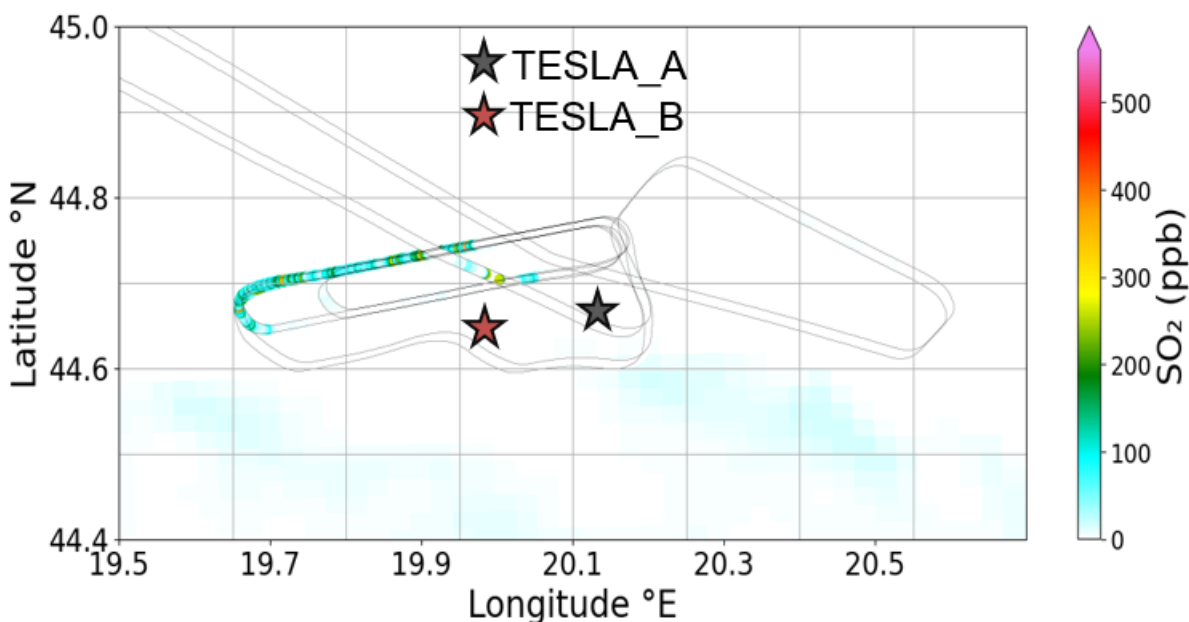


Figure 7.2: Geographical map of SO₂ mixing ratios in ppb from both, MECO(n) results and airborne measurements (colored SO₂ signals alongside the flight track). SO₂ mixing ratios simulated by MECO(n) are presented at the middle flight altitudes over the Nikola Tesla power plants, i.e. 750 m. The figure shows the analysis of the flight undertaken on the 7th November 2020 over the Nikola Tesla power plants in Serbia. The stars present the position of the power plants in Serbia.

The presented SO₂ mixing ratios from the MECO(n) model system are sampled at approximately 750 m height, corresponding to the middle flight altitudes over the Nikola Tesla power plants. Measured SO₂ mixing ratios from the Falcon aircraft are displayed alongside the flight route. Consistent with the time plots in Figure 7.1, notably low SO₂ mixing ratios from MECO(n) of approximately 60 ppb are detected on the 7th of November 2020 (shown by cyan color). Conversely, the corrected CIMS instrument onboard the DLR Falcon measures larger SO₂ mixing ratios of about 200 ppb and 600 ppb, which are measured along the flight tracks over the Nikola Tesla power plants (Figure 7.2).

To examine the factors contributing to the low simulated SO₂ mixing ratios over the power plants in Serbia, a curtain plot is produced to study the vertical distribution of SO₂ mixing ratios throughout the atmospheric column during the time of the measurement flight. Figure 7.3 shows the evolution along the flight track of simulated SO₂ mixing ratios with the altitude. Notably, on the 7th November 2020, the SO₂ mixing ratios only reach a peak altitude of around 300 meters above the point sources during the time of measurement. This altitude is actually below where the Falcon aircraft was measuring during that day (flight levels between approximately 400 and 1000 meters). This limitation is attributed to the boundary layer height (BLH) simulated by the MECO(n) model system (depicted by the orange solid line in Figure 7.3), which fluctuates within the range of 200 to 300

meters. Conversely, the BLH estimates derived from ERA5 (blue solid line in both panels) and the Falcon aircraft data (green dashed line) are positioned higher in the atmosphere, ranging between 500 and 900 meters on the 7th November 2020. Essentially, the model's boundary layer (BL) acts as a cover, limiting the SO₂ mixing ratios below it and hindering their upward dispersion. This explains the low simulated SO₂ mixing ratios at the flight levels, shown in Figures 7.1 and 7.2.

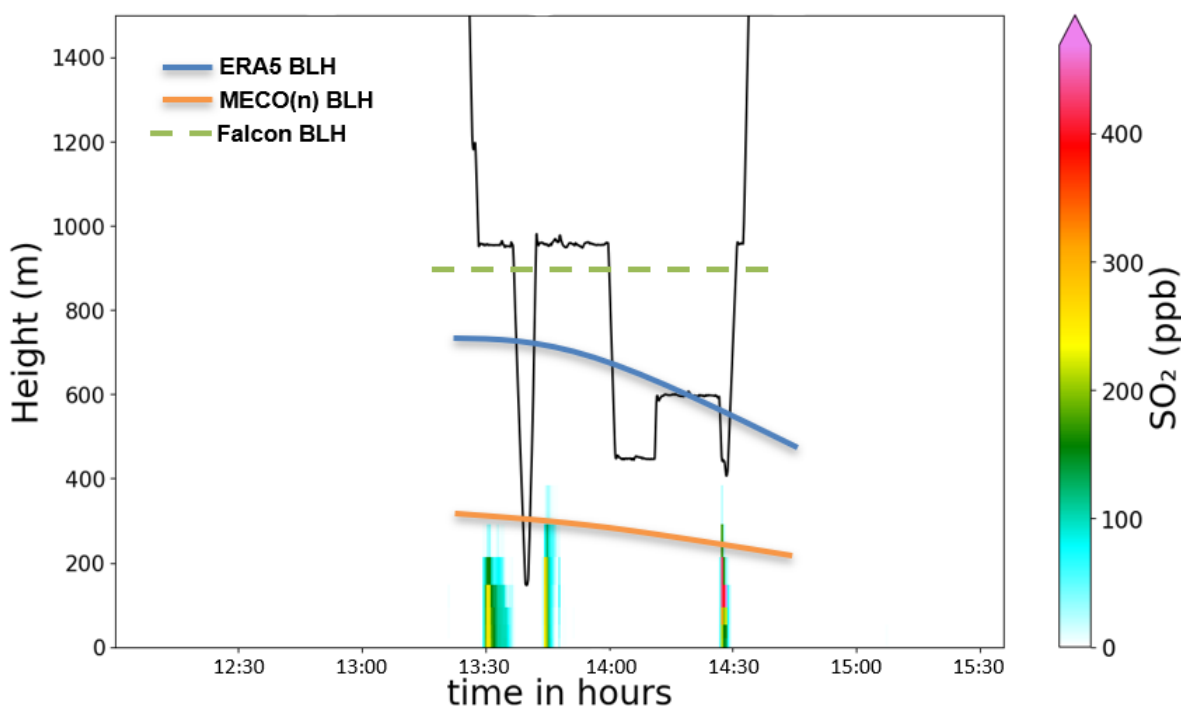


Figure 7.3: Curtain plot illustrating the vertical distribution of simulated SO₂ mixing ratios in ppb (color bar) alongside the flight route (black solid line). The SO₂ mixing ratios above the Nikola Tesla power plants are shown. The boundary layer height (BLH) from ERA5 and MECO(n) are depicted by blue and orange solid lines, respectively, whereas the BLH measured from the Falcon aircraft is represented by the green dashed line.

To verify this hypothesis, the analysis extends to examine the simulated SO₂ mixing ratios within the boundary layer, as described in detail in the upcoming section.

7.2 SO₂ mixing ratios within the boundary layer in Serbia

In this section, the SO₂ mixing ratios within the boundary layer (BL) of the MECO(n) model system are examined. For this, an evaluation of SO₂ mixing ratios at an altitude of about 200 meters above the surface is conducted, as shown in Figure 7.4. Consequently,

larger SO₂ mixing ratios (represented by red lines in Figure 7.4) are simulated by the MECO(n) model system compared to previously simulated SO₂ mixing ratios at the flight levels (represented by green lines in Figure 7.4) on the 7th November 2020. The simulated SO₂ mixing ratios within the BL (red lines) are around 550 ppb, compared to 60 ppb simulated by MECO(n) at the flight levels (green lines) at approximately 14:30 UTC. This means, that simulated SO₂ mixing ratios are larger by a factor of about 9 compared to simulated SO₂ mixing ratios at flight levels.

As a result, the simulated SO₂ mixing ratios within the BL (red lines) indicate maximum SO₂ mixing ratios of about 550 ppb on the 7th November 2020, which align more closely with the measured SO₂ mixing ratios (blue lines). Notably, unlike the simulated SO₂ mixing ratios at flight levels (green lines), the simulated SO₂ mixing ratios within the BL (red lines) successfully reproduce both the signals measured by the CIMS instrument between 13:30 and 14:00 UTC, as well as around 14:30 UTC. It is important to emphasize that a direct comparison between simulated SO₂ mixing ratios within the BL (red lines) and the airborne measurements (blue lines) is not feasible. This is because the MECO(n) SO₂ mixing ratios are simulated at a lower altitude in the atmosphere (approximately 200 meters within the boundary layer) while the airborne SO₂ measurements are executed at higher altitudes, between approximately 400 and 1000 meters above the surface.

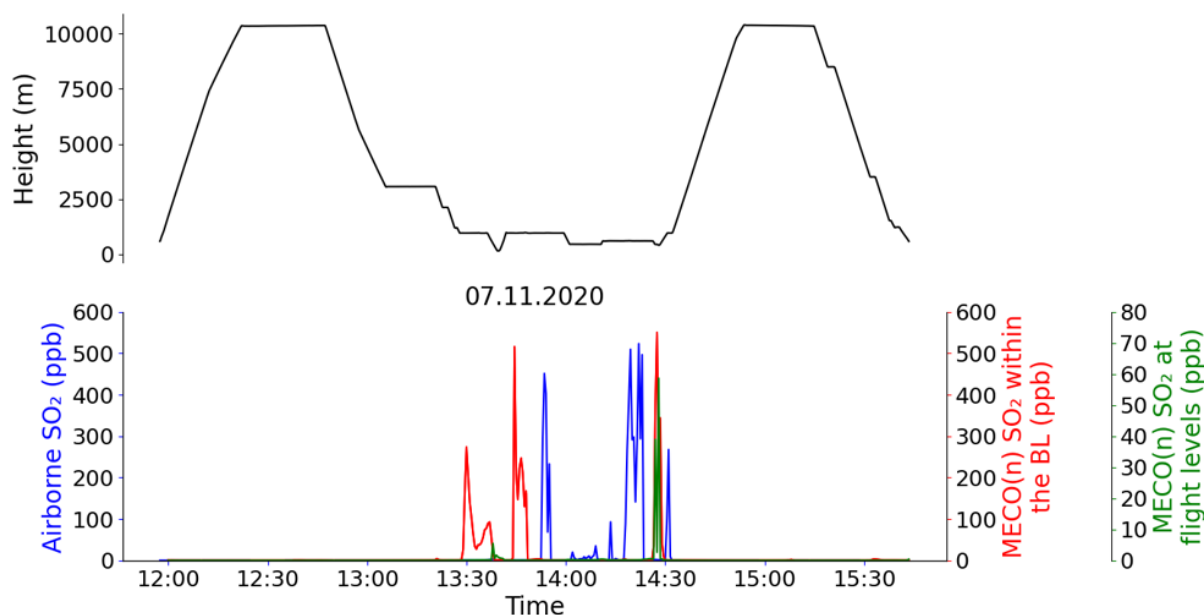


Figure 7.4: Shown are the simulated SO₂ mixing ratios in ppb within the BL (red lines), as well as simulated and measured SO₂ mixing ratios in ppb at flight altitudes during the time of measurements (green and blue lines, respectively). Flight altitude levels (in meters) are indicated by black lines in the upper panel. The lower panel illustrates the case study of the flight conducted on the 7th November 2020 over the Nikola Tesla power plants in Serbia.

Consequently, Figure 7.5 illustrates the spatial distribution of the simulated SO₂ mixing ratios within the boundary layer (lower panel) and at flight levels (upper panel) on a geographical map. In this case, it is evident that the point sources for TESLA_A, and TESLA_B, as well as the corresponding SO₂ plumes are clearly identifiable for the simulated SO₂ mixing ratios within the boundary layer (lower panel in Figure 7.5). This is unlike the spatial distribution of simulated SO₂ mixing ratios at flight levels (upper panel in Figure 7.5), where no identification of the point sources or the SO₂ plumes is possible. Figure 7.5 also highlights the enhanced simulated SO₂ mixing ratios within the boundary layer over the Nikola Tesla power plants (lower panel) exceeding 600 ppb.

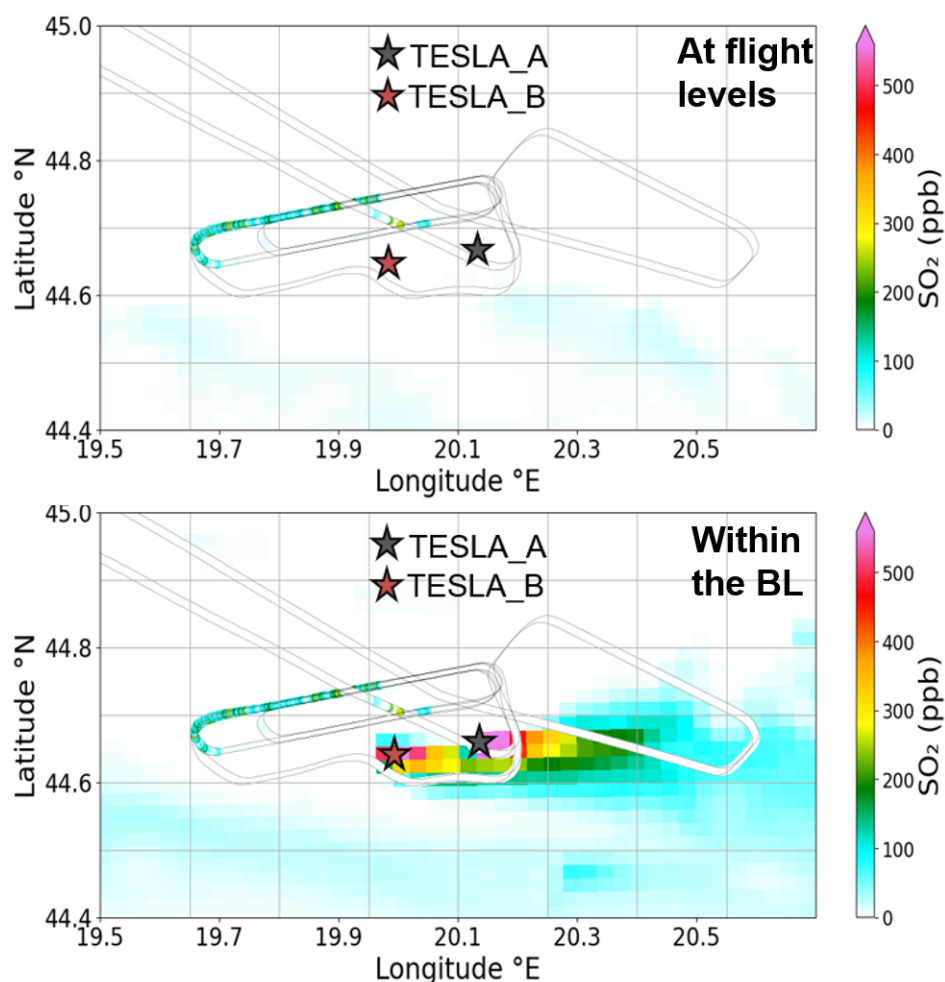


Figure 7.5: Geographical map of the SO₂ mixing ratios in ppb from both, MECO(n) and airborne measurements (colored SO₂ signals alongside the flight track). The upper panel illustrates the previously presented SO₂ mixing ratios in MECO(n) at flight levels in Figure 7.2. The lower panel shows the simulated SO₂ mixing ratios by MECO(n) within the boundary layer at about 200 meters above the surface. Both panels present the analysis of the flight undertaken on the 7th November 2020 over the Nikola Tesla power plants in Serbia. The stars present the position of the studied power plants in Serbia.

This confirms the hypothesis presented in Section 7.1 that the low simulated SO₂ mixing ratios by MECO(n) at the flight levels are attributed to the low planetary boundary layer in the model, which hinders the SO₂ from reaching higher altitudes in the atmosphere. Consequently, the enhanced SO₂ mixing ratios can only be detected within the boundary layer, as illustrated in Figures 7.4 and 7.5.

7.3 Discussion and conclusion

The analysis of the SO₂ mixing ratios from the MECO(n) model system compared to airborne in situ measurements during the METHANE-To-Go-Europe campaign provides important insights into the model's performance and limitations.

For the measurement flight on the 7th November 2020, noticeable differences between the simulated and measured SO₂ mixing ratios at flight altitudes were derived. The MECO(n) model system simulates approximately 8 times smaller SO₂ mixing ratios at flight altitudes over the Nikola Tesla power plants, compared to measured and corrected values by the CIMS instrument (see Figures 7.1 and 7.2). These discrepancies highlight the challenges faced by the MECO(n) model system in accurately simulating SO₂ mixing ratios from specific point sources, particularly at higher altitudes. Consequently, the curtain plot (see Figure 7.3) revealed that the MECO(n) model's BLH is significantly lower than the BLH estimated from ERA5 reanalysis and the Falcon aircraft data. This discrepancy suggests that the MECO(n) model system may inaccurately represent and define the BLH. This issue has been extensively documented and discussed in the scientific literature, indicating a common challenge in atmospheric modeling. Lee and Ngan (2011); Zhang et al. (2014); Morgenstern et al. (2017) and Liu et al. (2023) highlight the challenges and uncertainties in accurately representing the boundary layer in Chemistry-Climate Models (CCMs). This limitation in the BLH presentation results in preventing the SO₂ from reaching higher altitudes, especially there where the aircraft measure. For this, further SO₂ analysis within the boundary layer (approximately 200 meters above the surface) are made, showing larger SO₂ mixing ratios (see Figures 7.4 and 7.5), compared to the SO₂ mixing ratios at the flight levels (see Figures 7.1 and 7.2). This explains, that the low simulated SO₂ mixing ratios at flight levels are primarily due to the boundary layer limitation within the MECO(n) model system. This indicates that in reality, the aircraft is measuring directly within the boundary layer, while in the model, the aircraft is flying significantly above the simulated boundary layer, capturing only very low SO₂.

It is noteworthy that slight temporal differences between the simulated and observed SO₂ mixing ratios were also noticed in both cases, as shown in Figures 7.1 and 7.4. These discrepancies arise from minor variations in wind speed and direction between the model results and airborne measurements, as illustrated in Figure 7.6. Between 13:30 UTC and 14:30 UTC, when the aircraft was attempting to measure near the power plant plumes, both the model and the Falcon measurements consistently show weak wind speeds below 5 m/s (panel (b) in Figure 7.6). During this time frame, where the wind speed is low, the wind direction deviates significantly (panel (c) in Figure 7.6). However, at such low wind speeds, the direction becomes arbitrary, as the airflow lacks the strength to maintain a consistent trajectory, thus minimizing its influence on the measurement outcomes.

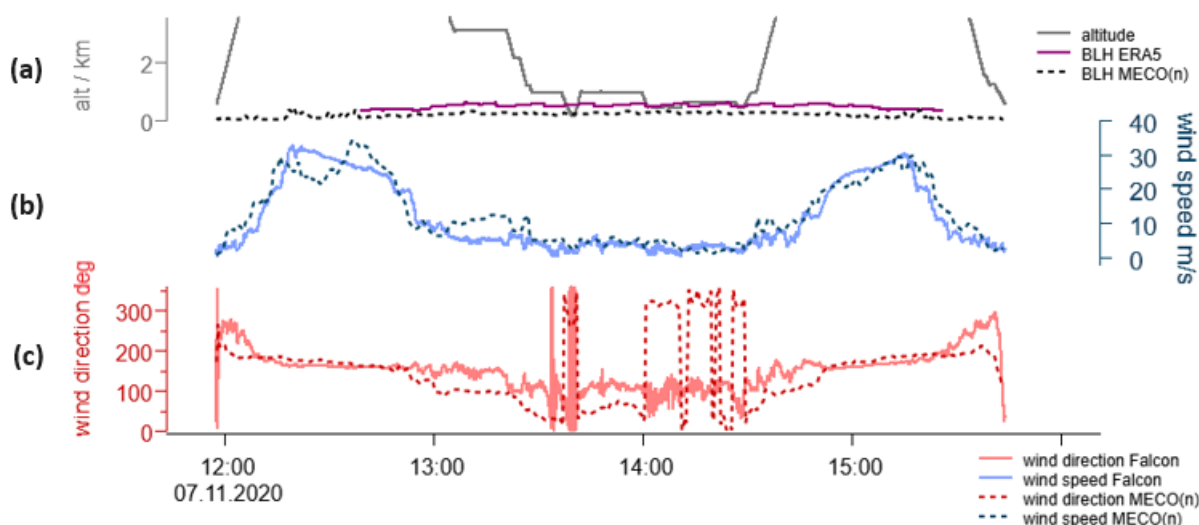


Figure 7.6: Shown are the simulated (MECO(n)) and the measured (DLR Falcon aircraft) wind speed (panel (b)) in meters per seconds (m/s) and wind direction (panel(c)) in degrees (deg) along the flight route (panel (a)) on the 7th November 2020 over the Nikola Tesla power plants.

This analysis further supports the previous hypothesis that the main challenge and limitation in the MECO(n) model system is associated with the boundary layer height.

As a conclusion, the localized comparison of SO_2 mixing ratios from the MECO(n) model system against airborne in situ measurements during the METHANE-To-Go-Europe campaign reveals significant limitations and challenges in reproducing SO_2 mixing ratios at flight altitudes above major point sources, primarily due to an inaccurate representation of the simulated BLH. This section highlighted the importance of accurately representing the boundary layer in atmospheric models to improve the simulation of pollutant dispersion.

This work also underscores the significant ratios between the simulated SO_2 mixing ratios within the model's boundary layer and at aircraft flight levels. These findings emphasize the need to improve the model's representation of boundary layer height, especially for regional air quality assessments. By addressing this in future studies, models can better reproduce the vertical dispersion of pollutants such as SO_2 , thereby providing more accurate data.

Finally, the conducted comparisons between the MECO(n) model system results and Falcon measurements at flight levels (see Figures 7.1 and 7.2) are highly challenging due to the differing small-scale temperature and wind conditions. More accurate comparisons can be achieved by evaluating VCDs, as demonstrated by Huntrieser et al. (2023). VCD comparisons are less dependent on these small-scale structures and can also be effectively compared with satellite data.

Chapter 8

Conclusions and Outlook

With the objective of targeting the general research question regarding the global distribution and behavior of sulfur dioxide in the atmosphere, particularly in the troposphere, this chapter answers the detailed research questions (RQs) formulated in Section 1.2 and summarizes the major findings described in detail in the previous four chapters. To recap, Chapter 4 presents the basis of the analysis conducted in this work by assessing the sulfur budget in the EMAC model simulation (RD1SD-base-01). Furthermore, Chapter 5 shows a comparison between the SO₂ vertical column densities (VCDs) in the RD1SD-base-01 simulation and the satellite measurements; globally and for two cases of eruptive volcanic events. Additionally, Chapter 6 evaluates the SO₂ concentration and sulfur deposition fluxes against ground-based measurements over the USA, Europe and China-Japan. Finally, Chapter 7 examines the SO₂ mixing ratios in the MECO(n) model compared to airborne measurements over specific power plant sources.

In the following text, comprehensive answers are presented with respect to the research questions raised in the beginning of this thesis, summarizing the major findings of this work.

RQ 1: How well do we understand the tropospheric sulfur budget, and how do contemporary emission inventories represent SO₂ emissions?

The sulfur budget within the EMAC RD1SD-base-01 model simulation is analyzed in this work, using prescribed SO₂ emission data from the CMIP6 emission inventory. Anthropogenic sources, particularly the combustion of fossil fuels, represent the primary contributor to tropospheric SO₂ emissions with about 50%. This is consistent with existing literature (Section 2.2.1).

As RD1SD-base-01 simulation results show, released SO₂ is subsequently removed from the troposphere through wet and dry deposition. For the RD1SD-base-01 simulation setup, a sulfur budget deficit is consistently visible in results for all the studied years between 2010 and 2019. To address this issue, a sensitivity simulation is performed where all sulfur species are explicitly considered in the aqueous phase. This sensitivity simulation achieves

a mass balance within the model, resulting in a nearly complete sulfur budget closure. The deficit in the standard setup can thus be attributed to incomplete diagnostics, i.e. missing output of liquid deposition fluxes. For further analysis, the sulfur budget of the EMAC RD1SD-base-01 simulation is compared with the budget of the STOCHEM-Ed simulation (Stevenson et al., 2003) and the Intergovernmental Panel on Climate Change Third Assessment Report (IPCC AR3) (Penner et al., 2001) for the year 1990. This comparison demonstrates the validity of the prescribed SO_2 emissions in EMAC and the simulated sulfur deposition fluxes compared to the STOCHEM-Ed model and the IPCC AR3.

Finally, it is important to note that the RD1SD-base-01 simulation does not include any aerosol interactions. To investigate the effects of aerosols on SO_2 , two sensitivity simulations based on the EMAC model instance of the MESSy-fied ECHAM and COSMO models nested n -times (MECO(n)) are conducted: one with and another without an interactive aerosol submodel. The results indicate a minimal difference in SO_2 mixing ratios between the two simulations, with a variation between 1% and 2.5%. Consequently, the EMAC simulation without an interactive aerosol submodel is utilized further in this study to reduce computation time.

RQ 2: *What is the global distribution of atmospheric SO_2 , and can anthropogenic and natural emission hotspots be identified with observations from satellite instruments? Do state-of-the-art CCM simulations represent these hotspots correctly?*

For a comprehensive global evaluation of the simulated SO_2 VCDs within the EMAC RD1SD-base-01 model simulation for the year 2019, data from the TROPospheric Monitoring Instrument (TROPOMI) onboard the Sentinel-5P satellite is utilized in this study. For this evaluation, SO_2 VCDs from both datasets were derived for a standard case of polluted profiles by using the polluted averaging kernel (AK_polluted) (see Section 3.3.1). The retrieved TROPOMI measurements and the respective EMAC results are consistent in identifying the geographical distribution of both, natural and anthropogenic emission hotspots on a global scale. Differences between satellite observations and model results were identified, which can be attributed to the unaccounted emissions of explosive volcanic eruptions in the emission inventories.

Nevertheless, significant discrepancies in magnitude exist between SO_2 VCDs from EMAC results and those retrieved from TROPOMI on a global scale. The strongest SO_2 emission hotspots are located in the Northern Hemisphere, where industrial activity is concentrated, and volcanic activity is more prevalent. For instance, the RD1SD-base-01 simulation indicates larger SO_2 VCDs compared to those retrieved from TROPOMI by factors of 7, 6, 5, and 2.5 over Etna, Tajumulco, Mount Fuji, and Nevado Ojos del Salado volcanoes, respectively. These differences are attributed to prescribed emissions in the AeroCom volcanic emission inventory used within EMAC, which may not accurately reflect the actual volcanic activity. Regarding anthropogenic emission sources, the EMAC RD1SD-base-01 simulation results show a good agreement with the TROPOMI retriev-

als over background regions such as central Africa and the South Atlantic Ocean, with differences of about 10% and 20%, respectively. However, over more heavily polluted regions, such as Europe, the USA, Southeastern and Northeastern China, the EMAC results indicate larger SO₂ VCDs by factors of 1.6, 1.8, 2, and 3.2 respectively.

These discrepancies vary depending on the emission source type, the emission source height, and the regions analyzed. Future work should focus on refining emission inventories and their representation of vertical profiles, particularly for volcanic sources. Additionally, it is important to note that the satellites face challenges in measuring the SO₂ signal near the Earth's surface. The signal received on a satellite is weakened by scattering and absorption by molecules and aerosols throughout the atmospheric column, reducing its ability to accurately detect trace gases near the surface. The insights gained from this study contribute to advancing our knowledge of the global SO₂ distribution and underscore the importance of continued efforts to refine observational capabilities for monitoring atmospheric composition.

RQ 3: *How does the emitted and deposited mass of SO₂ evolve over time following an eruptive volcanic event?*

The eruption of the Raikoke and Ulawun volcanoes in June 2019, observed by the TROPOMI instrument, provide an important natural event for a sensitivity simulation case study on the effects of such large eruptions on the emitted and deposited SO₂ mass in the EMAC model. In this study, three different sensitivity simulations, based on the previously used RD1SD-base-01 simulation, are conducted to determine which simulation best represents the retrieved emitted SO₂ mass. The raik-02 and raik-03 simulations differ in the emitted SO₂ mass and the injection heights of the Raikoke volcano, while the raik-04 simulation considers both the Raikoke and Ulawun eruptions (see Table 5.2 in Section 5.2). For this case study of eruptive volcanoes emitting into the stratosphere, the SO₂ VCDs for a 15 km box profile case (reflecting an explosive volcanic eruption case) are derived for both, EMAC and TROPOMI. The raik-04 simulation shows the best agreement among the sensitivity simulations, following the same temporal evolution and decay rate of the retrieved TROPOMI SO₂ mass during three weeks after the Raikoke eruption on 22-23 June 2019. Additionally, the SO₂ deposition after the Raikoke eruption in raik-02 and raik-03, and after both, the Raikoke and Ulawun eruptions in raik-04, exhibits different rates. These differences are related to the amount of emitted SO₂ mass and the prescribed emission profiles. In all three sensitivity simulations, the emitted SO₂ mass is subsequently deposited adequately, confirming the EMAC model's capability in conserving mass, as described in Section 4.1.

The results demonstrate the importance of accurately representing vertical emission profiles in CCMs. Based on the inter-comparison of observed (TROPOMI retrieved) and simulated (EMAC) decay rates for SO₂ mass after the two volcanic eruptions, it can be concluded that the tropospheric residence time of SO₂ is well simulated by EMAC.

RQ 4: *What are the spatial patterns and long-term temporal trends of SO₂ concentrations and deposition fluxes of sulfur-containing species at the Earth's surface in highly polluted regions of the world (USA, Europe, and East Asia)?*

The simulated SO₂ concentrations near the Earth's surface and deposited sulfur particles reproduce the declining trend measured by the ground-based networks between 2000 and 2019 in both, the USA and Europe. However, the simulated temporal evolution over China and Japan do not reproduce the trend measured by the Acid Deposition Monitoring Network in East Asia (EANET) network for the same period. Additionally, both, the EMAC RD1SD-base-01 model simulation and the ground-based measurements, indicate the same hotspot emission sites in these regions. In the USA, the Eastern observational sites (East of 100°W) show larger SO₂ concentrations compared to the Western observational sites (West of 100°W) in both datasets. Similarly, in Europe, Eastern regions, particularly around the Balkan area, exhibit larger SO₂ concentrations near the Earth's surface compared to Western Europe. In the studied East Asian region, larger SO₂ concentrations are simulated by EMAC and measured by the EANET ground-based network over observational sites in China compared to Japan for the studied period.

The RD1SD-base-01 simulation used in this work is driven by the CMIP6 emission inventory, which results in larger simulated SO₂ concentrations at the Earth's surface compared to the observational networks in 2019 over the USA, Europe, and China-Japan with ratios of approximately 1.6, 1.45, and 1.8, respectively. These factors align well with the bias derived between the simulated SO₂ vertical column densities (VCDs) in EMAC and those retrieved by TROPOMI (factor 1.8 over the USA, 1.6 over Europe and a factor of 2 over Southeastern China). This implies that the bias between the simulated and the measured SO₂ concentrations at the Earth's surface corresponds consistently to the bias between the simulated and the retrieved SO₂ VCDs. This is a strong indication that the prescribed SO₂ emissions in the RD1SD-base-01 simulation might be overestimated.

RQ 5: *How does the uncertainty in the representation of the boundary layer height in the CCM limit the interpretation of localized tropospheric SO₂ mixing ratio measurements for evaluating point source emission strengths?*

For the case study of point source emissions, the MESSy-fied ECHAM and COSMO models nested n-times (MECO(n)) system (see Section 3.1.3) is utilized. The higher resolved MECO(n) simulation results are evaluated with airborne measurements conducted with the Chemical Ionization Mass Spectrometry (CIMS) instrument over the Nikola TESLA A and B (TESLA_A and TESLA_B) power plants in Serbia on the 7th November 2020.

At the aircraft flight altitudes, MECO(n) encounters difficulties in reproducing the measured SO₂ mixing ratios over both emission sources, with 8 times lower simulated SO₂ mixing ratios compared to airborne measurements. This limitation is attributed to the inaccurate representation of the boundary layer height (BLH) in MECO(n), which shows lower BLH compared to the BLH from the ERA5 reanalysis and the aircraft data. The low BLH in MECO(n) shields the SO₂ mixing ratios below it, hindering their vertical distribu-

tion into higher atmospheric layers. This hypothesis is confirmed, as simulated SO₂ mixing ratios below the model's BLH (approximately 200 m above the surface) show larger values, compared to SO₂ mixing ratios simulated at flight altitudes. Additionally, the simulated SO₂ mixing ratios below the model's BLH reproduce the signals measured by the CIMS instrument, matching the observed SO₂ magnitudes. The limitation of the MECO(n) model system in accurately simulating the BLH is a common and known challenge in atmospheric modeling, as reported by Lee and Ngan (2011); Zhang et al. (2014); Morgenstern et al. (2017) and Liu et al. (2023).

In summary, the results in this work indicate that while the CCM simulations demonstrate notable strengths, there are also areas that require improvement.

Understanding the tropospheric sulfur budget forms the groundwork for the subsequent analyses and examinations. This analysis is conducted using the EMAC RD1SD-base-01 model simulation with the CMIP6 SO₂ emission data. By accounting for all sulfur species in the aqueous phase, the model demonstrates a closed sulfur budget, which has been compared with established literature. This assessment indicates a consistent representation of the model's internal processes, such as emissions, transport, chemical kinetics, and deposition. A closed sulfur budget allows for the evaluation of the EMAC model against other observational data. By utilizing TROPOMI/Sentinel-5P measurements, the global distribution of natural and anthropogenic SO₂ is identified in the EMAC model, showing different magnitudes compared to the SO₂ VCDs measured by the satellites instrument. Notably, the model indicates larger SO₂ VCDs, especially around regions with outgassing volcanic emissions. This discrepancy is attributed to the AeroCom emission inventory (Dentener et al., 2006) used within the EMAC model, which may not accurately reflect current outgassing volcanic activity. Given that the current emission inventory dates back to 2006, a new emission inventory for outgassing volcanic activities in the troposphere (Brühl et al., 2021) can be implemented in future EMAC model setups (personal communication with Mattia Righi). This update aims to enhance the accuracy and representation of volcanic SO₂ emissions within the model. On the other hand, the eruptive volcanic activity from the Raikoke and Ulawun volcanoes, as observed by the TROPOMI instrument, is accurately reproduced by the EMAC model. The emitted SO₂ mass and its temporal evolution are mostly captured by EMAC. Additionally, the deposited SO₂ mass confirms EMAC's ability to conserve mass, indicating that the relevant processes in EMAC are considered adequately.

Regarding the regions studied in this work, the bias calculated between the SO₂ VCDs from EMAC results and TROPOMI measurements, as well as the SO₂ concentrations between EMAC results and ground-based measurements over the USA, Europe and China-Japan in 2019, are consistent. The EMAC model simulates larger values, indicating an overestimation of the prescribed SO₂ emission data. In this work the utilized CMIP6 is compared to another emission inventory (EDGAR5). Especially over the Western USA and Europe regions, the CMIP6 inventory shows 45% and 20% larger SO₂ emissions, respectively, between 2000 and 2015 compared to the EDGAR5 emission inventory. This overestimation results in larger SO₂ concentrations simulated by EMAC compared to the

SO₂ concentrations measured by the ground-based networks. This suggests that for this period and regions, using the EDGAR5 inventory instead of CMIP6 would likely result in a closer alignment between the model results and measurements, thereby reducing the bias between the simulated and observed data. In contrast, over the Eastern USA, the CMIP6 emission inventory results in a good agreement between the SO₂ concentrations simulated by EMAC and the ground-based measurements. For China and Japan, both emission inventories indicate the same temporal evolution, showing an increase in SO₂ emissions between 2000 and 2012. Accordingly, this leads to an increase in the simulated SO₂ concentration over this period, which does not match the descending trend observed in the SO₂ concentrations measured by the Asian EANET network. These results indicate that the CMIP6 emission inventory provides realistic SO₂ emission data in some regions, but inaccurate data in others. This underscores the importance of investigating the EMAC model using various emission inventories to assess the range and sources of uncertainties, leading to a better understanding of the behavior of SO₂ emissions across different regions.

Another important aspect to consider is the accuracy of the model in reproducing aircraft measurements. Aircraft measurements can only be accurately interpreted, if the BLH is correctly defined and represented within the CCMs. A correct representation of the boundary layer is essential for accurately simulating the vertical distribution of SO₂, which in turn is crucial for evaluating how well the model replicates the measured SO₂ mixing ratios observed along the flight paths. Ensuring an accurate boundary layer representation allows for more precise comparisons between model outputs and observational data, thereby enhancing the reliability of the model's performance in capturing SO₂ at the aircraft's flight altitude.

The shipping sector is one of the main contributors to anthropogenic SO₂ emissions, which can affect the environment and human health. To mitigate the negative effects of SO₂ emissions, the International Maritime Organization (IMO) decided to reduce the maximum allowable sulfur content in marine fuel from 3.5% in 2012 to 0.5% in 2020 (Smith et al., 2021). This regulation led to interest in checking whether the regulations have been globally applied, which is relevant for policy-making. To address this topic, a combination of model simulations and satellite data is suggested. In the RD1SD-base-01 simulation, the CMIP6 considers SO₂ emissions from the shipping sector, allowing identification of shipping routes. This approach has been previously tested (not shown in this work) and reported by Feng et al. (2020). Consequently, VCDs over shipping routes could also be simulated using the EMAC model. For instance, SO₂ VCDs over shipping routes in the Southern Hemisphere (chosen to avoid interference from heavily polluted sources in the Northern Hemisphere) show values of about 0.01 DU in 2019. However, SO₂ VCDs from the TROPOMI instrument did not detect SO₂ VCDs over the shipping routes, and the signal is noisy at such low polluted SO₂ levels. This analysis is not shown in this work due to the low sensitivity of TROPOMI in measuring low pollution levels, especially near the surface. Additionally, Van Roy et al. (2023) also reported that the sensitivity of the TROPOMI instrument is insufficient to measure SO₂ pollution levels from ship emissions, because of the lower SO₂ pollution levels from this sector.

Building on the findings and conclusions of this thesis, further questions, and ideas for future scientific work arise. Below, personal suggestions for future research are presented:

- The selection of the emission inventory significantly influences the simulated SO₂ concentrations, which consequently impacts the deposition processes. To enhance the understanding of these impacts, it is recommended to conduct sensitivity simulations using various emission inventories and evaluate the model results against space-, air-, and ground-based measurements. These simulations will help to quantify the uncertainties and variabilities associated with different inventories in different regions, leading to more accurate simulated SO₂ concentrations and sulfur depositions.
- Challenges were encountered when evaluating simulated SO₂ at the Earth's surface with ground-based measurements from the Asian EANET network due to the difficulty in finding representative monitoring stations that provide continuous, long-term datasets of measured SO₂ concentrations and sulfur deposition fluxes. Therefore, future reliable measurements in these regions can be used to better constrain CCMs and could support the interpretation of measurements/observations.
- Future research should focus on evaluating the simulated SO₂ VCDs using high-resolution satellite instruments. Unlike the TROPOMI instrument, which provides a daily global coverage, the Geostationary Environment Monitoring Spectrometer (GEMS) launched in 2020 (Kim et al., 2020), the Tropospheric Emissions: Monitoring of Pollution (TEMPO) instrument launched in 2023 (Zoogman et al., 2017), and the Sentinel-4 instrument (Stark et al., 2013) (planned for launch in 2025) are dedicated to measuring air quality across Asia, North America, and Europe, respectively, every hour. The available high-frequency, near-real-time data provide a robust basis for validating the model's ability in simulating atmospheric SO₂ and capturing short-term variations and transient events, such as pollution spikes and weather-related changes.
- The improvement of the BLH representation within CCMs is important for an accurate interpretation of aircraft measurements. Developing and integrating advanced BLH schemes that more accurately reflect real-world atmospheric conditions would improve the model's capability in capturing SO₂ mixing ratios at research aircraft flight altitudes.
- The detection of the SO₂ signal from shipping sectors using the TROPOMI/Sentinel-5P satellite instrument is challenging, due to its low sensitivity near the surface and its inability to measure low SO₂ concentrations. Therefore, reliable measurement systems installed on ships or highly sensitive satellite instruments capable of detecting low SO₂ pollution levels are important. These systems, combined with data from CCMs, are essential for accurately tracking SO₂ emissions from the shipping sector.
- This thesis mainly focuses on the global distribution and behavior of SO₂ within the CCM EMAC by providing an important basis for the future development of

the model. Upcoming works could include the incorporation of advanced aerosol chemistry and a more detailed assessment of the climate impact of stratospheric aerosols. Such advancements would improve the model's capability to simulate the complex interactions between aerosols and climate processes, thereby offering a more comprehensive understanding of atmospheric chemistry and climate change.

Acronyms

R_a	aerodynamic resistance
R_{qbr}	quasi-laminar boundary layer resistance
R_s	surface resistance
$Tg(S)/a$	Teragrams of Sulfur per annum or year
ACCMIP	Atmospheric Chemistry and Climate-Model Intercomparison Project
AeroCom	Aerosol Inter Comparison
AI	Aerosol Index
AK	Averaging Kernel
Ar	argon
AR6	Sixth Assessment Report
awb	agricultural waste burning
BL	boundary layer
BLH	boundary layer height
BMIL	basemodel interface layer
BML	basemodel layer
CASTnet	Clean Air Status and Trends Network
CCM	Chemistry-Climate Model
CCMI-2	Phase 2 of the Chemistry Climate Model Initiative
CCN	cloud condensation nuclei
CFCs	chlorofluorocarbons
CH ₄	methane
CIMS	Chemical Ionization Mass Spectrometry
Cl	chlorine
CMIP5	Coupled Model Intercomparison Project Phase 5

CMIP6	Coupled Model Intercomparison Project Phase 6
CO ₂	carbon dioxide
COBRA	Covariance-Based Retrieval Algorithm
COSMO	Consortium for Small-scale Modeling
CS ₂	carbon disulfide
CTM	Chemistry-Transport Model
DMS	Dimethyl Sulfide
DOAS	Differential Optical Absorption Spectroscopy
DU	Dobson Units
E-PRTR	European Pollutant Release and Transfer Register
EANET	Acid Deposition Monitoring Network in East Asia
ECHAM5	5th generation European Center Hamburg general circulation model
ECMWF	European Centre for Medium-Range Weather Forecasts
EDGAR	Emissions Database For Global Atmospheric Research
EMAC	ECHAM/MESSy Atmospheric Chemistry
EMEP	European Monitoring and Evaluation Program
ESA	European Space Agency
ESM	Earth System Model
FFSL	flux form semi-Lagrangian
FGD	flue gas desulfurization
GCM	General Circulation Model
GEIA	Global Emissions Inventory Activity
GEMS	Geostationary Environment Monitoring Spectrometer
GHGs	greenhouse gases
GOME-2	Global Ozone Monitoring Experiment-2
H ₂ O	water vapor
H ₂ O ₂	hydrogen peroxide

H ₂ S	hydrogen sulfide
H ₂ SO ₃	sulfurous acid
H ₂ SO ₄	sulfuric acid
Hg	mercury
HSO ₃ ⁻	bisulfite ions
IMO	International Maritime Organization
IPCC	Intergovernmental Panel on Climate Change
KPP	Kinetic PreProcessor
LIDORT	Linearized Discrete Ordinate Radiative Transfer
MACC/CityZEN EU MECCA	European Commission, MACC and CityZen Module Efficiently Calculating the Chemistry of the Atmosphere
MECO(n)	MESSy-fied ECHAM and COSMO models nested n-times
MESSy MESSy2	Modular Earth Submodel System second version of the Modular Earth Sub- model System
MIM1	Mainz Isoprene Mechanism
MLM	Multi-Layer Model
MMD	Multi-Model-Driver
MSA	Methyl Sulfonic Acid
N ₂	nitrogen
N ₂ O	nitrous oxide
NMVOCs	non-methane volatile organic compounds
NWP	numerical weather prediction
O ₂	molecular oxygen
O ₃	ozone
OCS	Carbonyl Sulfide
ODEs	ordinary differential equations
OH	hydroxyl radical
OMI	Ozone Monitoring Instrument
ppb	part per billion
ppt	part per trillion

PSCs	Polar Stratospheric Clouds
RCPs	Representative Concentration Pathways
RF	radiative forcing
S	sulfur
sAOD	stratospheric Aerosol Optical Depth
SCD	Slant Column Density
SCIAMACHY	Scanning Imaging Absorption Spectrometer for Atmospheric Chartography
SD	specified dynamics
Sentinel-5P	Copernicus Sentinel-5 Precursor mission
SMCL	submodel core layer
SMIL	submodel interface layer
SO ₂	sulfur dioxide
SO ₃	sulfur trioxide
SO ₃ ²⁻	sulfite ions
SO ₄ ²⁻	sulfate ion
SSPs	shared socioeconomic pathways
SZA	solar zenith angle
TEMPO	Tropospheric Emissions: Monitoring of Pollution
Tg	Teragram
TM5	Tracer Model 5
TOMS	Total Ozone Mapping Spectrometer
TROPOMI	TROPOspheric Monitoring Instrument
USA	the United States of America
UTC	Coordinated Universal Time
UTLS	Upper Troposphere and Lower Stratosphere
VCD	Vertical Column Density
W m ⁻²	Watt per square meter

Appendix A

Appendices

A.1 Mechanism of the liquid phase chemistry

The presented document illustrates the chemical liquid phase reaction mechanism calculated by the SCAV submodel (see Section 3.1.7) within the EMAC RD1SD-base-01 simulation used in this work.

The Chemical Mechanism of SCAV

Table 1: Heterogeneous reactions

#	labels	reaction	rate coefficient	reference
H1000f	TrAraSc	$O_2 \rightarrow O_2(aq)$	$k_{\text{exf}}(KPP_O2)$	see note
H1000b	TrAraSc	$O_2(aq) \rightarrow O_2$	$k_{\text{exb}}(KPP_O2)$	see note
H1001f	TrAraMblScScm	$O_3 \rightarrow O_3(aq)$	$k_{\text{exf}}(KPP_O3)$	see note
H1001b	TrAraMblScScm	$O_3(aq) \rightarrow O_3$	$k_{\text{exb}}(KPP_O3)$	see note
H2100f	TrAraSc	$OH \rightarrow OH(aq)$	$k_{\text{exf}}(KPP_OH)$	see note
H2100b	TrAraSc	$OH(aq) \rightarrow OH$	$k_{\text{exb}}(KPP_OH)$	see note
H2101f	TrAraSc	$HO_2 \rightarrow HO_2(aq)$	$k_{\text{exf}}(KPP_HO2)$	see note
H2101b	TrAraSc	$HO_2(aq) \rightarrow HO_2$	$k_{\text{exb}}(KPP_HO2)$	see note
H2102f	TrAraMblScScm	$H_2O_2 \rightarrow H_2O_2(aq)$	$k_{\text{exf}}(KPP_H2O2)$	see note
H2102b	TrAraMblScScm	$H_2O_2(aq) \rightarrow H_2O_2$	$k_{\text{exb}}(KPP_H2O2)$	see note
H3100f	TrAraNSc	$NO \rightarrow NO(aq)$	$k_{\text{exf}}(KPP_NO)$	see note
H3100b	TrAraNSc	$NO(aq) \rightarrow NO$	$k_{\text{exb}}(KPP_NO)$	see note
H3101f	TrAraNSc	$NO_2 \rightarrow NO_2(aq)$	$k_{\text{exf}}(KPP_NO2)$	see note
H3101b	TrAraNSc	$NO_2(aq) \rightarrow NO_2$	$k_{\text{exb}}(KPP_NO2)$	see note
H3102f	TrAraNSc	$NO_3 \rightarrow NO_3(aq)$	$k_{\text{exf}}(KPP_NO3)$	see note
H3102b	TrAraNSc	$NO_3(aq) \rightarrow NO_3$	$k_{\text{exb}}(KPP_NO3)$	see note
H3200f	TrAraMblScScm	$NH_3 \rightarrow NH_3(aq)$	$k_{\text{exf}}(KPP_NH3)$	see note
H3200b	TrAraMblScScm	$NH_3(aq) \rightarrow NH_3$	$k_{\text{exb}}(KPP_NH3)$	see note
H3201	TrAraMblNScScm	$N_2O_5 \rightarrow HNO_3(aq) + HNO_3(aq)$	$k_{\text{exf}}(KPP_N2O5_C(KPP_H2O_1))$	Behnke et al. (1994), Behnke et al. (1997)
H3202f	TrAraNSc	$HONO \rightarrow HONO(aq)$	$k_{\text{exf}}(KPP_HONO)$	see note
H3202b	TrAraNSc	$HONO(aq) \rightarrow HONO$	$k_{\text{exb}}(KPP_HONO)$	see note
H3203f	TrAraMblNScScm	$HNO_3 \rightarrow HNO_3(aq)$	$k_{\text{exf}}(KPP_HNO3)$	see note
H3203b	TrAraMblNScScm	$HNO_3(aq) \rightarrow HNO_3$	$k_{\text{exb}}(KPP_HNO3)$	see note
H3204f	TrAraNSc	$HNO_4 \rightarrow HNO_4(aq)$	$k_{\text{exf}}(KPP_HNO4)$	see note
H3204b	TrAraNSc	$HNO_4(aq) \rightarrow HNO_4$	$k_{\text{exb}}(KPP_HNO4)$	see note

Table 1: Heterogeneous reactions

#	labels	reaction	rate coefficient	reference
H4100f	TrAraMblScScm	$CO_2 \rightarrow CO_2(aq)$	$k_{\text{exf}}(KPP_CO2)$	see note
H4100b	TrAraMblScScm	$CO_2(aq) \rightarrow CO_2$	$k_{\text{exb}}(KPP_CO2)$	see note
H4101f	TrAraScScm	$HCHO \rightarrow HCHO(aq)$	$k_{\text{exf}}(KPP_HCHO)$	see note
H4101b	TrAraScScm	$HCHO(aq) \rightarrow HCHO$	$k_{\text{exb}}(KPP_HCHO)$	see note
H4102f	TrAraSc	$CH_3O_2 \rightarrow CH_3OO(aq)$	$k_{\text{exf}}(KPP_CH3O2)$	see note
H4102b	TrAraSc	$CH_3OO(aq) \rightarrow CH_3O_2$	$k_{\text{exb}}(KPP_CH3O2)$	see note
H4103f	TrAraScScm	$HCOOH \rightarrow HCOOH(aq)$	$k_{\text{exf}}(KPP_HCOOH)$	see note
H4103b	TrAraScScm	$HCOOH(aq) \rightarrow HCOOH$	$k_{\text{exb}}(KPP_HCOOH)$	see note
H4104f	TrAraScScm	$CH_3OOH \rightarrow CH_3OOH(aq)$	$k_{\text{exf}}(KPP_CH3OOH)$	see note
H4104b	TrAraScScm	$CH_3OOH(aq) \rightarrow CH_3OOH$	$k_{\text{exb}}(KPP_CH3OOH)$	see note
H4105f	TrAraSc	$CH_3OH \rightarrow CH_3OH(aq)$	$k_{\text{exf}}(KPP_CH3OH)$	see note
H4105b	TrAraSc	$CH_3OH(aq) \rightarrow CH_3OH$	$k_{\text{exb}}(KPP_CH3OH)$	see note
H4200f	TrAraCScScm	$CH_3COOH \rightarrow CH_3COOH(aq)$	$k_{\text{exf}}(KPP_CH3COOH)$	see note
H4200b	TrAraCScScm	$CH_3COOH(aq) \rightarrow CH_3COOH$	$k_{\text{exb}}(KPP_CH3COOH)$	see note
H4201f	TrAraCSc	$CH_3CHO \rightarrow CH_3CHO(aq)$	$k_{\text{exf}}(KPP_CH3CHO)$	see note
H4201b	TrAraCSc	$CH_3CHO(aq) \rightarrow CH_3CHO$	$k_{\text{exb}}(KPP_CH3CHO)$	see note
H4202f	TrAraCSc	$PAN \rightarrow PAN(aq)$	$k_{\text{exf}}(KPP_PAN)$	see note
H4202b	TrAraCSc	$PAN(aq) \rightarrow PAN$	$k_{\text{exb}}(KPP_PAN)$	see note
H4300f	TrAraCSc	$CH_3COCH_3 \rightarrow CH_3COCH_3(aq)$	$k_{\text{exf}}(KPP_CH3COCH3)$	see note
H4300b	TrAraCSc	$CH_3COCH_3(aq) \rightarrow CH_3COCH_3$	$k_{\text{exb}}(KPP_CH3COCH3)$	see note
H6000f	TrAraClMblSc	$Cl_2 \rightarrow Cl_2(aq)$	$k_{\text{exf}}(KPP_Cl2)$	see note
H6000b	TrAraClMblSc	$Cl_2(aq) \rightarrow Cl_2$	$k_{\text{exb}}(KPP_Cl2)$	see note
H6200f	TrAraClMblScScm	$HCl \rightarrow HCl(aq)$	$k_{\text{exf}}(KPP_HCl)$	see note
H6200b	TrAraClMblScScm	$HCl(aq) \rightarrow HCl$	$k_{\text{exb}}(KPP_HCl)$	see note
H6201f	TrAraClMblSc	$HOCl \rightarrow HOCl(aq)$	$k_{\text{exf}}(KPP_HOCl)$	see note
H6201b	TrAraClMblSc	$HOCl(aq) \rightarrow HOCl$	$k_{\text{exb}}(KPP_HOCl)$	see note
H7000f	TrAraBrMblSc	$Br_2 \rightarrow Br_2(aq)$	$k_{\text{exf}}(KPP_Br2)$	see note
H7000b	TrAraBrMblSc	$Br_2(aq) \rightarrow Br_2$	$k_{\text{exb}}(KPP_Br2)$	see note
H7200f	TrAraBrMblScScm	$HBr \rightarrow HBr(aq)$	$k_{\text{exf}}(KPP_HBr)$	see note
H7200b	TrAraBrMblScScm	$HBr(aq) \rightarrow HBr$	$k_{\text{exb}}(KPP_HBr)$	see note
H7201f	TrAraBrMblSc	$HOBr \rightarrow HOBr(aq)$	$k_{\text{exf}}(KPP_HOBr)$	see note
H7201b	TrAraBrMblSc	$HOBr(aq) \rightarrow HOBr$	$k_{\text{exb}}(KPP_HOBr)$	see note
H7600f	TrAraClBrMblSc	$BrCl \rightarrow BrCl(aq)$	$k_{\text{exf}}(KPP_BrCl)$	see note
H7600b	TrAraClBrMblSc	$BrCl(aq) \rightarrow BrCl$	$k_{\text{exb}}(KPP_BrCl)$	see note
H9100f	TrAraSMblScScm	$SO_2 \rightarrow SO_2(aq)$	$k_{\text{exf}}(KPP_SO2)$	see note

Table 1: Heterogeneous reactions

#	labels	reaction	rate coefficient	reference
H9100b	TrAraSMblScScm	SO ₂ (aq) → SO ₂	k _{exb} (KPP_S02)	see note
H9200	TrAraSMblScScm	H ₂ SO ₄ → H ₂ SO ₄ (aq)	k _{exf} (KPP_H2S04)	see note
H9400f	TrAraSSc	DMSO → DMSO(aq)	k _{exf} (KPP_DMSO)	see note
H9400b	TrAraSSc	DMSO(aq) → DMSO	k _{exb} (KPP_DMSO)	see note
H9401	TrAraSMblSc	CH ₃ SO ₃ H → CH ₃ SO ₃ ⁻ (aq) + H ⁺ (aq)	k _{exf} (KPP_CH3S03H)	see note
H1101f	TrAraHgSc	Hg → Hg(aq)	k _{exf} (KPP_Hg)	see note
H1101b	TrAraHgSc	Hg(aq) → Hg	k _{exb} (KPP_Hg)	see note
H1102	TrAraHgSc	HgO → Hg(aq)	k _{exf_RGM*C} (KPP_H20_1)	see note
H1103	TrAraHgSc	HgCl → Hg(aq)	k _{exf_RGM*C} (KPP_H20_1)	see note
H1104	TrAraHgSc	HgCl ₂ → Hg(aq)	k _{exf_RGM*C} (KPP_H20_1)	see note
H1105	TrAraHgSc	HgBr → Hg(aq)	k _{exf_RGM*C} (KPP_H20_1)	see note
H1106	TrAraHgSc	HgBr ₂ → Hg(aq)	k _{exf_RGM*C} (KPP_H20_1)	see note
H1107	TrAraHgSc	ClHgBr → Hg(aq)	k _{exf_RGM*C} (KPP_H20_1)	see note
H1108	TrAraHgSc	BrHgOBr → Hg(aq)	k _{exf_RGM*C} (KPP_H20_1)	see note
H1109	TrAraHgSc	ClHgOBr → Hg(aq)	k _{exf_RGM*C} (KPP_H20_1)	see note

*Notes:

The forward (k_{exf}) and backward (k_{exb}) rate coefficients are calculated in the file `messy_sca_v_base.f90` using the accommodation coefficients in subroutine `sca_v_alpha` and Henry's law constants in subroutine `sca_v_henry`.

k_{mt} = mass transfer coefficient

lwc = liquid water content of aerosol mode

$f_{het}(X, Y) = k_{mt}(X) \times lwc \times f(Y)[Y]/Het_T$, with $f(H_2O) = 1$, $f(Cl^-) = 5.0E2$, and $f(Br^-) = 3.0E5$, $[Y]$ = concentration of Y; $Het_T = [H_2O] + f(Cl^-)[Cl^-] + f(Br^-)[Br^-]$

H6301, H6302, H7601: The total uptake is determined by k_{mt}(ClNO₂). The relative rates are assumed to be the same as for N₂O₅ (H3201, H6300, H7300).

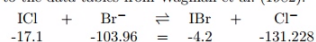
H7301, H7302, H7602: The total uptake is determined by k_{mt}(BrNO₂). The relative rates are assumed to be the same as for N₂O₅ (H3201, H6300, H7300).

Table 2: Acid-base and other equilibria

#	labels	reaction	K ₀ [M ^{m-n}]	-ΔH/R[K]	reference
EQ20	TrAraSc	HO ₂ ⇌ O ₂ ⁻ + H ⁺	1.6E-5		Weinstein-Lloyd and Schwartz (1991)
EQ21	TrAraMblScScm	H ₂ O ⇌ H ⁺ + OH ⁻	1.0E-16	-6716	Chameides (1984)
EQ30	TrAraMblNScScm	NH ₃ ⁺ ⇌ H ⁺ + NH ₃	5.88E-10	-2391	Chameides (1984)
EQ31	TrAraNSc	HONO ⇌ H ⁺ + NO ₂ ⁻	5.1E-4	-1260	Schwartz and White (1981)
EQ32	TrAraMblNScScm	HNO ₃ ⇌ H ⁺ + NO ₃ ⁻	15	8700	Davis and de Bruin (1964)
EQ33	TrAraNSc	HNO ₄ ⇌ NO ₄ ⁻ + H ⁺	1.E-5		Warneck (1999)
EQ40	TrAraMblScScm	CO ₂ ⇌ H ⁺ + HCO ₃ ⁻	4.3E-7	-913	Chameides (1984)
EQ41	TrAraScScm	HCOOH ⇌ H ⁺ + HCOO ⁻	1.8E-4		Weast (1980)
EQ42	TrAraCScScm	CH ₃ COOH ⇌ H ⁺ + CH ₃ COO ⁻	1.75E-5	-46	see note
EQ61	TrAraClMblScScm	HCl ⇌ H ⁺ + Cl ⁻	1.7E6	6896	Marsh and McElroy (1985)
EQ62	TrAraClSc	HOCl ⇌ H ⁺ + ClO ⁻	3.2E-8		Lax (1969)
EQ71	TrAraBrMblScScm	HBr ⇌ H ⁺ + Br ⁻	1.0E9		Lax (1969)
EQ72	TrAraBrSc	HOBr ⇌ H ⁺ + BrO ⁻	2.3E-9	-3091	Kelley and Tartar (1956)
EQ90	TrAraSMblScScm	SO ₂ ⇌ H ⁺ + HSO ₃ ⁻	1.7E-2	2090	Chameides (1984)
EQ91	TrAraSMblScScm	HSO ₃ ⁻ ⇌ H ⁺ + SO ₃ ²⁻	6.0E-8	1120	Chameides (1984)
EQ92	TrAraSMblScScm	HSO ₄ ⁻ ⇌ H ⁺ + SO ₄ ²⁻	1.2E-2	2720	Seinfeld and Pandis (1998)
EQ93	TrAraSMblScScm	H ₂ SO ₄ ⇌ H ⁺ + HSO ₄ ⁻	1.0E3		Seinfeld and Pandis (1998)

*Notes:

EQ82 and EQ83: Thermodynamic calculations on the IBr/ICl equilibrium according to the data tables from Wagman et al. (1982):



$$\frac{\Delta G}{[\text{kJ/mol}]} = -4.2 - 131.228 - (-17.1 - 103.96) = -14.368$$

$$K = \frac{[\text{IBr}] \times [\text{Cl}^-]}{[\text{ICl}] \times [\text{Br}^-]} = \exp\left(\frac{-\Delta G}{RT}\right) = \exp\left(\frac{14368}{8.314 \times 298}\right) = 330$$

This means we have equal amounts of IBr and ICl when the [Cl⁻]/[Br⁻] ratio equals 330.

Table 3: Aqueous phase reactions

#	labels	reaction	k_0 [$M^{1-n}s^{-1}$]	$-E_a/R[K]$	reference
A1000	TrAraSc	$O_3 + O_2^- \rightarrow OH + OH^-$	1.5E9		Sehested et al. (1983)
A2100	TrAraSc	$OH + O_2^- \rightarrow OH^-$	1.0E10		Sehested et al. (1968)
A2101	TrAraSc	$OH + OH \rightarrow H_2O_2$	5.5E9		Buxton et al. (1988)
A2102	TrAraSc	$HO_2 + O_2^- \rightarrow H_2O_2 + OH^-$	1.0E8	-900	Christensen and Sehested (1988)
A2103	TrAraSc	$HO_2 + OH \rightarrow H_2O$	7.1E9		Sehested et al. (1968)
A2104	TrAraSc	$HO_2 + HO_2 \rightarrow H_2O_2$	9.7E5	-2500	Christensen and Sehested (1988)
A2105	TrAraSc	$H_2O_2 + OH \rightarrow HO_2$	2.7E7	-1684	Christensen et al. (1982)
A3100	TrAraNSc	$NO_2^- + O_3 \rightarrow NO_3^-$	5.0E5	-6950	Damschen and Martin (1983)
A3101	TrAraNSc	$NO_2 + NO_2 \rightarrow HNO_3 + HONO$	1.0E8		Lee and Schwartz (1981)
A3102	TrAraNSc	$NO_4^- \rightarrow NO_2^-$	8.0E1		Warneck (1999)
A3200	TrAraNSc	$NO_2 + HO_2 \rightarrow HNO_4$	1.8E9		Warneck (1999)
A3201	TrAraNSc	$NO_2^- + OH \rightarrow NO_2 + OH^-$	1.0E10		Wingenter et al. (1999)
A3202	TrAraNSc	$NO_3 + OH^- \rightarrow NO_3^- + OH$	8.2E7	-2700	Exner et al. (1992)
A3203	TrAraNSc	$HONO + OH \rightarrow NO_2$	1.0E10		Barker et al. (1970)
A3204	TrAraNSc	$HONO + H_2O_2 \rightarrow HNO_3$	4.6E3	-6800	Damschen and Martin (1983)
A4100	TrAraSc	$CO_3^- + O_2^- \rightarrow HCO_3^- + OH^-$	6.5E8		Ross et al. (1992)
A4101	TrAraSc	$CO_3^- + H_2O_2 \rightarrow HCO_3^- + HO_2$	4.3E5		Ross et al. (1992)
A4102	TrAraSc	$HCOO^- + CO_2^- \rightarrow 2 HCO_3^- + HO_2$	1.5E5		Ross et al. (1992)
A4103	TrAraSc	$HCOO^- + OH \rightarrow OH^- + HO_2 + CO_2$	3.1E9	-1240	Chin and Wine (1994)
A4104	TrAraSc	$HCO_3^- + OH \rightarrow CO_3^-$	8.5E6		Ross et al. (1992)
A4105	TrAraSc	$HCHO + OH \rightarrow HCOOH + HO_2$	7.7E8	-1020	Chin and Wine (1994)
A4106	TrAraSc	$HCOOH + OH \rightarrow HO_2 + CO_2$	1.1E8	-991	Chin and Wine (1994)
A4107	TrAraSc	$CH_3OO + O_2^- \rightarrow CH_3OOH + OH^-$	5.0E7		Jacob (1986)
A4108	TrAraSc	$CH_3OO + HO_2 \rightarrow CH_3OOH$	4.3E5		Jacob (1986)
A4109	TrAraSc	$CH_3OH + OH \rightarrow HCHO + HO_2$	9.7E8		Buxton et al. (1988)
A4110a	TrAraSc	$CH_3OOH + OH \rightarrow CH_3OO$	2.7E7	-1715	Jacob (1986)
A4110b	TrAraSc	$CH_3OOH + OH \rightarrow HCHO + OH$	1.1E7	-1715	Jacob (1986)
A9100	TrAraSSc	$SO_3^- + O_2 \rightarrow SO_4^-$	1.5E9		Huie and Neta (1987)
A9101	TrAraSmbIScScem	$SO_3^- + O_3 \rightarrow SO_4^-$	1.5E9	-5300	Hoffmann (1986)
A9102	TrAraSSc	$SO_4^- + O_2^- \rightarrow SO_4^{2-}$	3.5E9		Jiang et al. (1992)
A9103	TrAraSSc	$SO_4^- + SO_3^{2-} \rightarrow SO_5^- + SO_4^{2-}$	4.6E8		Huie and Neta (1987)
A9104	TrAraSSc	$SO_4^- + O_2^- \rightarrow HSO_4^- + OH^-$	2.3E8		Buxton et al. (1996)
A9200	TrAraSSc	$SO_3^{2-} + OH \rightarrow SO_3^- + OH^-$	5.5E9		Buxton et al. (1988)
A9201	TrAraSSc	$SO_4^- + OH \rightarrow HSO_4^-$	1.0E9		Jiang et al. (1992)

Table 3: Aqueous phase reactions (...continued)

#	labels	reaction	k_0 [$M^{1-n}s^{-1}$]	$-E_a/R[K]$	reference
A9202	TrAraSSc	$SO_4^- + HO_2 \rightarrow SO_4^{2-} + H^+$	3.5E9		Jiang et al. (1992)
A9203	TrAraSSc	$SO_4^- + H_2O \rightarrow SO_4^{2-} + H^+ + OH$	1.1E1	-1110	Herrmann et al. (1995)
A9204	TrAraSSc	$SO_4^- + H_2O_2 \rightarrow SO_4^{2-} + H^+ + HO_2$	1.2E7		Wine et al. (1989)
A9205	TrAraSSc	$HSO_3^- + O_2^- \rightarrow SO_3^{2-} + OH$	3.0E3		see note
A9206	TrAraSmbIScScem	$HSO_3^- + O_3 \rightarrow SO_3^{2-} + H^+$	3.7E5	-5500	Hoffmann (1986)
A9207	TrAraSSc	$HSO_3^- + OH \rightarrow SO_3^{2-}$	4.5E9		Buxton et al. (1988)
A9208	TrAraSSc	$HSO_3^- + HO_2 \rightarrow SO_3^{2-} + OH + H^+$	3.0E3		see note
A9209	TrAraSmbIScScem	$HSO_3^- + H_2O_2 \rightarrow SO_3^{2-} + H^+$	5.2E6	-3650	Martin and Damschen (1981)
A9210	TrAraSSc	$HSO_3^- + SO_4^- \rightarrow SO_3^{2-} + SO_4^{2-} + H^+$	8.0E8		Huie and Neta (1987)
A9212	TrAraSSc	$HSO_3^- + HSO_3^- \rightarrow 2 SO_3^{2-} + 2 H^+$	7.1E6		Betterton and Hoffmann (1988)
A9300	TrAraSSc	$SO_3^{2-} + NO_2 \rightarrow SO_3^- + 2 HONO - NO_2$	2.0E7		Clifton et al. (1988)
A9301	TrAraSSc	$SO_4^- + NO_2^- \rightarrow SO_4^{2-} + NO_3$	5.0E4		Exner et al. (1992)
A9302	TrAraSSc	$SO_4^{2-} + NO_3 \rightarrow NO_3^- + SO_4^-$	1.0E5		Logager et al. (1993)
A9303	TrAraSSc	$HSO_3^- + NO_2 \rightarrow HSO_4^- + 2 HONO - NO_2$	2.0E7		Clifton et al. (1988)
A9304	TrAraSSc	$HSO_3^- + NO_3 \rightarrow SO_3^- + NO_3^- + H^+$	1.4E9	-2000	Exner et al. (1992)
A9305	TrAraSSc	$HSO_3^- + HNO_4 \rightarrow HSO_4^- + NO_3^- + H^+$	3.1E5		Warneck (1999)
A9400	TrAraSSc	$SO_3^{2-} + HCHO \rightarrow CH_2OHSO_3^- + OH^-$	1.4E4		Boyce and Hoffmann (1984)
A9401	TrAraSSc	$SO_3^{2-} + CH_3OOH \rightarrow SO_3^- + CH_3OH$	1.6E7	-3800	Lind et al. (1987)
A9402	TrAraSSc	$HSO_3^- + HCHO \rightarrow CH_2OHSO_3^-$	4.3E-1		Boyce and Hoffmann (1984)
A9403	TrAraSSc	$HSO_3^- + CH_3OOH \rightarrow SO_3^{2-} + H^+ + CH_3OH$	1.6E7	-3800	Lind et al. (1987)
A9404	TrAraSSc	$CH_2OHSO_3^- + OH^- \rightarrow SO_3^{2-} + HCHO$	3.6E3		Seinfeld and Pandis (1998)

A6102: Jacobi (1996) found an upper limit of 6E9 and cite an upper limit from another study of 2E9. Here, we set the rate coefficient to 1E9.

A6301: There is also an earlier study by Exner et al. (1992) which found a smaller rate coefficient but did not consider the back reaction.

A7400: assumed to be the same as for $Br_2^- + H_2O_2$.

A9106: see also: (Huie and Neta, 1987; Warneck, 1991). If this reaction produces a lot of SO_4^- , it will have an effect. However, we currently assume only the stable $S_2O_8^{2-}$ as product.

A9205: D. Sedlak, pers. comm. (1993)

A9208: D. Sedlak, pers. comm. (1993)

A9105: The rate coefficient for the sum of the paths (leading to either HSO_3^- or SO_4^{2-}) is from Huie and Neta (1987), the ratio 0.28/0.72 is from Deister and Warneck (1990).

A9605: assumed to be the same as for $SO_3^{2-} + HOCl$.

A9705: assumed to be the same as for $SO_3^{2-} + HOBr$.

Table 4: Photolysis reactions

#	labels	reaction	rate coefficient	reference
PH2100	TrAraScJ	$H_2O_2 + h\nu \rightarrow 2 OH$	JX(1p_H202)*2.33	see note

*Notes: J-values are calculated with an external module and then supplied to the SCAV chemistry

A.2 Mechanism of the gas phase chemistry

The presented document illustrates the chemical gas phase reaction mechanism calculated by the MECCA submodel (see Section 3.1.8) within the EMAC RD1SD-base-01 simulation used in this work.

The Chemical Mechanism of MECCA

```
KPP version: 2.2.3_rs3
MECCA version: 4.4.0.m2
Date: June 28, 2024
Batch file: CCM1/CCMI2-base-01
Integrator: rosenbrock_mz
Gas equation file: gas.eqn
Replacement file: mim1-CCMI2-base-01
Selected reactions:
“((Tr && (G || Het) && !I) || St) && !Hg)”
Number of aerosol phases: 0
Number of species in selected mechanism:
  Gas phase:      157
  Aqueous phase:  0
  All species:    157
Number of reactions in selected mechanism:
  Gas phase (Gnn):      261
  Aqueous phase (Annn): 0
  Henry (Hnn):          0
  Photolysis (Jnn):     80
  Aqueous phase photolysis (PHnn): 0
  Heterogeneous (HETnn): 12
  Equilibria (EQnn):    0
  Isotope exchange (IEXnn): 0
  Kinetic tagging (TAGnn): 0
  Dummy (Dnn):          0
  All equations:        353
```

Table 1: Gas phase reactions

#	labels	reaction	rate coefficient	reference
G1000	UpStTrG	$O_2 + O(^1D) \rightarrow O(^3P) + O_2$	$3.3E-11 \cdot \text{EXP}(55./\text{temp})$	Burkholder et al. (2015)
G1001	UpStTrG	$O_2 + O(^3P) \rightarrow O_3$	$6.0E-34 \cdot ((\text{temp}/300.)^{**}(-2.4)) \cdot (\text{cair})$	Burkholder et al. (2015)
G1002a	UpStG	$O_3 + O(^1D) \rightarrow 2.0 \text{ LossO3O} + 2.0 \text{ LossO3} + 2 O_2$	1.2E-10	Burkholder et al. (2015)*
G1003	UpStG	$O_3 + O(^3P) \rightarrow 2.0 \text{ LossO3O} + 2.0 \text{ LossO3} + 2 O_2$	$8.0E-12 \cdot \text{EXP}(-2060./\text{temp})$	Burkholder et al. (2015)
G2100	UpStTrG	$H + O_2 \rightarrow HO_2$	$k_3rd(\text{temp}, \text{cair}, 4.4E-32, 1.3, 7.5E-11, -0.2, 0.6)$	Burkholder et al. (2015)
G2101	UpStG	$H + O_3 \rightarrow 1.0 \text{ LossO3H} + 1.0 \text{ LossO3} + OH + O_2$	$1.4E-10 \cdot \text{EXP}(-470./\text{temp})$	Burkholder et al. (2015)
G2102	UpStG	$H_2 + O(^1D) \rightarrow 1.0 \text{ LossO3H} + 1.0 \text{ LossO3} + H + OH$	1.2E-10	Burkholder et al. (2015)
G2103	UpStG	$OH + O(^3P) \rightarrow 1.0 \text{ LossO3H} + 1.0 \text{ LossO3} + H + O_2$	$1.8E-11 \cdot \text{EXP}(180./\text{temp})$	Burkholder et al. (2015)
G2104	UpStTrG	$OH + O_3 \rightarrow 1.0 \text{ LossO3H} + \text{LossOH} + 1.0 \text{ LossO3} + HO_2 + O_2$	$1.7E-12 \cdot \text{EXP}(-940./\text{temp})$	Burkholder et al. (2015)
G2105	UpStTrG	$OH + H_2 \rightarrow \text{ProdH2O} + H_2O + H$	$2.8E-12 \cdot \text{EXP}(-1800./\text{temp})$	Burkholder et al. (2015)
G2106	UpStG	$HO_2 + O(^3P) \rightarrow 1.0 \text{ LossO3H} + 1.0 \text{ LossO3} + OH + O_2$	$3.E-11 \cdot \text{EXP}(200./\text{temp})$	Burkholder et al. (2015)
G2107	UpStTrG	$HO_2 + O_3 \rightarrow 1.0 \text{ LossO3H} + \text{LossHO2} + 1.0 \text{ LossO3} + OH + 2 O_2$	$1.E-14 \cdot \text{EXP}(-490./\text{temp})$	Burkholder et al. (2015)
G2108a	UpStG	$HO_2 + H \rightarrow 2 OH$	7.2E-11	Burkholder et al. (2015)
G2108b	UpStG	$HO_2 + H \rightarrow H_2 + O_2$	6.9E-12	Burkholder et al. (2015)
G2108c	UpStG	$HO_2 + H \rightarrow \text{ProdH2O} + 1.0 \text{ ProdO3} + O(^3P) + H_2O$	1.6E-12	Burkholder et al. (2015)
G2109	UpStTrG	$HO_2 + OH \rightarrow \text{ProdH2O} + H_2O + O_2$	$4.8E-11 \cdot \text{EXP}(250./\text{temp})$	Burkholder et al. (2015)
G2110	UpStTrG	$HO_2 + HO_2 \rightarrow H_2O_2 + O_2$	k_H02_H02	Burkholder et al. (2015)*
G2111	UpStTrG	$H_2O + O(^1D) \rightarrow \text{LossH2O} + 1.0 \text{ LossO3O} + \text{LossO1D} + 1.0 \text{ LossO3} + 2 OH$	$1.63E-10 \cdot \text{EXP}(60./\text{temp})$	Burkholder et al. (2015)
G2112	UpStTrG	$H_2O_2 + OH \rightarrow \text{ProdH2O} + H_2O + HO_2$	1.8E-12	Burkholder et al. (2015)
G3100	UpStGN	$N + O_2 \rightarrow 1.0 \text{ ProdO3} + NO + O(^3P)$	$1.5E-11 \cdot \text{EXP}(-3600./\text{temp})$	Burkholder et al. (2015)
G3101	UpStTrGN	$N_2 + O(^1D) \rightarrow O(^3P) + N_2$	$2.15E-11 \cdot \text{EXP}(110./\text{temp})$	Burkholder et al. (2015)
G3102a	UpStGN	$N_2 + O(^1D) \rightarrow 1.0 \text{ LossO3O} + 1.0 \text{ LossO3} + 2 NO$	$7.259E-11 \cdot \text{EXP}(20./\text{temp})$	Burkholder et al. (2015)
G3102b	StGN	$N_2 + O(^1D) \rightarrow 1.0 \text{ LossO3O} + 1.0 \text{ LossO3} + N_2 + O_2$	$4.641E-11 \cdot \text{EXP}(20./\text{temp})$	Burkholder et al. (2015)
G3103	UpStTrGN	$NO + O_3 \rightarrow NO_2 + O_2$	$3.0E-12 \cdot \text{EXP}(-1500./\text{temp})$	Burkholder et al. (2015)
G3104	UpStGN	$NO + N \rightarrow 1.0 \text{ ProdO3} + O(^3P) + N_2$	$2.1E-11 \cdot \text{EXP}(100./\text{temp})$	Burkholder et al. (2015)
G3105	UpStGN	$NO + O(^3P) \rightarrow 2.0 \text{ LossO3N} + 2.0 \text{ LossO3} + NO + O_2$	$5.1E-12 \cdot \text{EXP}(210./\text{temp})$	Burkholder et al. (2015)
G3106	StTrGN	$NO_2 + O_3 \rightarrow NO_3 + O_2$	$1.2E-13 \cdot \text{EXP}(-2450./\text{temp})$	Burkholder et al. (2015)
G3107	UpStGN	$NO_2 + N \rightarrow N_2O + O(^3P)$	$5.8E-12 \cdot \text{EXP}(220./\text{temp})$	Burkholder et al. (2015)
G3108	StTrGN	$NO_3 + NO \rightarrow 2 NO_2$	$1.5E-11 \cdot \text{EXP}(170./\text{temp})$	Burkholder et al. (2015)

Table 1: Gas phase reactions (... continued)

#	labels	reaction	rate coefficient	reference
G3109	UpStTrGN	$NO_3 + NO_2 \rightarrow N_2O_5$	k_N03_N02	Burkholder et al. (2015)*
G3110	StTrGN	$N_2O_5 \rightarrow NO_2 + NO_3$	$k_N03_N02 / (5.8E-27 \cdot \text{EXP}(10840./\text{temp}))$	Burkholder et al. (2015)*
G3200	TrGN	$NO + OH \rightarrow HONO$	$k_3rd(\text{temp}, \text{cair}, 7.0E-31, 2.6, 3.6E-11, 0.1, 0.6)$	Burkholder et al. (2015)
G3201	UpStTrGN	$NO + HO_2 \rightarrow \text{ProdHO2} + 1.0 \text{ ProdO3} + NO_2 + OH$	$3.3E-12 \cdot \text{EXP}(270./\text{temp})$	Burkholder et al. (2015)
G3202	UpStTrGN	$NO + OH \rightarrow HNO_3$	$k_3rd(\text{temp}, \text{cair}, 1.8E-30, 3.0, 2.8E-11, 0., 0.6)$	Burkholder et al. (2015)
G3203	StTrGN	$NO_2 + HO_2 \rightarrow HNO_4$	k_N02_H02	Burkholder et al. (2015)*
G3204	TrGN	$NO_3 + HO_2 \rightarrow 1.0 \text{ LossO3N} + 1.0 \text{ LossO3} + NO_2 + OH + O_2$	3.5E-12	Burkholder et al. (2015)
G3205	TrGN	$HONO + OH \rightarrow \text{ProdH2O} + 1.0 \text{ ProdO3} + NO_2 + H_2O$	$1.8E-11 \cdot \text{EXP}(-390./\text{temp})$	Burkholder et al. (2015)
G3206	StTrGN	$HNO_3 + OH \rightarrow \text{ProdH2O} + 1.0 \text{ ProdO3} + H_2O + NO_3$	k_HNO3_OH	Dulitz et al. (2018)*
G3207	StTrGN	$HNO_4 \rightarrow NO_2 + HO_2$	$k_N02_H02 / (2.1E-27 \cdot \text{EXP}(10900./\text{temp}))$	Burkholder et al. (2015)*
G3208	StTrGN	$HNO_4 + OH \rightarrow \text{ProdH2O} + NO_2 + H_2O$	$1.3E-12 \cdot \text{EXP}(380./\text{temp})$	Burkholder et al. (2015)
G3209	TrGN	$NH_3 + OH \rightarrow \text{ProdH2O} + NH_2 + H_2O$	$1.7E-12 \cdot \text{EXP}(-710./\text{temp})$	Kohlmann and Poppe (1999)
G3210	TrGN	$NH_2 + O_3 \rightarrow 1.0 \text{ LossO3N} + 1.0 \text{ LossO3} + NH_2O + O_2$	$4.3E-12 \cdot \text{EXP}(-930./\text{temp})$	Kohlmann and Poppe (1999)
G3211	TrGN	$NH_2 + HO_2 \rightarrow NH_2O + OH$	$4.8E-07 \cdot \text{EXP}(-628./\text{temp}) \cdot (\text{temp})^{**}(-1.32)$	Kohlmann and Poppe (1999)
G3212	TrGN	$NH_2 + HO_2 \rightarrow \text{ProdH2O} + HNO + H_2O$	$9.4E-09 \cdot \text{EXP}(-356./\text{temp}) \cdot (\text{temp})^{**}(-1.12)$	Kohlmann and Poppe (1999)
G3213	TrGN	$NH_2 + NO \rightarrow HO_2 + OH + N_2$	$1.92E-12 \cdot ((\text{temp}/298.)^{**}(-1.5))$	Kohlmann and Poppe (1999)
G3214	TrGN	$NH_2 + NO \rightarrow \text{ProdH2O} + N_2 + H_2O$	$1.41E-11 \cdot ((\text{temp}/298.)^{**}(-1.5))$	Kohlmann and Poppe (1999)
G3215	TrGN	$NH_2 + NO_2 \rightarrow \text{ProdH2O} + 1.0 \text{ LossO3N} + 1.0 \text{ LossO3} + N_2O + H_2O$	$1.2E-11 \cdot ((\text{temp}/298.)^{**}(-2.0))$	Kohlmann and Poppe (1999)
G3216	TrGN	$NH_2 + NO_2 \rightarrow 1.0 \text{ LossO3N} + 1.0 \text{ LossO3} + NH_2O + NO$	$0.8E-11 \cdot ((\text{temp}/298.)^{**}(-2.0))$	Kohlmann and Poppe (1999)
G3217	TrGN	$NH_2O + O_3 \rightarrow 1.0 \text{ LossO3N} + 1.0 \text{ LossO3} + NH_2 + O_2$	1.2E-14	Kohlmann and Poppe (1999)
G3218	TrGN	$NH_2O \rightarrow NHOH$	1.3E3	Kohlmann and Poppe (1999)
G3219	TrGN	$HNO + OH \rightarrow \text{ProdH2O} + NO + H_2O$	$8.0E-11 \cdot \text{EXP}(-500./\text{temp})$	Kohlmann and Poppe (1999)
G3220	TrGN	$HNO + NHOH \rightarrow NH_2OH + NO$	$1.66E-12 \cdot \text{EXP}(-1500./\text{temp})$	Kohlmann and Poppe (1999)
G3221	TrGN	$HNO + NO_2 \rightarrow 1.0 \text{ LossO3N} + 1.0 \text{ LossO3} + HONO + NO$	$1.0E-12 \cdot \text{EXP}(-1000./\text{temp})$	Kohlmann and Poppe (1999)
G3222	TrGN	$NHOH + OH \rightarrow \text{ProdH2O} + HNO + H_2O$	1.66E-12	Kohlmann and Poppe (1999)
G3223	TrGN	$NH_2OH + OH \rightarrow \text{ProdH2O} + NHOH + H_2O$	$4.13E-11 \cdot \text{EXP}(-2138./\text{temp})$	Kohlmann and Poppe (1999)

Table 1: Gas phase reactions (... continued)

#	labels	reaction	rate coefficient	reference
G3224	TrGN	$\text{HNO} + \text{O}_2 \rightarrow \text{HO}_2 + \text{NO}$	$3.65\text{E-}14 \cdot \text{EXP}(-4600./\text{temp})$	Kohlmann and Poppe (1999)
G4100	UpStG	$\text{CH}_4 + \text{O}(\text{^1D}) \rightarrow 1.0 \text{ LossO3O} + 1.0 \text{ LossO3} + .75 \text{ CH}_3\text{O}_2 + .75 \text{ OH} + .25 \text{ HCHO} + .4 \text{ H} + .05 \text{ H}_2$	$1.75\text{E-}10$	Sander et al. (2011)
G4101	StTrG	$\text{CH}_4 + \text{OH} \rightarrow \text{ProdH2O} + \text{CH}_3\text{O}_2 + \text{H}_2\text{O}$	$1.85\text{E-}20 \cdot \text{EXP}(2.82 \cdot \text{LOG}(\text{temp}) - 987./\text{temp})$	Atkinson (2003)
G4102	TrG	$\text{CH}_3\text{OH} + \text{OH} \rightarrow \text{HCHO} + \text{HO}_2$	$2.9\text{E-}12 \cdot \text{EXP}(-345./\text{temp})$	Sander et al. (2011)
G4103	StTrG	$\text{CH}_3\text{O}_2 + \text{HO}_2 \rightarrow \text{CH}_3\text{OOH} + \text{O}_2$	$4.1\text{E-}13 \cdot \text{EXP}(750./\text{temp})$	Sander et al. (2011)*
G4104	UpStTrGN	$\text{CH}_3\text{O}_2 + \text{NO} \rightarrow \text{ProdMeO2} + 1.0 \text{ ProdO3} + \text{HCHO} + \text{NO}_2 + \text{HO}_2$	$2.8\text{E-}12 \cdot \text{EXP}(300./\text{temp})$	Sander et al. (2011)
G4105	TrGN	$\text{CH}_3\text{O}_2 + \text{NO}_3 \rightarrow 1.0 \text{ LossO3R} + 1.0 \text{ LossO3} + \text{HCHO} + \text{HO}_2 + \text{NO}_2$	$1.3\text{E-}12$	Atkinson et al. (2006)
G4106a	StTrG	$\text{CH}_3\text{O}_2 + \text{CH}_3\text{O}_2 \rightarrow 2 \text{ HCHO} + 2 \text{ HO}_2$	$9.5\text{E-}14 \cdot \text{EXP}(390./\text{temp}) / (1.+ 26.2 \cdot \text{EXP}(1130./\text{temp}))$	Sander et al. (2011)
G4106b	StTrG	$\text{CH}_3\text{O}_2 + \text{CH}_3\text{O}_2 \rightarrow \text{HCHO} + \text{CH}_3\text{OH} + \text{O}_2$	$9.5\text{E-}14 \cdot \text{EXP}(390./\text{temp}) / (1.+ 26.2 \cdot \text{EXP}(-1130./\text{temp}))$	Sander et al. (2011)
G4107	StTrG	$\text{CH}_3\text{OOH} + \text{OH} \rightarrow \text{ProdH2O} + .7 \text{ CH}_3\text{O}_2 + .3 \text{ HCHO} + .3 \text{ OH} + \text{H}_2\text{O}$	$k_{\text{CH300H_OH}}$	Wallington et al. (2018)
G4108	StTrG	$\text{HCHO} + \text{OH} \rightarrow \text{ProdH2O} + \text{CO} + \text{H}_2\text{O} + \text{HO}_2$	$9.52\text{E-}18 \cdot \text{EXP}(2.03 \cdot \text{LOG}(\text{temp}) + 636./\text{temp})$	Sivakumaran et al. (2003)
G4109	TrGN	$\text{HCHO} + \text{NO}_3 \rightarrow 1.0 \text{ LossO3R} + 1.0 \text{ LossO3} + \text{HNO}_3 + \text{CO} + \text{HO}_2$	$3.4\text{E-}13 \cdot \text{EXP}(-1900./\text{temp})$	Sander et al. (2011)*
G4110	UpStTrG	$\text{CO} + \text{OH} \rightarrow \text{H} + \text{CO}_2$	$(1.57\text{E-}13 \cdot \text{cair} \cdot 3.54\text{E-}33)$	McCabe et al. (2001)
G4111	TrG	$\text{HCOOH} + \text{OH} \rightarrow \text{ProdH2O} + \text{CO}_2 + \text{HO}_2 + \text{H}_2\text{O}$	$4.0\text{E-}13$	Sander et al. (2011)
G4200	TrGC	$\text{C}_2\text{H}_6 + \text{OH} \rightarrow \text{ProdH2O} + \text{C}_2\text{H}_5\text{O}_2 + \text{H}_2\text{O}$	$1.49\text{E-}17 \cdot \text{temp} \cdot \text{temp} \cdot \text{EXP}(-499./\text{temp})$	Atkinson (2003)
G4201	TrGC	$\text{C}_2\text{H}_4 + \text{O}_3 \rightarrow 1.0 \text{ LossO3R} + 1.0 \text{ LossO3} + \text{HCHO} + .63 \text{ CO} + .13 \text{ HO}_2 + 0.23125 \text{ HCOOH} + 0.13875 \text{ HCHO} + 0.13875 \text{ H}_2\text{O}_2 + .13 \text{ OH}$	$1.2\text{E-}14 \cdot \text{EXP}(-2630./\text{temp})$	Sander et al. (2011)*
G4202	TrGC	$\text{C}_2\text{H}_4 + \text{OH} \rightarrow .6666667 \text{ CH}_3\text{CH}(\text{O}_2)\text{CH}_2\text{OH}$	$k_{\text{3rd}}(\text{temp}, \text{cair}, 1.0\text{E-}28, 4.5, 7.5\text{E-}12, 0.85, 0.6)$	Sander et al. (2011)
G4203	TrGC	$\text{C}_2\text{H}_5\text{O}_2 + \text{HO}_2 \rightarrow \text{C}_2\text{H}_5\text{OOH}$	$7.5\text{E-}13 \cdot \text{EXP}(700./\text{temp})$	Sander et al. (2011)
G4204	TrGCN	$\text{C}_2\text{H}_5\text{O}_2 + \text{NO} \rightarrow \text{ProdRO2} + 1.0 \text{ ProdO3} + \text{CH}_3\text{CHO} + \text{HO}_2 + \text{NO}_2$	$2.6\text{E-}12 \cdot \text{EXP}(365./\text{temp})$	Sander et al. (2011)
G4205	TrGCN	$\text{C}_2\text{H}_5\text{O}_2 + \text{NO}_3 \rightarrow 1.0 \text{ LossO3R} + 1.0 \text{ LossO3} + \text{CH}_3\text{CHO} + \text{HO}_2 + \text{NO}_2$	$2.3\text{E-}12$	Wallington et al. (2018)

Table 1: Gas phase reactions (... continued)

#	labels	reaction	rate coefficient	reference
G4206	TrGC	$\text{C}_2\text{H}_5\text{O}_2 + \text{CH}_3\text{O}_2 \rightarrow .75 \text{ HCHO} + \text{HO}_2 + .75 \text{ CH}_3\text{CHO} + .25 \text{ CH}_3\text{OH}$	$1.6\text{E-}13 \cdot \text{EXP}(195./\text{temp})$	see note*
G4207	TrGC	$\text{C}_2\text{H}_5\text{OOH} + \text{OH} \rightarrow .3 \text{ C}_2\text{H}_5\text{O}_2 + .7 \text{ CH}_3\text{CHO} + .7 \text{ OH}$	$k_{\text{CH300H_OH}}$	see note*
G4208	TrGC	$\text{CH}_3\text{CHO} + \text{OH} \rightarrow \text{ProdH2O} + \text{CH}_3\text{C}(\text{O})\text{OO} + \text{H}_2\text{O}$	$4.4\text{E-}12 \cdot \text{EXP}(365./\text{temp})$	Atkinson et al. (2006)
G4209	TrGCN	$\text{CH}_3\text{CHO} + \text{NO}_3 \rightarrow 1.0 \text{ LossO3R} + 1.0 \text{ LossO3} + \text{CH}_3\text{C}(\text{O})\text{OO} + \text{HNO}_3$	$1.4\text{E-}12 \cdot \text{EXP}(-1900./\text{temp})$	Sander et al. (2011)
G4210	TrGC	$\text{CH}_3\text{COOH} + \text{OH} \rightarrow \text{ProdH2O} + \text{CH}_3\text{O}_2 + \text{CO}_2 + \text{H}_2\text{O}$	$4.2\text{E-}14 \cdot \text{EXP}(855./\text{temp})$	Atkinson et al. (2006)
G4211a	TrGC	$\text{CH}_3\text{C}(\text{O})\text{OO} + \text{HO}_2 \rightarrow \text{CH}_3\text{C}(\text{O})\text{OOH}$	$4.3\text{E-}13 \cdot \text{EXP}(1040./\text{temp}) / (1.+ 37. \cdot \text{EXP}(660./\text{temp}))$	Tyndall et al. (2001a)
G4211b	TrGC	$\text{CH}_3\text{C}(\text{O})\text{OO} + \text{HO}_2 \rightarrow 1.0 \text{ ProdO3} + \text{CH}_3\text{COOH} + \text{O}_3$	$4.3\text{E-}13 \cdot \text{EXP}(1040./\text{temp}) / (1.+ 37. \cdot \text{EXP}(-660./\text{temp}))$	Tyndall et al. (2001a)
G4212	TrGCN	$\text{CH}_3\text{C}(\text{O})\text{OO} + \text{NO} \rightarrow \text{ProdRO2} + 1.0 \text{ ProdO3} + \text{CH}_3\text{O}_2 + \text{CO}_2 + \text{NO}_2$	$8.1\text{E-}12 \cdot \text{EXP}(270./\text{temp})$	Tyndall et al. (2001a)
G4213	TrGCN	$\text{CH}_3\text{C}(\text{O})\text{OO} + \text{NO}_2 \rightarrow \text{PAN}$	$k_{\text{CH3CO3_NO2}}$	Sander et al. (2011)*
G4214	TrGCN	$\text{CH}_3\text{C}(\text{O})\text{OO} + \text{NO}_3 \rightarrow 1.0 \text{ LossO3R} + 1.0 \text{ LossO3} + \text{CH}_3\text{O}_2 + \text{NO}_2 + \text{CO}_2$	$4\text{E-}12$	Canosa-Mas et al. (1996)
G4215a	TrGC	$\text{CH}_3\text{C}(\text{O})\text{OO} + \text{CH}_3\text{O}_2 \rightarrow \text{HCHO} + \text{HO}_2 + \text{CH}_3\text{O}_2 + \text{CO}_2$	$0.9 \cdot 2.0\text{E-}12 \cdot \text{EXP}(500./\text{temp})$	Sander et al. (2011)
G4215b	TrGC	$\text{CH}_3\text{C}(\text{O})\text{OO} + \text{CH}_3\text{O}_2 \rightarrow \text{CH}_3\text{COOH} + \text{HCHO}$	$0.1 \cdot 2.0\text{E-}12 \cdot \text{EXP}(500./\text{temp})$	Sander et al. (2011)
G4216	TrGC	$\text{CH}_3\text{C}(\text{O})\text{OO} + \text{C}_2\text{H}_5\text{O}_2 \rightarrow .82 \text{ CH}_3\text{O}_2 + \text{CH}_3\text{CHO} + .82 \text{ HO}_2 + .18 \text{ CH}_3\text{COOH}$	$4.9\text{E-}12 \cdot \text{EXP}(211./\text{temp})$	Wallington et al. (2018), Kirchner and Stockwell (1996)
G4217	TrGC	$\text{CH}_3\text{C}(\text{O})\text{OO} + \text{CH}_3\text{C}(\text{O})\text{OO} \rightarrow 2 \text{ CH}_3\text{O}_2 + 2 \text{ CO}_2 + \text{O}_2$	$2.5\text{E-}12 \cdot \text{EXP}(500./\text{temp})$	Tyndall et al. (2001a)
G4218	TrGC	$\text{CH}_3\text{C}(\text{O})\text{OOH} + \text{OH} \rightarrow \text{ProdH2O} + \text{CH}_3\text{C}(\text{O})\text{OO} + \text{H}_2\text{O}$	$0.6 \cdot k_{\text{CH300H_OH}}$	Rickard and Pascoe (2009)
G4219	TrGCN	$\text{NACA} + \text{OH} \rightarrow \text{NO}_2 + \text{HCHO} + \text{CO}$	$5.6\text{E-}12 \cdot \text{EXP}(270./\text{temp})$	Pöschl et al. (2000)
G4220	TrGCN	$\text{PAN} + \text{OH} \rightarrow \text{ProdH2O} + \text{HCHO} + \text{CO} + \text{NO}_2 + \text{H}_2\text{O}$	$9.50\text{E-}13 \cdot \text{EXP}(-650./\text{temp})$	Rickard and Pascoe (2009)
G4221	TrGCN	$\text{PAN} \rightarrow \text{CH}_3\text{C}(\text{O})\text{OO} + \text{NO}_2$	$k_{\text{PAN_M}}$	Sander et al. (2011)*
G4222	TrGC	$\text{C}_2\text{H}_2 + \text{OH} \rightarrow \text{CH}_3\text{O}_2$	$k_{\text{3rd}}(\text{temp}, \text{cair}, 5.5\text{e-}30, 0.0, 8.3\text{e-}13, -2., 0.6)$	Sander et al. (2011)
G4300	TrGC	$\text{C}_3\text{H}_8 + \text{OH} \rightarrow \text{ProdH2O} + .82 \text{ iC}_3\text{H}_7\text{O}_2 + .18 \text{ C}_2\text{H}_5\text{O}_2 + \text{H}_2\text{O}$	$1.65\text{E-}17 \cdot \text{temp} \cdot \text{temp} \cdot \text{EXP}(-87./\text{temp})$	Atkinson (2003)
G4301	TrGC	$\text{C}_3\text{H}_6 + \text{O}_3 \rightarrow 1.0 \text{ LossO3R} + 1.0 \text{ LossO3} + .57 \text{ HCHO} + .47 \text{ CH}_3\text{CHO} + .33 \text{ OH} + .26 \text{ HO}_2 + .07 \text{ CH}_3\text{O}_2 + .06 \text{ C}_2\text{H}_5\text{O}_2 + .23 \text{ CH}_3\text{C}(\text{O})\text{OO} + .04 \text{ MGLYOX} + .06 \text{ CH}_4 + .31 \text{ CO} + .22 \text{ HCOOH} + .03 \text{ CH}_3\text{OH}$	$6.5\text{E-}15 \cdot \text{EXP}(-1900./\text{temp})$	Sander et al. (2011)
G4302	TrGC	$\text{C}_3\text{H}_6 + \text{OH} \rightarrow \text{CH}_3\text{CH}(\text{O}_2)\text{CH}_2\text{OH}$	$k_{\text{3rd}}(\text{temp}, \text{cair}, 8\text{E-}27, 3.5, 3\text{E-}11, 0., 0.5)$	Wallington et al. (2018)

Table 1: Gas phase reactions (... continued)

#	labels	reaction	rate coefficient	reference
G4303	TrGCN	$C_3H_6 + NO_3 \rightarrow 1.0 \text{ LossO3R} + 1.0 \text{ LossO3} + \text{LC4H9NO3}$	$4.6E-13 \cdot \text{EXP}(-1155./\text{temp})$	Wallington et al. (2018)
G4304	TrGC	$iC_3H_7O_2 + HO_2 \rightarrow iC_3H_7OOH$	k_{PrO2_HO2}	Atkinson (1997)
G4305	TrGCN	$iC_3H_7O_2 + NO \rightarrow \text{ProdRO2} + 1.0 \text{ ProdO3} + .96 \text{ CH}_3\text{COCH}_3 + .96 \text{ HO}_2 + .04 iC_3H_7\text{ONO}_2$	k_{PrO2_NO}	Wallington et al. (2018)
G4306	TrGC	$iC_3H_7O_2 + CH_3O_2 \rightarrow CH_3COCH_3 + .8 \text{ HCHO} + .8 \text{ HO}_2 + .2 \text{ CH}_3\text{OH}$	k_{PrO2_CH3O2}	Kirchner and Stockwell (1996)
G4307	TrGC	$iC_3H_7OOH + OH \rightarrow .3 iC_3H_7O_2 + .7 \text{ CH}_3\text{COCH}_3 + .7 \text{ OH}$	k_{CH300H_OH}	see note*
G4308	TrGC	$CH_3CH(O_2)CH_2OH + HO_2 \rightarrow CH_3CH(OOH)CH_2OH$	$6.5E-13 \cdot \text{EXP}(650./\text{temp})$	Müller and Brasseur (1995)
G4309	TrGCN	$CH_3CH(O_2)CH_2OH + NO \rightarrow \text{ProdRO2} + 1.0 \text{ ProdO3} + .98 \text{ CH}_3\text{CHO} + .98 \text{ HCHO} + .98 \text{ HO}_2 + .98 \text{ NO}_2 + .02 \text{ LC4H9NO3}$	$4.2E-12 \cdot \text{EXP}(180./\text{temp})$	Müller and Brasseur (1995)
G4310	TrGC	$CH_3CH(OOH)CH_2OH + OH \rightarrow \text{ProdH2O} + .5 \text{ CH}_3CH(O_2)CH_2OH + .5 \text{ CH}_3\text{COCH}_2\text{OH} + .5 \text{ OH} + \text{H}_2\text{O}$	$3.8E-12 \cdot \text{EXP}(200./\text{temp})$	Müller and Brasseur (1995)
G4311	TrGC	$CH_3COCH_3 + OH \rightarrow \text{ProdH2O} + \text{CH}_3\text{COCH}_2\text{O}_2 + \text{H}_2\text{O}$	$1.33E-13 + 3.82E-11 \cdot \text{EXP}(-2000./\text{temp})$	Sander et al. (2011)
G4312	TrGC	$CH_3COCH_2O_2 + HO_2 \rightarrow CH_3COCH_2O_2H$	$8.6E-13 \cdot \text{EXP}(700./\text{temp})$	Tyndall et al. (2001a)
G4313	TrGCN	$CH_3COCH_2O_2 + NO \rightarrow \text{ProdRO2} + 1.0 \text{ ProdO3} + \text{CH}_3\text{C(O)OO} + \text{HCHO} + \text{NO}_2$	$2.9E-12 \cdot \text{EXP}(300./\text{temp})$	Sander et al. (2011)
G4314	TrGC	$CH_3COCH_2O_2 + CH_3O_2 \rightarrow .5 \text{ MGLYOX} + .5 \text{ CH}_3\text{OH} + .3 \text{ CH}_3\text{C(O)OO} + .8 \text{ HCHO} + .3 \text{ HO}_2 + .2 \text{ CH}_3\text{COCH}_2\text{OH}$	$7.5E-13 \cdot \text{EXP}(500./\text{temp})$	Tyndall et al. (2001a)
G4315	TrGC	$CH_3COCH_2O_2H + OH \rightarrow .3 \text{ CH}_3\text{COCH}_2O_2 + .7 \text{ MGLYOX} + .7 \text{ OH}$	k_{CH300H_OH}	see note*
G4316	TrGC	$CH_3COCH_2OH + OH \rightarrow \text{MGLYOX} + \text{HO}_2$	$2.15E-12 \cdot \text{EXP}(305./\text{temp})$	Dillon et al. (2006)
G4317	TrGC	$\text{MGLYOX} + OH \rightarrow \text{CH}_3\text{C(O)OO} + \text{CO}$	$8.4E-13 \cdot \text{EXP}(830./\text{temp})$	Tyndall et al. (1995)
G4320	TrGCN	$iC_3H_7ONO_2 + OH \rightarrow \text{CH}_3\text{COCH}_3 + \text{NO}_2$	$6.2E-13 \cdot \text{EXP}(-230./\text{temp})$	Wallington et al. (2018)
G4400	TrGC	$C_4H_{10} + OH \rightarrow \text{ProdH2O} + \text{LC}_4\text{H}_9\text{O}_2 + \text{H}_2\text{O}$	$1.81E-17 \cdot \text{temp} \cdot \text{temp} \cdot \text{EXP}(114./\text{temp})$	Atkinson (2003)
G4401	TrGC	$\text{LC}_4\text{H}_9\text{O}_2 + \text{CH}_3\text{O}_2 \rightarrow .88 \text{ MEK} + .68 \text{ HCHO} + 1.23 \text{ HO}_2 + .12 \text{ CH}_3\text{CHO} + .12 \text{ C}_2\text{H}_5\text{O}_2 + .18 \text{ CH}_3\text{OH}$	k_{PrO2_CH3O2}	see note*
G4402	TrGC	$\text{LC}_4\text{H}_9\text{O}_2 + \text{HO}_2 \rightarrow \text{LC}_4\text{H}_9\text{OOH}$	k_{PrO2_HO2}	see note*
G4403	TrGCN	$\text{LC}_4\text{H}_9\text{O}_2 + \text{NO} \rightarrow \text{ProdRO2} + 1.0 \text{ ProdO3} + .84 \text{ NO}_2 + .56 \text{ MEK} + .56 \text{ HO}_2 + .28 \text{ C}_2\text{H}_5\text{O}_2 + .28 \text{ CH}_3\text{CHO} + .16 \text{ LC4H9NO3}$	k_{PrO2_NO}	see note*

Table 1: Gas phase reactions (... continued)

#	labels	reaction	rate coefficient	reference
G4404	TrGC	$\text{LC}_4\text{H}_9\text{OOH} + OH \rightarrow 0.85 \text{ ProdH2O} + .15 \text{ LC}_4\text{H}_9\text{O}_2 + .85 \text{ MEK} + .85 \text{ OH} + .85 \text{ H}_2\text{O}$	k_{CH300H_OH}	see note*
G4405	TrGC	$\text{MVK} + \text{O}_3 \rightarrow 1.0 \text{ LossO3R} + 1.0 \text{ LossO3} + .45 \text{ HCOOH} + .9 \text{ MGLYOX} + .1 \text{ CH}_3\text{C(O)OO} + .19 \text{ OH} + .22 \text{ CO} + .32 \text{ HO}_2$	$.5 \cdot (1.36E-15 \cdot \text{EXP}(-2112./\text{temp}) + 7.51E-16 \cdot \text{EXP}(-1521./\text{temp}))$	Pöschl et al. (2000)
G4406	TrGC	$\text{MVK} + OH \rightarrow \text{MVKO2}$	$.5 \cdot (4.1E-12 \cdot \text{EXP}(452./\text{temp}) + 1.9E-11 \cdot \text{EXP}(175./\text{temp}))$	Pöschl et al. (2000)
G4407	TrGC	$\text{MVKO2} + \text{HO}_2 \rightarrow \text{MVKOOH}$	$1.82E-13 \cdot \text{EXP}(1300./\text{temp})$	Pöschl et al. (2000)
G4408	TrGCN	$\text{MVKO2} + \text{NO} \rightarrow \text{ProdRO2} + 1.0 \text{ ProdO3} + \text{NO}_2 + .25 \text{ CH}_3\text{C(O)OO} + .25 \text{ CH}_3\text{COCH}_2\text{OH} + .75 \text{ HCHO} + .25 \text{ CO} + .75 \text{ HO}_2 + .5 \text{ MGLYOX}$	$2.54E-12 \cdot \text{EXP}(360./\text{temp})$	Pöschl et al. (2000)
G4409	TrGCN	$\text{MVKO2} + \text{NO}_2 \rightarrow \text{MPAN}$	$.25 \cdot k_{3rd}(\text{temp}, \text{cair}, 9.7E-29, 5.6, 9.3E-12, 1.5, 0.6)$	Pöschl et al. (2000)
G4410	TrGC	$\text{MVKO2} + \text{CH}_3\text{O}_2 \rightarrow .5 \text{ MGLYOX} + .375 \text{ CH}_3\text{COCH}_2\text{OH} + .125 \text{ CH}_3\text{C(O)OO} + 1.125 \text{ HCHO} + .875 \text{ HO}_2 + .125 \text{ CO} + .25 \text{ CH}_3\text{OH}$	$2.E-12$	von Kuhlmann (2001)
G4411	TrGC	$\text{MVKO2} + \text{MVKO2} \rightarrow \text{CH}_3\text{COCH}_2\text{OH} + \text{MGLYOX} + .5 \text{ CO} + .5 \text{ HCHO} + \text{HO}_2$	$2.E-12$	Pöschl et al. (2000)
G4412	TrGC	$\text{MVKOOH} + OH \rightarrow \text{MVKO2}$	$3.E-11$	Pöschl et al. (2000)
G4413	TrGC	$\text{MEK} + OH \rightarrow \text{LMEKO2}$	$1.3E-12 \cdot \text{EXP}(-25./\text{temp})$	Wallington et al. (2018)
G4414	TrGC	$\text{LMEKO2} + \text{HO}_2 \rightarrow \text{LMEKOOH}$	k_{PrO2_HO2}	see note*
G4415	TrGCN	$\text{LMEKO2} + \text{NO} \rightarrow \text{ProdRO2} + 1.0 \text{ ProdO3} + .985 \text{ CH}_3\text{CHO} + .985 \text{ CH}_3\text{C(O)OO} + .985 \text{ NO}_2 + .015 \text{ LC4H9NO3}$	k_{PrO2_NO}	see note*
G4416	TrGC	$\text{LMEKOOH} + OH \rightarrow .8 \text{ BLACET} + .8 \text{ OH} + .2 \text{ LMEKO2}$	k_{CH300H_OH}	see note*
G4417	TrGCN	$\text{LC4H9NO3} + OH \rightarrow \text{ProdH2O} + \text{MEK} + \text{NO}_2 + \text{H}_2\text{O}$	$1.7E-12$	Wallington et al. (2018)
G4418	TrGCN	$\text{MPAN} + OH \rightarrow \text{CH}_3\text{COCH}_2\text{OH} + \text{NO}_2$	$3.2E-11$	Orlando et al. (2002)
G4419	TrGCN	$\text{MPAN} \rightarrow \text{MVKO2} + \text{NO}_2$	k_{PAN_M}	see note*
G4500	TrGC	$C_5H_8 + \text{O}_3 \rightarrow 1.0 \text{ LossO3R} + 1.0 \text{ LossO3} + .28 \text{ HCOOH} + .65 \text{ MVK} + .1 \text{ MVKO2} + .1 \text{ CH}_3\text{C(O)OO} + .14 \text{ CO} + .58 \text{ HCHO} + .09 \text{ H}_2\text{O}_2 + .08 \text{ CH}_3\text{O}_2 + .25 \text{ OH} + .25 \text{ HO}_2$	$7.86E-15 \cdot \text{EXP}(-1913./\text{temp})$	Pöschl et al. (2000)
G4501	TrGC	$C_5H_8 + OH \rightarrow \text{ISO2}$	$2.54E-11 \cdot \text{EXP}(410./\text{temp})$	Pöschl et al. (2000)
G4502	TrGCN	$C_5H_8 + \text{NO}_3 \rightarrow 1.0 \text{ LossO3R} + 1.0 \text{ LossO3} + \text{ISON}$	$3.03E-12 \cdot \text{EXP}(-446./\text{temp})$	Pöschl et al. (2000)
G4503	TrGC	$\text{ISO2} + \text{HO}_2 \rightarrow \text{ISOOH}$	$2.22E-13 \cdot \text{EXP}(1300./\text{temp})$	Boyd et al. (2003)

Table 1: Gas phase reactions (... continued)

#	labels	reaction	rate coefficient	reference
G6404	StGCl	$\text{CCl}_4 + \text{O}(^1\text{D}) \rightarrow 4.0 \text{ ProdLCl} + \text{LCARBON} + \text{ClO} + 3 \text{ Cl}$	3.3E-10	Burkholder et al. (2015)
G6405	StGCl	$\text{CH}_3\text{Cl} + \text{O}(^1\text{D}) \rightarrow 1.0 \text{ ProdLCl} + 1.0 \text{ LossO3Cl} + 1.0 \text{ LossO3} + \text{OH} + \text{Cl}$	1.65E-10	see note*
G6406	StGCl	$\text{CH}_2\text{Cl} + \text{OH} \rightarrow \text{ProdH}_2\text{O} + 1.0 \text{ ProdLCl} + \text{LCARBON} + \text{H}_2\text{O} + \text{Cl}$	$1.96\text{E-}12 \cdot \text{EXP}(-1200./\text{temp})$	Burkholder et al. (2015)
G6407	StGCCl	$\text{CH}_3\text{CCl}_3 + \text{O}(^1\text{D}) \rightarrow 3.0 \text{ ProdLCl} + 1.0 \text{ LossO3Cl} + 1.0 \text{ LossO3} + 2 \text{ LCARBON} + \text{OH} + 3 \text{ Cl}$	3.25E-10	Burkholder et al. (2015)
G6408	StTrGCCl	$\text{CH}_2\text{CCl}_3 + \text{OH} \rightarrow \text{ProdH}_2\text{O} + 3.0 \text{ ProdLCl} + 2 \text{ LCARBON} + \text{H}_2\text{O} + 3 \text{ Cl}$	$1.64\text{E-}12 \cdot \text{EXP}(-1520./\text{temp})$	Burkholder et al. (2015)
G6409	TrGCCl	$\text{Cl} + \text{C}_2\text{H}_4 \rightarrow .6666667 \text{ CH}_3\text{CH}(\text{O}_2)\text{CH}_2\text{OH} + \text{HCl}$	$k_{3rd_iupac}(\text{temp}, \text{cair}, 1.85\text{E-}29, 3.3, 6.0\text{E-}10, 0.0, 0.4)$	Atkinson et al. (2006)
G6410	TrGCCl	$\text{Cl} + \text{CH}_3\text{CHO} \rightarrow \text{HCl} + \text{CH}_3\text{C}(\text{O})\text{OO}$	8.0e-11	Atkinson et al. (2006)
G6411	TrGCCl	$\text{C}_2\text{H}_2 + \text{Cl} \rightarrow \text{LCARBON} + \text{CH}_3\text{O}_2 + \text{HCl}$	$k_{3rd_iupac}(\text{temp}, \text{cair}, 6.1\text{E-}30, 3.0, 2.0\text{e-}10, 0., 0.6)$	Atkinson et al. (2006)*
G6412	TrGCCl	$\text{C}_2\text{H}_6 + \text{Cl} \rightarrow \text{C}_2\text{H}_5\text{O}_2 + \text{HCl}$	$8.3\text{E-}11 \cdot \text{EXP}(-100./\text{temp})$	Atkinson et al. (2006)
G6500	StGCIF	$\text{CF}_2\text{Cl}_2 + \text{O}(^1\text{D}) \rightarrow 2.0 \text{ ProdLCl} + \text{LCARBON} + 2 \text{ LFLUORINE} + \text{ClO} + \text{Cl}$	1.4E-10	Burkholder et al. (2015)
G6501	StGCIF	$\text{CFCl}_3 + \text{O}(^1\text{D}) \rightarrow 3.0 \text{ ProdLCl} + \text{LCARBON} + \text{LFLUORINE} + \text{ClO} + 2 \text{ Cl}$	2.3E-10	Burkholder et al. (2015)
G7100	StTrGBr	$\text{Br} + \text{O}_3 \rightarrow \text{BrO} + \text{O}_2$	$1.7\text{E-}11 \cdot \text{EXP}(-800./\text{temp})$	Atkinson et al. (2007)
G7101	StGBr	$\text{BrO} + \text{O}(^3\text{P}) \rightarrow 2.0 \text{ LossO3Br} + 2.0 \text{ LossO3} + \text{Br} + \text{O}_2$	$1.9\text{E-}11 \cdot \text{EXP}(230./\text{temp})$	Atkinson et al. (2007)
G7102a	StTrGBr	$\text{BrO} + \text{BrO} \rightarrow 2.0 \text{ LossO3Br} + 2.0 \text{ LossO3} + 2 \text{ Br} + \text{O}_2$	2.7E-12	Atkinson et al. (2007)
G7102b	StTrGBr	$\text{BrO} + \text{BrO} \rightarrow 2.0 \text{ LossO3Br} + 2.0 \text{ LossO3} + \text{Br}_2 + \text{O}_2$	$2.9\text{E-}14 \cdot \text{EXP}(840./\text{temp})$	Atkinson et al. (2007)
G7200	StTrGBr	$\text{Br} + \text{HO}_2 \rightarrow \text{HBr} + \text{O}_2$	$7.7\text{E-}12 \cdot \text{EXP}(-450./\text{temp})$	Atkinson et al. (2007)
G7201	StTrGBr	$\text{BrO} + \text{HO}_2 \rightarrow \text{HOBr} + \text{O}_2$	$4.5\text{E-}12 \cdot \text{EXP}(500./\text{temp})$	Atkinson et al. (2007)
G7202	StTrGBr	$\text{HBr} + \text{OH} \rightarrow \text{ProdH}_2\text{O} + \text{Br} + \text{H}_2\text{O}$	$6.7\text{E-}12 \cdot \text{EXP}(155./\text{temp})$	Atkinson et al. (2007)
G7203	StGBr	$\text{HOBr} + \text{O}(^3\text{P}) \rightarrow 1.0 \text{ LossO3Br} + 1.0 \text{ LossO3} + \text{OH} + \text{BrO}$	$1.2\text{E-}10 \cdot \text{EXP}(-430./\text{temp})$	Atkinson et al. (2007)
G7204	StTrGBr	$\text{Br}_2 + \text{OH} \rightarrow 1.0 \text{ ProdO3} + \text{HOBr} + \text{Br}$	$2.0\text{E-}11 \cdot \text{EXP}(240./\text{temp})$	Atkinson et al. (2007)
G7300	TrGBrN	$\text{Br} + \text{BrNO}_3 \rightarrow \text{Br}_2 + \text{NO}_3$	4.9E-11	Orlando and Tyndall (1996)
G7301	StTrGBrN	$\text{BrO} + \text{NO} \rightarrow \text{Br} + \text{NO}_2$	$8.7\text{E-}12 \cdot \text{EXP}(260./\text{temp})$	Atkinson et al. (2007)
G7302	StTrGBrN	$\text{BrO} + \text{NO}_2 \rightarrow \text{BrNO}_3$	k_{BrO_NO2}	Atkinson et al. (2007)*

Table 1: Gas phase reactions (... continued)

#	labels	reaction	rate coefficient	reference
G4504	TrGCN	$\text{ISO}_2 + \text{NO} \rightarrow \text{ProdRO}_2 + 1.0 \text{ ProdO}_3 + .956 \text{ NO}_2 + .956 \text{ MVK} + .956 \text{ HCHO} + .956 \text{ HO}_2 + .044 \text{ ISON}$	$2.54\text{E-}12 \cdot \text{EXP}(360./\text{temp})$	Pöschl et al. (2000)
G4505	TrGC	$\text{ISO}_2 + \text{CH}_3\text{O}_2 \rightarrow .5 \text{ MVK} + 1.25 \text{ HCHO} + \text{HO}_2 + .25 \text{ MGLYOX} + .25 \text{ CH}_3\text{COCH}_2\text{OH} + .25 \text{ CH}_3\text{OH}$	2.E-12	von Kuhlmann (2001)
G4506	TrGC	$\text{ISO}_2 + \text{ISO}_2 \rightarrow 2 \text{ MVK} + \text{HCHO} + \text{HO}_2$	2.E-12	Pöschl et al. (2000)
G4507	TrGC	$\text{ISOOH} + \text{OH} \rightarrow \text{MVK} + \text{OH}$	1.E-10	Pöschl et al. (2000)
G4508	TrGCN	$\text{ISON} + \text{OH} \rightarrow \text{CH}_3\text{COCH}_2\text{OH} + \text{NACA}$	1.3E-11	Pöschl et al. (2000)
G6100	UpStTrGCCl	$\text{Cl} + \text{O}_3 \rightarrow \text{ClO} + \text{O}_2$	$2.8\text{E-}11 \cdot \text{EXP}(-250./\text{temp})$	Atkinson et al. (2007)
G6101	UpStGCCl	$\text{ClO} + \text{O}(^3\text{P}) \rightarrow 2.0 \text{ LossO3Cl} + 2.0 \text{ LossO3} + \text{Cl} + \text{O}_2$	$2.5\text{E-}11 \cdot \text{EXP}(110./\text{temp})$	Atkinson et al. (2007)
G6102a	StTrGCCl	$\text{ClO} + \text{ClO} \rightarrow 2.0 \text{ LossO3Cl} + 2.0 \text{ LossO3} + \text{Cl}_2 + \text{O}_2$	$1.0\text{E-}12 \cdot \text{EXP}(-1590./\text{temp})$	Atkinson et al. (2007)
G6102b	StTrGCCl	$\text{ClO} + \text{ClO} \rightarrow 2.0 \text{ LossO3Cl} + 2.0 \text{ LossO3} + 2 \text{ Cl} + \text{O}_2$	$3.0\text{E-}11 \cdot \text{EXP}(-2450./\text{temp})$	Atkinson et al. (2007)
G6102c	StTrGCCl	$\text{ClO} + \text{ClO} \rightarrow 1.0 \text{ LossO3Cl} + 1.0 \text{ LossO3} + \text{Cl} + \text{OCIO}$	$3.5\text{E-}13 \cdot \text{EXP}(-1370./\text{temp})$	Atkinson et al. (2007)
G6102d	StTrGCCl	$\text{ClO} + \text{ClO} \rightarrow \text{Cl}_2\text{O}_2$	k_{ClO_ClO}	Burkholder et al. (2015)
G6103	StTrGCCl	$\text{Cl}_2\text{O}_2 \rightarrow \text{ClO} + \text{ClO}$	$k_{ClO_ClO} / (2.16\text{E-}27 \cdot \text{EXP}(8537./\text{temp}))$	Burkholder et al. (2015)*
G6200	StGCl	$\text{Cl} + \text{H}_2 \rightarrow \text{HCl} + \text{H}$	$3.9\text{E-}11 \cdot \text{EXP}(-2310./\text{temp})$	Atkinson et al. (2007)
G6201a	StGCl	$\text{Cl} + \text{HO}_2 \rightarrow \text{HCl} + \text{O}_2$	$4.4\text{E-}11 - 7.5\text{E-}11 \cdot \text{EXP}(-620./\text{temp})$	Atkinson et al. (2007)
G6201b	StGCl	$\text{Cl} + \text{HO}_2 \rightarrow 1.0 \text{ ProdO}_3 + \text{ClO} + \text{OH}$	$7.5\text{E-}11 \cdot \text{EXP}(-620./\text{temp})$	Atkinson et al. (2007)
G6202	StTrGCCl	$\text{Cl} + \text{H}_2\text{O}_2 \rightarrow \text{HCl} + \text{HO}_2$	$1.1\text{E-}11 \cdot \text{EXP}(-980./\text{temp})$	Atkinson et al. (2007)
G6203	StGCl	$\text{ClO} + \text{OH} \rightarrow 1.0 \text{ LossO3Cl} + 1.0 \text{ LossO3} + .94 \text{ Cl} + .94 \text{ HO}_2 + .06 \text{ HCl} + .06 \text{ O}_2$	$7.3\text{E-}12 \cdot \text{EXP}(300./\text{temp})$	Atkinson et al. (2007)
G6204	StTrGCCl	$\text{ClO} + \text{HO}_2 \rightarrow \text{HOCl} + \text{O}_2$	$2.2\text{E-}12 \cdot \text{EXP}(340./\text{temp})$	Atkinson et al. (2007)*
G6205	StTrGCCl	$\text{HCl} + \text{OH} \rightarrow \text{ProdH}_2\text{O} + \text{Cl} + \text{H}_2\text{O}$	$1.7\text{E-}12 \cdot \text{EXP}(-230./\text{temp})$	Atkinson et al. (2007)
G6206	StGCl	$\text{HOCl} + \text{OH} \rightarrow \text{ProdH}_2\text{O} + \text{ClO} + \text{H}_2\text{O}$	$3.0\text{E-}12 \cdot \text{EXP}(-500./\text{temp})$	Burkholder et al. (2015)
G6300	UpStTrGCIN	$\text{ClO} + \text{NO} \rightarrow \text{NO}_2 + \text{Cl}$	$6.2\text{E-}12 \cdot \text{EXP}(295./\text{temp})$	Atkinson et al. (2007)
G6301	StTrGCIN	$\text{ClO} + \text{NO}_2 \rightarrow \text{ClNO}_3$	$k_{3rd_iupac}(\text{temp}, \text{cair}, 1.6\text{E-}31, 3.4, 7\text{E-}11, 0., 0.4)$	Atkinson et al. (2007)
G6302	TrGCIN	$\text{ClNO}_3 \rightarrow \text{ClO} + \text{NO}_2$	$6.918\text{E-}7 \cdot \text{EXP}(-10909./\text{temp}) \cdot (\text{cair})$	Anderson and Fahey (1990)
G6303	StGCIN	$\text{ClNO}_3 + \text{O}(^3\text{P}) \rightarrow \text{ClO} + \text{NO}_3$	$4.5\text{E-}12 \cdot \text{EXP}(-900./\text{temp})$	Atkinson et al. (2007)
G6304	StTrGCIN	$\text{ClNO}_3 + \text{Cl} \rightarrow \text{Cl}_2 + \text{NO}_3$	$6.2\text{E-}12 \cdot \text{EXP}(145./\text{temp})$	Atkinson et al. (2007)
G6400	StTrGCCl	$\text{Cl} + \text{CH}_4 \rightarrow \text{HCl} + \text{CH}_3\text{O}_2$	$6.6\text{E-}12 \cdot \text{EXP}(-1240./\text{temp})$	Atkinson et al. (2006)
G6401	StTrGCCl	$\text{Cl} + \text{HCHO} \rightarrow \text{HCl} + \text{CO} + \text{HO}_2$	$8.1\text{E-}11 \cdot \text{EXP}(-34./\text{temp})$	Atkinson et al. (2006)
G6402	StTrGCCl	$\text{Cl} + \text{CH}_3\text{OOH} \rightarrow \text{HCHO} + \text{HCl} + \text{OH}$	5.9E-11	Atkinson et al. (2006)*
G6403	StTrGCCl	$\text{ClO} + \text{CH}_3\text{O}_2 \rightarrow 1.0 \text{ LossO3Cl} + 1.0 \text{ LossO3} + \text{HO}_2 + \text{Cl} + \text{HCHO}$	$1.8\text{E-}12 \cdot \text{EXP}(-600./\text{temp})$	Burkholder et al. (2015)

Table 1: Gas phase reactions (... continued)

#	labels	reaction	rate coefficient	reference
G7303	TrGBrN	$\text{BrNO}_3 \rightarrow \text{BrO} + \text{NO}_2$	$k_{\text{BrO_NO2}} / (5.44\text{E-}9 \cdot \text{EXP}(14192./\text{temp}) * 1.1\text{E}6 \cdot \text{R_gas} \cdot \text{temp} / (\text{atm}2\text{Pa} \cdot \text{N}_A))$	Orlando and Tyndall (1996), Atkinson et al. (2007)*
G7400	StTrGBr	$\text{Br} + \text{HCHO} \rightarrow \text{HBr} + \text{CO} + \text{HO}_2$	$7.7\text{E-}12 \cdot \text{EXP}(-580./\text{temp})$	Atkinson et al. (2006)
G7401	TrGBr	$\text{Br} + \text{CH}_3\text{OOH} \rightarrow \text{CH}_3\text{O}_2 + \text{HBr}$	$2.6\text{E-}12 \cdot \text{EXP}(-1600./\text{temp})$	Kondo and Benson (1984)
G7402a	TrGBr	$\text{BrO} + \text{CH}_3\text{O}_2 \rightarrow \text{HOBr} + \text{HCHO}$	$f_{\text{BrO_CH3O2}} * 5.7\text{E-}12$	Aranda et al. (1997)
G7402b	TrGBr	$\text{BrO} + \text{CH}_3\text{O}_2 \rightarrow 1.0 \text{ LossO3Br} + 1.0 \text{ LossO3} + \text{Br} + \text{HCHO} + \text{HO}_2$	$(1 - f_{\text{BrO_CH3O2}}) * 5.7\text{E-}12$	Aranda et al. (1997)
G7403	StTrGBr	$\text{CH}_3\text{Br} + \text{OH} \rightarrow \text{ProdH2O} + 1.0 \text{ ProdLBr} + \text{LCARBON} + \text{H}_2\text{O} + \text{Br}$	$1.42\text{E-}12 \cdot \text{EXP}(-1150./\text{temp})$	Burkholder et al. (2015)
G7404	TrGBrC	$\text{Br} + \text{C}_2\text{H}_4 \rightarrow .6666667 \text{ CH}_3\text{CH}(\text{O}_2)\text{CH}_2\text{OH} + \text{HBr}$	$2.8\text{E-}13 \cdot \text{EXP}(224./\text{temp}) / (1 + 1.13\text{E}24 \cdot \text{EXP}(-3200./\text{temp}) / \text{C}(\text{ind}_2))$	Atkinson et al. (2006)
G7405	TrGBrC	$\text{Br} + \text{CH}_3\text{CHO} \rightarrow \text{HBr} + \text{CH}_3\text{C}(\text{O})\text{OO}$	$1.8\text{E-}11 \cdot \text{EXP}(-460./\text{temp})$	Atkinson et al. (2006)
G7406	TrGBrC	$\text{Br} + \text{C}_2\text{H}_2 \rightarrow \text{LCARBON} + \text{CH}_3\text{O}_2 + \text{HBr}$	$6.35\text{E-}15 \cdot \text{EXP}(440./\text{temp})$	Atkinson et al. (2006)
G7407	TrGBr	$\text{CHBr}_3 + \text{OH} \rightarrow \text{ProdH2O} + 3.0 \text{ ProdSBr} + \text{LCARBON} + \text{H}_2\text{O} + 3 \text{ Br}$	$9.0\text{E-}13 \cdot \text{EXP}(-360./\text{temp})$	Burkholder et al. (2015)*
G7408	TrGBr	$\text{CH}_2\text{Br}_2 + \text{OH} \rightarrow \text{ProdH2O} + 2.0 \text{ ProdSBr} + \text{LCARBON} + \text{H}_2\text{O} + 2 \text{ Br}$	$2.0\text{E-}12 \cdot \text{EXP}(-840./\text{temp})$	Burkholder et al. (2015)*
G7600	TrGBrCl	$\text{Br} + \text{BrCl} \rightarrow \text{Br}_2 + \text{Cl}$	$3.32\text{E-}15$	Manion et al. (2015)
G7601	TrGBrCl	$\text{Br} + \text{Cl}_2 \rightarrow \text{BrCl} + \text{Cl}$	$1.10\text{E-}15$	Dolson and Leone (1987)
G7602	TrGBrCl	$\text{Br}_2 + \text{Cl} \rightarrow \text{BrCl} + \text{Br}$	$2.3\text{E-}10 \cdot \text{EXP}(135./\text{temp})$	Bedjanian et al. (1998)
G7603a	StTrGBrCl	$\text{BrO} + \text{ClO} \rightarrow 0.5 \text{ LossO3Br} + 0.5 \text{ LossO3Cl} + 1.0 \text{ LossO3} + \text{Br} + \text{OCLO}$	$1.6\text{E-}12 \cdot \text{EXP}(430./\text{temp})$	Atkinson et al. (2007)
G7603b	StTrGBrCl	$\text{BrO} + \text{ClO} \rightarrow 1.0 \text{ LossO3Br} + 1.0 \text{ LossO3Cl} + 2.0 \text{ LossO3} + \text{Br} + \text{Cl} + \text{O}_2$	$2.9\text{E-}12 \cdot \text{EXP}(220./\text{temp})$	Atkinson et al. (2007)
G7603c	StTrGBrCl	$\text{BrO} + \text{ClO} \rightarrow 1.0 \text{ LossO3Br} + 1.0 \text{ LossO3Cl} + 2.0 \text{ LossO3} + \text{BrCl} + \text{O}_2$	$5.8\text{E-}13 \cdot \text{EXP}(170./\text{temp})$	Atkinson et al. (2007)
G7604	TrGBrCl	$\text{BrCl} + \text{Cl} \rightarrow \text{Br} + \text{Cl}_2$	$1.45\text{E-}11$	Clyne and Cruse (1972)
G7605	TrGBrCl	$\text{CHCl}_2\text{Br} + \text{OH} \rightarrow \text{ProdH2O} + 1.0 \text{ ProdSBr} + 2.0 \text{ ProdSCL} + \text{LCARBON} + 2 \text{ Cl} + \text{H}_2\text{O} + \text{Br}$	$2.0\text{E-}12 \cdot \text{EXP}(-840./\text{temp})$	see note*
G7606	TrGBrCl	$\text{CHClBr}_2 + \text{OH} \rightarrow \text{ProdH2O} + 2.0 \text{ ProdSBr} + 1.0 \text{ ProdSCL} + \text{LCARBON} + \text{Cl} + \text{H}_2\text{O} + 2 \text{ Br}$	$2.0\text{E-}12 \cdot \text{EXP}(-840./\text{temp})$	see note*

Table 1: Gas phase reactions (... continued)

#	labels	reaction	rate coefficient	reference
G7607	TrGBrCl	$\text{CH}_2\text{ClBr} + \text{OH} \rightarrow \text{ProdH2O} + 1.0 \text{ ProdSBr} + 1.0 \text{ ProdSCL} + \text{LCARBON} + \text{Cl} + \text{H}_2\text{O} + \text{Br}$	$2.1\text{E-}12 \cdot \text{EXP}(-880./\text{temp})$	Burkholder et al. (2015)*
G9200a	StTrGS	$\text{SO}_2 + \text{OH} \rightarrow 1.0 \text{ ProdO3} + \text{SO}_3 + \text{HO}_2$	$k_{3\text{rd}}(\text{temp}, \text{cair}, 3.3\text{E-}31, 4.3, 1.6\text{E-}12, 0., 0.6)$	Sander et al. (2011)
G9400a	TrGCS	$\text{DMS} + \text{OH} \rightarrow 1.0 \text{ ProdO3} + \text{CH}_3\text{SO}_2 + \text{HCHO}$	$1.13\text{E-}11 \cdot \text{EXP}(-253./\text{temp})$	Atkinson et al. (2004)*
G9400b	TrGCS	$\text{DMS} + \text{OH} \rightarrow 1.0 \text{ ProdO3} + \text{DMSO} + \text{HO}_2$	$k_{\text{DMS_OH}}$	Atkinson et al. (2004)*
G9401	TrGCNS	$\text{DMS} + \text{NO}_3 \rightarrow \text{CH}_3\text{SO}_2 + \text{HNO}_3 + \text{HCHO}$	$1.9\text{E-}13 \cdot \text{EXP}(520./\text{temp})$	Atkinson et al. (2004)
G9402	TrGCS	$\text{DMSO} + \text{OH} \rightarrow 0.40 \text{ ProdO3} + .6 \text{ SO}_2 + \text{HCHO} + .6 \text{ CH}_3\text{O}_2 + .4 \text{ HO}_2 + .4 \text{ CH}_3\text{SO}_3\text{H}$	$1\text{E-}10$	Hynes and Wine (1996)
G9403	TrGS	$\text{CH}_3\text{SO}_2 \rightarrow \text{SO}_2 + \text{CH}_3\text{O}_2$	$1.8\text{E}13 \cdot \text{EXP}(-8661./\text{temp})$	Barone et al. (1995)
G9404	TrGS	$\text{CH}_3\text{SO}_2 + \text{O}_3 \rightarrow \text{CH}_3\text{SO}_3$	$3\text{E-}13$	Barone et al. (1995)
G9405	TrGS	$\text{CH}_3\text{SO}_3 + \text{HO}_2 \rightarrow \text{CH}_3\text{SO}_3\text{H}$	$5\text{E-}11$	Barone et al. (1995)
G9600	TrGCCIS	$\text{DMS} + \text{Cl} \rightarrow 1.0 \text{ ProdO3} + \text{CH}_3\text{SO}_2 + \text{HCl} + \text{HCHO}$	$3.3\text{E-}10$	Atkinson et al. (2004)
G9700	TrGBrCS	$\text{DMS} + \text{Br} \rightarrow 1.0 \text{ ProdO3} + \text{CH}_3\text{SO}_2 + \text{HBr} + \text{HCHO}$	$9\text{E-}11 \cdot \text{EXP}(-2386./\text{temp})$	Jefferson et al. (1994)
G9701	TrGBrCS	$\text{DMS} + \text{BrO} \rightarrow \text{DMSO} + \text{Br}$	$4.4\text{E-}13$	Ingham et al. (1999)
G01Diag	StTrG	$\text{O}_3(\text{s}) \rightarrow \text{LO}_3(\text{s})$	$k_{03\text{s}}$	Roelofs and Lelieveld (1997)
G42085abS	TrGCN	$\text{CH}_3\text{CN} + \text{OH} \rightarrow \text{OH}$	$8.1\text{E-}13 \cdot \text{EXP}(-1080./\text{temp})$	Atkinson et al. (2006), Tyndall et al. (2001b)
G42086bcS	TrGCN	$\text{CH}_3\text{CN} + \text{O}(^1\text{D}) \rightarrow \text{O}(^1\text{D})$	$2.54\text{E-}10 \cdot \text{EXP}(-24./\text{temp}) * (1 - 0.0269 \cdot \text{EXP}(137./\text{temp}))$	Strekowski et al. (2010)
G6416S	TrGCCIN	$\text{Cl} + \text{CH}_3\text{CN} \rightarrow \text{Cl}$	$1.6\text{E-}11 \cdot \text{EXP}(-2104./\text{temp})$	Tyndall et al. (1996), Tyndall et al. (2001b), Sander et al. (2019)
G6500dc01	StGClF	$\text{CHF}_2\text{Cl} + \text{O}(^1\text{D}) \rightarrow 0.72 \text{ ProdLCl} + 0.17 \text{ LossO3O} + 0.17 \text{ LossO3} + 0.55 \text{ ClO} + 0.05 \text{ OH} + 0.28 \text{ O}(^3\text{P}) + 0.28 \text{ CHF}_2\text{Cl} + 0.72 \text{ LCARBON} + 0.17 \text{ Cl}$	$1.0\text{E-}10$	Sander et al. (2011)
G6500dc02	StG	$\text{CHF}_2\text{Cl} + \text{OH} \rightarrow \text{ProdH2O} + \text{LCARBON} + \text{H}_2\text{O} + 2 \text{ LFLUORINE} + \text{Cl}$	$1.05\text{E-}12 \cdot \text{EXP}(-1600./\text{temp})$	Sander et al. (2011)
G6500dc03	StG	$\text{CHF}_2\text{Cl} + \text{Cl} \rightarrow \text{HCl} + \text{LCARBON} + 2 \text{ LFLUORINE} + \text{Cl}$	$5.6\text{E-}12 \cdot \text{EXP}(-2430./\text{temp})$	Sander et al. (2011)
G5300dc01	StGCF	$\text{CH}_2\text{FCF}_3 + \text{O}(^1\text{D}) \rightarrow 0.35 \text{ LossO3O} + 0.35 \text{ LossO3} + 0.65 \text{ O}(^3\text{P}) + 0.65 \text{ CH}_2\text{FCF}_3 + 0.24 \text{ OH} + 0.70 \text{ LCARBON} + 1.4 \text{ LFLUORINE}$	$4.9\text{E-}11$	Sander et al. (2011)*
G5300dc02	StG	$\text{CH}_2\text{FCF}_3 + \text{OH} \rightarrow \text{ProdH2O} + 2 \text{ LCARBON} + \text{H}_2\text{O} + 4 \text{ LFLUORINE}$	$1.05\text{E-}12 \cdot \text{EXP}(-1630./\text{temp})$	Sander et al. (2011)

Table 1: Gas phase reactions (... continued)

#	labels	reaction	rate coefficient	reference
G6500dc11	StG	$\text{CF}_3\text{CF}_2\text{Cl} + \text{O}(^1\text{D}) \rightarrow 0.30 \text{ LossO3O} + 0.30 \text{ LossO3} + 0.7 \text{ O}(^3\text{P}) + 0.7 \text{ CF}_3\text{CF}_2\text{Cl} + 0.6 \text{ L CARBON} + 1.5 \text{ LFLUORINE} + 0.3 \text{ Cl}$	5.0E-11	Sander et al. (2011)
G5300dc10	StG	$\text{CH}_2\text{F}_2 + \text{O}(^1\text{D}) \rightarrow 0.30 \text{ LossO3O} + 0.30 \text{ LossO3} + 0.7 \text{ O}(^3\text{P}) + 0.7 \text{ CH}_2\text{F}_2 + 0.3 \text{ L CARBON} + 0.6 \text{ LFLUORINE}$	5.1e-11	Sander et al. (2011)
G5300dc11	StG	$\text{CH}_2\text{F}_2 + \text{OH} \rightarrow \text{ProdH2O} + \text{H}_2\text{O} + \text{L CARBON} + 2 \text{ LFLUORINE}$	1.7e-12*EXP(-1500./temp)	Sander et al. (2011)
G5300dc12	StG	$\text{CH}_3\text{CHF}_2 + \text{O}(^1\text{D}) \rightarrow 0.66 \text{ LossO3O} + 0.66 \text{ LossO3} + 0.34 \text{ O}(^3\text{P}) + 0.34 \text{ CH}_3\text{CHF}_2 + 0.15 \text{ OH} + 1.32 \text{ L CARBON} + 1.32 \text{ LFLUORINE}$	1.75e-10	Sander et al. (2011)
G5300dc13	StG	$\text{CH}_3\text{CHF}_2 + \text{OH} \rightarrow 2 \text{ L CARBON} + 2 \text{ LFLUORINE}$	8.7e-13*EXP(-975./temp)	Sander et al. (2011)
G6500dc12	StG	$\text{CH}_3\text{CHF}_2 + \text{Cl} \rightarrow \text{HCl} + 2 \text{ L CARBON} + 2 \text{ LFLUORINE}$	6.0e-12*EXP(-960./temp)	Sander et al. (2011)
G9100	TrStGS	$\text{SO} + \text{O}_2 \rightarrow 2.0 \text{ ProdO3} + \text{SO}_2 + \text{O}(^3\text{P})$	1.25e-13*exp(-2190./temp)	Sander et al. (2011)
G9101	TrStGS	$\text{SO} + \text{O}_3 \rightarrow \text{SO}_2 + \text{O}_2$	3.4e-12*exp(-1100./temp)	Sander et al. (2011)
G9102	TrStGS	$\text{S} + \text{O}_2 \rightarrow 1.0 \text{ ProdO3} + \text{SO} + \text{O}(^3\text{P})$	2.3e-12	Sander et al. (2011)
G9201	TrStGS	$\text{SH} + \text{O}_2 \rightarrow \text{OH} + \text{SO}$	4.e-19	Sander et al. (2011)
G9202	TrStGS	$\text{SO}_3 + \text{H}_2\text{O} \rightarrow \text{LossH2O} + \text{H}_2\text{SO}_4$	8.5e-41*exp(6540./temp)*C(ind_H2O)	Sander et al. (2003)
G9406	TrStGS	$\text{OCS} + \text{OH} \rightarrow \text{SH} + \text{CO}_2$	1.1e-13*exp(-1200./temp)	Sander et al. (2011)
G9407	TrStGS	$\text{OCS} + \text{O}(^3\text{P}) \rightarrow 1.0 \text{ LossO3Su} + 1.0 \text{ LossO3} + \text{CO} + \text{SO}$	2.1e-11*exp(-2200./temp)	Sander et al. (2011)

Table 1: Gas phase reactions (... continued)

#	labels	reaction	rate coefficient	reference
G5300dc03	StG	$\text{CH}_2\text{FCF}_3 + \text{Cl} \rightarrow \text{HCl} + 2 \text{ L CARBON} + 4 \text{ LFLUORINE}$	2.4e-12*EXP(-2200./temp)	Sander et al. (2011)
G6500dc04	StG	$\text{CF}_2\text{CFCF}_2 + \text{O}(^1\text{D}) \rightarrow 2.4 \text{ ProdLCl} + 0.2 \text{ O}(^3\text{P}) + 0.2 \text{ CF}_2\text{CFCF}_2 + 0.8 \text{ ClO} + 1.6 \text{ L CARBON} + 1.6 \text{ Cl} + 2.4 \text{ LFLUORINE}$	2.0E-10	Sander et al. (2011)
G6400dc01	StG	$\text{CH}_2\text{Cl}_2 + \text{OH} \rightarrow \text{ProdH2O} + \text{L CARBON} + \text{H}_2\text{O} + 2 \text{ Cl}$	1.9e-12*EXP(-870./temp)	Sander et al. (2011)
G6400dc02	StG	$\text{CH}_2\text{Cl}_2 + \text{Cl} \rightarrow \text{L CARBON} + \text{HCl} + 2 \text{ Cl}$	7.4e-12*EXP(-910./temp)	Sander et al. (2011)
G5300dc04	StG	$\text{CHF}_3 + \text{O}(^1\text{D}) \rightarrow 0.23 \text{ LossO3O} + 0.23 \text{ LossO3} + 0.77 \text{ O}(^3\text{P}) + 0.77 \text{ CHF}_3 + 0.23 \text{ L CARBON} + 0.69 \text{ LFLUORINE}$	9.1E-12	Sander et al. (2011)*
G5300dc05	StG	$\text{CHF}_3 + \text{OH} \rightarrow \text{ProdH2O} + \text{L CARBON} + \text{H}_2\text{O} + 3 \text{ LFLUORINE}$	5.2e-13*EXP(-2210./temp)	Sander et al. (2011)
G6500dc05	StG	$\text{CH}_3\text{CFCl}_2 + \text{O}(^1\text{D}) \rightarrow 0.69 \text{ LossO3O} + 0.69 \text{ LossO3} + 0.31 \text{ O}(^3\text{P}) + 0.31 \text{ CH}_3\text{CFCl}_2 + 1.38 \text{ L CARBON} + 1.38 \text{ Cl} + 1 \text{ LFLUORINE}$	2.6E-10	Sander et al. (2011)*
G6500dc06	StG	$\text{CH}_3\text{CFCl}_2 + \text{OH} \rightarrow \text{ProdH2O} + \text{H}_2\text{O} + 2 \text{ L CARBON} + 1 \text{ LFLUORINE} + 2 \text{ Cl}$	1.25e-12*EXP(-1600./temp)	Sander et al. (2011)
G6500dc07	StG	$\text{CH}_3\text{CFCl}_2 + \text{Cl} \rightarrow \text{HCl} + 2 \text{ L CARBON} + 1 \text{ LFLUORINE} + 2 \text{ Cl}$	3.4e-12*EXP(-2200./temp)	Sander et al. (2011)
G6500dc08	StG	$\text{CF}_2\text{CFCF}_2 + \text{O}(^1\text{D}) \rightarrow 0.75 \text{ LossO3O} + 0.75 \text{ LossO3} + 0.25 \text{ O}(^3\text{P}) + 0.25 \text{ CF}_2\text{CFCF}_2 + 1.5 \text{ L CARBON} + 1.5 \text{ Cl} + 3 \text{ LFLUORINE}$	1.3E-10	Sander et al. (2011)
G5300dc06	StG	$\text{CHF}_2\text{CF}_3 + \text{O}(^1\text{D}) \rightarrow 0.76 \text{ LossO3O} + 0.76 \text{ LossO3} + 0.24 \text{ O}(^3\text{P}) + 0.24 \text{ CHF}_2\text{CF}_3 + 0.6 \text{ OH} + 1.52 \text{ L CARBON} + 3.8 \text{ LFLUORINE}$	1.2E-10	Sander et al. (2011)*
G5300dc07	StG	$\text{CHF}_2\text{CF}_3 + \text{OH} \rightarrow \text{ProdH2O} + \text{H}_2\text{O} + 2 \text{ L CARBON} + 5 \text{ LFLUORINE}$	6.0e-13*EXP(-1700./temp)	Sander et al. (2011)
G6500dc09	StG	$\text{CHF}_2\text{CF}_3 + \text{Cl} \rightarrow \text{HCl} + 2 \text{ L CARBON} + 5 \text{ LFLUORINE}$	1.8e-12*EXP(-2600./temp)	Sander et al. (2011)
G5300dc08	StG	$\text{CH}_3\text{CF}_3 + \text{O}(^1\text{D}) \rightarrow 0.82 \text{ LossO3O} + 0.82 \text{ LossO3} + 0.18 \text{ O}(^3\text{P}) + 0.18 \text{ CH}_3\text{CF}_3 + 0.38 \text{ OH} + 1.64 \text{ L CARBON} + 2.46 \text{ LFLUORINE}$	4.4E-11	Sander et al. (2011)*
G5300dc09	StG	$\text{CH}_3\text{CF}_3 + \text{OH} \rightarrow \text{ProdH2O} + \text{H}_2\text{O} + 2 \text{ L CARBON} + 3 \text{ LFLUORINE}$	1.1e-12*EXP(-2010./temp)	Sander et al. (2011)
G6500dc10	StG	$\text{CH}_3\text{CF}_3 + \text{Cl} \rightarrow \text{HCl} + 2 \text{ L CARBON} + 3 \text{ LFLUORINE}$	1.44e-11*EXP(-3940./temp)	Sander et al. (2011)
G6400dc03	StG	$\text{CHCl}_3 + \text{OH} \rightarrow \text{ProdH2O} + \text{H}_2\text{O} + \text{L CARBON} + 3 \text{ Cl}$	2.2e-12*EXP(-920./temp)	Sander et al. (2011)
G6400dc04	StG	$\text{CHCl}_3 + \text{Cl} \rightarrow \text{HCl} + \text{L CARBON} + 3 \text{ Cl}$	3.31e-12*EXP(-990./temp)	Sander et al. (2011)

General notes

Three-body reactions

Rate coefficients for three-body reactions are defined via the function $k_{\text{3rd}}(T, M, k_0^{300}, n, k_{\text{inf}}^{300}, m, f_c)$. In the code, the temperature T is called **temp** and the concentration of "air molecules" M is called **cair**. Using the auxiliary variables $k_0(T)$, $k_{\text{inf}}(T)$, and k_{ratio} , k_{3rd} is defined as:

$$k_0(T) = k_0^{300} \times \left(\frac{300\text{K}}{T}\right)^n \quad (1)$$

$$k_{\text{inf}}(T) = k_{\text{inf}}^{300} \times \left(\frac{300\text{K}}{T}\right)^m \quad (2)$$

$$k_{\text{ratio}} = \frac{k_0(T)M}{k_{\text{inf}}(T)} \quad (3)$$

$$k_{\text{3rd}} = \frac{k_0(T)M}{1 + k_{\text{ratio}}} \times f_c^{\left(\frac{1}{1 + (0.9810/k_{\text{ratio}})^2}\right)} \quad (4)$$

A similar function, called $k_{\text{3rd_iupac}}$ here, is used by Wallington et al. (2018) for three-body reactions. It has the same function parameters as k_{3rd} and it is defined as:

$$k_0(T) = k_0^{300} \times \left(\frac{300\text{K}}{T}\right)^n \quad (5)$$

$$k_{\text{inf}}(T) = k_{\text{inf}}^{300} \times \left(\frac{300\text{K}}{T}\right)^m \quad (6)$$

$$k_{\text{ratio}} = \frac{k_0(T)M}{k_{\text{inf}}(T)} \quad (7)$$

$$N = 0.75 - 1.27 \times \log_{10}(f_c) \quad (8)$$

$$k_{\text{3rd_iupac}} = \frac{k_0(T)M}{1 + k_{\text{ratio}}} \times f_c^{\left(\frac{1}{1 + (0.9810/k_{\text{ratio}})^N}\right)} \quad (9)$$

Structure-Activity Relationships (SAR)

Some unmeasured rate coefficients are estimated with structure-activity relationships, using the following parameters and substituent factors:

k for H-abstraction by OH in $\text{cm}^{-3}\text{s}^{-1}$	
$k_{\text{-p}}$	$4.49 \times 10^{-18} \times (T/\text{K})^2 \exp(-320 \text{K}/T)$
$k_{\text{-s}}$	$4.50 \times 10^{-18} \times (T/\text{K})^2 \exp(253 \text{K}/T)$
$k_{\text{-t}}$	$2.12 \times 10^{-18} \times (T/\text{K})^2 \exp(696 \text{K}/T)$
$k_{\text{-ROHRO}}$	$2.1 \times 10^{-18} \times (T/\text{K})^2 \exp(-85 \text{K}/T)$
$k_{\text{-CO2H}}$	$0.7 \times k_{\text{CH}_3\text{CO}_2\text{H}+\text{OH}}$
$k_{\text{-ROOHR}}$	$0.6 \times k_{\text{CH}_3\text{COH}+\text{OH}}$
$f_{\text{-alk}}$	1.23
$f_{\text{-sOH}}$	3.44
$f_{\text{-tOH}}$	2.68
$f_{\text{-sOOH}}$	8.
$f_{\text{-tOOH}}$	8.
$f_{\text{-ONO2}}$	0.04
$f_{\text{-CH2ONO2}}$	0.20
$f_{\text{-cpan}}$	0.25
$f_{\text{-allyl}}$	3.6
$f_{\text{-CHO}}$	0.55
$f_{\text{-CO2H}}$	1.67
$f_{\text{-CO}}$	0.73
$f_{\text{-O}}$	8.15
$f_{\text{-pCH2OH}}$	1.29
$f_{\text{-tCH2OH}}$	0.53

k for OH-addition to double bonds in $\text{cm}^{-3}\text{s}^{-1}$

$k_{\text{-adp}}$	$4.5 \times 10^{-12} \times (T/300 \text{K})^{-0.85}$
$k_{\text{-ads}}$	$1/4 \times (1.1 \times 10^{-11} \times \exp(485 \text{K}/T) + 1.0 \times 10^{-11} \times \exp(553 \text{K}/T))$
$k_{\text{-adt}}$	$1.922 \times 10^{-11} \times \exp(450 \text{K}/T) - k_{\text{-ads}}$
$k_{\text{-adsecprim}}$	3.0×10^{-11}
$k_{\text{-adtertprim}}$	5.7×10^{-11}
$a_{\text{-PAN}}$	0.56
$a_{\text{-CHO}}$	0.31
$a_{\text{-COCH3}}$	0.76
$a_{\text{-CH2OH}}$	1.7
$a_{\text{-CH2OOH}}$	1.7
$a_{\text{-COH}}$	2.2
$a_{\text{-COOH}}$	2.2
$a_{\text{-CO2H}}$	0.25
$a_{\text{-CH2ONO2}}$	0.64

 RO_2 self and cross reactions

The self and cross reactions of organic peroxy radicals are treated according to the permutation reaction formalism as implemented in the MCM (Rickard and Pascoe, 2009), as described by Jenkin et al. (1997). Every organic peroxy radical reacts in a pseudo-first-order reaction with a rate constant that is expressed as $k^{\text{self}} = 2 \times \sqrt{k_{\text{self}}} \times k_{\text{CH3O2}} \times [\text{RO}_2]$ where k_{self} = second-order rate coefficient of the self reaction of the organic peroxy radical, k_{CH3O2} = second-order rate coefficient of the self reaction of CH_3O_2 , and $[\text{RO}_2]$ = sum of the concentrations of all organic peroxy radicals.

Specific notes

G1002a: The path leading to 2 O(³P) + O₂ results in a null cycle regarding odd oxygen and is neglected.
G2110: The rate coefficient is: $k_{\text{H02_H02}} = (3.0\text{E-}13 \cdot \text{EXP}(460./\text{temp}) + 2.1\text{E-}33 \cdot \text{EXP}(920./\text{temp}) \cdot \text{cair}) \cdot (1. + 1.4\text{E-}21 \cdot \text{EXP}(2200./\text{temp}) \cdot \text{C}(\text{ind_H2O}))$.
G3109: The rate coefficient is: $k_{\text{N03_N02}} = k_{\text{3rd}}(\text{temp}, \text{cair}, 2.4\text{E-}30, 3.0, 1.6\text{E-}12, -0.1, 0.6)$.
G3110: The rate coefficient is defined as backward reaction divided by equilibrium constant.
G3203: The rate coefficient is: $k_{\text{N02_H02}} = k_{\text{3rd}}(\text{temp}, \text{cair}, 1.9\text{E-}31, 3.4, 4.0\text{E-}12, 0.3, 0.6)$.
G3206: The rate coefficient is: $k_{\text{HN03_OH}} = 1.32\text{E-}14 \cdot \text{EXP}(527/\text{temp}) + 1 / (1 / (7.39\text{E-}32 \cdot \text{EXP}(453/\text{temp}) \cdot \text{cair}) + 1 / (9.73\text{E-}17 \cdot \text{EXP}(1910/\text{temp})))$.
G3207: The rate coefficient is defined as backward reaction divided by equilibrium constant.
G4103: Sander et al. (2006) recommend a zero product yield for HCHO.
G4109: The same temperature dependence assumed as for CH₃CHO+NO₂. At 298 K, $k = 5.8 \times 10^{-16}$.
G4201: The product distribution is from Rickard and Pascoe (2009), after substitution of the Criegee intermediate by its decomposition products.
G4206: The product C₂H₅OH, which reacts only with OH, is substituted by its degradation products $\approx 0.1 \text{HOCH}_2\text{CH}_2\text{O}_2 + 0.9 \text{CH}_3\text{CHO} + 0.9 \text{HO}_2$.
G4207: Same value as for G4107
G4213: The rate coefficient is: $k_{\text{CH3CO3_N02}} = k_{\text{3rd}}(\text{temp}, \text{cair}, 9.7\text{E-}29, 5.6, 9.3\text{E-}12, 1.5, 0.6)$.
G4221: The rate coefficient $\text{isk}_{\text{PAN_M}} = k_{\text{CH3CO3_N02}}/9.9\text{E-}29 \cdot \text{EXP}(-14000./\text{temp})$, i.e. the rate coefficient is defined as backward reaction divided by equilibrium constant.

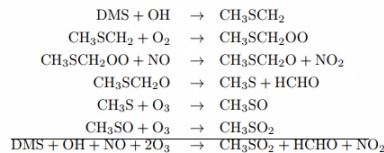
G4307: Same value as for G4107
G4315: Same value as for G4107
G4401: Same value as for G4306
G4402: Same value as for G4304
G4403: Same value as for G4305
G4404: Same value as for G4107
G4414: Same value as for G4304
G4415: Same value as for G4305
G4416: Same value as for G4107
G4419: Same value as for G4221
G6103: The rate coefficient is defined as backward reaction divided by equilibrium constant.
G6204: At low temperatures, there may be a minor reaction channel leading to O₃+HCl. See Finkbeiner et al. (1995) for details. It is neglected here.
G6402: The initial products are probably HCl and CH₂OOH (Atkinson et al., 2006). It is assumed that CH₂OOH dissociates into HCHO and OH.
G6405: Sander et al. (2006), but simplified shortcut to release all Cl
G6411: CH₃ is assumed to promptly convert to CH₃O₂ in MIM (similar to G6400)
G7302: The rate coefficient is: $k_{\text{Br0_N02}} = k_{\text{3rd}}(\text{temp}, \text{cair}, 5.2\text{E-}31, 3.2, 6.9\text{E-}12, 2.9, 0.6)$.
G7303: The rate coefficient is defined as backward reaction (Atkinson et al., 2007) divided by equilibrium constant (Orlando and Tyndall, 1996).
G7407: It is assumed that the reaction liberates all Br atoms. The fate of the carbon atom is currently not considered.
G7408: It is assumed that the reaction liberates all Br atoms. The fate of the carbon atom is currently not considered.
G7605: Same value as for G7408: CH₂Br₂+OH assumed. It is assumed that the reaction liberates all

Br and all Cl. The fate of the carbon atom is currently not considered.

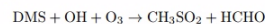
G7606: Same value as for G7408: CH₂Br₂+OH assumed. It is assumed that the reaction liberates all Br atoms and also Cl. The fate of the carbon atom is currently not considered.

G7607: It is assumed that the reaction liberates all Br atoms and also Cl. The fate of the carbon atom is currently not considered.

G9400a: For the abstraction path, the assumed reaction sequence (omitting H₂O and O₂ as products) according to Yin et al. (1990) is:



Neglecting the effect on O₃ and NO_x, the remaining reaction is:



G9400b: For the addition path, the rate coefficient is: $k_{\text{DMS_OH}} = 1.0\text{E-}39 \cdot \text{EXP}(5820./\text{temp}) \cdot \text{C}(\text{ind_O2}) / (1. + 5.0\text{E-}30 \cdot \text{EXP}(6280./\text{temp}) \cdot \text{C}(\text{ind_O2}))$.

G5300dc01: Kono and Matsumi 2001

G5300dc04: force and wiesefeld 1981

G6500dc05: physical quenching (O1D-*o*O3P) Warren 1991

G5300dc06: Kono and Matsumi

G5300dc08: Kono and Matsumi

Table 2: Photolysis reactions

#	labels	reaction	rate coefficient	reference
J1000a	UpStTrGJ	O ₂ + hν → 2.0 ProdO3 + O(³ P) + O(¹ D)	jx(ip_02)	Sander et al. (2014)
J1001a	UpStTrGJ	O ₃ + hν → O(¹ D) + O ₂	jx(ip_01D)	Sander et al. (2014)
J1001b	UpStTrGJ	O ₃ + hν → O(³ P) + O ₂	jx(ip_03P)	Sander et al. (2014)
J2100a	UpStGJ	H ₂ O + hν → LossH2O + H + OH	jx(ip_H2O)	Sander et al. (2014)
J2101	UpStTrGJ	H ₂ O ₂ + hν → 2 OH	jx(ip_H2O2)	Sander et al. (2014)
J3100	UpStGJN	N ₂ O + hν → 1.0 ProdO3 + O(¹ D) + N ₂	jx(ip_N2O)	Sander et al. (2014)
J3101	UpStTrGJN	NO ₂ + hν → NO + O(³ P)	jx(ip_N02)	Sander et al. (2014)
J3102a	UpStGJN	NO + hν → 1.0 ProdO3 + N + O(³ P)	jx(ip_N0)	Sander et al. (2014)
J3103a	UpStTrGJN	NO ₃ + hν → NO ₂ + O(³ P)	jx(ip_N020)	Sander et al. (2014)
J3103b	UpStTrGJN	NO ₃ + hν → 2.0 LossO3N + 2.0 LossO3 + NO + O ₂	jx(ip_N002)	Sander et al. (2014)
J3104	StTrGJN	N ₂ O ₅ + hν → NO ₂ + NO ₃	jx(ip_N205)	Sander et al. (2014)
J3200	TrGJN	HONO + hν → NO + OH	jx(ip_HONO)	Sander et al. (2014)
J3201	StTrGJN	HNO ₃ + hν → NO ₂ + OH	jx(ip_HN03)	Sander et al. (2014)
J3202	StTrGJN	HNO ₄ + hν → 0.333 ProdO3 + .667 NO ₂ + .667 HO ₂ + .333 NO ₃ + .333 OH	jx(ip_HN04)	Sander et al. (2014)
J4100	StTrGJ	CH ₃ OOH + hν → HCHO + OH + HO ₂	jx(ip_CH300H)	Sander et al. (2014)
J4101a	StTrGJ	HCHO + hν → H ₂ + CO	jx(ip_COH2)	Sander et al. (2014)
J4101b	StTrGJ	HCHO + hν → H + CO + HO ₂	jx(ip_CH0H)	Sander et al. (2014)
J4102	StGJ	CO ₂ + hν → 1.0 ProdO3 + CO + O(³ P)	jx(ip_CO2)	Sander et al. (2014)
J4103	StGJ	CH ₄ + hν → 1.155 ProdH2O + CO + 0.31 H + 0.69 H ₂ + 1.155 H ₂ O	jx(ip_CH4)	Sander et al. (2014)
J4200	TrGJC	C ₂ H ₅ OOH + hν → CH ₃ CHO + HO ₂ + OH	jx(ip_CH300H)	von Kuhlmann (2001)
J4201	TrGJC	CH ₃ CHO + hν → CH ₃ O ₂ + HO ₂ + CO	jx(ip_CH3CHO)	Sander et al. (2014)
J4202	TrGJC	CH ₃ C(O)OOH + hν → CH ₃ O ₂ + OH + CO ₂	jx(ip_CH3CO3H)	Sander et al. (2014)
J4203	TrGJCN	NACA + hν → NO ₂ + HCHO + CO	0.19*jx(ip_CH0H)	von Kuhlmann (2001)
J4204	TrGJCN	PAN + hν → CH ₃ C(O)OO + NO ₂	jx(ip_PAN)	Sander et al. (2014)
J4300	TrGJC	iC ₃ H ₇ OOH + hν → CH ₃ COCH ₃ + HO ₂ + OH	jx(ip_CH300H)	von Kuhlmann (2001)
J4301	TrGJC	CH ₃ COCH ₃ + hν → CH ₃ C(O)OO + CH ₃ O ₂	jx(ip_CH3COCH3)	Sander et al. (2014)
J4302	TrGJC	CH ₃ COCH ₂ OH + hν → CH ₃ C(O)OO + HCHO + HO ₂	0.074*jx(ip_CH0H)	see note*
J4303	TrGJC	MGLYOX + hν → CH ₃ C(O)OO + CO + HO ₂	jx(ip_MGLYOX)	Sander et al. (2014)
J4304	TrGJC	CH ₃ COCH ₂ O ₂ H + hν → CH ₃ C(O)OO + HCHO + OH	jx(ip_CH300H)	see note*
J4306	TrGJCN	iC ₃ H ₇ ONO ₂ + hν → CH ₃ COCH ₃ + NO ₂ + HO ₂	3.7*jx(ip_PAN)	von Kuhlmann et al. (2003)*

Table 2: Photolysis reactions (... continued)

#	labels	reaction	rate coefficient	reference
J4400	TrGJC	$\text{LC}_2\text{H}_3\text{OOH} + h\nu \rightarrow \text{OH} + .67 \text{ MEK} + .67 \text{ HO}_2 + .33 \text{ C}_2\text{H}_5\text{O}_2 + .33 \text{ CH}_3\text{CHO}$	$\text{jx}(\text{ip_CH300H})$	Rickard and Pascoe (2009)
J4401	TrGJC	$\text{MVK} + h\nu \rightarrow \text{CH}_3\text{C}(\text{O})\text{OO} + \text{HCHO} + \text{CO} + \text{HO}_2$	$0.019 * \text{jx}(\text{ip_COH2}) + .015 * \text{jx}(\text{ip_MGLYOX})$	Sander et al. (2014)
J4402	TrGJC	$\text{MVKOOH} + h\nu \rightarrow \text{OH} + .5 \text{ MGLYOX} + .25 \text{ CH}_3\text{COCH}_2\text{OH} + .75 \text{ HCHO} + .75 \text{ HO}_2 + .25 \text{ CH}_3\text{C}(\text{O})\text{OO} + .25 \text{ CO}$	$\text{jx}(\text{ip_CH300H})$	see note*
J4403	TrGJC	$\text{MEK} + h\nu \rightarrow \text{CH}_3\text{C}(\text{O})\text{OO} + \text{C}_2\text{H}_5\text{O}_2$	$0.42 * \text{jx}(\text{ip_CHOH})$	von Kuhlmann et al. (2003)
J4404	TrGJC	$\text{LMEKOOH} + h\nu \rightarrow \text{CH}_3\text{C}(\text{O})\text{OO} + \text{CH}_3\text{CHO} + \text{OH}$	$\text{jx}(\text{ip_CH300H})$	Rickard and Pascoe (2009)
J4405	TrGJC	$\text{BIACET} + h\nu \rightarrow 2 \text{ CH}_3\text{C}(\text{O})\text{OO}$	$2.15 * \text{jx}(\text{ip_MGLYOX})$	see note*
J4406	TrGJCN	$\text{LC4H9NO3} + h\nu \rightarrow \text{NO}_2 + .67 \text{ MEK} + .67 \text{ HO}_2 + .33 \text{ C}_2\text{H}_5\text{O}_2 + .33 \text{ CH}_3\text{CHO}$	$3.7 * \text{jx}(\text{ip_PAN})$	von Kuhlmann (2001)
J4407	TrGJCN	$\text{MPAN} + h\nu \rightarrow \text{CH}_3\text{COCH}_2\text{OH} + \text{NO}_2$	$\text{jx}(\text{ip_PAN})$	see note*
J4500	TrGJC	$\text{ISOOH} + h\nu \rightarrow \text{MVK} + \text{HCHO} + \text{HO}_2 + \text{OH}$	$\text{jx}(\text{ip_CH300H})$	see note*
J4501	TrGJCN	$\text{ISON} + h\nu \rightarrow \text{MVK} + \text{HCHO} + \text{NO}_2 + \text{HO}_2$	$3.7 * \text{jx}(\text{ip_PAN})$	von Kuhlmann (2001)
J6000	StTrGJCl	$\text{Cl}_2 + h\nu \rightarrow \text{Cl} + \text{Cl}$	$\text{jx}(\text{ip_Cl2})$	Sander et al. (2014)
J6100	StTrGJCl	$\text{Cl}_2\text{O}_2 + h\nu \rightarrow 2.0 \text{ LossO3Cl} + 2.0 \text{ LossO3} + 2 \text{ Cl}$	$\text{jx}(\text{ip_Cl2O2})$	Sander et al. (2014)
J6101	StTrGJCl	$\text{OClO} + h\nu \rightarrow 1.0 \text{ ProdO3} + \text{ClO} + \text{O}(^3\text{P})$	$\text{jx}(\text{ip_OClO})$	Sander et al. (2014)
J6200	StGJCl	$\text{HCl} + h\nu \rightarrow \text{Cl} + \text{H}$	$\text{jx}(\text{ip_HCl})$	Sander et al. (2014)
J6201	StTrGJCl	$\text{HOCl} + h\nu \rightarrow 1.0 \text{ LossO3Cl} + 1.0 \text{ LossO3} + \text{OH} + \text{Cl}$	$\text{jx}(\text{ip_HOCl})$	Sander et al. (2014)
J6300	TrGJCN	$\text{ClNO}_2 + h\nu \rightarrow 1.0 \text{ ProdO3} + \text{Cl} + \text{NO}_2$	$\text{jx}(\text{ip_ClNO2})$	Sander et al. (2014)
J6301a	StTrGJClN	$\text{ClNO}_3 + h\nu \rightarrow \text{Cl} + \text{NO}_3$	$\text{jx}(\text{ip_ClNO3})$	Sander et al. (2014)
J6301b	StTrGJClN	$\text{ClNO}_3 + h\nu \rightarrow \text{ClO} + \text{NO}_2$	$\text{jx}(\text{ip_ClNO3O2})$	Sander et al. (2014)
J6400	StGJCl	$\text{CH}_3\text{Cl} + h\nu \rightarrow 1.0 \text{ ProdLCl} + \text{Cl} + \text{CH}_3\text{O}_2$	$\text{jx}(\text{ip_CH3Cl})$	Sander et al. (2014)
J6401	StGJCl	$\text{CCl}_4 + h\nu \rightarrow 4.0 \text{ ProdLCl} + \text{LCARBON} + 4 \text{ Cl}$	$\text{jx}(\text{ip_CCl4})$	Sander et al. (2014)
J6402	StGJCCl	$\text{CH}_3\text{CCl}_3 + h\nu \rightarrow 3.0 \text{ ProdLCl} + 2 \text{ LFCARBON} + 3 \text{ Cl}$	$\text{jx}(\text{ip_CH3CCl3})$	Sander et al. (2014)
J6500	StGJClF	$\text{CFCl}_3 + h\nu \rightarrow 3.0 \text{ ProdLCl} + 3 \text{ Cl} + \text{LCARBON} + \text{LFLUORINE}$	$\text{jx}(\text{ip_CFCl3})$	Sander et al. (2014)
J6501	StGJClF	$\text{CF}_2\text{Cl}_2 + h\nu \rightarrow 2.0 \text{ ProdLCl} + 2 \text{ Cl} + \text{LCARBON} + 2 \text{ LFLUORINE}$	$\text{jx}(\text{ip_CF2Cl2})$	Sander et al. (2014)
J7000	StTrGJBr	$\text{Br}_2 + h\nu \rightarrow \text{Br} + \text{Br}$	$\text{jx}(\text{ip_Br2})$	Sander et al. (2014)
J7100	StTrGJBr	$\text{BrO} + h\nu \rightarrow \text{Br} + \text{O}(^3\text{P})$	$\text{jx}(\text{ip_BrO})$	Sander et al. (2014)
J7200	StTrGJBr	$\text{HOBr} + h\nu \rightarrow 1.0 \text{ LossO3Br} + 1.0 \text{ LossO3} + \text{Br} + \text{OH}$	$\text{jx}(\text{ip_HOBr})$	Sander et al. (2014)
J7300	TrGJBrN	$\text{BrNO}_2 + h\nu \rightarrow 1.0 \text{ ProdO3} + \text{Br} + \text{NO}_2$	$\text{jx}(\text{ip_BrNO2})$	Sander et al. (2014)
J7301	StTrGJBrN	$\text{BrNO}_3 + h\nu \rightarrow .85 \text{ Br} + .85 \text{ NO}_3 + .15 \text{ BrO} + .15 \text{ NO}_2$	$\text{jx}(\text{ip_BrNO3})$	Sander et al. (2014)*
J7400	StGJBr	$\text{CH}_3\text{Br} + h\nu \rightarrow 1.0 \text{ ProdLBr} + \text{Br} + \text{CH}_3\text{O}_2$	$\text{jx}(\text{ip_CH3Br})$	Sander et al. (2014)

Table 2: Photolysis reactions (... continued)

#	labels	reaction	rate coefficient	reference
J7401	TrGJBr	$\text{CH}_2\text{Br}_2 + h\nu \rightarrow 2.0 \text{ ProdSBr} + \text{LCARBON} + 2 \text{ Br}$	$\text{jx}(\text{ip_CH2Br2})$	Sander et al. (2014)
J7402	TrGJBr	$\text{CHBr}_3 + h\nu \rightarrow 3.0 \text{ ProdSBr} + \text{LCARBON} + 3 \text{ Br}$	$\text{jx}(\text{ip_CHBr3})$	Sander et al. (2014)
J7500	StGJBrF	$\text{CF}_3\text{Br} + h\nu \rightarrow 1.0 \text{ ProdLBr} + \text{LCARBON} + 3 \text{ LFLUORINE} + \text{Br}$	$\text{jx}(\text{ip_CF3Br})$	Sander et al. (2014)
J7600	StTrGJBrCl	$\text{BrCl} + h\nu \rightarrow \text{Br} + \text{Cl}$	$\text{jx}(\text{ip_BrCl})$	Sander et al. (2014)
J7601	StGJBrClF	$\text{CF}_2\text{ClBr} + h\nu \rightarrow 1.0 \text{ ProdLBr} + 1.0 \text{ ProdLCl} + \text{LCARBON} + 2 \text{ LFLUORINE} + \text{Br} + \text{Cl}$	$\text{jx}(\text{ip_CF2ClBr})$	Sander et al. (2014)
J7602	TrGJBrCl	$\text{CH}_2\text{ClBr} + h\nu \rightarrow 1.0 \text{ ProdSBr} + 1.0 \text{ ProdSCl} + \text{LCARBON} + \text{Br} + \text{Cl}$	$\text{jx}(\text{ip_CH2ClBr})$	Sander et al. (2014)
J7603	TrGJBrCl	$\text{CHCl}_2\text{Br} + h\nu \rightarrow 1.0 \text{ ProdSBr} + 2.0 \text{ ProdSCl} + \text{LCARBON} + \text{Br} + 2 \text{ Cl}$	$\text{jx}(\text{ip_CHCl2Br})$	Sander et al. (2014)
J7604	TrGJBrCl	$\text{CHClBr}_2 + h\nu \rightarrow 2.0 \text{ ProdSBr} + 1.0 \text{ ProdSCl} + \text{LCARBON} + 2 \text{ Br} + \text{Cl}$	$\text{jx}(\text{ip_CHClBr2})$	Sander et al. (2014)
J8401	StTrGJI	$\text{CH}_3\text{I} + h\nu \rightarrow \text{CH}_3\text{O}_2$	$\text{JX}(\text{ip_CH3I})$	Sander et al. (2014)
J6500dc01	StGJClF	$\text{CHF}_2\text{Cl} + h\nu \rightarrow 1.0 \text{ ProdLCl} + \text{Cl} + \text{LCARBON} + 2 \text{ LFLUORINE}$	$\text{jx}(\text{ip_CHF2Cl})$	Sander et al. (2011)*
J6500dc02	StGJCClF	$\text{CF}_2\text{ClCFCl}_2 + h\nu \rightarrow 3.0 \text{ ProdLCl} + 3 \text{ Cl} + 2 \text{ LFCARBON} + 3 \text{ LFLUORINE}$	$\text{jx}(\text{ip_CF2ClCFCl2})$	Sander et al. (2011)
J6400dc01	StGJCl	$\text{CH}_2\text{Cl}_2 + h\nu \rightarrow 2.0 \text{ ProdLCl} + 2 \text{ Cl} + \text{LCARBON}$	$\text{jx}(\text{ip_CH2Cl2})$	Sander et al. (2011)
J6500dc03	StGJCClF	$\text{CH}_3\text{CFCl}_2 + h\nu \rightarrow 2.0 \text{ ProdLCl} + 2 \text{ Cl} + 2 \text{ LFCARBON} + 1 \text{ LFLUORINE}$	$\text{jx}(\text{ip_CH3CFCl2})$	Sander et al. (2011)
J6500dc04	StGJCClF	$\text{CF}_2\text{ClCF}_2\text{Cl} + h\nu \rightarrow 2.0 \text{ ProdLCl} + 2 \text{ Cl} + 2 \text{ LFCARBON} + 4 \text{ LFLUORINE}$	$\text{jx}(\text{ip_CF2ClCF2Cl})$	Sander et al. (2011)
J6400dc02	StGJCl	$\text{CHCl}_3 + h\nu \rightarrow 3.0 \text{ ProdLCl} + 3 \text{ Cl} + \text{LCARBON}$	$\text{jx}(\text{ip_CHCl3})$	Sander et al. (2011)
J6500dc05	StGJCClF	$\text{CF}_3\text{CF}_2\text{Cl} + h\nu \rightarrow 1.0 \text{ ProdLCl} + \text{Cl} + 2 \text{ LFCARBON} + 5 \text{ LFLUORINE}$	$\text{jx}(\text{ip_CF3CF2Cl})$	Sander et al. (2011)
J6500dc06	StG	$\text{CH}_2\text{F}_2 + \text{Cl} \rightarrow \text{HCl} + \text{LCARBON} + 2 \text{ LFLUORINE}$	$4.9\text{e-}12 * \text{EXP}(-1500./\text{temp})$	Sander et al. (2011)
J9000	TrStGJS	$\text{OCS} + h\nu \rightarrow \text{CO} + \text{S}$	$\text{JX}(\text{ip_OCS})$	■■■■
J9001	TrStGJS	$\text{SO}_2 + h\nu \rightarrow \text{SO} + \text{O}(^3\text{P})$	$60 * \text{JX}(\text{ip_OCS})$	■■■■
J9002	TrStGJS	$\text{SO}_3 + h\nu \rightarrow \text{SO}_2 + \text{O}(^3\text{P})$	$\text{JX}(\text{ip_SO3})$	■■■■
J9003	TrStGJS	$\text{H}_2\text{SO}_4 + h\nu \rightarrow \text{ProdH}_2\text{O} + \text{SO}_3 + \text{H}_2\text{O}$	$\text{JX}(\text{ip_H2SO4})$	■■■■
PH (aqueous)				

General notes

j -values are calculated with an external module (e.g., JVAL) and then supplied to the MECCA chemistry.

Values that originate from the Master Chemical Mechanism (MCM) by Rickard and Pascoe (2009) are translated according in the following way:

j(11) → jx(ip_COH2)
 j(12) → jx(ip_CHOH)
 j(15) → jx(ip_HOCH2CHO)
 j(18) → jx(ip_MACR)
 j(22) → jx(ip_ACETOL)
 j(23)+j(24) → jx(ip_MVK)
 j(31)+j(32)+j(33) → jx(ip_GLYOX)
 j(34) → jx(ip_MGLYOX)

j(41) → jx(ip_CH3OOH)
 j(53) → j(isopropyl nitrate)
 j(54) → j(isopropyl nitrate)
 j(55) → j(isopropyl nitrate)
 j(56)+j(57) → jx(ip_NOA)

Specific notes

J4302: It is assumed that J(CH₃COCH₂OH) is 0.074 times that of J4101b.

J4304: It is assumed that J(CH₃COCH₂O₂H) is the same as J(CH₃OOH).

J4306: Following von Kuhlmann et al. (2003), we use J(iC₃H₇ONO₂) = 3.7*jx(ip_PAN).

J4402: It is assumed that J(MVKOOH) is the same as J(CH₃OOH).

J4405: It is assumed that J(BIACET) is 2.15 times larger than J(MGLYOX), consistent with the photolysis rate coefficients used in the MCM (Rickard and Pascoe, 2009).

J4407: It is assumed that J(MPAN) is the same as J(PAN).

J4500: It is assumed that J(ISOOH) is the same as J(CH₃OOH).

J7301: The quantum yields are recommended by Burkholder et al. (2015) for λ > 300nm and used here for the entire spectrum.

J6500dc01: OKAY!

Table 3: Reversible (Henry's law) equilibria and irreversible ("heterogenous") uptake

#	labels	reaction	rate coefficient	reference
---	--------	----------	------------------	-----------

General notes

The forward (k_{exf}) and backward (k_{exb}) rate coefficients are calculated in sub-routine `accem_aero_calc_k_ex` in the file `messy_accem_aero.f90` using accommodation coefficients and Henry's law constants from chemprop (see `chemprop.pdf`).

For uptake of X (X = N₂O₅, ClNO₃, or BrNO₃) and

subsequent reaction with H₂O, Cl⁻, and Br⁻ in H3201, H6300, H6301, H6302, H7300, H7301, H7302, H7601, and H7602, we define:

$$k_{\text{exf}}(X) = \frac{k_{\text{mt}}(X) \times \text{LWC}}{[\text{H}_2\text{O}] + 5 \times 10^2 [\text{Cl}^-] + 3 \times 10^5 [\text{Br}^-]}$$

Here, k_{mt} = mass transfer coefficient, and LWC = liquid water content of the aerosol. The total uptake rate of X is only determined by k_{mt} . The factors only affect

the branching between hydrolysis and the halide reactions. The factor 5×10^2 was chosen such that the chloride reaction dominates over hydrolysis at about [Cl⁻] > 0.1 M (see Fig. 3 in Behnke et al. (1997)), i.e. when the ratio [H₂O]/[Cl⁻] is less than 5×10^2 . The ratio $5 \times 10^2 / 3 \times 10^5$ was chosen such that the reactions with chloride and bromide are roughly equal for sea water composition (Behnke et al., 1994). These ratios were measured for uptake of N₂O₅. Here, they are also used for ClNO₃ and BrNO₃.

Table 4: Heterogeneous reactions

#	labels	reaction	rate coefficient	reference
HET200	StHetN	N ₂ O ₅ + H ₂ O → LossH2O + 1.0 LossO3N + 1.0 LossO3 + 2 HNO ₃	<code>khet_St(ihs_N205_H2O)</code>	see general notes*
HET201	TrHetN	N ₂ O ₅ → 3.0 LossO3N + 3.0 LossO3 + 2 NO ₃ ⁻ (cs) + 2 H ⁺ (cs)	<code>khet_Tr(iht_N205)</code>	see general notes*
HET410	StHetCl	HOCl + HCl → ProdH2O + 1.0 LossO3Cl + 1.0 LossO3 + Cl ₂ + H ₂ O	<code>khet_St(ihs_HOCl_HCl)</code>	see general notes*
HET420	StHetClN	ClNO ₃ + HCl → 0.5 LossO3Cl + 0.5 LossO3N + 1.0 LossO3 + Cl ₂ + HNO ₃	<code>khet_St(ihs_ClNO3_HCl)</code>	see general notes*
HET421	StHetClN	ClNO ₃ + H ₂ O → LossH2O + HOCl + HNO ₃	<code>khet_St(ihs_ClNO3_H2O)</code>	see general notes*
HET422	StHetClN	N ₂ O ₅ + HCl → 1.0 LossO3Cl + 1.0 LossO3N + 2.0 LossO3 + ClNO ₂ + HNO ₃	<code>khet_St(ihs_N205_HCl)</code>	see general notes*
HET510	StHetBr	HOBr + HBr → ProdH2O + 1.0 LossO3Br + 1.0 LossO3 + Br ₂ + H ₂ O	<code>khet_St(ihs_HOBr_HBr)</code>	see general notes*
HET520	StHetBrN	BrNO ₃ + H ₂ O → LossH2O + HOBr + HNO ₃	<code>khet_St(ihs_BrNO3_H2O)</code>	see general notes*
HET540	StHetBrClN	ClNO ₃ + HBr → 0.333333 LossO3Br + 0.333333 LossO3Cl + 0.333333 LossO3N + 1.0 LossO3 + BrCl + HNO ₃	<code>khet_St(ihs_ClNO3_HBr)</code>	see general notes*
HET541	StHetBrClN	BrNO ₃ + HCl → 0.333333 LossO3Br + 0.333333 LossO3Cl + 0.333333 LossO3N + 1.0 LossO3 + BrCl + HNO ₃	<code>khet_St(ihs_BrNO3_HCl)</code>	see general notes*
HET542	StHetBrCl	HOCl + HBr → ProdH2O + 0.5 LossO3Br + 0.5 LossO3Cl + 1.0 LossO3 + BrCl + H ₂ O	<code>khet_St(ihs_HOCl_HBr)</code>	see general notes*
HET543	StHetBrCl	HOBr + HCl → ProdH2O + 0.5 LossO3Br + 0.5 LossO3Cl + 1.0 LossO3 + BrCl + H ₂ O	<code>khet_St(ihs_HOBr_HCl)</code>	see general notes*

General notes

Heterogeneous reaction rates are calculated with an external module (e.g., MECCA_KHET) and then supplied to the MECCA chemistry (see www.messy-interface.org for details)

References

- Aas, W., Mortier, A., Bowersox, V., Cherian, R., Faluvegi, G., Fagerli, H., Hand, J., Klimont, Z., Galy-Lacaux, C., Lehmann, C. M. B., Myhre, C. L., Myhre, G., Olivié, D., Sato, K., Quaas, J., Rao, P. S. P., Schulz, M., Shindell, D., Skeie, R. B., Stein, A., Takemura, T., Tsyro, S., Vet, R., and Xu, X. (2019). Global and regional trends of atmospheric sulfur. *Scientific Reports*, 9(1). DOI:10.1038/s41598-018-37304-0.
- Albrecht, B. A. (1989). Aerosols, cloud microphysics, and fractional cloudiness. *Science*, 245(4923):1227–1230. DOI:10.1126/science.245.4923.1227.
- Andreae, M. O. and Crutzen, P. J. (1997). Atmospheric aerosols: Biogeochemical sources and role in atmospheric chemistry. *Science*, 276(5315):1052–1058. DOI:10.1126/science.276.5315.1052.
- Andres, R. and Kasgnoc, A. (1998). A time-averaged inventory of subaerial volcanic sulfur emissions. *Journal of Geophysical Research: Atmospheres*, 103(D19):25251–25261. DOI:10.1029/98jd02091.
- Archer, D. and Brovkin, V. (2008). The millennial atmospheric lifetime of anthropogenic CO₂. *Climatic Change*, 90(3):283–297. DOI:10.1007/s10584-008-9413-1.
- Archer, D., Eby, M., Brovkin, V., Ridgwell, A., Cao, L., Mikolajewicz, U., Caldeira, K., Matsumoto, K., Munhoven, G., Montenegro, A., and Tokos, K. (2009). Atmospheric lifetime of fossil fuel carbon dioxide. *Annual review of earth and planetary sciences*, 37(1):117–134. DOI:10.1146/annurev.earth.031208.100206.
- Arias, P., Bellouin, N., Coppola, E., Jones, R., Krinner, G., Marotzke, J., Naik, V., Palmer, M., Plattner, G.-K., Rogelj, J., Rojas, M., Sillmann, J., Storelvmo, T., Thorne, P., and Trewin (2021). *Climate Change 2021: The Physical Science Basis. Contribution of Working Group I to the Sixth Assessment Report of the Intergovernmental Panel on Climate Change. Technical Summary.*, pages 33–144. Cambridge University Press, Cambridge, United Kingdom and New York, NY, USA. DOI:10.1017/9781009157896.002.
- Bates, T. S., Cline, J. D., Gammon, R. H., and Kelly-Hansen, S. R. (1987). Regional and seasonal variations in the flux of oceanic dimethylsulfide to the atmosphere. *Journal of Geophysical Research: Oceans*, 92(C3):2930–2938. DOI:10.1029/jc092ic03p02930.

- Baumgardner, R. E., Lavery, T. F., Rogers, C. M., , and Isil, S. S. (2002). Estimates of the atmospheric deposition of sulfur and nitrogen species: Clean air status and trends network, 1990–2000. *ACS publications*. DOI:10.1021/es011146g.
- Betterton, E. A. and Hoffmann, M. R. (1988). Oxidation of aqueous sulfur dioxide by peroxymonosulfate. *The Journal of Physical Chemistry*, 92(21):5962–5965. DOI:10.1021/j100332a025.
- Bieser, J., Aulinger, A., Matthias, V., Quante, M., and van der Gon, H. D. (2011). Vertical emission profiles for Europe based on plume rise calculations. *Environmental Pollution*, 159(10):2935–2946. DOI:10.1016/j.envpol.2011.04.030.
- Bluth, G. J. S., Doiron, S. D., Schnetzler, C. C., Krueger, A. J., and Walter, L. S. (1992). Global tracking of the SO₂ clouds from the June, 1991 Mount Pinatubo eruptions. *Geophysical Research Letters*, 19(2):151–154. DOI:10.1029/91gl02792.
- Boucher, O., Randall, D., Artaxo, P., Bretherton, C., Feingold, G., Forster, P., Kerminen, V.-M., Kondo, Y., Liao, H., Lohmann, U., Rasch, P., Satheesh, S. K., Sherwood, S., Stevens, B., and Zhang, X. Y. (2013). *Clouds and aerosols*, pages 571–657. Cambridge University Press, Cambridge, UK. DOI:10.1017/CBO9781107415324.016.
- Brühl, C., Schallock, J., and Diehl, T. (2021). Volcanic SO₂ data derived from limb viewing satellites for the lower stratosphere from 1990 to 2019, and from nadir viewing satellites for the troposphere. DOI:10.26050/WDCC/SSIRC_2.
- Buchard, V., Da Silva, A. M., Colarco, P., Krotkov, N., Dickerson, R. R., Stehr, J. W., Mount, G., Spinei, E., Arkinson, H. L., and He, H. (2014). Evaluation of GEOS-5 sulfur dioxide simulations during the Frostburg, MD 2010 field campaign. *Atmospheric chemistry and physics*, 14(4):1929–1941. DOI:10.5194/acp-14-1929-2014.
- Caffrey, P., Hoppel, W., Frick, G., Pasternack, L., Fitzgerald, J., Hegg, D., Gao, S., Leaitch, R., Shantz, N., Albrechtinski, T., and Ambrusko, J. (2001). In-cloud oxidation of SO₂ by O₃ and H₂O₂: Cloud chamber measurements and modeling of particle growth. *Journal of Geophysical Research: Atmospheres*, 106(D21):27587–27601. DOI:10.1029/2000jd900844.
- Cai, Z., Griessbach, S., and Hoffmann, L. (2022). Improved estimation of volcanic SO₂ injections from satellite observations and lagrangian transport simulations: the 2019 raikoke eruption. *Atmospheric Chemistry and Physics*, 22(10):6787–6809. DOI:10.5194/acp-22-6787-2022.
- Calvin, K., Dasgupta, D., Krinner, G., Mukherji, A., Thorne, P. W., Trisos, C., Romero, J., Aldunce, P., Barrett, K., Blanco, G., Cheung, W. W., Connors, S., Denton, F., Diongue-Niang, A., Dodman, D., Garschagen, M., Geden, O., Hayward, B., Jones, C., Jotzo, F., Krug, T., Lasco, R., Lee, Y.-Y., Masson-Delmotte, V., Meinshausen, M., Mintenbeck, K., Mokssit, A., Otto, F. E., Pathak, M., Pirani, A., Poloczanska, E.,

- Pörtner, H.-O., Revi, A., Roberts, D. C., Roy, J., Ruane, A. C., Skea, J., Shukla, P. R., Slade, R., Slangen, A., Sokona, Y., Sörensson, A. A., Tignor, M., Van Vuuren, D., Wei, Y.-M., Winkler, H., Zhai, P., Zommers, Z., Hourcade, J.-C., Johnson, F. X., Pachauri, S., Simpson, N. P., Singh, C., Thomas, A., Totin, E., Alegría, A., Armour, K., Bednar-Friedl, B., Blok, K., Cissé, G., Dentener, F., Eriksen, S., Fischer, E., Garner, G., Guivarch, C., Haasnoot, M., Hansen, G., Hauser, M., Hawkins, E., Hermans, T., Kopp, R., Leprince-Ringuet, N., Lewis, J., Ley, D., Ludden, C., Niamir, L., Nicholls, Z., Some, S., Szopa, S., Trewin, B., Van Der Wijst, K.-I., Winter, G., Witting, M., Birt, A., and Ha, M. (2023). *IPCC, 2023: Climate Change 2023: Synthesis Report. Contribution of Working Groups I, II and III to the Sixth Assessment Report of the Intergovernmental Panel on Climate Change [Core Writing Team, H. Lee and J. Romero (eds.)]*. Geneva, Switzerland. IPCC. DOI:10.59327/ipcc/ar6-9789291691647.
- CCMI (2023). The Chemistry Climate Model Initiative. Technical report, Chemistry-Climate Model Initiative. available at: <https://blogs.reading.ac.uk/ccmi/> (last access: 10.07.2024).
- Charlson, R. J., Covert, D. S., Larson, T. V., and Waggoner, A. P. (1978). *Chemical Properties of Tropospheric Sulfur Aerosols*, pages 39–53. Elsevier. DOI:10.1016/b978-0-08-022932-4.50009-4.
- Chin, M., Rood, R. B., Lin, S., Müller, J., and Thompson, A. M. (2000). Atmospheric sulfur cycle simulated in the global model GOCART: Model description and global properties. *Journal of Geophysical Research: Atmospheres*, 105(D20):24671–24687. DOI:10.1029/2000jd900384.
- Crafford, A. E. and Venzke, E. (2019). Report on Raikoke (Russia). *Bulletin of the Global Volcanism Network*, 44(8). DOI:10.5479/si.gvp.bgvn201908-290250.
- Crippa, M., Solazzo, E., Guizzardi, D., Tubiello, F. N., and Leip, A. (2022). Climate goals require food systems emission inventories. *Nature Food*, 3(1):1. DOI:10.1038/s43016-021-00450-2.
- Dahiya, S., Anhäuser, A., Farrow, A., Thieriot, H., Kumar, A., and Myllyvirta, L. (2020). Global SO₂ Emission Hotspot Database.
- Damian, V., Sandu, A., Damian, M., Potra, F., and Carmichael, G. R. (2002). The kinetic preprocessor KPP—a software environment for solving chemical kinetics. *Computers & Chemical Engineering*, 26(11):1567–1579. DOI:10.1016/s0098-1354(02)00128-x.
- De Leeuw, J., Schmidt, A., Witham, C. S., Theys, N., Taylor, I. A., Grainger, R. G., Pope, R. J., Haywood, J., Osborne, M., and Kristiansen, N. I. (2021). The 2019 Raikoke volcanic eruption — Part 1: Dispersion model simulations and satellite retrievals of volcanic sulfur dioxide. *Atmospheric Chemistry and Physics*, 21(14):10851–10879. DOI:10.5194/acp-21-10851-2021.

- Dentener, F., Kinne, S., Bond, T., Boucher, O., Cofala, J., Generoso, S., Ginoux, P., Gong, S., Hoelzemann, J. J., Ito, A., Marelli, L., Penner, J. E., Putaud, J.-P., Textor, C., Schulz, M., van der Werf, G. R., and Wilson, J. (2006). Emissions of primary aerosol and precursor gases in the years 2000 and 1750 prescribed data-sets for AeroCom. *Atmospheric Chemistry and Physics*, 6(12):4321–4344. DOI:10.5194/acp-6-4321-2006.
- Dickinson, R. E. and Cicerone, R. J. (1986). Future global warming from atmospheric trace gases. *Nature*, 319(6049):109–115. DOI:10.1038/319109a0.
- ESA (2017). Sentinel-5p factsheet. Available at: https://esamultimedia.esa.int/docs/EarthObservation/Sentinel-5p_factsheet_171211.pdf (last access: 12.07.2024).
- Eskes, H. J. and Boersma, K. F. (2003). Averaging kernels for DOAS total-column satellite retrievals. *Atmospheric Chemistry and Physics*, 3(5):1285–1291. DOI:10.5194/acp-3-1285-2003.
- Exner, M., Herrmann, H., and Zellner, R. (1992). Laser-based studies of reactions of the nitrate radical in aqueous solution. *Berichte der Bunsengesellschaft für physikalische Chemie*, 96(3):470–477. DOI:10.1002/bbpc.19920960347.
- Eyring, V., Bony, S., Meehl, G. A., Senior, C. A., Stevens, B., Stouffer, R. J., and Taylor, K. E. (2016). Overview of the coupled model intercomparison project phase 6 (CMIP6) experimental design and organization. *Geoscientific Model Development*, 9(5):1937–1958. DOI:10.5194/gmd-9-1937-2016.
- Feng, L., Smith, S. J., Braun, C., Crippa, M., Gidden, M. J., Hoesly, R., Klimont, Z., van Marle, M., van den Berg, M., and van der Werf, G. R. (2020). The generation of gridded emissions data for CMIP6. *Geoscientific Model Development*, 13(2):461–482. DOI:10.5194/gmd-13-461-2020.
- Finkelstein, P. L., Ellestad, T. G., Clarke, J. F., Meyers, T. P., Schwede, D. B., Hebert, E. O., and Neal, J. A. (2000). Ozone and sulfur dioxide dry deposition to forests: Observations and model evaluation. *Journal of Geophysical Research: Atmospheres*, 105(D12):15365–15377. DOI:10.1029/2000jd900185.
- Fioletov, V., McLinden, C. A., Griffin, D., Theys, N., Loyola, D. G., Hedelt, P., Krotkov, N. A., and Li, C. (2020). Anthropogenic and volcanic point source SO₂ emissions derived from TROPOMI on board Sentinel-5 Precursor: first results. *Atmospheric Chemistry and Physics*, 20(9):5591–5607. DOI:10.5194/acp-20-5591-2020.
- Forster, P., Storelvmo, T., Armour, K., Collins, W., Dufresne, J.-L., Frame, D., Mauritsen, D. L. T., Palmer, M., Watanabe, M., Wild, M., and Zhang, H. (2021). *The Earth’s Energy Budget, Climate Feedbacks, and Climate Sensitivity. In Climate Change 2021: The Physical Science Basis. Contribution of Working Group I to the Sixth Assessment Report of the Intergovernmental Panel on Climate Change [Masson-Delmotte, V., P. Zhai, A.*

- Pirani, S.L. Connors, C. Péan, S. Berger, N. Caud, Y. Chen, L. Goldfarb, M.I. Gomis, M. Huang, K. Leitzell, E. Lonnoy, J.B.R. Matthews, T.K. Maycock, T. Waterfield, O. Yelekçi, R. Yu, and B. Zhou (eds.)*], pages 923–1045. Cambridge University Press, Cambridge, United Kingdom and New York, NY, USA. DOI:10.1017/9781009157896.009.
- Granier, C., Bessagnet, B., Bond, T., D’Angiola, A., Denier van der Gon, H., Frost, G. J., Heil, A., Kaiser, J. W., Kinne, S., Klimont, Z., Kloster, S., Lamarque, J.-F., Liousse, C., Masui, T., Meleux, F., Mieville, A., Ohara, T., Raut, J.-C., Riahi, K., Schultz, M. G., Smith, S. J., Thompson, A., van Aardenne, J., van der Werf, G. R., and van Vuuren, D. P. (2011). Evolution of anthropogenic and biomass burning emissions of air pollutants at global and regional scales during the 1980–2010 period. *Climatic Change*, 109(1–2):163–190. DOI:10.1007/s10584-011-0154-1.
- Halmer, M., Schmincke, H.-U., and Graf, H.-F. (2002). The annual volcanic gas input into the atmosphere, in particular into the stratosphere: a global data set for the past 100 years. *Journal of Volcanology and Geothermal Research*, 115(3–4):511–528. DOI:10.1016/s0377-0273(01)00318-3.
- Hanif, M. A., Ibrahim, N., and Abdul Jalil, A. (2020). Sulfur dioxide removal: An overview of regenerative flue gas desulfurization and factors affecting desulfurization capacity and sorbent regeneration. *Environmental Science and Pollution Research*, 27(22):27515–27540. DOI:10.1007/s11356-020-09191-4.
- Hansen, J., Lacis, A., Rind, D., Russell, G., Stone, P., Fung, I., Ruedy, R., and Lerner, J. (1984). *Climate sensitivity: Analysis of feedback mechanisms*, pages 130–163. AGU Geophysical Monograph 29, Maurice Ewing Vol. 5. American Geophysical Union, Washington, D.C.
- Hardacre, C., Mulcahy, J. P., Pope, R. J., Jones, C. G., Rumbold, S. T., Li, C., Johnson, C., and Turnock, S. T. (2021). Evaluation of SO₂, SO₄²⁻ and an updated SO₂ dry deposition parameterization in the United Kingdom Earth System Model. *Atmospheric Chemistry and Physics*, 21(24):18465–18497. DOI:10.5194/acp-21-18465-2021.
- Harris, E., Sinha, B., van Pinxteren, D., Tilgner, A., Fomba, K. W., Schneider, J., Roth, A., Gnauk, T., Fahlbusch, B., Mertes, S., Lee, T., Collett, J., Foley, S., Borrmann, S., Hoppe, P., and Herrmann, H. (2013). Enhanced Role of Transition Metal Ion Catalysis During In-Cloud Oxidation of SO₂. *Science*, 340(6133):727–730. DOI:10.1126/science.1230911.
- Haynes, W. M. (2016-2017). *CRC Handbook of Chemistry and Physics, 97th Edition*. CRC Press. ISBN:9781498754286.
- Hedelt, P., Efremenko, D. S., Loyola, D. G., Spurr, R., and Clarisse, L. (2019). Sulfur dioxide layer height retrieval from Sentinel-5 Precursor/TROPOMI using FP_ILM. *Atmospheric Measurement Techniques*, 12(10):5503–5517. DOI:10.5194/amt-12-5503-2019.

- Hersbach, H., Bell, B., Berrisford, P., Hirahara, S., Horányi, A., Muñoz-Sabater, J., Nicolas, J., Peubey, C., Radu, R., Schepers, D., Simmons, A., Soci, C., Abdalla, S., Abellan, X., Balsamo, G., Bechtold, P., Biavati, G., Bidlot, J., Bonavita, M., Chiara, G., Dahlgren, P., Dee, D., Diamantakis, M., Dragani, R., Flemming, J., Forbes, R., Fuentes, M., Geer, A., Haimberger, L., Healy, S., Hogan, R. J., Hólm, E., Janisková, M., Keeley, S., Laloyaux, P., Lopez, P., Lupu, C., Radnoti, G., Rosnay, P., Rozum, I., Vamborg, F., Villaume, S., and Thépaut, J.-N. (2020). The ERA5 global reanalysis. *Quarterly Journal of the Royal Meteorological Society*, 146(730):1999–2049. DOI:10.1002/qj.3803.
- Höpfner, M., Boone, C. D., Funke, B., Glatthor, N., Grabowski, U., Günther, A., Kellmann, S., Kiefer, M., Linden, A., Lossow, S., Pumphrey, H. C., Read, W. G., Roiger, A., Stiller, G., Schlager, H., von Clarmann, T., and Wissmüller, K. (2015). Sulfur dioxide (SO₂) from MIPAS in the upper troposphere and lower stratosphere 2002–2012. *Atmospheric Chemistry and Physics*, 15(12):7017–7037. DOI:10.5194/acp-15-7017-2015.
- Huijnen, V., Williams, J., van Weele, M., van Noije, T., Krol, M., Dentener, F., Segers, A., Houweling, S., Peters, W., de Laat, J., Boersma, F., Bergamaschi, P., van Velthoven, P., Le Sager, P., Eskes, H., Alkemade, F., Scheele, R., Nédélec, P., and Pätz, H.-W. (2010). The global chemistry transport model TM5: description and evaluation of the tropospheric chemistry version 3.0. *Geoscientific Model Development*, 3(2):445–473. DOI:10.5194/gmd-3-445-2010.
- Huntrieser, H., Klausner, T., Aufmhoff, H., Baumann, R., Fiehn, A., Gottschaldt, K.-D., Hedelt, P., Lutz, R., Kurilic, S., Podrascanin, Z., Ilic, P., Theys, N., Jöckel, P., Loyola, D., Makroum, I., Mertens, M., and Roiger, A.-E. (2021). Satellite validation of TROPOMI–SO₂ over the balkan region by airborne SO₂ measurements of coal-fired power plants. *The first international conference on sustainable environment and technologies “Create sustainable community”*, pages 79–88. <https://elib.dlr.de/146017/> (last access: 07.07.2024).
- Huntrieser, H., Klausner-Harlaß, T., Aufmhoff, H., Baumann, R., Fiehn, A., Hedelt, P., Gottschaldt, K.-D., Lutz, R., Kurilić, S. M., Podrašćanin, Z., Ilić, P., Theys, N., Jöckel, P., Loyola, D., Makroum, I., Mertens, M., and Roiger, A. (2023). Emissions of Sulphur Dioxide from Coal-Fired Power Plants in Serbia and Bosnia-Herzegovina: First Attempts of a Validation of TROPOMI Satellite Products with Airborne In Situ Measurements. In book: *Ilić P, Govedar Z, Pržulj N (eds), Edition: Sustainable Development and Management of Natural Resources of the Republic of Srpska*. Chapter: 6, Publisher: Academy of Sciences and Arts of the Republic of Srpska, Banja Luka, Monograph XI, 169-201. DOI:10.7251/EORU2309169H.
- Jacimovski, S., Miladinovic, S., and Radovanovic, R. (2016). Analysis of the emission of SO₂, NO_x, and suspended particles from the thermal power plants Kostolac (Serbia). *Human and ecological risk assessment*, 22(5):1208–1223. 10.1080/10807039.2016.1151347.

- Jiménez, S. and Ballester, J. (2005). Influence of operating conditions and the role of sulfur in the formation of aerosols from biomass combustion. *Combustion and Flame*, 140(4):346–358. DOI:10.1016/j.combustflame.2004.12.004.
- Jing, D., He, Y., Yin, Z., Liu, F., Yi, Y., and Yi, F. (2023). Evolution of aerosol plumes from 2019 Raikoke volcanic eruption observed with polarization lidar over central China. *Atmospheric Environment*, 309:119880. DOI:10.1016/j.atmosenv.2023.119880.
- Jöckel, P., Kerkweg, A., Pozzer, A., Sander, R., Tost, H., Riede, H., Baumgärtner, A., Gromov, S., and Kern, B. (2010). Development cycle 2 of the Modular Earth Submodel System (MESSy2). *Geoscientific Model Development*, 3(2):717–752. DOI:10.5194/gmd-3-717-2010.
- Jöckel, P., Sander, R., Kerkweg, A., Tost, H., and Lelieveld, J. (2005). Technical note: The Modular Earth Submodel System (MESSy) – a new approach towards Earth System Modeling. *Atmospheric Chemistry and Physics*, 5(2):433–444. DOI:10.5194/acp-5-433-2005.
- Jöckel, P., Tost, H., Pozzer, A., Brühl, C., Buchholz, J., Ganzeveld, L., Hoor, P., Kerkweg, A., Lawrence, M. G., Sander, R., Steil, B., Stiller, G., Tanarhte, M., Taraborrelli, D., van Aardenne, J., and Lelieveld, J. (2006). The atmospheric chemistry general circulation model ECHAM5/MESSy1: consistent simulation of ozone from the surface to the mesosphere. *Atmospheric Chemistry and Physics*, 6(12):5067–5104. DOI:10.5194/acp-6-5067-2006.
- Jöckel, P., Tost, H., Pozzer, A., Kunze, M., Kirner, O., Brenninkmeijer, C. A. M., Brinkop, S., Cai, D. S., Dyroff, C., Eckstein, J., Frank, F., Garny, H., Gottschaldt, K.-D., Graf, P., Grewe, V., Kerkweg, A., Kern, B., Matthes, S., Mertens, M., Meul, S., Neumaier, M., Nützel, M., Oberländer-Hayn, S., Ruhnke, R., Runde, T., Sander, R., Scharffe, D., and Zahn, A. (2016). Earth System Chemistry integrated Modelling (ESCiMo) with the Modular Earth Submodel System (MESSy) version 2.51. *Geoscientific Model Development*, 9(3):1153–1200. DOI:10.5194/gmd-9-1153-2016.
- Kanda, K.-i., Tsuruta, H., and Minami, K. (1992). Emission of dimethyl sulfide, carbonyl sulfide, and carbon bisulfide from paddy fields. *Soil Science and Plant Nutrition*, 38(4):709–716. DOI:10.1080/00380768.1992.10416701.
- Kerkweg, A., Buchholz, J., Ganzeveld, L., Pozzer, A., Tost, H., and Jöckel, P. (2006a). Technical note: An implementation of the dry removal processes DRY DEPosition and SEDimentation in the Modular Earth Submodel System (MESSy). *Atmospheric Chemistry and Physics*, 6(12):4617–4632. DOI:10.5194/acp-6-4617-2006.
- Kerkweg, A., Hofmann, C., Jöckel, P., Mertens, M., and Pante, G. (2018). The on-line coupled atmospheric chemistry model system MECO(n) — part 5: Expanding the Multi-Model-Driver (MMD v2.0) for 2-way data exchange including data interpolation

- via GRID (v1.0). *Geoscientific Model Development*, 11(3):1059–1076. DOI:10.5194/gmd-11-1059-2018.
- Kerkweg, A. and Jöckel, P. (2012). The 1-way on-line coupled atmospheric chemistry model system MECO(n) – part 1: Description of the limited-area atmospheric chemistry model COSMO/MESSy. *Geoscientific Model Development*, 5(1):87–110. DOI:10.5194/gmd-5-87-2012.
- Kerkweg, A. and Jöckel, P. (2015). The infrastructure MESSy submodels GRID (v1.0) and IMPORT (v1.0). *GMD*. DOI:10.5194/gmdd-8-8607-2015.
- Kerkweg, A., Sander, R., Tost, H., and Jöckel, P. (2006b). Technical note: Implementation of prescribed (OFFLEM), calculated (ONLEM), and pseudo-emissions (TNUDGE) of chemical species in the Modular Earth Submodel System (MESSy). *Atmospheric Chemistry and Physics*, 6(11):3603–3609. DOI:10.5194/acp-6-3603-2006.
- Khaykin, S. M., de Laat, A. T. J., Godin-Beekmann, S., Hauchecorne, A., and Ratynski, M. (2022). Unexpected self-lofting and dynamical confinement of volcanic plumes: the Raikoke 2019 case. *Scientific Reports*, 12(1). DOI:10.1038/s41598-022-27021-0.
- Kim, J., Jeong, U., Ahn, M.-H., Kim, J. H., Park, R. J., Lee, H., Song, C. H., Choi, Y.-S., Lee, K.-H., Yoo, J.-M., Jeong, M.-J., Park, S. K., Lee, K.-M., Song, C.-K., Kim, S.-W., Kim, Y. J., Kim, S.-W., Kim, M., Go, S., Liu, X., Chance, K., Chan Miller, C., Al-Saadi, J., Veihelmann, B., Bhartia, P. K., Torres, O., Abad, G. G., Haffner, D. P., Ko, D. H., Lee, S. H., Woo, J.-H., Chong, H., Park, S. S., Nicks, D., Choi, W. J., Moon, K.-J., Cho, A., Yoon, J., Kim, S.-k., Hong, H., Lee, K., Lee, H., Lee, S., Choi, M., Veefkind, P., Levelt, P. F., Edwards, D. P., Kang, M., Eo, M., Bak, J., Baek, K., Kwon, H.-A., Yang, J., Park, J., Han, K. M., Kim, B.-R., Shin, H.-W., Choi, H., Lee, E., Chong, J., Cha, Y., Koo, J.-H., Irie, H., Hayashida, S., Kasai, Y., Kanaya, Y., Liu, C., Lin, J., Crawford, J. H., Carmichael, G. R., Newchurch, M. J., Lefer, B. L., Herman, J. R., Swap, R. J., Lau, A. K. H., Kurosu, T. P., Jaross, G., Ahlers, B., Dobber, M., McElroy, C. T., and Choi, Y. (2020). New Era of Air Quality Monitoring from Space: Geostationary Environment Monitoring Spectrometer (GEMS). *Bulletin of the American Meteorological Society*, 101(1):E1–E22. DOI:10.1175/bams-d-18-0013.1.
- Klimarechenzentrum, D. (1993). The ECHAM3 Atmospheric General Circulation Model. World Data Center for Climate (WDCC) at DKRZ. *Techn. Rep*, 6. DOI:10.2312/WDCC/DKRZ_Report_No06 (last access: 06.08.2024).
- Kloss, C., Berthet, G., Sellitto, P., Ploeger, F., Taha, G., Tidiga, M., Eremenko, M., Bossolasco, A., Jégou, F., Renard, J.-B., and Legras, B. (2021). Stratospheric aerosol layer perturbation caused by the 2019 Raikoke and Ulawun eruptions and their radiative forcing. *Atmospheric Chemistry and Physics*, 21(1):535–560. DOI:10.5194/acp-21-535-2021.

- Koch, D., Jacob, D., Tegen, I., Rind, D., and Chin, M. (1999). Tropospheric sulfur simulation and sulfate direct radiative forcing in the Goddard Institute for Space Studies general circulation model. *Journal of Geophysical Research: Atmospheres*, 104(D19):23799–23822. DOI:10.1029/1999jd900248.
- Krishna-Pillai Sukumara-Pillai, K., Bala, G., Cao, L., Duan, L., and Caldeira, K. (2019). Climate system response to stratospheric sulfate aerosols: Sensitivity to altitude of aerosol layer. *EGU*. DOI:10.5194/esd-2019-21.
- Kumar, V., Remmers, J., Beirle, S., Fallmann, J., Kerkweg, A., Lelieveld, J., Mertens, M., Pozzer, A., Steil, B., Barra, M., Tost, H., and Wagner, T. (2021). Evaluation of the coupled high-resolution atmospheric chemistry model system MECO(n) using in situ and MAX-DOAS NO₂ measurements. *Atmospheric Measurement Techniques*, 14(7):5241–5269. DOI:10.5194/amt-14-5241-2021.
- Kuribayashi, M., Ohara, T., Morino, Y., Uno, I., Kurokawa, J.-i., and Hara, H. (2012). Long-term trends of sulfur deposition in East Asia during 1981–2005. *Atmospheric Environment*, 59:461–475. DOI:10.1016/j.atmosenv.2012.04.060.
- Lamarque, J.-F., Bond, T. C., Eyring, V., Granier, C., Heil, A., Klimont, Z., Lee, D., Lioussé, C., Mieville, A., Owen, B., Schultz, M. G., Shindell, D., Smith, S. J., Stehfest, E., Van Aardenne, J., Cooper, O. R., Kainuma, M., Mahowald, N., McConnell, J. R., Naik, V., Riahi, K., and van Vuuren, D. P. (2010). Historical (1850–2000) gridded anthropogenic and biomass burning emissions of reactive gases and aerosols: methodology and application. *Atmospheric Chemistry and Physics*, 10(15):7017–7039. DOI:10.5194/acp-10-7017-2010.
- Lana, A., Bell, T. G., Simó, R., Vallina, S. M., Ballabrera-Poy, J., Kettle, A. J., Dachs, J., Bopp, L., Saltzman, E. S., Stefels, J., Johnson, J. E., and Liss, P. S. (2011). An updated climatology of surface dimethylsulfide concentrations and emission fluxes in the global ocean: UPDATED DMS CLIMATOLOGY. *Global Biogeochemical Cycles*, 25(1). DOI:10.1029/2010gb003850.
- Lappalainen, H. K., Kerminen, V.-M., Petäjä, T., Kurten, T., Baklanov, A., Shvidenko, A., Bäck, J., Vihma, T., Alekseychik, P., Arnold, S., Arshinov, M., Asmi, E., Belan, B., Bobylev, L., Chalov, S., Cheng, Y., Chubarova, N., de Leeuw, G., Ding, A., Dobrolyubov, S., Dubtsov, S., Dyukarev, E., Elansky, N., Eleftheriadis, K., Esau, I., Filatov, N., Flint, M., Fu, C., Glezer, O., Gliko, A., Heimann, M., Holtslag, A. A. M., Hörrak, U., Janhunen, J., Juhola, S., Järvi, L., Järvinen, H., Kanukhina, A., Konstantinov, P., Kotlyakov, V., Kieloaho, A.-J., Komarov, A. S., Kujansuu, J., Kukkonen, I., Kyrö, E., Laaksonen, A., Laurila, T., Lihavainen, H., Lisitzin, A., Mahura, A., Makshtas, A., Mareev, E., Mazon, S., Matishov, D., Melnikov, V., Mikhailov, E., Moisseev, D., Nigmatulin, R., Noe, S. M., Ojala, A., Pihlatie, M., Popovicheva, O., Pumpanen, J., Regerand, T., Repina, I., Shcherbinin, A., Shevchenko, V., Sipilä, M., Skorokhod, A., Spracklen, D. V., Su, H., Subetto, D. A., Sun, J., Terzhevskiy, A. Y., Timofeyev, Y., Troitskaya, Y.,

- Tynkkynen, V.-P., Kharuk, V. I., Zaytseva, N., Zhang, J., Viisanen, Y., Vesala, T., Hari, P., Hansson, H. C., Matvienko, G. G., Kasimov, N. S., Guo, H., Bondur, V., Zilitinkevich, S., and Kulmala, M. (2016). Pan–Eurasian Experiment (PEEX): Towards holistic understanding of the feedbacks and interactions in the land–atmosphere–ocean–society continuum in the Northern Eurasian region. *EGU*. DOI:10.5194/acp-2016-186.
- Lee, C., Martin, R. V., van Donkelaar, A., Lee, H., Dickerson, R. R., Hains, J. C., Krotkov, N., Richter, A., Vinnikov, K., and Schwab, J. J. (2011). SO₂ emissions and lifetimes: Estimates from inverse modeling using in situ and global, space-based (SCIAMACHY and OMI) observations. *Journal of Geophysical Research*, 116(D6). DOI:10.1029/2010jd014758.
- Lee, P. and Ngan, F. (2011). Coupling of important physical processes in the planetary boundary layer between meteorological and chemistry models for regional to continental scale air quality forecasting: An overview. *Atmosphere*, 2(3):464–483. DOI:10.3390/atmos2030464.
- Likens, G. E., Wright, R. F., Galloway, J. N., and Butler, T. J. (1979). Acid rain. *Scientific American*, 241(4):43–51. DOI:10.1038/scientificamerican1079-43.
- Lin, S.-J. and Rood, R. B. (1996). Multidimensional Flux–Form Semi–Lagrangian Transport Schemes. *Monthly Weather Review*, 124(9):2046–2070. DOI:10.1175/1520-0493(1996)124<2046:MFFSLT>2.0.CO;2.
- Liu, F., Choi, S., Li, C., Fioletov, V. E., McLinden, C. A., Joiner, J., Krotkov, N. A., Bian, H., Janssens-Maenhout, G., Darmenov, A. S., and da Silva, A. M. (2018). A new global anthropogenic SO₂ emission inventory for the last decade: a mosaic of satellite-derived and bottom–up emissions. *Atmospheric Chemistry and Physics*, 18(22):16571–16586. DOI:10.5194/acp-18-16571-2018.
- Liu, X., Wang, Y., Wasti, S., Li, W., Soleimanian, E., Flynn, J., Griggs, T., Alvarez, S., Sullivan, J. T., Roots, M., Twigg, L., Gronoff, G., Berkoff, T., Walter, P., Estes, M., Hair, J. W., Shingler, T., Scarino, A. J., Fenn, M., and Judd, L. (2023). Evaluating WRF–GC v2.0 predictions of boundary layer height and vertical ozone profile during the 2021 TRACER-AQ campaign in Houston, Texas. *Geoscientific Model Development*, 16(18):5493–5514. DOI:10.5194/gmd-16-5493-2023.
- Lowe, D. and MacKenzie, A. R. (2008). Polar stratospheric cloud microphysics and chemistry. *Journal of Atmospheric and Solar-Terrestrial Physics*, 70(1):13–40. DOI:10.1016/j.jastp.2007.09.011.
- Lu, Z., Streets, D. G., Zhang, Q., Wang, S., Carmichael, G. R., Cheng, Y. F., Wei, C., Chin, M., Diehl, T., and Tan, Q. (2010). Sulfur dioxide emissions in China and sulfur trends in East Asia since 2000. *Atmospheric Chemistry and Physics*, 10(13):6311–6331. DOI:10.5194/acp-10-6311-2010.

- McInnes, G. (2001). EMEP/CORINAIR Emission Inventory Guidebook – 3rd edition. *European Environment Agency, Technical report No 30*. Available at: http://reports.eea.eu.int/technical_report_2001_3/en (last access: 12.07.2024).
- McKee, K., Smith, C. M., Reath, K., Snee, E., Maher, S., Matoza, R. S., Carn, S., Roman, D. C., Mastin, L., Anderson, K., Damby, D., Itikarai, I., Mulina, K., Saunders, S., Assink, J. D., de Negri Leiva, R., and Perttu, A. (2021). Evaluating the state-of-the-art in remote volcanic eruption characterization Part II: Ulawun volcano, Papua New Guinea. *Journal of Volcanology and Geothermal Research*, 420:107381. DOI:10.1016/j.jvolgeores.2021.107381.
- Mertens, M., Kerkweg, A., Grewe, V., Jöckel, P., and Sausen, R. (2020). Attributing ozone and its precursors to land transport emissions in Europe and Germany. *Atmospheric Chemistry and Physics*, 20(13):7843–7873. DOI:10.5194/acp-20-7843-2020.
- Mertens, M., Kerkweg, A., Jöckel, P., Tost, H., and Hofmann, C. (2016). The 1-way on-line coupled model system MECO(n) – part 4: Chemical evaluation (based on MESSy v2.52). *Geoscientific Model Development*, 9(10):3545–3567. DOI:10.5194/gmd-9-3545-2016.
- Meyers, T. P., Finkelstein, P., Clarke, J., Ellestad, T. G., and Sims, P. F. (1998). A multilayer model for inferring dry deposition using standard meteorological measurements. *Journal of Geophysical Research: Atmospheres*, 103(D17):22645–22661. DOI:10.1029/98jd01564.
- Morgenstern, O., Hegglin, M. I., Rozanov, E., O’Connor, F. M., Abraham, N. L., Akiyoshi, H., Archibald, A. T., Bekki, S., Butchart, N., Chipperfield, M. P., Deushi, M., Dhomse, S. S., Garcia, R. R., Hardiman, S. C., Horowitz, L. W., Jöckel, P., Josse, B., Kinnison, D., Lin, M., Mancini, E., Manyin, M. E., Marchand, M., Marécal, V., Michou, M., Oman, L. D., Pitari, G., Plummer, D. A., Revell, L. E., Saint-Martin, D., Schofield, R., Stenke, A., Stone, K., Sudo, K., Tanaka, T. Y., Tilmes, S., Yamashita, Y., Yoshida, K., and Zeng, G. (2017). Review of the global models used within phase 1 of the Chemistry—Climate Model Initiative (CCMI). *Geoscientific Model Development*, 10(2):639–671. DOI:10.5194/gmd-10-639-2017.
- Mulcahy, J. P., Johnson, C., Jones, C. G., Povey, A. C., Scott, C. E., Sellar, A., Turnock, S. T., Woodhouse, M. T., Abraham, N. L., Andrews, M. B., Bellouin, N., Browse, J., Carslaw, K. S., Dalvi, M., Folberth, G. A., Glover, M., Grosvenor, D. P., Hardacre, C., Hill, R., Johnson, B., Jones, A., Kipling, Z., Mann, G., Mollard, J., O’Connor, F. M., Palmiéri, J., Reddington, C., Rumbold, S. T., Richardson, M., Schutgens, N. A. J., Stier, P., Stringer, M., Tang, Y., Walton, J., Woodward, S., and Yool, A. (2020). Description and evaluation of aerosol in UKESM1 and HadGEM3-GC3.1 CMIP6 historical simulations. *Geoscientific model development*, 13(12):6383–6423. DOI:10.5194/gmd-13-6383-2020.

- Muser, L. O., Hoshyaripour, G. A., Bruckert, J., Horváth, Á., Malinina, E., Wallis, S., Prata, F. J., Rozanov, A., von Savigny, C., Vogel, H., and Vogel, B. (2020). Particle aging and aerosol–radiation interaction affect volcanic plume dispersion: evidence from the Raikoke 2019 eruption. *Atmospheric Chemistry and Physics*, 20(23):15015–15036. DOI:10.5194/acp-20-15015-2020.
- Myhre, G., Berglen, T. F., Myhre, C. E. L., and Isaksen, I. S. (2004). The radiative effect of the anthropogenic influence on the stratospheric sulfate aerosol layer. *Tellus B: Chemical and Physical Meteorology*, 56(3):294. DOI:10.3402/tellusb.v56i3.16431.
- Nickl, A.-L., Mertens, M., Roiger, A., Fix, A., Amediek, A., Fiehn, A., Gerbig, C., Galkowski, M., Kerkweg, A., Klausner, T., Eckl, M., and Jöckel, P. (2020). Hindcasting and forecasting of regional methane from coal mine emissions in the Upper Silesian Coal Basin using the online nested global regional chemistry–climate model MECO(n) (MESSy v2.53). *Geoscientific Model Development*, 13(4):1925–1943. DOI:10.5194/gmd-13-1925-2020.
- Nordborg, M., Arvidsson, R., Finnveden, G., Cederberg, C., Sörme, L., Palm, V., Stamy, K., and Molander, S. (2017). Updated indicators of Swedish national human toxicity and ecotoxicity footprints using USEtox 2.01. *Environmental Impact Assessment Review*, 62:110–114. DOI:10.1016/j.eiar.2016.08.004.
- Ohara, T., Akimoto, H., Kurokawa, J., Horii, N., Yamaji, K., Yan, X., and Hayasaka, T. (2007). An Asian emission inventory of anthropogenic emission sources for the period 1980–2020. *Atmospheric Chemistry and Physics*, 7(16):4419–4444. DOI:10.5194/acp-7-4419-2007.
- Ohizumi, T. (2023). *Acid Deposition Monitoring Network in East Asia (EANET)*, pages 157–166. Springer Nature Singapore. DOI:10.1007/978-981-15-2760-9_11.
- Palmer, P. I., Jacob, D. J., Chance, K., Martin, R. V., Spurr, R. J. D., Kurosu, T. P., Bey, I., Yantosca, R., Fiore, A., and Li, Q. (2001). Air mass factor formulation for spectroscopic measurements from satellites: Application to formaldehyde retrievals from the global ozone monitoring experiment. *Journal of Geophysical Research: Atmospheres*, 106(D13):14539–14550. DOI:10.1029/2000jd900772.
- Penner, J., Andreae, M., Annegarn, H., Barrie, L., Feichter, J., Hegg, D., Achuthan, J., Leaitch, R., Murphy, D., Nganga, J., and Pitari, G. (2001). Aerosols, their direct and indirect effects. *Climate Change 2001: The Scientific Basis. Contribution of Working Group I to the Third Assessment Report of the Intergovernmental Panel on Climate Change, 289-348 (2001)*.
- Platt, U. and Stutz, J. (2008). *Differential Absorption Spectroscopy*, pages 135–174. Springer Berlin Heidelberg. DOI:10.1007/978-3-540-75776-4_6.

- Pope, R. J., Hardacre, C., Li, C., and Chipperfield, M. P. (2021). United Kingdom Earth System Model – Ozone Monitoring Instrument Total Column Sulphur Dioxide Comparisons. Tech. rep., Prepared for U.K. Met Office Hadley Centre, Met Office, Exeter, EX1 3PB, UK. Available at: https://digital.nmla.metoffice.gov.uk/io_697df5d9-e371-4492-82b9-12f9cfce64d7/ (last access: 14.12.2021).
- Pöschl, U., von Kuhlmann, R., Poisson, N., and Crutzen, P. J. (2000). Development and intercomparison of condensed isoprene oxidation mechanisms for global atmospheric modeling. *Journal of Atmospheric Chemistry*, 37(1):29–52. DOI:10.1023/a:1006391009798.
- Pozzer, A., Jöckel, P., Sander, R., Williams, J., Ganzeveld, L., and Lelieveld, J. (2006). Technical note: The MESSy-submodel AIRSEA calculating the air-sea exchange of chemical species. *Atmospheric Chemistry and Physics*, 6(12):5435–5444. DOI:10.5194/acp-6-5435-2006.
- Qu, Z., Henze, D. K., Li, C., Theys, N., Wang, Y., Wang, J., Wang, W., Han, J., Shim, C., Dickerson, R. R., and Ren, X. (2019). SO₂ Emission Estimates Using OMI SO₂ Retrievals for 2005–2017. *Journal of Geophysical Research: Atmospheres*, 124(14):8336–8359. DOI:10.1029/2019jd030243.
- Ramanathan, V. (2020). Climate change, air pollution, and health: Common sources, similar impacts, and common solutions. In *Health of People, Health of Planet and Our Responsibility*, pages 49–59. Springer International Publishing. DOI:10.1007/978-3-030-31125-4_5.
- Randel, W. J. and Jensen, E. J. (2013). Physical processes in the tropical tropopause layer and their roles in a changing climate. *Nature Geoscience*, 6(3):169–176. DOI:10.1038/ngeo1733.
- Riahi, K., van Vuuren, D. P., Kriegler, E., Edmonds, J., O’Neill, B. C., Fujimori, S., Bauer, N., Calvin, K., Dellink, R., Fricko, O., Lutz, W., Popp, A., Cuaresma, J. C., KC, S., Leimbach, M., Jiang, L., Kram, T., Rao, S., Emmerling, J., Ebi, K., Hasegawa, T., Havlik, P., Humpenöder, F., Da Silva, L. A., Smith, S., Stehfest, E., Bosetti, V., Eom, J., Gernaat, D., Masui, T., Rogelj, J., Strefler, J., Drouet, L., Krey, V., Luderer, G., Harmsen, M., Takahashi, K., Baumstark, L., Doelman, J. C., Kainuma, M., Klimont, Z., Marangoni, G., Lotze-Campen, H., Obersteiner, M., Tabeau, A., and Tavoni, M. (2017). The shared socioeconomic pathways and their energy, land use, and greenhouse gas emissions implications: An overview. *Global Environmental Change*, 42:153–168. DOI:10.1016/j.gloenvcha.2016.05.009.
- Richter, A., Wittrock, F., and Burrows, J. P. (2006). SO₂ measurements with SCIAMACHY. In *Proc. Atmospheric Science Conference*, pages 8–12.
- Rockel, B., Will, A., and Hense, A. (2008). The regional climate model COSMO-CLM (CCLM). *Meteorologische Zeitschrift*, 17(4):347–348. DOI:10.1127/0941-2948/2008/0309.

- Röckner, E., Arpe, K., Bengtsson, L., Christoph, M., Claussen, M., Dümenil, L., Esch, M., Giorgetta, M., Schlese, U., and Schulzweida, U. (1996). The atmospheric general circulation model ECHAM-4: Model description and simulation of present-day climate. *Max-Planck-Inst. für Meteorologie, Hamburg, Germany*. Tech. Rep. 218.
- Röckner, E., Bäuml, G., Bonaventura, L., Brokopf, R., Giorgetta, M. E., Hagemann, S., Kirchner, I., Manzini, L. K., Rhodin, A., Schlese, U., Schulzweida, U., and Tompkins, A. (2003). The atmospheric general circulation model ECHAM5—Part I: Model description. *Max Planck Institute for Meteorology Report 349*. Available at: https://pure.mpg.de/rest/items/item_995269_4/component/file_995268/content (last access: 12.07.2024).
- Röckner, E., Brokopf, R., Esch, M., Giorgetta, M., Hagemann, S., Kornblüeh, L., Manzini, E., Schlese, U., and Schulzweida, U. (2006). Sensitivity of simulated climate to horizontal and vertical resolution in the ECHAM5 atmosphere model. *Journal of Climate*, 19(16):3771–3791. DOI:10.1175/jcli3824.1.
- Rodgers, C. D. (2000). *Inverse Methods for Atmospheric Sounding: Theory and Practice*. WORLD SCIENTIFIC. DOI:10.1142/3171.
- Rollins, A. W., Thornberry, T. D., Watts, L. A., Yu, P., Rosenlof, K. H., Mills, M., Baumann, E., Giorgetta, F. R., Bui, T. V., Höpfner, M., Walker, K. A., Boone, C., Bernath, P. F., Colarco, P. R., Newman, P. A., Fahey, D. W., and Gao, R. S. (2017). The role of sulfur dioxide in stratospheric aerosol formation evaluated by using in situ measurements in the tropical lower stratosphere. *Geophysical Research Letters*, 44(9):4280–4286. DOI:10.1002/2017gl072754.
- Romahn, F., Pedergnana, M., Loyola, D., Apituley, A., Snee, M., and Veeffkind, P. J. (2023). Sentinel-5 precursor/TROPOMI Level 2 Product User Manual Sulphur Dioxide SO₂. Technical report, BIRA-IASB.
- Ronald, Johannes Van der A ;Mijling, B., Ding, J., Koukouli, M. E., Liu, F., Li, Q., Mao, H., and Theys, N. (2016). Cleaning up the air: effectiveness of air quality policy for SO₂ and NO_x emissions in China. *Atmos. Chem. Phys.* DOI:10.5194/acp-2016-445.
- Sander, R., Baumgärtner, A., Cabrera-Perez, D., Frank, F., Gromov, S., Groß, J.-U., Harder, H., Huijnen, V., Jöckel, P., Karydis, V. A., Niemeyer, K. E., Pozzer, A., Riede, H., Schultz, M. G., Taraborrelli, D., and Tauer, S. (2019). The community atmospheric chemistry box model CAABA/MECCA-4.0. *Geoscientific Model Development*, 12(4):1365–1385. DOI:10.5194/gmd-12-1365-2019.
- Sander, R., Kerkweg, A., Jöckel, P., and Lelieveld, J. (2005). Technical note: The new comprehensive atmospheric chemistry module MECCA. *Atmospheric Chemistry and Physics*, 5(2):445–450. DOI:10.5194/acp-5-445-2005.

- Sandu, A. and Sander, R. (2006). Technical note: Simulating chemical systems in Fortran90 and Matlab with the Kinetic PreProcessor KPP-2.1. *Atmospheric Chemistry and Physics*, 6(1):187–195. DOI:10.5194/acp-6-187-2006.
- Saylor, R. D., Wolfe, G. M., Meyers, T. P., and Hicks, B. B. (2014). A corrected formulation of the Multilayer Model (MLM) for inferring gaseous dry deposition to vegetated surfaces. *Atmospheric Environment*, 92:141–145. DOI:10.1016/j.atmosenv.2014.03.056.
- Seinfeld, J. H. and Pandis, S. N. (2006). *Atmospheric chemistry and physics: from air pollution to climate change*. John Wiley & Sons.
- Smirnov, S., Nizametdinov, I., Timina, T., Kotov, A., Sekisova, V., Kuzmin, D., Kalacheva, E., Rashidov, V., Rybin, A., Lavrenchuk, A., Degterev, A., Maksimovich, I., and Abersteiner, A. (2021). High explosivity of the June 21, 2019 eruption of Raikoke volcano (Central Kuril Islands); mineralogical and petrological constraints on the pyroclastic materials. *Journal of Volcanology and Geothermal Research*, 418:107346. DOI:10.1016/j.jvolgeores.2021.107346.
- Smith, S. J., Pitcher, H., and Wigley, T. (2001). Global and regional anthropogenic sulfur dioxide emissions. *Global and Planetary Change*, 29(1–2):99–119. DOI:10.1016/S0921-8181(00)00057-6.
- Smith, T. W., Jalkanen, J. P., Anderson, B. A., Corbett, J. J., Faber, J., Hanayama, S., O’Keeffe, E., Parker, S., Johansson, L., Aldous, L., Raucci, C., Traut, M., Ettinger, S., Nelissen, D., Lee, D. S., Ng, S., Agrawal, A., Winebrake, J. J., Hoen, M., Chesworth, S., and Pandey, A. (2021). Third IMO GHG study. Tech. rep., International Maritime Organization (IMO). Available at: <https://www.imo.org/en/ourwork/environment/pages/greenhouse-gas-studies-2014.aspx> (last access: 12.07.2024).
- Solomon, S. (1999). Stratospheric ozone depletion: A review of concepts and history. *Reviews of Geophysics*, 37(3):275–316. DOI:10.1029/1999rg900008.
- Sörme, L., Palm, V., and Finnveden, G. (2016). Using E-PRTR data on point source emissions to air and water—First steps towards a national chemical footprint. *Environmental Impact Assessment Review*, 56:102–112. DOI:10.1016/j.eiar.2015.09.007.
- SPARC (2006). SPARC Assessment of Stratospheric Aerosol Properties (ASAP). Report 4, SPARC. WCRP-124, WMO/TD – No. 1295, available at <http://www.sparc-climate.org/publications/sparc-reports/> (last access: 14.05.2024).
- Spiro, P. A., Jacob, D. J., and Logan, J. A. (1992). Global inventory of sulfur emissions with $1^\circ \times 1^\circ$ resolution. *Journal of Geophysical Research: Atmospheres*, 97(D5):6023–6036. DOI:10.1029/91jd03139.
- Spurr, R., Kurosu, T., and Chance, K. (2001). A linearized discrete ordinate radiative transfer model for atmospheric remote-sensing retrieval. *Journal of Quantitative Spectroscopy and Radiative Transfer*, 68(6):689–735. DOI:10.1016/S0022-4073(00)00055-8.

- Stark, H. R., Moeller, H., Courreges-Lacoste, G., Koopman, R., Mezzasoma, S., and Veihelmann, B. (2013). The Sentinel-4 mission and its implementation. In *ESA Living Planet Symposium*, volume 722, page 139. Vol. 722 of ESA Special Publication Edinburgh, UK.
- Steppeler, J., Doms, G., Schättler, U., Bitzer, H. W., Gassmann, A., Damrath, U., and Gregoric, G. (2003). Meso-gamma scale forecasts using the nonhydrostatic model LM. *Meteorology and Atmospheric Physics*, 82(1-4):75–96. DOI:10.1007/s00703-001-0592-9.
- Stevenson, D. S., Johnson, C. E., Collins, W. J., and Derwent, R. G. (2003). The tropospheric sulphur cycle and the role of volcanic SO₂. *Geological Society, London, Special Publications*, 213(1):295–305. 10.1144/gsl.sp.2003.213.01.18.
- Stocker, T., Qin, D., Plattner, G.-K., Tignor, M., Allen, S., Boschung, J., Nauels, A., Xia, Y., Bex, V., and Midgley, P. (2013). IPCC, 2013: Climate Change 2013: The Physical Science Basis. contribution of Working Group I to the Fifth Assessment Report of the Intergovernmental Panel on Climate Change. Technical report, Cambridge University Press, Cambridge, United Kingdom and New York, NY, USA.
- Stockwell, W. R. and Calvert, J. G. (1983). The mechanism of the HO–SO₂ reaction. *Atmospheric Environment (1967)*, 17(11):2231–2235. DOI:10.1016/0004-6981(83)90220-2.
- Taylor, K. E., Stouffer, R. J., and Meehl, G. A. (2012). An overview of CMIP5 and the Experiment Design. *Bulletin of the American Meteorological Society*, 93(4):485–498. DOI:10.1175/bams-d-11-00094.1.
- Textor, C., Schulz, M., Guibert, S., Kinne, S., Balkanski, Y., Bauer, S., Berntsen, T., Berglen, T., Boucher, O., Chin, M., Dentener, F., Diehl, T., Easter, R., Feichter, H., Fillmore, D., Ghan, S., Ginoux, P., Gong, S., Grini, A., Hendricks, J., Horowitz, L., Huang, P., Isaksen, I., Iversen, I., Kloster, S., Koch, D., Kirkevåg, A., Kristjansson, J. E., Krol, M., Lauer, A., Lamarque, J. F., Liu, X., Montanaro, V., Myhre, G., Penner, J., Pitari, G., Reddy, S., Seland, O., Stier, P., Takemura, T., and Tie, X. (2006). Analysis and quantification of the diversities of aerosol life cycles within AeroCom. *Atmospheric Chemistry and Physics*, 6(7):1777–1813. DOI:10.5194/acp-6-1777-2006.
- Theys, N. (2023). S5P COBRA Sulphur Dioxide [L2_SO2-CBR_] Readme. Technical Report S5P-BIRA-PRF-SO2CBR, BIRA-IASB.
- Theys, N., De Smedt, I., Yu, H., Danckaert, T., van Gent, J., Hörmann, C., Wagner, T., Hedelt, P., Bauer, H., Romahn, F., Pedergnana, M., Loyola, D., and Van Roozendaal, M. (2017). Sulfur dioxide retrievals from TROPOMI onboard Sentinel-5 Precursor: algorithm theoretical basis. *Atmospheric Measurement Techniques*, 10(1):119–153. DOI:10.5194/amt-10-119-2017.
- Theys, N., Fioletov, V., Li, C., De Smedt, I., Lerot, C., McLinden, C., Krotkov, N., Griffin, D., Clarisse, L., Hedelt, P., Loyola, D., Wagner, T., Kumar, V., Innes, A., Ribas,

- R., Hendrick, F., Vlietinck, J., Brenot, H., and Van Roozendael, M. (2021). A sulfur dioxide Covariance-Based Retrieval Algorithm (COBRA): application to TROPOMI reveals new emission sources. *Atmospheric Chemistry and Physics*, 21(22):16727–16744. DOI:10.5194/acp-21-16727-2021.
- Theys, N., Isabelle, D. S., Christophe, L., Huan, Y., Michel, V. R., and Pascal, H. (2022). S5P/TROPOMI SO₂ ATBD. Technical Report S5P-BIRA-L2-400E-ATBD, BIRA-IASB.
- Thomas, W., Aberle, B., Balzer, W., Loyola, D., Mikusch, E., Ruppert, T., Schmid, C., Slijkhuis, S., Spurr, R. J. D., Tuerk, A., and Wolflueller, M. (1996). Ground segment of ERS-2 and GOME Sensor at the german D-PAF. In Fischer, J., editor, *Satellite Remote Sensing and Modeling of Clouds and the Atmosphere*. SPIE. DOI:10.1117/12.262487.
- Tidiga, M., Berthet, G., Jégou, F., Kloss, C., Bègue, N., Vernier, J.-P., Renard, J.-B., Bos-solasco, A., Clarisse, L., Taha, G., Portafaix, T., Deshler, T., Wienhold, F. G., Godin-Beekmann, S., Payen, G., Metzger, J.-M., Dufflot, V., and Marquestaut, N. (2022). Variability of the aerosol content in the tropical lower stratosphere from 2013 to 2019: Evidence of volcanic eruption impacts. *Atmosphere*, 13(2):250. DOI:10.3390/atmos13020250.
- Tørseth, K., Aas, W., Breivik, K., Fjæraa, A. M., Fiebig, M., Hjellbrekke, A. G., Lund Myhre, C., Solberg, S., and Yttri, K. E. (2012). Introduction to the European Monitoring and Evaluation Programme (EMEP) and observed atmospheric composition change during 1972–2009. *Atmospheric Chemistry and Physics*, 12(12):5447–5481. DOI:10.5194/acp-12-5447-2012.
- Tost, H., Jöckel, P., Kerkweg, A., Sander, R., and Lelieveld, J. (2006). Technical note: A new comprehensive scavenging submodel for global atmospheric chemistry modelling. *Atmospheric Chemistry and Physics*, 6(3):565–574. DOI:10.5194/acp-6-565-2006.
- United Nations Office for Disaster Risk Reduction (2021). Terminology: Disaster risk reduction. <https://www.undrr.org/understanding-disaster-risk/terminology/hips/mh0033> (Last access: 21.06.2024).
- U.S. National Park Service (2023). Human Health – Sulfur Dioxide. <https://www.nps.gov/subjects/air/humanhealth-sulfur.htm> (Last access: 21.06.2024).
- Vallina, S. M. and Simó, R. (2007). Strong Relationship Between DMS and the Solar Radiation Dose over the Global Surface Ocean. *Science*, 315(5811):506–508. DOI:10.1126/science.1133680.
- van Aardenne, J. and Pulles, T. (2002). Uncertainty in emission inventories: What do we mean and how could we assess it? *TNO Institute of Environmental Sciences, Energy and Process Innovation*.
- van Geffen, J. H. G. M., Boersma, K. F., Eskes, H. J., Maasakkers, J. D., and Veefkind, J. P. (2016). TROPOMI ATBD of the total and tropospheric NO₂ data products. *Royal Netherlands Meteorological Institute*.

- Van Roy, W., Van Roozendaal, B., Vigin, L., Van Nieuwenhove, A., Scheldeman, K., Merveille, J.-B., Weigelt, A., Mellqvist, J., Van Vliet, J., van Dinther, D., Beecken, J., Tack, F., Theys, N., and Maes, F. (2023). International maritime regulation decreases sulfur dioxide but increases nitrogen oxide emissions in the north and baltic sea. *Communications Earth & Environment*, 4(1). DOI:10.1038/s43247-023-01050-7.
- van Vuuren, D. P., Edmonds, J., Kainuma, M., Riahi, K., Thomson, A., Hibbard, K., Hurtt, G. C., Kram, T., Krey, V., Lamarque, J.-F., Masui, T., Meinshausen, M., Nakicenovic, N., Smith, S. J., and Rose, S. K. (2011). The representative concentration pathways: an overview. *Climatic Change*, 109(1–2):5–31. DOI:10.1007/s10584-011-0148-z.
- Vaughan, G., Wareing, D., and Ricketts, H. (2021). Measurement Report: Lidar measurements of stratospheric aerosol following the 2019 Raikoke and Ulawun volcanic eruptions. *Atmospheric Chemistry and Physics*, 21(7):5597–5604. DOI:10.5194/acp-21-5597-2021.
- Veefkind, J., Aben, I., McMullan, K., Förster, H., de Vries, J., Otter, G., Claas, J., Eskes, H., de Haan, J., Kleipool, Q., van Weele, M., Hasekamp, O., Hoogeveen, R., Landgraf, J., Snel, R., Tol, P., Ingmann, P., Voors, R., Kruizinga, B., Vink, R., Visser, H., and Levelt, P. (2012). TROPOMI on the ESA Sentinel-5 Precursor: A GMES mission for global observations of the atmospheric composition for climate, air quality and ozone layer applications. *Remote Sensing of Environment*, 120:70–83. DOI:10.1016/j.rse.2011.09.027.
- von Glasow, R., Bobrowski, N., and Kern, C. (2009). The effects of volcanic eruptions on atmospheric chemistry. *Chemical Geology*, 263(1–4):131–142. DOI:10.1016/j.chemgeo.2008.08.020.
- Warneck, P. (1999). The relative importance of various pathways for the oxidation of sulfur dioxide and nitrogen dioxide in sunlit continental fair weather clouds. *Physical Chemistry Chemical Physics*, 1(24):5471–5483. DOI:10.1039/a906555j.
- Wei, J., Li, Z., Wang, J., Li, C., Gupta, P., and Cribb, M. (2023). Ground-level gaseous pollutants (NO₂, SO₂, and CO) in China: daily seamless mapping and spatiotemporal variations. *Atmospheric Chemistry and Physics*, 23(2):1511–1532. DOI:10.5194/acp-23-1511-2023.
- Wine, P. H., Tang, Y., Thorn, R. P., Wells, J. R., and Davis, D. D. (1989). Kinetics of aqueous phase reactions of the SO₄⁻ radical with potential importance in cloud chemistry. *Journal of Geophysical Research: Atmospheres*, 94(D1):1085–1094. DOI:10.1029/jd094id01p01085.
- Wood, R., Vogt, M. A., and McCoy, I. L. (2024). Aggressive Aerosol Mitigation Policies Reduce Chances of Keeping Global Warming to Below 2C. *Earth's Future*, 12(7). DOI:10.1029/2023ef004233.

-
- Ye, C., Lu, K., Song, H., Mu, Y., Chen, J., and Zhang, Y. (2023). A critical review of sulfate aerosol formation mechanisms during winter polluted periods. *Journal of Environmental Sciences*, 123:387–399. DOI:10.1016/j.jes.2022.07.011.
- Zhang, Y., Gao, Z., Li, D., Li, Y., Zhang, N., Zhao, X., and Chen, J. (2014). On the computation of planetary boundary-layer height using the bulk Richardson number method. *Geoscientific Model Development*, 7(6):2599–2611. DOI:10.5194/gmd-7-2599-2014.
- Zhu, Y., Toon, O. B., Jensen, E. J., Bardeen, C. G., Mills, M. J., Tolbert, M. A., Yu, P., and Woods, S. (2020). Persisting volcanic ash particles impact stratospheric SO₂ lifetime and aerosol optical properties. *Nature Communications*, 11(1). DOI:10.1038/s41467-020-18352-5.
- Zoogman, P., Liu, X., Suleiman, R., Pennington, W., Flittner, D., Al-Saadi, J., Hilton, B., Nicks, D., Newchurch, M., Carr, J., Janz, S., Andraschko, M., Arola, A., Baker, B., Canova, B., Chan Miller, C., Cohen, R., Davis, J., Dussault, M., Edwards, D., Fishman, J., Ghulam, A., González Abad, G., Grutter, M., Herman, J., Houck, J., Jacob, D., Joiner, J., Kerridge, B., Kim, J., Krotkov, N., Lamsal, L., Li, C., Lindfors, A., Martin, R., McElroy, C., McLinden, C., Natraj, V., Neil, D., Nowlan, C., OSullivan, E., Palmer, P., Pierce, R., Pippin, M., Saiz-Lopez, A., Spurr, R., Szykman, J., Torres, O., Veefkind, J., Veihelmann, B., Wang, H., Wang, J., and Chance, K. (2017). Tropospheric emissions: Monitoring of pollution (TEMPO). *Journal of Quantitative Spectroscopy and Radiative Transfer*, 186:17–39. DOI:10.1016/j.jqsrt.2016.05.008.

Danksagung

Mein besonderer Dank gilt meinem Doktorvater, **Prof. Martin Dameris**. Seit dem ersten Tag unterstützte er mich bei allen wissenschaftlichen, administrativen und auch privaten Anliegen. Besonders schätze ich seine ununterbrochene Unterstützung in den letzten Monaten vor seiner Pensionierung, als er trotz seines wohlverdienten Urlaubs meine Arbeit weiterbegleitete und mir bis zum letzten Tag mit Rat und Tat zur Seite stand. Seine entspannte und freundliche Art hat mir ein gutes Gefühl gegeben und fühlte sich trotz des gegenseitigen Respekts wie mit einem besten Freund an. An dieser Stelle wünsche ich **Prof. Dameris** eine wohlverdiente und erfüllte Rentenzeit. Möge er in dieser neuen Lebensphase ebenso viel Freude und Erfolg finden, wie er es in seiner beeindruckenden wissenschaftlichen Laufbahn getan hat. Vielen Dank für alles!

Des Weiteren möchte ich mich bei **Prof. Bernhard Mayer** bedanken, der sich trotz seiner Verpflichtungen an der Universität, sowie an den Messkampagnen bereit erklärt hat, die Rolle des Zweitgutachters für diese Arbeit zu übernehmen.

Ein großes Dankeschön geht an meinen Betreuer **Dr. Patrick Jöckel**, der mich permanent bei allen technischen und inhaltlichen Fragen, insbesondere rund um das Modellsystem, unterstützt hat. Außerdem möchte ich mich herzlich für seine Korrekturen und Verbesserungsvorschläge während der Entstehung meiner Doktorarbeit bedanken.

Ebenso möchte ich mich bei **Dr. Nicolas Theys** für die wertvollen Diskussionen über die TROPOMI-Daten bedanken. Ebenfalls danke ich **Dr. Markus Kilian** für die Zusammenarbeit beim Bearbeiten der TROPOMI-Daten und für den Vergleich mit den Modell-Ergebnissen. Ein weiterer Dank gilt **Dr. Johannes De Leeuw** und unserer Abteilungsleiterin **Prof. Anja Schmidt** für die Bereitstellung der Daten zu den Vulkanausbrüchen von Raikoke und Ulawun. Zudem möchte ich mich bei **Prof. Schmidt** herzlich für ihr Interesse an meiner Arbeit und die wertvollen Meetings bedanken.

Dr. Mariano Mertens möchte ich meinen herzlichen Dank aussprechen für die Erstellung der regionalen MECO(n)-Simulation zur Evaluierung des Modells anhand der Messdaten der METHANE-To-Go-Europe Kampagne. In diesem Zusammenhang möchte ich **Dr. Heidi Huntrieser** für die Bereitstellung der Daten dieser Kampagne, sowie für ihre sorgfältige Überprüfung der Ergebnisse danken.

Ganz besonders bedanken möchte ich mich auch bei **Dr. Laura Stecher**, die mir in den letzten vier Jahren, insbesondere während der Corona-Zeit, bei all meinen anfänglichen Fragen rund um das Modell und das Programmieren zur Seite stand. Sie hat sich immer Zeit genommen, um mir zu helfen, und ihre Unterstützung erstreckte sich bis hin zur

Korrektur meiner Doktorarbeit.

Ein großes Dankeschön geht an alle Kolleginnen und Kollegen der Abteilung ESM, insbesondere an meine Bürokollegen, **Patrick Peter, Moritz Menken, Anna-Maria Götz, Sina Hofer, Georg von Bonhorst und Dario Pascal Sperber**, für die angenehme Atmosphäre sowie die wissenschaftlichen und privaten Diskussionen, die wir täglich geführt haben. Die gemeinsamen Unternehmungen, sei es bei den Mittagspausen, Weihnachtsmarktbesuchen, Spiele-, sowie Grillabenden, habe ich sehr genossen und geschätzt. Ich habe mich in der Abteilung wie zuhause gefühlt.

Im Zusammenhang mit dem Gefühl von „Zuhause“ möchte ich mich besonders bei meinen Eltern, **Khadija Lazreq und Driss Makroum**, sowie meinen Geschwistern, **Douae Makroum und Mohammed Makroum** bedanken. **Mohammed** war nach meiner ersten Operation trotz seiner beruflichen und studienbedingten Verpflichtungen sowie der Distanz stets für mich da. Er hat sich liebevoll um mich gekümmert, mich moralisch unterstützt und alles getan, um mir in diesen schwierigen Zeiten, zur Seite zu stehen. Trotz der räumlichen Entfernung war meine Familie immer an meiner Seite, hatten ein offenes Ohr für mich, wenn ich Unterstützung benötigte, und äußerten ihre wertvollen Meinungen, die mir in meinem Leben sehr geholfen haben. Sie haben mir die Freiheit gelassen, meine eigenen Wege zu gehen, und mich dabei sowohl finanziell als auch moralisch unterstützt. Ein herzliches Dankeschön geht auch an meine Frau, **Christin Galloth**, die in den letzten Jahren für mich da war, insbesondere in den Zeiten nach meinen Knie-Operationen. Sie hat alles dafür getan, dass ich mich auf meine Arbeit konzentrieren konnte, und wusste immer, wie sie mich beruhigen konnte, wenn ich gestresst war oder schlechte Laune nach Hause brachte. Sie war mein Ruhepol, an dem alles gut und friedlich war. Besonders schätze ich die täglichen gesunden Mitbringsel, die sie mir liebevoll mit auf den Weg gegeben hat. Ein besonderes Dankeschön möchte ich auch meiner zweiten Familie aussprechen, insbesondere an **Ulrike Obereisenbuchner-Galloth und Anton Galloth**, die mich wie ihren eigenen Sohn behandelt haben. Besonders in Erinnerung bleiben mir die gemeinsamen Sonntagsfrühstücke, Geburtstagsfeiern und Feiertage, an denen wir viele leckere Speisen genossen haben.

Ohne meine große und kleine Familie, sowie meine Kolleginnen und Kollegen wäre ich nicht dort, wo ich heute bin, und diese Arbeit wäre nicht entstanden. Dafür werde ich ihnen immer dankbar sein.